Study of ΣN interaction in nuclei using meson beams

博士論文

Study of ΣN interaction in nuclei using meson beams

(中間子ビームによる核内ΣN相互作用の研究)

本多 良太郎

平成２６年

Abstract

In order to study the ΣN interaction in the neutron excess environment in light nuclei, we succeeded to obtain the missing mass spectrum of the ^{6}Li(π^-, K^+)X double-charge exchange reaction from the mass region of below the Λ-binding threshold to a part of Σ quasi-free region via the ^{6}Li(π^-, K^+)X reaction at the beam momentum of 1.2 GeV/c.

The Σ-nucleus potential in light nuclei has strong isospin dependence owing to strong isospin dependence in the two-body ΣN interaction. In the present experiment, the Σ-nucleus potential strength which reflects a possible strong repulsive force in the ΣN ($s = 1, t = 3/2$) channel due to Pauli blocking between quarks can be derived from the shape analysis for the measured spectrum.

The experiment (J-PARC E10) was performed using the Superconducting Kaon Spectrometer (SKS) system at the J-PARC K1.8 beamline. Owing to a wide momentum acceptance and a good momentum resolution of the SKS system, we successfully obtained a spectrum with a missing mass resolution of 3.4 MeV/c^2 and the mass range of 5790-5920 MeV/c^2. Since the cross section below the Σ-binding threshold via the (π^-, K^+) was quite small (order of nano barn), the use of the high rate beam (5 MHz) was proposed. In the present experiment, we succeeded in handling the pion beam up to 6 MHz by installing the scintillation fiber tracker system, which we developed for high rate secondary beams. Finally, the total number of pion beam injected to the ^{6}Li target with the thickness of 3.5 g/cm^2 was 1.7×10^{12}. We obtained production cross sections of the ^{6}Li(π^-, K^+)X reaction as a function of the missing mass at the beam momentum of 1.2 GeV/c between 2-14 degrees of the reaction angle and the production cross section of $\Sigma^\pm$ via $\pi^\pm p \to K^+\Sigma^\pm$ at the beam momentum of 1.37 GeV/c between 2-16 degree.

The experimental spectra were fitted with theoretical ones calculated by T. Harada with the framework of Distorted-Wave Impulse Approximation (DWIA). By assuming the complex Σ-nucleus optical potential in the Woods-Saxon form, the optimal real and imaginary potential strengths were determined to be $+40$ and -10 MeV, respectively, which is almost consistent with the predictions from the BB interaction models based on quark picture. Further theoretical analysis is necessary because the Woods-Saxon form is not realistic in such a light nucleus. Then, more precise calculation based on few-body microscopic calculations, which based on the two-body BB interaction, is expected.

Contents

List of Figures

List of Tables

Acknowledgements

First of all, I would like to thank all the people who worked together with me, gave advice, supported, and encouraged me to complete the present work. Particularly, I would like to express my sincere thanks to my supervisor, Prof. H. Tamura, who led me to the strangeness nuclear physics. I took interest in this field by his lecture, when I was undergraduate student, and the fact that the nuclear force is not completely understood was wonderful for me. I could learn the essential knowledge to become a researcher in the graduate school. In addition, I appreciate his supports to write the present thesis.

I would like to deeply acknowledge Prof. A. Sakaguchi who is the spokesperson of the present experiment. He gladly accepted me as a member of the E10 collaboration and a doctor candidate, when I was a doctor course student. His detailed advices were quite helpful for me to analyze present data.

I would like to express my great thanks to Prof. T. Harada. I could not discuss the present experimental results and extract physics information without his theoretical calculations used in the present thesis.

I am grateful Dr. K. Miwa who taught me a lot of practical experimental techniques and analysis methods. Moreover, he gave me a lot of chance to take part in various development works such as the fiber tracker and the DAQ system. Owing to those experiences, I could get skills to construct "the system", which contains all essential components to carry out the experiment.

I would like to thank the E10 collaboration, especially, the members who worked together with me. The present experiment could not be carried out without their efforts. Dr. H. Sugimura took the most important role in this experiment. The present experiment succeeded under his leadership. I am grateful to Mr. R. Ota and Mr. S. Hayakawa for their works during the preparation and the experiment. All the detector system worked well without a trouble by their efforts. Owing to Mr. T. Soyama and Ms. M. Nakagawa, the scattered fiber tracker and BH2, which were key detectors to handle the high intensity beam, could be developed. I appreciate expert members for SSD, Dr. R. Kiuchi, Mr. C. W. Joo, and Mr. J. Y. Lee and also acknowledge Mr. S. B. Yang who was a expert of SDC3·4.

I would like to thank the Hyperball group members. We developed the beamline fiber tracker together with Mr. N. Chiga and Mr. Y. Matsumoto. I would like to acknowledge Mr. Chiga for his fiber tracker frame design. Owing to the Mr. Matsumoto's works, we obtained information, which are necessary to construct and operate the fiber tracker system. Prof. T. Koike and Dr. M. Ukai supported and encouraged me many times during wring this thesis. I would like to thank the members who participated in the experimental shift, Mr. T. O. Yamamoto, Mr. Y. Sasaki, Mr. Y. Akazawa, Mr. K. Tanabe, Mr. Y. Yamamoto, and Mr. T. Shiozaki. I am also grateful the professors of the Strangeness Nuclear Physics group, S. N. Nakamura, Y. Fujii, and M. Kaneta for their advices. I am thankful to the group members, Dr. K. Hosomi, Dr. S. Gogami, and Mr. S. Nagao, for good days spent with them.

The K1.8 beamline and SKS collaboration gave me an opportunity to participate in all the experiments performed in J-PARC K1.8, E19-1st, E19-2nd, E27, E10, and E13. From these experiments, I could learn a lot. I would like to greatly thank Prof. T. Takahashi. He managed a lot of tasks for us and valued my works in this beamline. I would like to express my thanks to Prof. M. Naruki and Prof. T. Nagae who are the spokespersons of E19 and E27, respectively. I would like to also thank collaborators, Dr. K. Shirotori, Dr. T. N. Takahashi, Dr. A. O. Tokiyasu, Mr. M. Moritsu, Mr. Y. Ichikawa, Mr. H. Ekawa,

and Mr. S. Kanatsuki. Their supports and advices were always helpful for me.

In order to develop the EASIROC readout electronics, a lot of supports were essential. Mr. S. Callier, Mr. L. Raux, and Dr. C. D. Taille taught me the practical usage of the EASIROC chip. The technical supports from Mr. M. Ikeno, Dr. T. Uchida, and Prof. M. Tanaka in Open-It were quite important to develop the board. I am also grateful Dr. I. Nakamura and Prof. K. Yoshimura for the SPIROC/EASIROC collaboration.

I spent one year in ASRC in JAEA when I was first degree of doctor course. I would like to thank Prof. K. Imai and Dr. S. Hasegawa for the development of the beamline fiber tracker.

The present experiment was successfully performed owing to the staffs of J-PARC and KEK. I would like to acknowledge the Hadron beam channel group and the accelerator group.

Finally, but not the least, I want to express my thanks to my parents for their understanding.

Chapter 1

introduction

1.1 Baryon-Baryon interaction in the flavor $\mathrm{SU_f}(3)$ symmetry

All the atomic nuclei comprising materials in our world consist of protons and neutrons bound together by the nuclear force. Its dynamical property that the interaction is attractive in a long range ($\gtrsim$1.5 fm) and strongly repulsive in a short range ($\lesssim$ 0.5 fm) is essential to stabilize nuclei. However, the mechanism for the complicated properties of the nuclear force are still not completely understood. The interactions between all kinds of baryons should be described from the same view point as the nuclear force because they originates from the strong interaction. Nowadays, it is known that six kinds of quarks with different flavors exist. Since the masses of u, d, and s quarks are lighter than the scale parameter of Quantum Chromo-Dynamics (QCD), the symmetry among them is expected to be approximately held. The interactions between two baryons composed of u, d and s quarks are expected to be understood from the flavor $\mathrm{SU_f}(3)$ symmetry. This is one of the most essential topics in hadron and nuclear physics. By introducing s quark, the ground-state baryons made of u and d quarks with spin 1/2, namely, nucleons, are extended to the baryon octet as shown in Figure 1.1. The multiplets such as this baryon octet in $\mathrm{SU_f}(3)$ are identified by non-negative integers: (α, β) where α and β denote the number of steps between the particles on the top and bottom of the multiplet diagram. Then, the baryon octet in $\mathrm{SU_f}(3)$ is represented as (11). The BB interaction between the baryon octet members is decomposed to the following irreducible subspaces,

$$(11) \otimes (11) = (22) \oplus (11)_s \oplus (00) \oplus (03) \oplus (30) \oplus (11)_a. \tag{1.1}$$

Here, the first three multiplets are symmetric and the others are anti-symmetric under a flavor exchange of two baryons. The interaction between two baryons are represented by combinations of these multiplets in the flavor SU(3) symmetry. Combinations corresponding to NN, ΛN and ΣN systems in the isospin basis are summarized in Table 1.1. The qualitative behavior of each BB interaction channel is characterized by the property of each multiplet. For the $(11)_s$ and (30) multiplets, the quark cluster model [1] predicts strong repulsive cores due to Pauli blocking between quarks. Since the ΣN ($s = 1, t = 3/2$) channel belongs to the (30) multiplet only, this channel should be a good probe to access the repulsive force from Pauli blocking between quarks. Hence, investigation of the ΣN interaction is essential to understand the BB interaction, especially, the origin of the repulsive core.

Table 1.1: *The irreducible representation of the BB potentials for NN, ΛN, and ΣN interactions in the isospin basis.*

$BB(t)$	flavor symmetric	flavor anti-symmetric
$NN(t=0)$	-	(03)
$NN(t=1)$	(22)	-
$\Lambda N(t=1/2)$	$\frac{1}{\sqrt{10}}((11)_s + 3(22))$	$\frac{1}{\sqrt{2}}(-(11)_a + (03))$
$\Sigma N(t=1/2)$	$\frac{1}{\sqrt{10}}(3(11)_s - (22))$	$\frac{1}{\sqrt{2}}((11)_a + (03))$
$\Sigma N(t=3/2)$	(22)	(30)

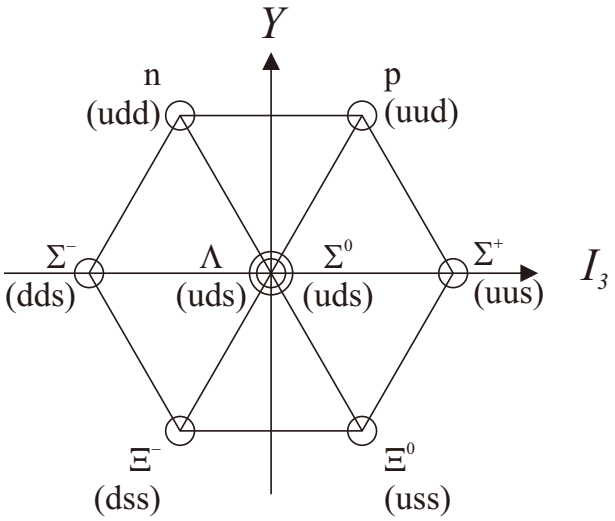

Figure 1.1: *The baryon octet in the $SU_f(3)$ symmetry with spin 1/2. I_3 and Y represent z component of isospin and hyper charge, respectively.*

1.2 Two-body ΣN interaction

Here we briefly introduce several theoretical models describing the two-body interaction in $\mathrm{SU_f(3)}$.

The one boson exchange model

The One Boson Exchange Potential (OBEP) is a model based on the boson field which results from the boson exchange between two baryons. One of the popular OBEP models used in $\mathrm{SU_f(3)}$ is the Nijmegen model. This model was constructed in 1970s using data on nucleon-nucleon (NN) and hyperon-nucleon (YN) scatterings to describe the BB interaction in $\mathrm{SU_f(3)}$. In the first Nijmegen models (Nijmegen Model-D, E and F) [3][4][5], simple repulsive potential cores (hard core) which are common to all the BB channels were used. Later, the Nijmegen Soft-Core model (NSC97) [6] was proposed to explain most of the hypernuclear data, especially, those of the spin dependent ΛN interaction. In NSC models, the repulsive core was modeled by the heavy particle exchange such as the pomeron exchange representing the phenomenological multiple gluon exchange. Recently,

the Nijmegen Extended Soft-Core (ESC04, 06, 08) [7] models which explicitly treated not only one boson exchange but also two boson exchange and the boson-pair exchange were proposed. In these theories, exchange of pseudo-scalar, vector, scalar and axial-vector mesons were taken into account. Furthermore, in ESC08, the repulsive core was improved to describe the strong short-range repulsion in the ΣN interaction suggested from experiments [27]. Then, in ESC08, the repulsive force in the ΣN ($s = 1, t = 3/2$) channel was strongest in the Nijmegen models.

In the OBEP framework, the general expression for the central part of the potential is written as

$$V(r) = (V_0(r) + \boldsymbol{\tau_1} \cdot \boldsymbol{\tau_2} V_\tau(r)) + (V_s(r) + \boldsymbol{\tau_1} \cdot \boldsymbol{\tau_2} V_{\tau s}(r))(\boldsymbol{\sigma_1} \cdot \boldsymbol{\sigma_2}), \tag{1.2}$$

where $\boldsymbol{\tau}$ and $\boldsymbol{\sigma}$ represent the isospin and spin operators for each baryon. The qualitative property of the ΣN potentials, that is, attraction or repulsion, in each spin-isospin channel is similar in various Nijmegen models. However, the meson-baryon coupling constants are free parameters in the OBE model and the ΣN scattering data which are necessary to determine the parameters are quite poor. Thus, the strength of attractive/repulsive force in each spin-isospin channel was very different among them.

The quark model

Models describing the BB interaction at quark level (FSS and fss2) were proposed [8]; they were based on the Resonating Group Method (RGM) between $(3q)$-$(3q)$ clusters. In this model, several two-body interactions between constituent quarks were introduced besides the kinetic terms to describe the Hamiltonian. The Hamiltonian between two baryons is defined as

$$H = \sum_{i=1}^{6} \boldsymbol{t}_i + \boldsymbol{T}_G + \sum_{i<j}^{6} \boldsymbol{v}_{ij}^{conf} + \sum_{i<j}^{6} \boldsymbol{v}_{ij}^{OGEP} + \sum_{i<j}^{6} \boldsymbol{v}_{ij}^{EMEP}, \tag{1.3}$$

where the first two terms denote the kinetic terms, $\boldsymbol{v}_{ij}^{conf}$ is the phenomenological quark confinement potential, $\boldsymbol{v}_{ij}^{OGEP}$ is the one gluon exchange potential, and $\boldsymbol{v}_{ij}^{EMEP}$ is the effective meson exchange potential between quarks. There are four parameters related to quarks, namely, the baryon size, the mass of constituent ud quarks, the coupling constant between a quark and a gluon, and the ratio of the masses of constituent s quark and ud quarks. On the other hand, parameters of EMEP are the quark-meson coupling constants for scalar and pseudo-scalar mesons in $\mathrm{SU_f}(3)$ and the masses of scalar mesons. These parameters were determined to fit NN and YN scattering data. The feature of this model is that the short-range repulsion is naturally produced from the quark-quark interaction. A quite strong repulsive force in the ΣN ($s = 1, t = 3/2$) channel was predicted in this model.

Lattice QCD

Recently, the numerical QCD simulation called Lattice-QCD was successfully carried out for the BB interactions owing to developments of calculation techniques and great progress of computer performance. One remarkable result of the Lattice-QCD simulation in the $\mathrm{SU_f}(3)$ limit is shown in Figure 1.2 [9]. The potentials shown in Figure 1.2 as $V^{\mathbf{27}}$, $V^{\mathbf{10^*}}$, $V^{\mathbf{8_s}}$, $V^{\mathbf{10}}$, $V^{\mathbf{1}}$, and $V^{\mathbf{8_a}}$ belong to the multiplets (22), (03), $(11)_s$, (30), (00), and $(11)_a$, respectively. In Figure 1.2, exotic behaviors are qualitatively visible, such as quite strong repulsive cores in $V^{\mathbf{8_s}}$ and $V^{\mathbf{10}}$, a deep attractive pocket of $V^{\mathbf{8_a}}$, and an attractive core

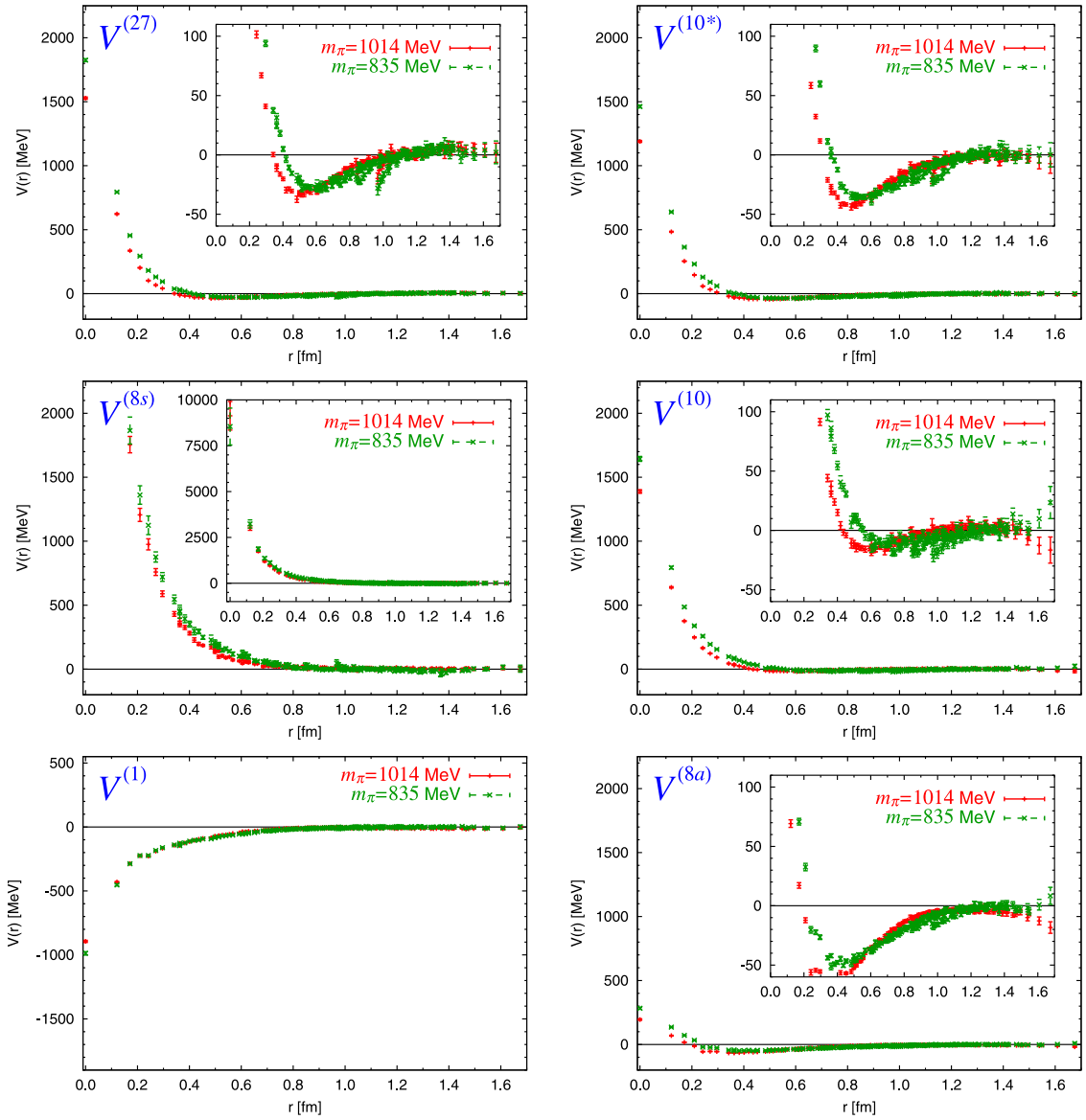

Figure 1.2: *Six potentials corresponding to irreducible flavor multiplets in the $SU_f(3)$ limit derived by the Lattice-QCD simulation [9].*

in $V^{\mathbf{1}}$. Quite strong repulsive cores in $V^{\mathbf{8_s}}$ and $V^{\mathbf{10}}$ are consistent with the previous predictions by the quark cluster model, in which Pauli blocking between quarks gives rise to the strong repulsive core. However, the Lattice QCD simulation cannot give us quantitative information at the present stage because the simulation is carried out in the $\mathrm{SU_f}(3)$ limit with the heavy pion mass (835 MeV/c^2).

Thus, the ΣN interaction is not yet conclusive in any models. Hence, experimental investigation of the ΣN interaction is necessary in order to give a constraint on the theoretical models.

Table 1.2: *The potential strengths as a result of the G-matrix calculations.*

Models	(s,t) (0, 1/2) (MeV)	(1, 1/2) (MeV)	(0, 3/2) (MeV)	(1, 3/2) (MeV)	Sum* (MeV)	Ref.
NSC97f	14.9	−9.6	−12.2	−4.2	−13.9	[7]
ESC04d	6.5	−21.0	−10.1	14.0	−26.0	[7]
ESC08a	11.3	−23.9	−11.7	44.8	13.4	[7]
ESC08b	10.3	−26.2	−10.6	52.7	20.3	[7]
fss2	6.7	−23.9	−9.2	41.2	7.5	[8]

(*Sum includes the contribution from other partial waves.)

1.3 The ΣN interaction in nuclei

For investigation of the two-body baryon-baryon interaction, the scattering experiment is the most important. This is obvious from the fact that data on NN and YN scatterings are used to construct theoretical models. However, YN scattering data was quite limited due to experimental difficulties caused by short lifetime of hyperons. Then, the ΣN interaction was historically studied through the interaction between a Σ particle and nuclei. (About the details of historical backgrounds, see Appendix D.) In order to consider the YN interaction in nuclei from the two-body YN interaction in free space, effects from other nucleons in nuclei have to be taken into account. Such effects in nuclear matter are renormalized into the reaction matrix (G-matrix), and then, the single-particle potential in nuclei can be derived. The strengths of the single-particle potentials of a Σ particle are calculated for several two-body interaction models by the G-matrix method as summarized in Table 1.2. These values represent the strength of the Σ-nucleus potential in nuclear matter at the normal nuclear density. The sum values in the table include the contribution from other partial waves, that is, p and d wave. The repulsive Σ-nucleus potentials were predicted from the recent models. By extracting the strength of the Σ-nucleus potential from experiments and comparing it with the sum values in Table 1.2, we can give a constraint to theoretical models.

The general expression of the Σ-nucleus potential is written as

$$U_0^\Sigma + U_\tau^\Sigma(\mathbf{T_C} \cdot \mathbf{t_\Sigma})/\mathrm{A_{core}}. \tag{1.4}$$

Here, U_0^Σ is the isospin independent (averaged) potential and U_τ^Σ is the isospin dependent term, namely, the Lane's term. $\mathbf{T_C}$ and $\mathbf{t_\Sigma}$ represent the isospin operators for the core nucleus and a Σ particle. $\mathrm{A_{core}}$ is a mass number of the core nucleus. Thus, the Σ-nucleus potential is described with the Lane's term which originates from the isospin dependence of the two-body ΣN interaction. However, the contribution from the Lane's term is inversely proportional to the mass number of the core nucleus. Hence, one can notice that the strong isospin dependence should appear in light nuclei while the isospin independent term is dominant in heavy nuclei.

1.3.1 The observation of ${}^{4}_{\Sigma}$He

The most important phenomenon which reflects the role of the Lane's term well in the light nucleus was the existence of the ${}^{4}_{\Sigma}$He bound state. The bound state of ${}^{4}_{\Sigma}$He was theoretically predicted [22] and observed in the KEK-PS E167 experiment [23] via the $(K^-_{stopped}, \pi^\mp)$

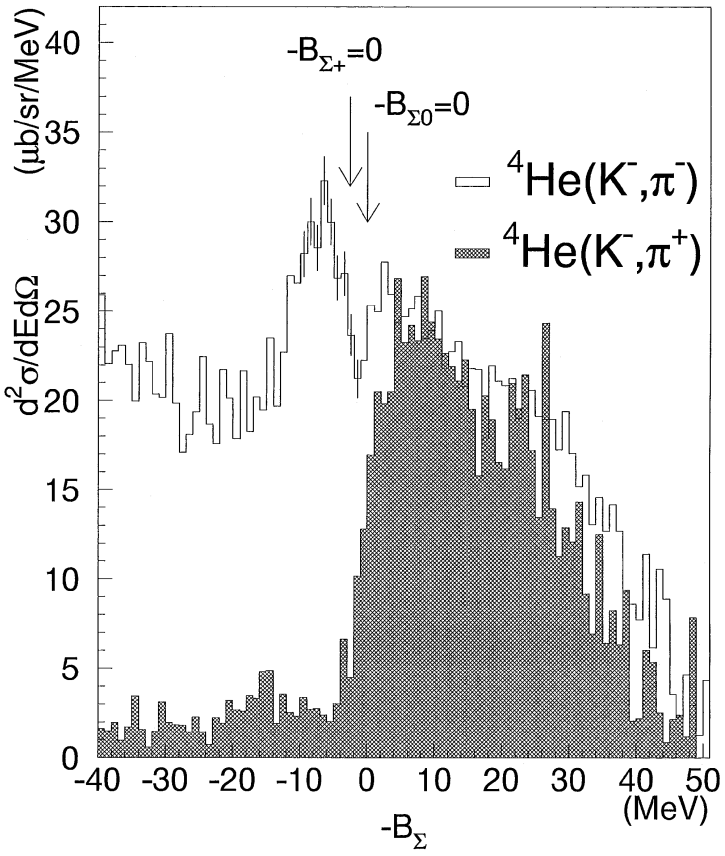

Figure 1.3: *Energy spectra of the (K^-, π^-) and (K^-, π^+) reaction at a reaction angle of 4° [24]. The binding energy threshold was determined by that of the Σ^0 production for the (K^-, π^-) reaction and that of the Σ^- production for the (K^-, π^+) reaction.*

reaction. Soon after, the bound state was confirmed in the BNL-AGS E905 experiment [24] via the in-flight $(K^-, \pi^\mp)$ reaction as shown in Figure 1.3. From the difference between the distribution of events lying below the Σ-binding threshold, it was found that the Σ-nucleus potential in the four-body system strongly depends on the total isospin (T). Since the $T = 3/2$ state only is populated in the case of the (K^-, π^+) reaction, interpretation for the spectrum of the (K^-, π^+) reaction is simple. The Σ-nucleus potential in the $T = 3/2$ state should be repulsive because there are almost no event below the Σ-binding threshold in the spectrum of the (K^-, π^+) reaction. On the other hand, the (K^-, π^-) spectrum, which contains both $T = 3/2$ and $T = 1/2$ states, exhibited a prominent peak below the Σ-binding threshold, which is interpreted as a $T = 1/2$ bound state of ${}^4_\Sigma$He. Thus, the $T = 1/2$ potential was found to be attractive. The observed results agreed with the theoretical prediction [22]. Thus, the contribution from the Lane's term plays an essential role in light nuclei. Since the extra attraction caused by the Lane's term becomes smaller in heavier nuclei, ${}^4_\Sigma$He is still the only experimental sample of Σ hypernuclear bound states.

1.3.2 Study in heavy nuclei

On the other hand, the isospin averaged potential was studied using the heavier nuclei, carbon, silicon, indium and bismuth as experimental targets in the KEK-PS E438 experiment [27] via the (π^-, K^+) reaction. As one of the experimental results, the missing mass spectrum for the silicon target is shown in Figure 1.4. The distribution over the Σ-binding threshold is the quasi-free Σ production while events lying below the threshold are produced via the absorption of a Σ particle in nuclei. In order to extract information on the Σ-nucleus potential, the spectrum shape was analyzed using the Distorted-Wave Impulse Approximation (DWIA) framework [77]. The spectrum was fitted with the theoretically calculated spectrum shape obtained with several potential conditions. For the calculation, the isospin averaged potential was assumed to have the Woods-Saxon (WS) form as

$$U^{\Sigma} = (V_0^{\Sigma} + iW_0^{\Sigma})/[1 + \exp((r - R)/a)], \tag{1.5}$$

where V_0^{Σ} and W_0^{Σ} were the strengths of the real and imaginary parts of the potential. The best-fit curve calculated with (V_0^{Σ}, $-W_0^{\Sigma}$) = (30 MeV, 40 MeV) is illustrated by a solid line in Figure 1.5. From this result, it was found that the single particle potential of a Σ particle in nuclei is repulsive. Nowadays, we expect that this property is related to the strong repulsive force in the two-body ΣN ($s = 1, t = 3/2$) interaction.

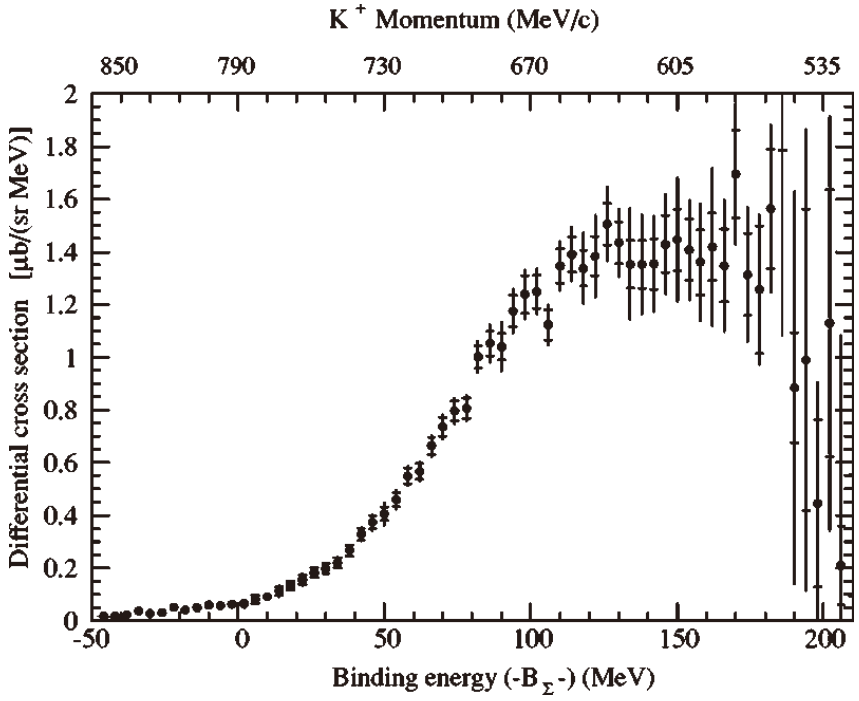

Figure 1.4: *The missing mass spectrum of the (π^-, K^+) reaction for the silicon target at the beam momentum of 1.2 GeV/c obtained in KEK-PS E438 [27].*

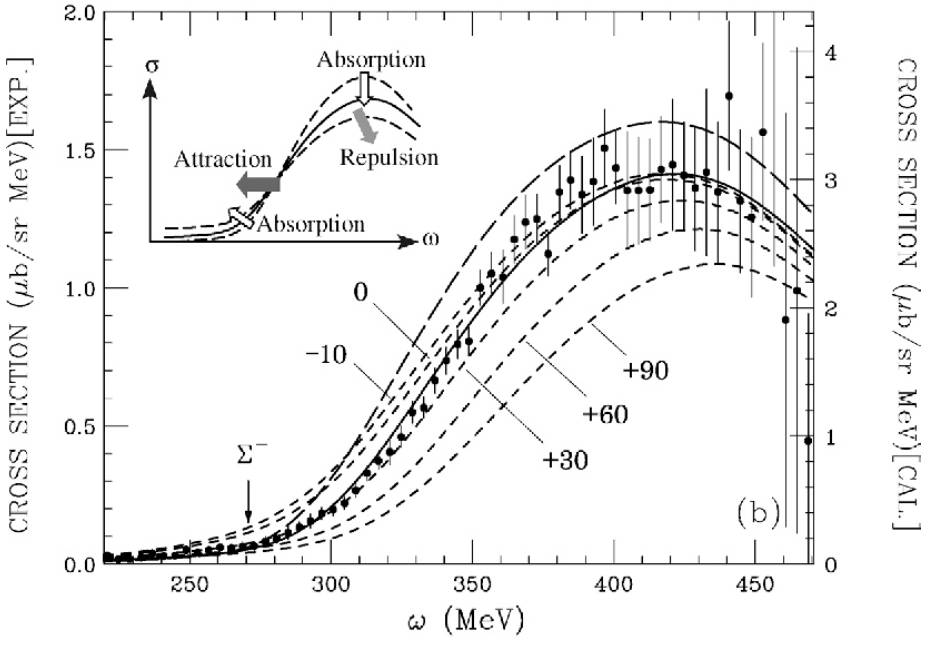

Figure 1.5: *The DWIA calculation results with several conditions of the Σ-nucleus potential and the experimental result of E438 for the silicon target [77].*

1.3.3 Absorption of a Σ particle in nuclei

In the case of the double-charge exchange (DCX) reaction such as the (π^-, K^+) reaction, a Λ particle cannot be directly produced. However, a Σ particle is strongly absorbed in nuclei and converted to a lighter hyperon, that is, a Λ particle by the $\Sigma N \to \Lambda N$ interaction. Then, the region below the Σ-binding threshold in the missing mass spectrum corresponds to those events, in which a Λ hyperon is produced through the virtual Σ production. Furthermore, the Λ hypernucleus would be exist below the Λ-binding threshold. A Λ and Σ particles are no longer independent and can be mixed with each other in nuclei. The shape of the "Λ continuum" produced via the DCX reaction contains information on the $\Lambda N \leftrightarrow \Sigma N$ conversion. However, the production mechanism of the Λ continuum and the Λ hypernuclei via the DCX reaction is not simple. Nowadays, two types of different process to produce the Λ hypernucleus can be considered. One is the production based on the multiple scattering theory, that is, *the two-step process*. This process is represented by the meson charge exchange as follows

$$\pi^- p \to \pi^0 n,\ \pi^0 p \to K^+ \Lambda,$$

or

$$\pi^- p \to K^0 \Lambda,\ K^0 p \to K^+ n.$$

The other is the direct production of the Λ hypernucleus via the virtual Σ mixed in the Λ hypernuclear state, namely, *the one-step process*,

$$\begin{aligned} \pi^- p &\to K^+ \Sigma^-, \\ \Sigma^- p &\leftrightarrow \Lambda n. \end{aligned}$$

In the case of the one-step process, the production of the Λ continuum comes from absorption of a Σ particle; it is described by the imaginary part of the Σ-nucleus potential. Thus, the spectrum of the Λ continuum via the DCX reaction gives us information on the ΛN-ΣN interaction.

The spectrum reported by the KEK-PS E438 experiment included this region. However, since the purpose of the E438 experiment was to obtain the quasi-free Σ production spectrum, a part of the Λ continuum above $-B_\Sigma = -50$ MeV only was reported with a large statistical error ($\sim 50\%$). In addition, the cross section of the Λ continuum region is quite small comparing to that of the quasi-free Σ production as shown in Figure 1.4. The number of pions irradiated was $\sim 1 \times 10^{11}$. Then, a large number of beam pions are necessary to make the statistical error small.

A similar spectrum was reported in the KEK-PS E521 experiment, of which the purpose was production of the neutron-rich Λ hypernucleus ($^{10}_{\Lambda}$Li) via the (π^-, K^+) reaction [29]. The missing mass spectrum of the ^{10}B(π^-, K^+)X reaction at the beam momentum of 1.2 GeV/c is shown in Figure 1.6. Although the clear peak structure was not observed, we found events below the Λ-binding threshold. The number of events and the production cross section between −20 to 0 MeV of $-B_\Lambda$ were 47 events and 11.3±1.9 nb/sr, respectively [29]. Furthermore, the Λ continuum spectrum was observed with the smaller statistical error than that of the spectrum in E438. In order to obtain this spectrum, the ^{10}B target with thickness of 3.5 g/cm^2 was irradiated with $\sim 1 \times 10^{12}$ pions. The spectrum shape was analyzed and well reproduced by the calculation in the same framework used for the shape analysis in the E438 experiment [31]. In addition, the same spectrum was also obtained at the beam momentum of 1.05 GeV/c in this experiment. Its cross section between −20 to 0 MeV of $-B_\Lambda$ was 5.8±2.2 nb/sr. From the momentum dependence of the production cross

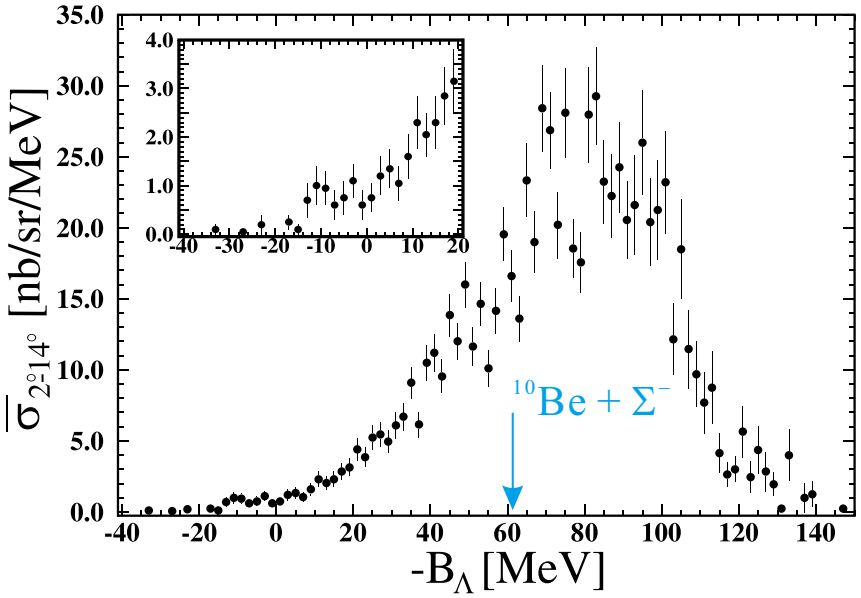

Figure 1.6: *The missing mass spectrum of the $^{10}B(\pi^-, K^+)X$ reaction obtained in KEK-PS E521 [29].*

section, it was found that the one-step process was dominant to produce the Λ hypernucleus via the (π^-, K^+) reaction. However, unfortunately, since the experimental setup of E521 was dedicated to the neutron-rich Λ hypernucleus, kaons produced through the quasi-free Σ production were out of the momentum acceptance of the kaon spectrometer. As mentioned above, the spectrum of the quasi-free Σ production is necessary to discuss the real part of the potential. Therefore, the strengths of the Σ-nucleus potential were not able to be precisely analyzed because the spectrum shape of the Λ continuum was affected by not only the imaginary part but also the real part.

1.3.4 Summary of the ΣN interaction in nuclei

The Σ-nucleus potential can be separated to the isospin averaged term and the isospin dependent term, namely, the Lane's term, coming from the isospin dependence of the two-body ΣN interaction. As is obvious from the experimental result of BNL-AGS E905 [24], the Lane's term plays the essential role in light nuclei. On the other hand, the Σ-nucleus potential can be described by the isospin averaged term only in heavy nuclei. The property of the isospin independent term was revealed by the KEK-PS E438 experiment [27] and was repulsive [77]. It is suggested that This repulsion originates from the strong repulsive force in the ΣN $(s = 1, t = 3/2)$ channel caused by Pauli blocking between quarks. However, since the Σ-nucleus potential has a sizable imaginary strength affecting the spectrum shape, the quality of the Λ continuum region is also important to even determine the real part potential. The spectrum including not only the quasi-free Σ production but also the Λ continuum with a small statistics error has not been reported due to experimental difficulties such as the spectrometer acceptance and the number of beam used.

1.4 Present experiment: J-PARC E10

The J-PARC E10 experiment was proposed to investigate the ΛN and ΣN interaction in the neutron excess environment in light nuclei. The purpose of this experiment is to obtain background free missing mass spectra via the (π^-, K^+) reaction on ^{6}Li and ^{9}Be targets at the beam momentum of 1.2 GeV/c. The present thesis describes the ^{6}Li target run carried out in 2012 and 2013. The final state of the $^6\mathrm{Li}(\pi^-, K^+)\mathrm{X}$ reaction will be ($1p$, $4n$, Λ), ($1p$, $4n$, Σ^0), and ($2p$, $3n$, Σ^-). Especially, the final state with a Σ^- particle can be considered as $\alpha + n + \Sigma^-$. Since both of the Σ^--α and Σ^--n potentials are suggested to be strongly repulsive, a strong repulsion is expected in this final state.

Another purpose of the present experiment is to produce the neutron-rich hypernucleus, $^6_\Lambda$H. Recently, three candidate events of $^6_\Lambda$H were reported from the FINUDA experiment in DAΦNE [33]. The $^6_\Lambda$H hypernucleus is a quite exotic neutron-rich hypernucleus because the core nucleus, ^{5}H, was reported as a resonance state [37] [38] [39] [40]. This unbound system could be bound by implanting a Λ particle owing to the attractive ΛN interaction [34] [35]. Furthermore, Akaishi *et al.* suggested that the additional attractive interaction due to the ΛNN three-body force induced by ΛN-ΣN coupling in the neutron excess environment makes the $^6_\Lambda$H hypernucleus more deeply bound [36]. Consequently, a deeply bound state of $-B_\Lambda = -4.1$ MeV with respect to $^3\mathrm{H} + 2n + \Lambda$ system was predicted [36].

In the present experiment, a wide momentum acceptance of the kaon spectrometer and a sufficient kaon detection efficiency with the background free condition were simultaneously achieved. This is an unique feature that the past experiments did not realize. Since the KEK-PS E521 experiment was dedicated to neutron-rich hypernuclei, Σ quasi-free production events were not obtained due to the limited momentum acceptance. Then, the real part of the Σ-nucleus potential was not able to be studied because it is related to the shape of the quasi-free Σ production spectrum. On the other hand, in the KEK-PS E438 experiment or BNL-AGS experiments, the entire spectra of the Σ quasi-free production via the (π^-, K^+) or (K^-, π^+) reaction were obtained while the number of events below the Σ-binding threshold was small. The momentum acceptance of the kaon spectrometer in the E10 experiment is set to be sufficiently wide to obtain not only a part of the quasi-free Σ production region but also the Λ continuum region. On the other hand, since the present experiment proposed 3×10^{12} pions injection in order to produce the neutron-rich Λ hypernucleus, a smaller statistical error comparing to that of E438 is expected. Hence, a good opportunity to investigate the ΣN interaction in nuclei, especially, the repulsive force in the Σ-nucleus system, is given in the present experiment.

The present paper consists of seven chapters. In Chapter 2, the experimental setup and conditions are described. In Chapter 3, the scintillation fiber tracker system, which is a key apparatus of the present experiment, is explained. In Chapter 4 and 5, analysis procedures and experimental results are described. Finally, we will discuss the ΣN interaction using the experimental result in Chapter 6. A summary of this thesis is given in Chapter 7.

Chapter 2

Experiment

2.1 Overview

The J-PARC E10 experiment is an experiment to obtain the inclusive missing mass spectrum via the (π^-, K^+) double charge-exchange reaction in order to study the ΛN and ΣN interaction in the neutron-rich environment. The first stage of E10 was carried out with the ^{6}Li target at the K1.8 beamline in J-PARC in 2012 and 2013. The ^{6}Li target, which was 3.5 g/cm^2 in thickness, was irradiated with 1.7×10^{12} π^- beams with the beam momentum of 1.2 GeV/c.

Incident beam pions are analyzed by the K1.8 beamline spectrometer. This spectrometer is designed to realize excellent momentum resolution of the order of 10^{-4}; it consists of $QQDQQ$ magnets, tracking detectors and timing counters. On the other hand, the outgoing kaons are measured by the Superconducting Kaon Spectrometer (SKS) system. It is comprised of a large superconducting dipole magnet, tracking detectors and trigger counters, which can identify kaons in the trigger level. The SKS system has a large acceptance of 100 msr with a good momentum resolution of 0.2% (FWHM). Such specifications of the SKS system are suitable for hypernuclear spectroscopy experiments with a small production cross section. The energy resolution of 2.5 MeV/c^2 is expected with these resolutions by taking into account the energy-loss straggling in the experimental target. Moreover, the wide momentum acceptance of the SKS system is also important in the present experiment. Since the SKS magnet is excited to 300 A (2.16 T), the momentum range of the outgoing kaons of 0.7-1.0 GeV/c is accepted; this range corresponds to the mass region from the bound region of $^6_\Lambda$H up to a part of Σ quasi-free production. Thus, we can simultaneously investigate both of the ΣN interaction in nuclei and the structure of the neutron-rich hypernucleus.

In the present experiment, an yield in the Λ continuum region is the most important to make the statistical error as small as possible and to observe the peak structure of the neutron-rich hypernucleus. As mentioned in Chapter 1, the production of the neutron-rich Λ-hypernuclei, $^{10}_\Lambda$Li, via the (π^-, K^+) reaction was attempted for the first time in the KEK-PS E521 experiment [29]. Several events around the bound region were found; however, a clear peak was not observed. As a result of the previous experiment, production cross sections of $^{10}_\Lambda$Li were 5.8 ± 2.2 nb/sr at 1.05 GeV/c and 11.3 ± 1.9 nb/sr at 1.20 GeV/c, respectively. These cross sections are roughly three-order of magnitudes smaller than that of the (π^+, K^+) reaction such as $^{12}_\Lambda$C [41]. Therefore, the use of the high intensity pion beam of 10^7 pions during 2 sec. was proposed for the higher yield in the present experiment. The K1.8 beamline is presently the unique beamline, providing such a high intensity pion beam with a beam momentum of 1.2 GeV/c. Handling the high intensity beam is an important

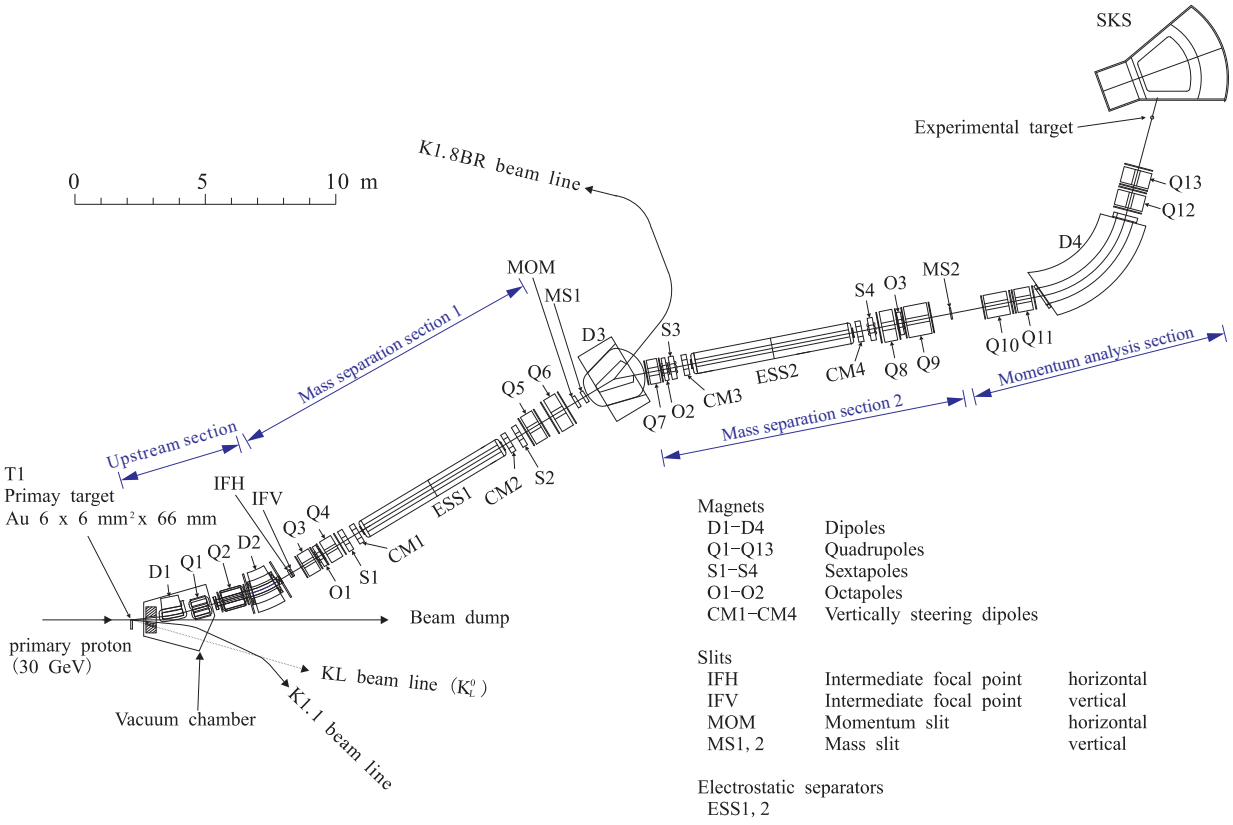

Figure 2.1: *A schematic view of the K1.8 beamline.*

issue to carry out the present experiment. Hence, new tracking detectors using scintillation fibers and Multi-Pixel Photon Counter (MPPC) are developed and installed replacing a part of wire chambers in each spectrometer system. Accidental background hits under a high intensity condition can be suppressed with the good timing resolution of 0.77 ns (σ) of these detectors. These detectors are introduced in this chapter and will be described in Chapter 3.

2.2 K1.8 beamline

The K1.8 beamline is a general-purpose beamline which can supply various mass-separated secondary hadron beams [43][44]. In particular, the beamline was designed as a high intensity and a high purity kaon beamline for Ξ experiments using the (K^-, K^+) reaction. The maximum beam momentum is 2.0 GeV/c because the production cross section of Ξ via the (K^-, K^+) reaction becomes maximum at the beam momentum of 1.8 GeV/c. In order to supply a high purity kaon beam, a double electrostatic separator (ESS) system is adopted. Figure 2.1 shows a schematic view of the K1.8 beamline. The K1.8 beamline is made from four sections, namely, the upstream section, the mass separation section 1 and 2, and the momentum analysis section.

The primary proton beam is extracted and delivered to a primary target (T1) over ∼2 sec within a 6 second period synchronized to a operation cycle of the J-PARC proton synchrotron, the main ring (MR). This duration of 2 sec is called as a spill. The secondary beam generated on the primary target, an Au rod ($\phi 6 \times 60$ mm), is separated from the primary beam in the upstream section. This section consists of two dipole magnets (D1,

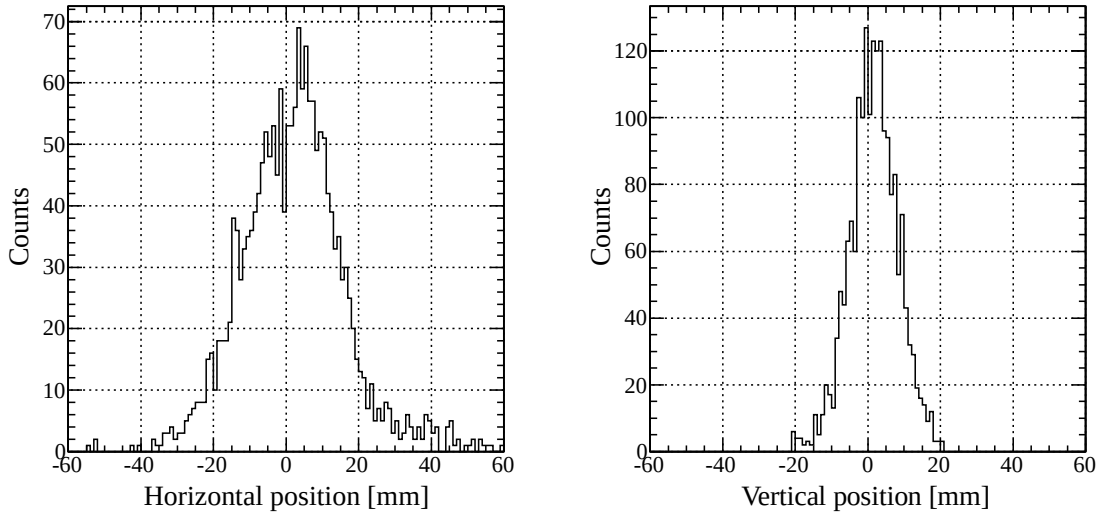

Figure 2.2: *The typical beam profile at the experimental target.*

D2), and two quadruple magnets (Q1, Q2). The intermediate focus (IF) slits are installed behind the D2 magnet to reject the cloud pions produced by the decay of K_s^0 and the scattered pions in upstream materials. IF slits have horizontal and vertical components, i.e. IFH and IFV.

The masses of beam particles are separated by the ESS1 and ESS2 system in mass separation sections. The first mass separation section is comprised of four quadruple magnets (Q3-Q6), two sextupole magnets (S1, S2), a octupole magnet (O1), and ESS1 with two correction magnets (CM1, CM2). Particles except for pions are filtered out by the vertical slit (MS1) located before the D3 magnet. The horizontal momentum slit (MOM) is placed between the Q6 magnet and MS1 to determine a momentum bite. The D3 magnet located between the first and second mass separation sections directs the beam either to the K1.8 or the K1.8BR experimental area. The configuration of the second mass separation section is similar to the first one. It consists of three quadruple magnets (Q7-Q9), two sextupole magnets (S3, S4), two octupole magnets (O2, O3), and ESS2 with two correction magnets (CM3, CM4) and the mass slit (MS2).

Finally, the beam is analyzed in the beam analysis section called as the K1.8 beamline spectrometer. The configuration of magnets is a $QQDQQ$ system (Q10-Q13, D4). The beam is focused at the experimental target by two quadruple magnets (Q12, Q13). A typical beam profile at the experimental target in the present experiment is shown in Figure 2.2.

Table 2.1: *The list of specifications of the K1.8 beamline spectrometer.*

Momentum resolution	3.3×10^{-4} (FWHM)
Maximum Momentum	2.0 GeV/c
Bending angle	64°

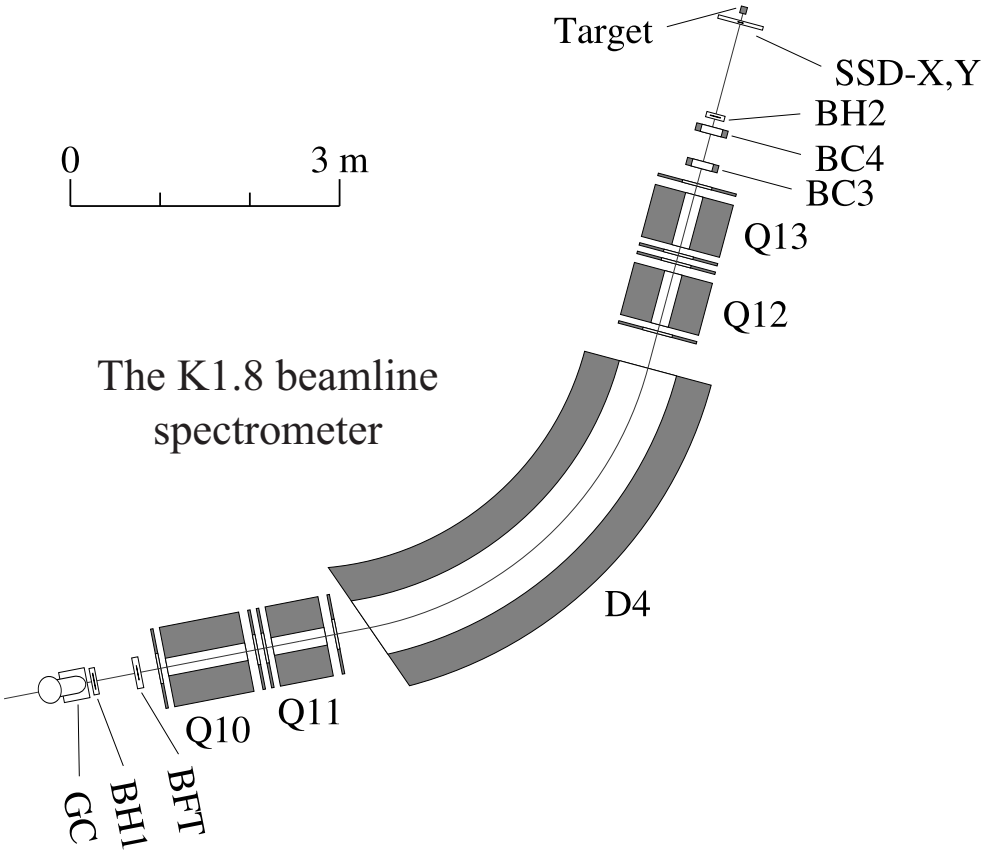

Figure 2.3: *The schematic view of the K1.8 beamline spectrometer.*

2.3 K1.8 beamline spectrometer

The K1.8 beamline spectrometer at the end of the K1.8 beamline is a momentum analyzer. The π^- beam is analyzed by the spectrometer event by event. Design specifications of the spectrometer are listed in Table 2.1. In this section, detectors to measure beam trajectories and to analyze the beam momentum are described.

2.3.1 Outline

A schematic view of the spectrometer is shown in Figure 2.3. This spectrometer consists of tracking detectors (BFT, BC3,4) installed at the entrance and the exit of the *QQDQQ* magnets, two sets of silicon-strip detectors (SSD-X,Y), and trigger counters (GC, BH1, BH2). The horizontal beam positions were measured by the beamline fiber tracker (BFT) installed at the entrance of the *QQDQQ* magnets. On the other hand, the three-dimentional beam trajectories at the exit of magnets are measured by two sets of multi-wire drift chambers (BC3,4). Furthermore, the beam trajectories and hits on SSD-X,Y are used to

Table 2.2: *The list of specifications of trigger counters in the K1.8 experimental area.*

Name	Sensitive area W × H × T (mm)	Specifications	Photon detector (HPK)
GC	340×80 (mirror), 290^{L}	iso-C_4H_{10}, n∼1.002 (0.15 MPa)	R1250-03 (UV glass)
BH1	$170 \times 66 \times 5$	11 segments, 3-stage booster	H6524MOD
BH2	$118 \times 60 \times 5$	8 segments, 3-stage booster	R9880U-110MOD
TOF	$2240 \times 1000 \times 30$	32 segments	H1949
LAC	2080×1200	Aerogel; n = 1.05	R1584-01, 8854 (Burle)
LC	$2800 \times 1400 \times 40$	28 segments, Acrylic; n = 1.49	H1949, H6410
AC1	1050×1200	Aerogel; n = 1.05	R1584-02

reconstruct reaction vertexes. The beam momentum is reconstructed from the horizontal position at the entrance and the trajectories at the exit by using the third-order transfer matrix. The design value of the momentum resolution is $\Delta p/p = 3.3 \times 10^{-4}$ (FWHM) with a position resolution of 200 μm (r.m.s.) [45]. The central momentum is determined by the magnetic field of the D4 magnet. Since the fluctuation of the magnetic field affects the momentum resolution during data taking, the magnetic field is monitored by the high resolution Hall probe [Digital Teslameter 151 (DTM-151)] [46]. The observed fluctuation of the magnetic field is 0.01%.

2.3.2 Trigger counters

Specifications of trigger counters are listed in Table 2.2.

GC

A gas Čerenkov counter (GC), in which isobutane-gas (0.15 MPa) is enclosed, is located just downstream of MS2 to reject an electron contamination in the π^- beam. The detection efficiency for electrons and positrons was found to be 99.5% [47].

BH1

The beam hodoscope 1 (BH1) located just downstream of GC is a segmented plastic scintillation counter [47]. It consists of 11 pieces of plastic scintillators (Saint-Gobain BC-420) with thickness of 5 mm to reduce the counting rate of each segment. Figure 2.4 shows a schematic drawing of BH1. Each segment is arranged in a staggered relation with an overlap of 1 mm with each other. Scintillating lights are collected by Photo-Multiplier Tubes (PMT), HPK H6524MOD, from both vertical ends.

BH2

The beam hodoscope 2 (BH2) [48] is also a segmented plastic scintillation counter consisting of 8 pieces of plastic scintillator (Saint-Gobain BC-420). The structure of BH2 is similar to that of BH1; however, there is no overlap between each segment. Although each segment is arranged without an overlap, there is no insensitive region. The horizontal size of each segment is adjusted so that the single rate of each segment becomes the same. Figure 2.5 shows a schematic drawing of BH2. PMT (HPK R9880U-110MOD) suffering smaller gain

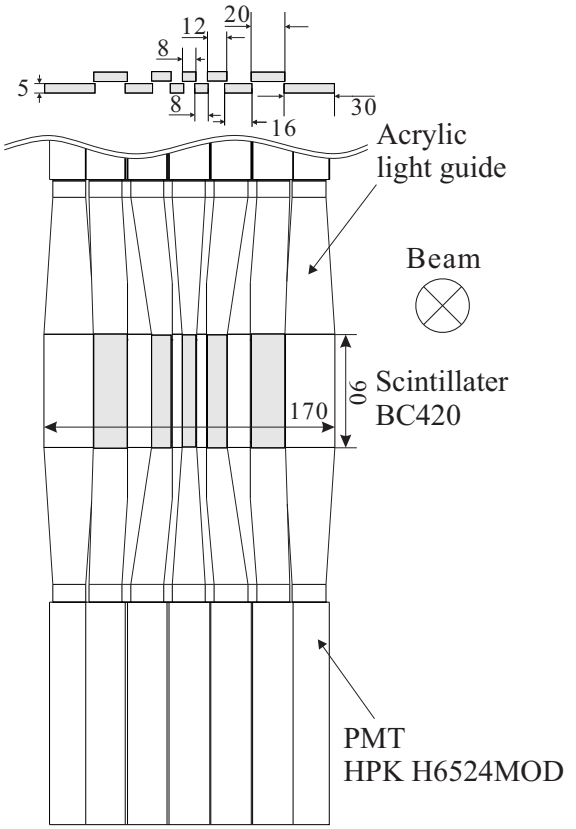

Figure 2.4: *The schematic drawing of BH1.*

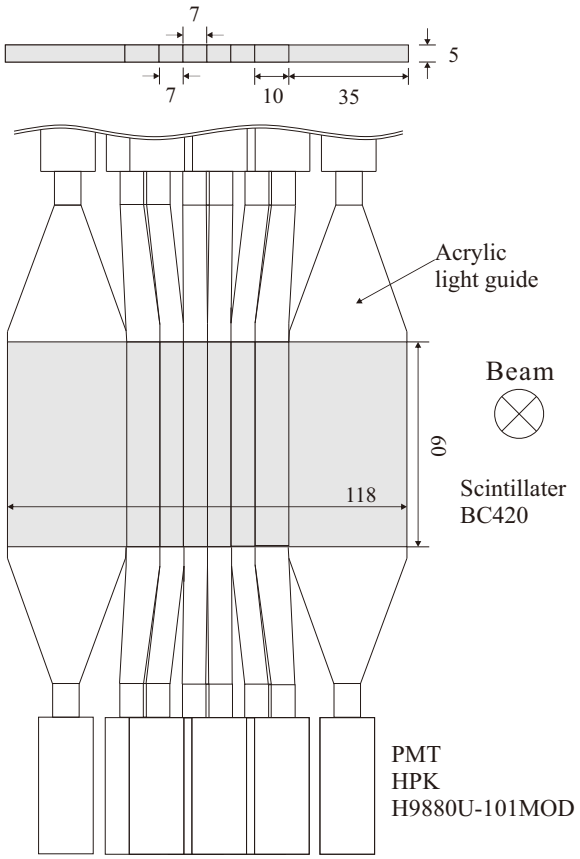

Figure 2.5: *The schematic drawing of BH2.*

decrease in a magnetic field than that of H6524MOD is used because a fringing field of the SKS magnet reaches BH2. A high voltage power is applied to each PMT of BH1·2 by a power supply with a three-stage booster to prevent the voltage from dropping under the high intensity condition. BH2 is used as the time zero counter to determine the start timing of the DAQ system.

The time-of-flight (TOF) of beam particles is measured by BH1 and BH2, which are placed 10.4 m apart from each other. The typical timing resolution of the beam TOF was found to be ∼125 ps [48].

2.3.3 Tracking detector

The specifications of wire chambers are summarized in Table 2.3.

Fiber tracker

A finely segmented scintillation fiber hodoscope called as a beamline fiber tracker (BFT) is installed just upstream of the Q10 magnet because the beam is defocused horizontally at this point. The horizontal position only is measured in the upstream section of the *QQDQQ* system by BFT. BFT has two planes consisting of cylindrical scintillation fibers (Kuraray SCSF-78MJ)[61] with diameter of 1 mm. Each fiber is read by a photon detector, MPPC. Fibers are arranged in a staggered relation with an overlap of 0.5 mm to reduce the insensitive region. Furthermore, this configuration provides the better position resolution than that of no overlapping configuration. As the result, the position resolution of 180 μm

Table 2.3: *The list of specifications of wire chambers in the K1.8 experimental area.*

Name	Sensitive area W × H (mm)	Drift space (mm)	Wires	Resolution (μm)
BC3	192 × 100	1.5	$xx'vv'uu'$	200
BC4	192 × 100	1.5	$uu'vv'xx'$	200
SDC2	400 × 150	2.5	$vv'uu'xx'$	200
SDC3	2140 × 1140	10	$vxuvxu$	300
SDC4	2140 × 1140	10	$vxuvxu$	300

(σ) is obtained. Since one plane is made of 160 scintillation fibers, the effective horizontal area is 160 mm. Details of the fiber tracker system are described in Chapter 3.

Multi-wire drift chambers

The multi-wire drift chambers with an anode-anode spacing of 3 mm are located just the downstream of the Q13 magnet; these chambers are called as the beam chamber 3 and 4 (BC3·4) [45]. Since BC3·4 are exposed to a high intensity secondary beam of up to 10 MHz, the anode-anode spacing of 3 mm is adopted to reduce a single rate of each wire. Since the measured horizontal beam size at BC3 in the present experiment is 100 mm, the counting rate is 150 kHz per wire.

Each chamber has six layers (xx', uu', vv'), where wires in the u and v planes are tilted by 15° and −15° with respected to those in x layer, respectively. A set of two layers such as xx', uu' and vv' is called as a pair plane. In the pair plane, wire positions are shifted by a half cell size of 1.5 mm to solve the left/right ambiguity of each hit as shown in Figure 2.6. Anode wires are tungsten wires whose diameter is 12.5 μm. On the other hand, gold-plated wires whose diameter is 75 μm are used as potential wires. The cathode plane is an aramid film, on which graphite is pasted. The thickness of the film and graphite layer is 12 μm and 20 μm, respectively. The distance between the anode and the cathode plane is 2.0 mm.

Mixed gas of Ar(76%), iso-C_4H_{10}(20%), and Methylal(4%) is used. Methylal is used to prevent anode wires from sputtering caused by beam particles. The operation voltage of the cathode planes and the potential wires of BC3·4 are −1.23 kV and −1.25 kV, respectively. The readout card, on which Amplifier Shaper Discriminator (ASD) chips are mounted, are attached to MWDCs. This chip was developed for the ATLAS thin gap chamber [49].

Silicon strip detector

Two sets of a silicon strip detector (SSD) having 768 strips with a 80 μm pitch are installed just upstream of the experimental target. One SSD with direction x (SSD-X) is located at upstream of the other one with direction y (SSD-Y). We used a p-in-n type single side strip sensor fabricated by Hamamatsu Photonics K.K.. This silicon sensor was originally developed by the ATLAS SCT collaboration [50]. The effective area of the sensor is 62.0 × 61.6 mm^2, and its thickness is 300 μm. An analog signal induced from each strip is read by the Application Specific Integrated Chip (ASIC), APV25-s1 [51], placed near the sensor. Therefore, the sensor and the APV chip are assembled on a Printed Circuit Board (PCB). We call this PCB as a front-end part of the SSD DAQ system.

The role of SSD is to correct the beam trajectories obtained by BC3·4 because the

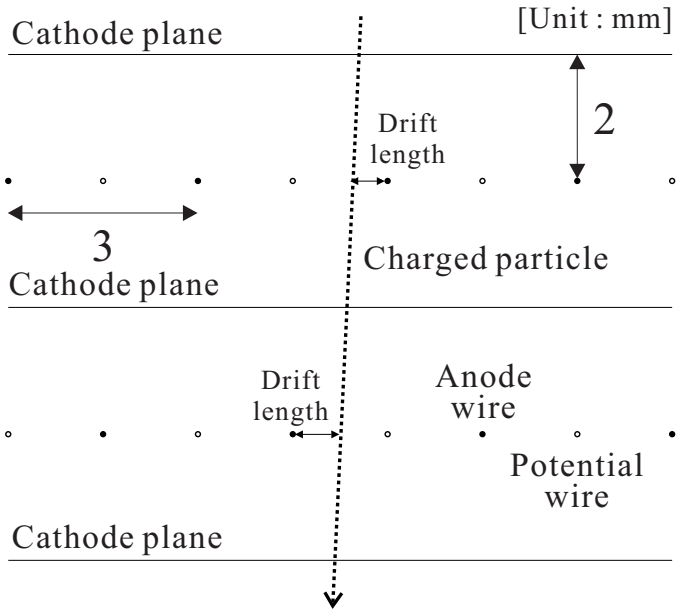

Figure 2.6: *The schematic view of the pair plane of BC3 and 4.*

experimental target is located far from BC3·4. The distance between BC3·4 and the target is ∼1300 mm. Hence, the effect of multiple scatterings in BH2 and air are no longer negligible when we extrapolate the beam trajectories to the reaction vertex. The angle and x-y positions of beam trajectories at the target position are corrected by using SSD hit information.

2.4 Kaon Spectrometer

The scattered K^+ produced by the (π^-, K^+) reaction is analyzed by the SKS system configured for kaon detections. In this section, we describe the detector system to identify and analyze kaons.

2.4.1 Outline

As shown in Figure 2.7, the SKS system is comprised of the SKS magnet, four sets of tracking detectors (SFT, SDC2·3·4), and trigger counters (TOF, LAC, LC), which can identify kaons in the on-line level. The scattered particle trajectories at the entrance and the exit of the SKS magnet are measured by tracking detectors. The scattered fiber tracker (SFT) is used instead of one of MWDCs at the entrance because tracking apparatus at the entrance is exposed to the high intensity π^- beam. Under a such condition, the number of combinations corresponding to track candidates becomes too large by using two sets of drift chambers because it is impossible to apply a tight timing gate due to the drift time. Therefore, the fiber tracker having a good timing resolution better than 1 ns (σ) is adopted to reduce the number of combinations. In addition, an amount of material has to be minimal to maintain the momentum resolution. Thus, one of MWDCs is replaced by the fiber tracker (SFT). On the other hand, since the polarity of the SKS magnet is opposite to that of the beamline, no beam passes through the downstream detectors. Therefore, two sets of a large MWDC (SDC3,4) having a cell size of 10 mm are used as tracking devices

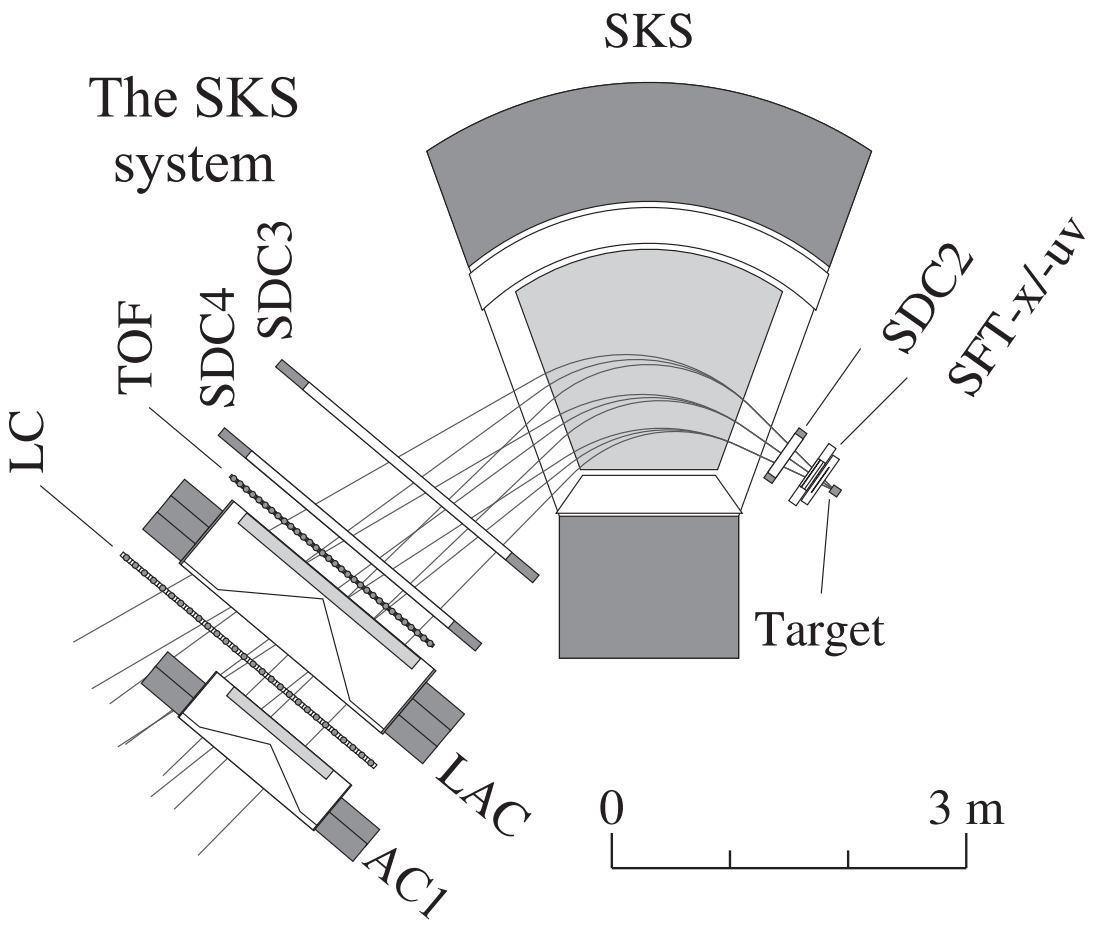

Figure 2.7: *The schematic view of the SKS system.*

at the exit of the SKS magnet. Scattered particle momenta are obtained by reconstructing the flight path from the entrance to the exit of the SKS magnet particle by particle. A flight path in the calculated magnetic field to minimize χ^2 with hits on tracking devices is obtained by numerical iteration with the Runge-Kutta method. In order to reduce multiple scattering effects, helium bags are installed in the SKS magnet and upstream of SDC3.

For the particle identification (PID), three types of different counters are installed at downstream of SDC3·4, i.e. the time of flight counter (TOF), the large aerogel Čerenkov counter (LAC), and the Lucite Čerenkov counter (LC). The TOF wall, which is a plastic scintillator wall, measures the time of flight from BH2 to TOF. LAC and LC are β-threshold type Čerenkov counters. The SKS system is designed to shorten the flight path length as short as possible to minimize kaon decays. Here, we define the central trajectory as a track that is incident perpendicular to all the tracking detectors. The path length for the central trajectory from the target to LAC is $\sim$5 m. In the present experiment, one more small aerogel Čerenkov counter (AC1) is placed behind LC to be included in the (π^+, K^+) trigger. A data for the ${}^{12}_{\Lambda}$C production at the beam momentum of 1.2 GeV/c is planned. In such the case, the π^+ beams pass through radiators in LAC and make a large dead time. Therefore, AC1 is additionally used to identify kaons when using the (π^+, K^+) trigger at the beam momentum of 1.2 GeV/c.

SKS achieves a good momentum resolution of 0.2% (FWHM) for the hypernuclear spectroscopy; at the same time, it has the large acceptance of $\sim$100 msr owing to a wide

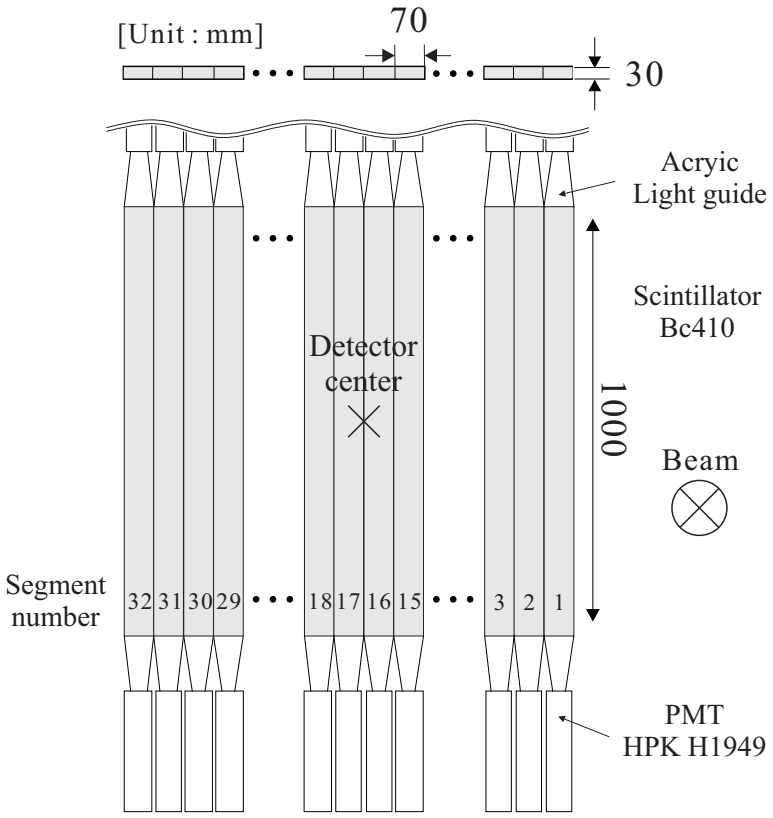

Figure 2.8: *The schematic drawing of the TOF wall.*

apperture (500 mm) of the pole gap. The wide momentum acceptance is also necessary to study the ΣN interaction in the present experiment. The SKS magnet is exited to 300 A (2.16 T mode). In this case, kaons having the momentum range of 0.7-1.1 GeV/c can be identified by trigger counters. A scattered kaon has the momentum of 0.87 GeV/c when an expected ground state of ${}^{6}_{\Lambda}$H is produced with the beam momentum of 1.2 GeV/c. On the other hand, the end point of Σ^- quasi-free production corresponds to the kaon momentum of 0.78 GeV/c. Therefore, we were able to obtain data for not only the Λ mass region but also a part of the Σ region.

2.4.2 Trigger counters

Three types of different counters (TOF, LAC, LC) are located at downstream of the SKS magnet. The particle identification in the on-line level is done by using the combination of these counters. Specifications of trigger counters are summarized in Table 2.2.

TOF

The time-of-flight wall is located downstream of SDC3 to measure the time-of-flight from BH2 to TOF; TOF consists of 32 pieces of plastic scintillator (Saint-Gobain BC-410) with thickness of 30 mm. Figure 2.8 shows a schematic drawing of TOF. Scintillating lights are detected by PMT, HPK H1949, from both vertical ends via acrylic light guides. The typical timing resolution between BH2 and TOF is 200 ps (σ).

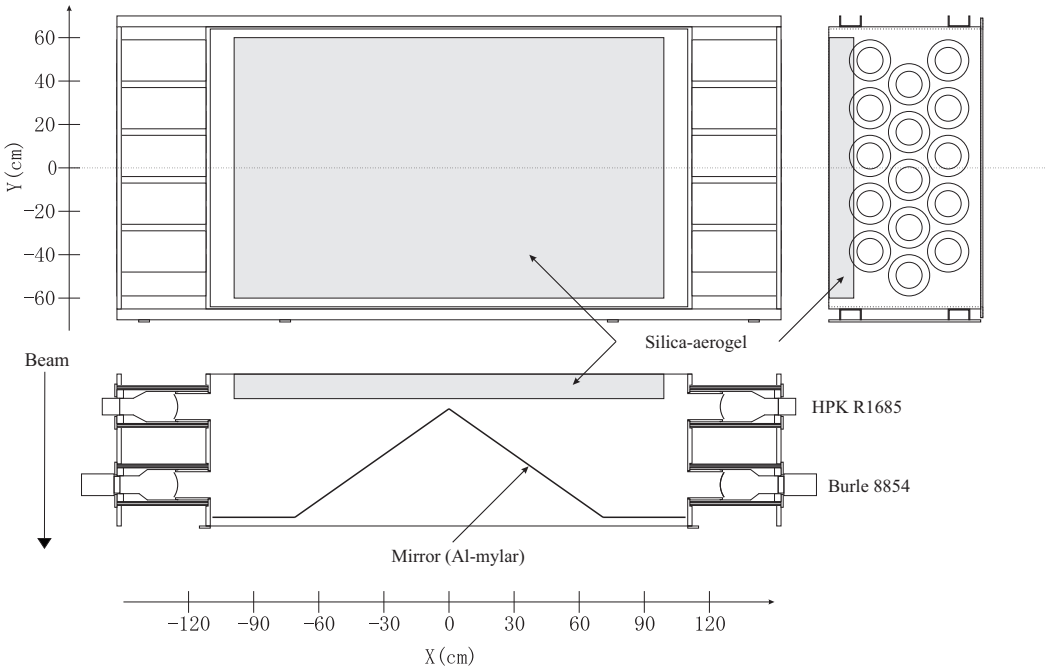

Figure 2.9: *The schematic drawing of LAC.*

LAC

The silica aerogel Čerenkov counter (LAC) to identify pions is located behind of TOF. The silica aerogel, of which reflective index is 1.05, is used as Čerenkov radiators. LAC is sensitive to charged particles whose β is higher than 0.95. This β corresponds to a momentum about 0.4 GeV/c, if particles are charged pions. The schematic drawing of LAC is shown in Figure 2.9. The size of sensitive area is $2080 \times 1200 \times 113$ mm^3. The aluminized mylar with thickness of 50 μm is pasted on the mirror and inside of the LAC frame to reflect Čerenkov lights. Čerenkov lights are detected by 30 PMTs attached horizontally to the frame. Among them 20 are of HPK R1584-01 model and 10 are of Burle 8854 type. The efficiency of 99.7% for the pion detection is obtained [52].

LC

The Lucite Čerenkov counter (LC) to identify protons is located just downstream of LAC. It is segmented to 28 pieces of Lucite (Acrylic) radiators with reflective index of 1.49. LC is also a β threshold-type Čerenkov counter, which is sensitive to charged particles whose β is higher than 0.67. Therefore, protons with a momentum of less than 0.85 GeV/c are rejected by LC. As shown in Figure 2.10, each radiator is equipped with PMTs (HPK H1949) on top and bottom of both sides. Since the emission angle of Čerenkov lights depends on β of incident particles, a wave-length shifter of bis-MBS is mixed by 10 ppm in weight in radiators for an uniform light emission.

2.4.3 Additional trigger counter

In the present experiment, kaons produced by the (π^-, K^+) reaction are identified in the trigger level by counters described above. On the other hand, an additional trigger counter, an aerogel Čerenkov counter called as AC1, is included into the (π^+, K^+) trigger, when

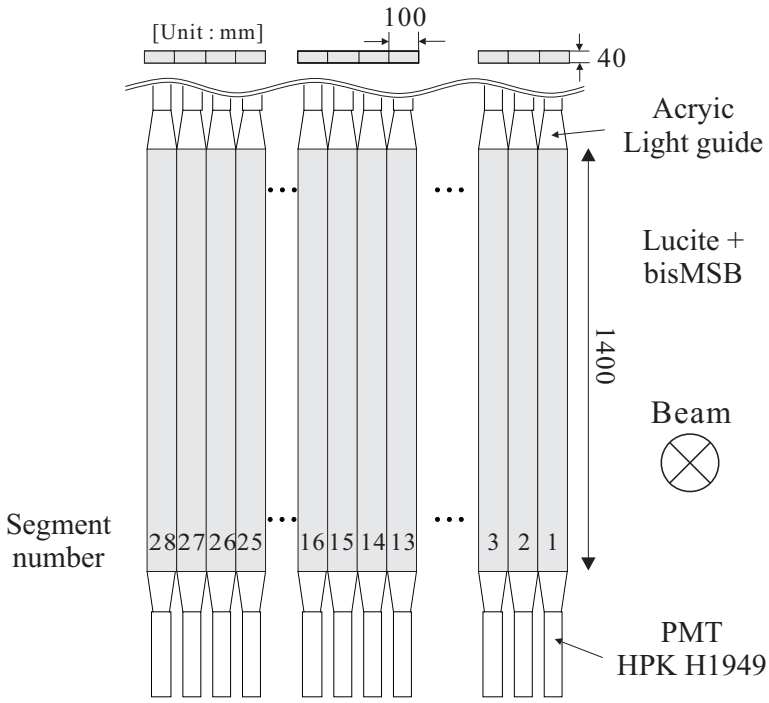

Figure 2.10: *The schematic drawing of LC.*

we use the π^+ beam with the momentum of 1.2 GeV/c for the ${}^{12}_{\Lambda}$C production. In our experimental setup, the π^+ beams with the momentum of 1.2 GeV/c pass through radiators and hit PMTs of LAC. Since LAC is not expected be irradiated with beam particles, LAC cannot keep the efficiency for detecting pions under such a high counting rate condition. Therefore, AC1 supports LAC to reject pions in the trigger level. The structure of AC1 is basically the same as LAC; however, the horizontal size of 1050 mm is smaller than that of LAC.

2.4.4 Tracking detectors

Four sets of tracking detectors are installed at the entrance and the exit of the SKS magnet to measure scattered particle trajectories. We call the entrance part and the exit part as SdcIn (SFT, SDC2) and SdcOut (SDC3·4), respectively. Specifications of MWDCs are summarized in Table 2.3.

Scattered fiber tracker

The scattered fiber tracker (SFT) is an upstream tracking detector of SdcIn. SFT is also a scintillation fiber detector read by MPPC like BFT. Although BFT has only a x plane, SFT has three independent planes (x,u,v) in order to participate in three-dimentional tracking. Scintillation fibers in u and v plane are tilted by 45° and −45° with respected to those in x plane, respectively. The structure of the x plane is the same as BFT; however, the number of fibers used is more than that in BFT so that SFT can detect particles with the scattering angle of up to 20°. Hence, SFT has the sensitive area whose horizontal size is 256 mm; the area consists of 512 scintillation fibers with diameter of 1 mm. On the other hand, scintillation fibers with diameter of 0.5 mm are used for the u and v planes to reduce the energy-loss straggling as low as possible. Although the total number of fibers used is

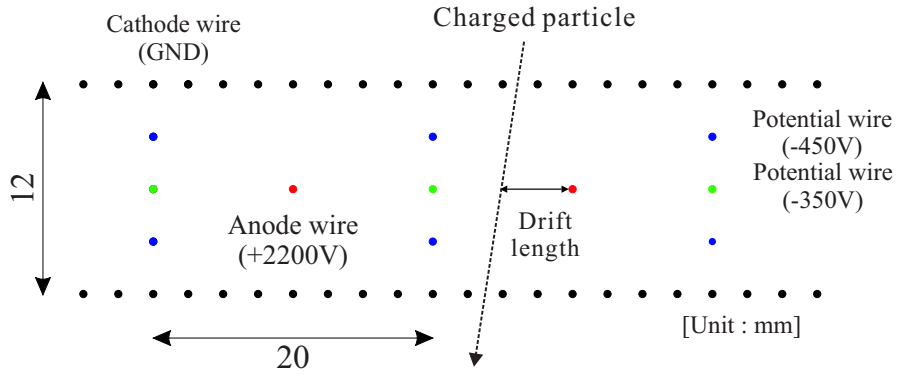

Figure 2.11: *The cell structure of SDC3·4.*

960, three fibers are combined to be read out by one MPPC in order to reduce the number of readout channels. The size of sensitive area of the u and v plane is 280×160 mm^2. The details of SFT are also described in Chapter 3.

SDC2

SDC2, which is MWDC whose the anode-anode spacing is 5 mm, is located just downstream of SFT. The design of SDC2 is similar to BC3·4 except for the anode-anode spacing. Anode wires, potential wires, and cathode planes are the same as BC3·4. However, the distance between the anode plane and the cathode plane is 2.5 mm because its G10 plate is thicker than that of BC3·4. SDC2 has six layers (vv', uu', xx'). The configuration of wires in the u and v planes are also the same as BC3·4.

Since the beam passes through SDC2, a mixed gas used for BC3·4 is used. The operation voltage of the cathode plane and the potential wires of SDC2 is -1.30 kV.

SDC3 and 4

The MWDCs, which have a large sensitive area of 2140×1140 mm^2, are located at the exit of the SKS magnet. SDC3·4 have six layers with the layer configuration ($vxuvxu$). Wires in the u and v planes are tilted by 30° and $-30°$ with respected to those in the x layer, respectively. Furthermore, the cell structure is also different; it is shown in Figure 2.11. The cell, which has a drift space of 10 mm, is comprised of an anode wire, two types of different potential wires, and the cathode wires. Anode wires are gold-plated wires with diameter of 25 μm. On the other hand, potential wires and cathode wires are gold-plated wires with diameter of 80 μm.

In the present experiment, a part of the sensitive area in high momentum side are not used in order to reduce the data size because kaons do not pass through such the region. High voltage is not applied to this region. As the result, we lost the sensitive area of 150 mm horizontally. In addition, when we use the π^+ beam, high voltage is not supplied to the region where the beam passes through. Mixed gas of Ar(50%) and C_2H_6(50%) is used by considering the gas gain. The operation voltage of anode wires is 2200 kV and cathode wires are connected to the ground. On the other hand, high voltages of potential wires are -350 kV and -450 kV.

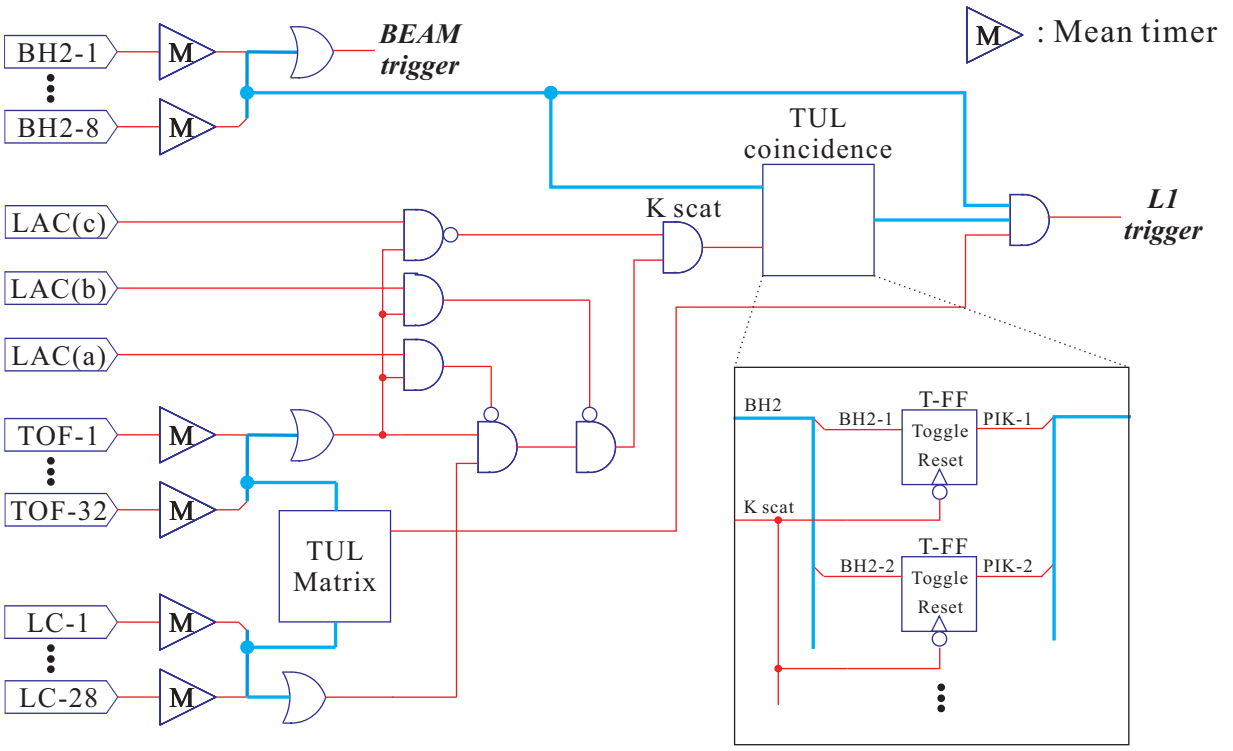

Figure 2.12: *The logic diagram of the L1 trigger.*

2.4.5 Trigger

We have to select (π^-, K^+) events from a large background by using a triggering system. The majority of beam pions are selected by the double mass-separation system. Therefore, the main backgrounds in the present experiment using the (π^-, K^+) reaction are the (π^-, π^+) or the (π^-, p) reactions because the cross section of such reactions are much lager than that of strangeness involving reactions. In the present experiment, we did not have to consider elastic and inelastic scattering events because the polarity of the SKS magnet is opposite to that of the beamline. To select the (π^-, K^+) events, we use two types of different triggers, i.e. the level 1 trigger (L1) and the level 2 trigger (L2). The L1 trigger is defined as a coincidence between the trigger counters. In this stage, Čerenkov counters play an essential role to eliminate pions and protons. The scattered pions are rejected by LAC with an efficiency of 99% while LC cannot reject protons with β, which is higher than the threshold of Lucite. At the L1 stage, the main background of the (π^-, K^+) events are the (π^-, p) events. Hence, the mass trigger (MsT) is prepared to reject scattered protons; the trigger is made from the time-of-flight information on TOF and the hit combination of TOF and LC segments. The final trigger rate is about 600 triggers/spill for 10 M pions per spill. Owing to these trigger systems, an acceptable DAQ efficiency of 80% is achieved under the high rate beam condition.

Level 1 trigger

The role of the L1 trigger is to identify the (π^-, K^+) reactions with a minimum trigger latency using only fast signals from scintillation counters and Čerenkov counters. The logic diagram of the L1 trigger is shown in Figure 2.12. The L1 trigger is a coincidence between the beam trigger and the scattered kaon trigger both of which are independently defined.

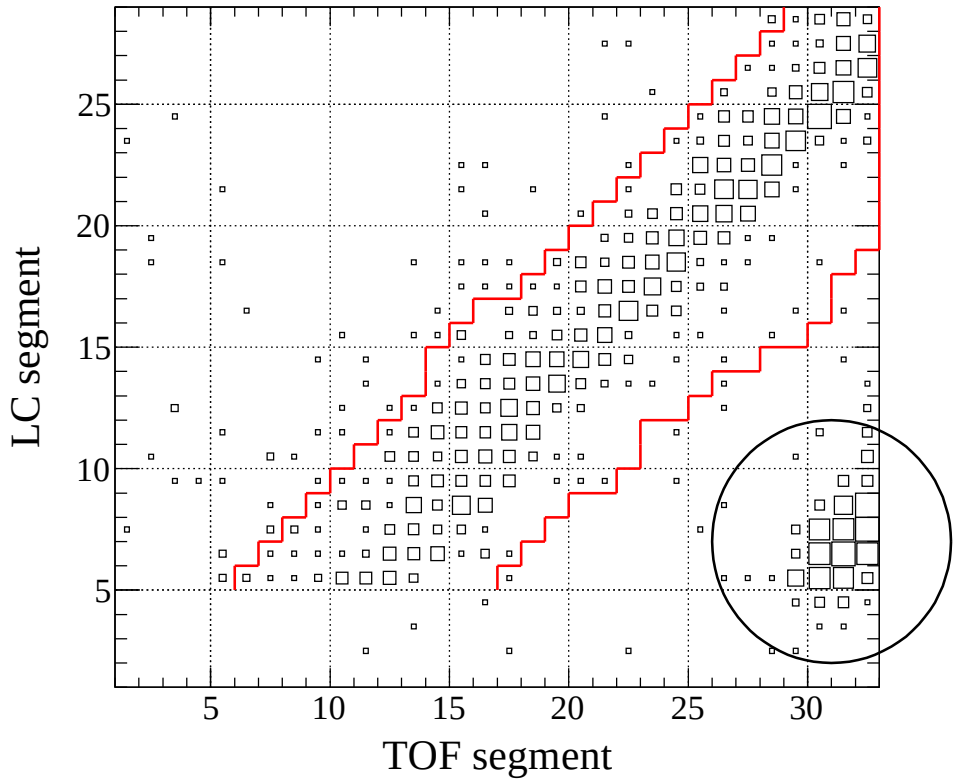

Figure 2.13: *The combination of the hit TOF and LC segments. The accepted region is surrounded by the solid line. A loose matrix gate is applied because the purpose of MT is a rejection of the backgrounds coming only from the target. Those are circled in the figure.*

The beam trigger is defined as

$$BEAM \equiv BH2.$$

In experiments using π beams, the coincidence of two timing counters and the gas Čerenkov counter is normally used to reject the contamination of protons (anti protons) and positrons (electrons). However, the contamination from anti protons is almost zero owing to the double mass-separator system. Furthermore, the contribution from the (e, K^+) reaction via virtual photons is negligible. Therefore, only signals from BH2 are used for the beam trigger.

For the scattered kaon trigger, Čerenkov counters (LAC, LC) are used to eliminate pions and protons as described above. In addition, the matrix trigger (MT), which is a coincidence matrix between TOF and LC segments, participates in the trigger to reject the particles coming from the target directly. As shown in Figure 2.13, particles passing through the SKS magnet make a correlation in hit segments between TOF and LC. On the other hand, events in the circled region in the matrix originates from a direct scattering from the target. Therefore, the region between the solid lines only is accepted. The matrix combination is implemented using the FPGA module, Tohoku Universal Logic (TUL). All discriminated signals from TOF and LC are input to TUL to check whether the hit combination of TOF and LC is within the accepted region.

Thus, the L1 trigger is defined as

$$L1 \equiv BEAM \times TOF \times \overline{LAC} \times LC \times MT.$$

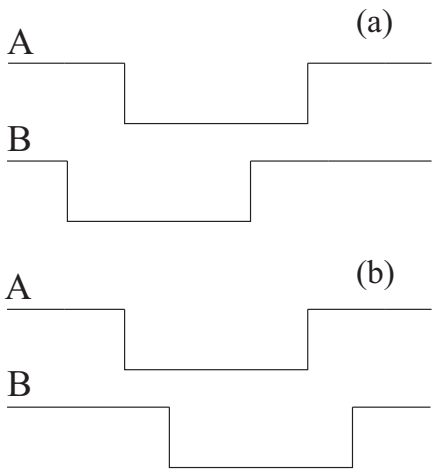

Figure 2.14: *The timing diagram. Both (a) and (b) are logic true for a level sensitive gate. On the other hand, only (b) is logic true by using TFF as a coincidence gate. In that case, A is an enable signal and B is a toggle signal.*

The edge sensitive type coincidence module is adopted for the coincidence of the beam trigger and the scattered kaon trigger. The module is shown as the TUL coincidence in Figure 2.12. In this module, toggle flip-flops (TFF), which are used as a coincidence gate, are implemented into FPGA on TUL so that the start timing can be determined by each segment of BH2 in the trigger level. The reason of adopting this module is the following. The OR signal of all segments of the timing counter usually joins to the L1 trigger. The coincidence timing between the beam trigger and the scattered kaon trigger is adjusted so that the start timing is determined by the beam trigger. However, it is difficult to guarantee that the timing is determined by the beam trigger in the high rate condition because the long OR signal could be generated if several segments fire with short intervals. In such the case, the start timing could be determined by the kaon trigger because the NIM coincidence module is just a AND gate: a level sensitive gate. Both of Figure2.14 (a) and (b) are logic true for a level sensitive AND gate. Then, TFF, which can detect the transition edge, is used as a coincidence gate.

For TFF, the Figure2.14 (b) case only is logic true by assuming that A is an enable signal and B is a toggle signal. Furthermore, the start timing determination becomes more certain using TFF for each segment of BH2. The each discriminated BH2 signal is connected to the toggle port of each TFF. On the other hand, the kaon trigger is connected to the enable port of all TFFs.

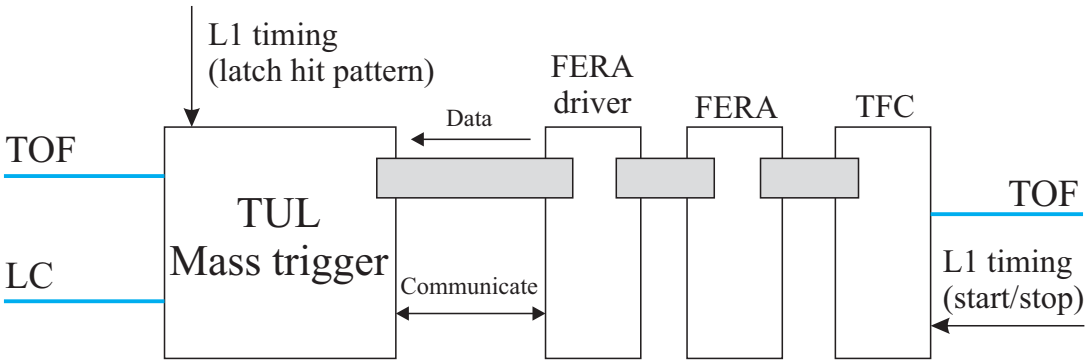

Figure 2.15: *The schema of the mass trigger.*

Level 2 trigger

The mass trigger (MsT) can reject protons faster than β threshold of Lucite using time-of-flight information on the TOF wall. The L2 trigger is defined as

$$L2 \equiv L1 \times MsT.$$

Since the hit combination of TOF and LC is roughly correlated to momenta of scattered particles, the difference of particle masses is reflected in their time-of-flight for each hit combination. Therefore, protons can be rejected by setting an acceptable TDC region for each combination. The scheme of MsT is illustrated in Figure 2.15. The TDC region table is stored in the TUL module, to which TOF and LC signals are connected. Each discriminated signal of TOF is connected to the LeCroy Model 4303 Time-to-FERA Converter (TFC), which is a time-to-charge converter. Its outputs are connected to the LeCroy Model 4300 Fast Encoding and Readout ADC (FERA). The digitized timing information and the hit address are sent to the TUL module from the FERA driver. If there is at least one acceptable hit combination, MsT outputs the trigger signal.

The decision time of MsT is 15 μs. If the TDC information is out of range, the fast clear signal is fired to reset DAQ modules. The trigger rate of L1 is reduced to half by MsT.

2.4.6 Data acquisition system

In the data acquisition (DAQ) system of the K1.8 experimental area, a new network oriented readout module, KEK-VME/COPPER [53] and a MPPC readout system with EASIROC [56], are adopted while several traditional readout systems such as CAMAC/FERA, KEK TKO [54], and the conventional VME bus are used as well. These different DAQ subsystems are integrated by a network based DAQ software, Hadron DAQ (HDDAQ) [55]. Today, networking communication among the inter-subsystem has become the most common method. Data from each subsystem are gathered by controllers having network interfaces with TCP/IP protocol. However, since the network is an asynchronous communication, the event identification becomes an issue. Therefore, the master trigger module (MTM) and the receiver module (RM) [55] are adopted; the system distributes an event tag to each subsystem. The entire scheme of the DAQ system is illustrated in Figure 2.16, and subsystems are shown in Figure 2.17.

MTM manages functions controlling the DAQ system such as triggers, clear, busy, and the event tag. These information are distributed via the Ethernet cable from MTM to RM

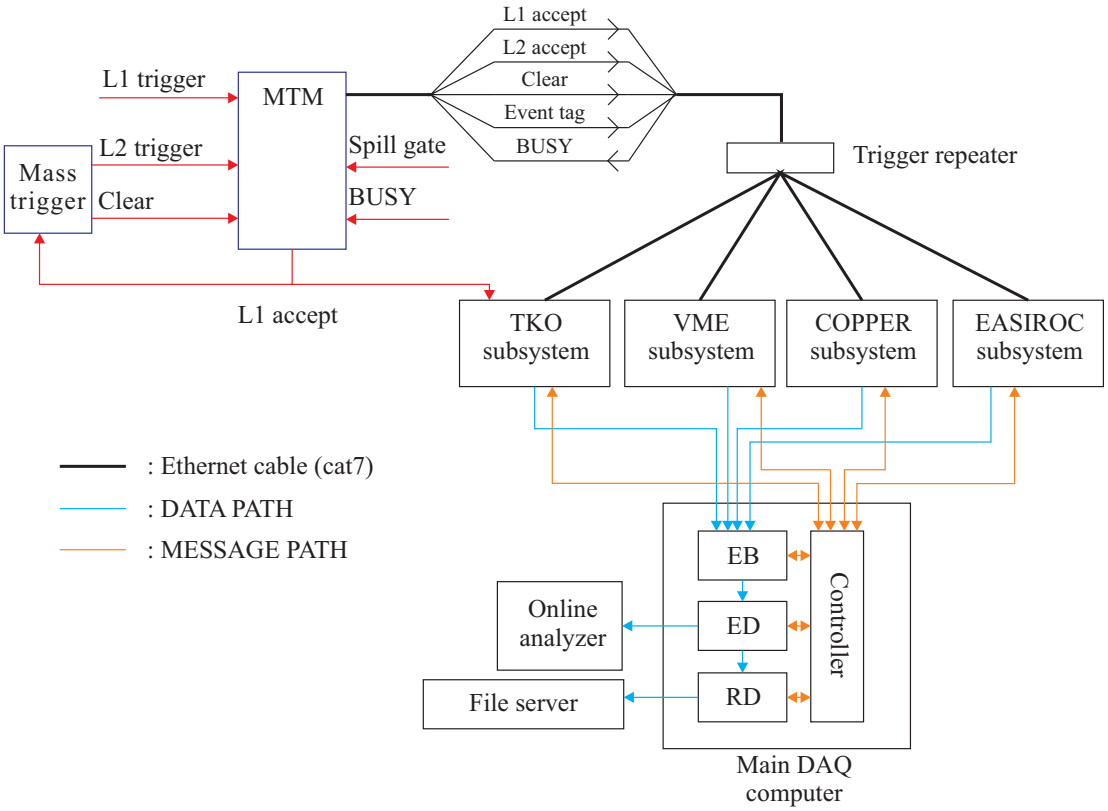

Figure 2.16: *The schema of the main DAQ logic.*

in each subsystem in real time. The L1 trigger is used as the start/stop timing of ADC gate and TDC. After finishing the A/D conversion, the data transmission begins at the L2 timing. On the other hand, all stored data and module state in each module are reset by a clear signal, when MsT rejects the event. Busy issued in each subsystem can veto the next trigger on MTM. The event tag is decoded in RM and embedded to an event packet at the L2 timing.

TKO

All PMT signals are read by ADC and TDC of the TKO system and Dr.T2 is used to readout SDC3·4 signals. Currently, the TKO subsystem is used together with the VME bus. TKO bus is accessed by Super Memory Partner (SMP), which is a memory module of VME, via Super Control Header (SCH) [57]. Data on the memory are gathered by the on-board CPU VME controller, GE V7807RC [58], and transmitted via TCP Ethernet.

VME

The VME bus subsystem is used for the readout of SSD. A special VME module, APVDAQ, reads and controls APV25 chips; the module was developed by the Electronics-2 group at the Austrian Academy of Sciences [59]. The analog signal multiplexed by the APV25 chip is transferred via the Ethernet cable (CAT7) to APVDAQ. An incoming signal is digitized by a 10-bit Flash-ADC and stored in a memory in FPGA. To operate SSD DAQ under high rate conditions, the zero suppression logic and the multi-buffer are implemented by upgrading the FPGA firmware. The on-board CPU VME controller, GE XVB601 [58],

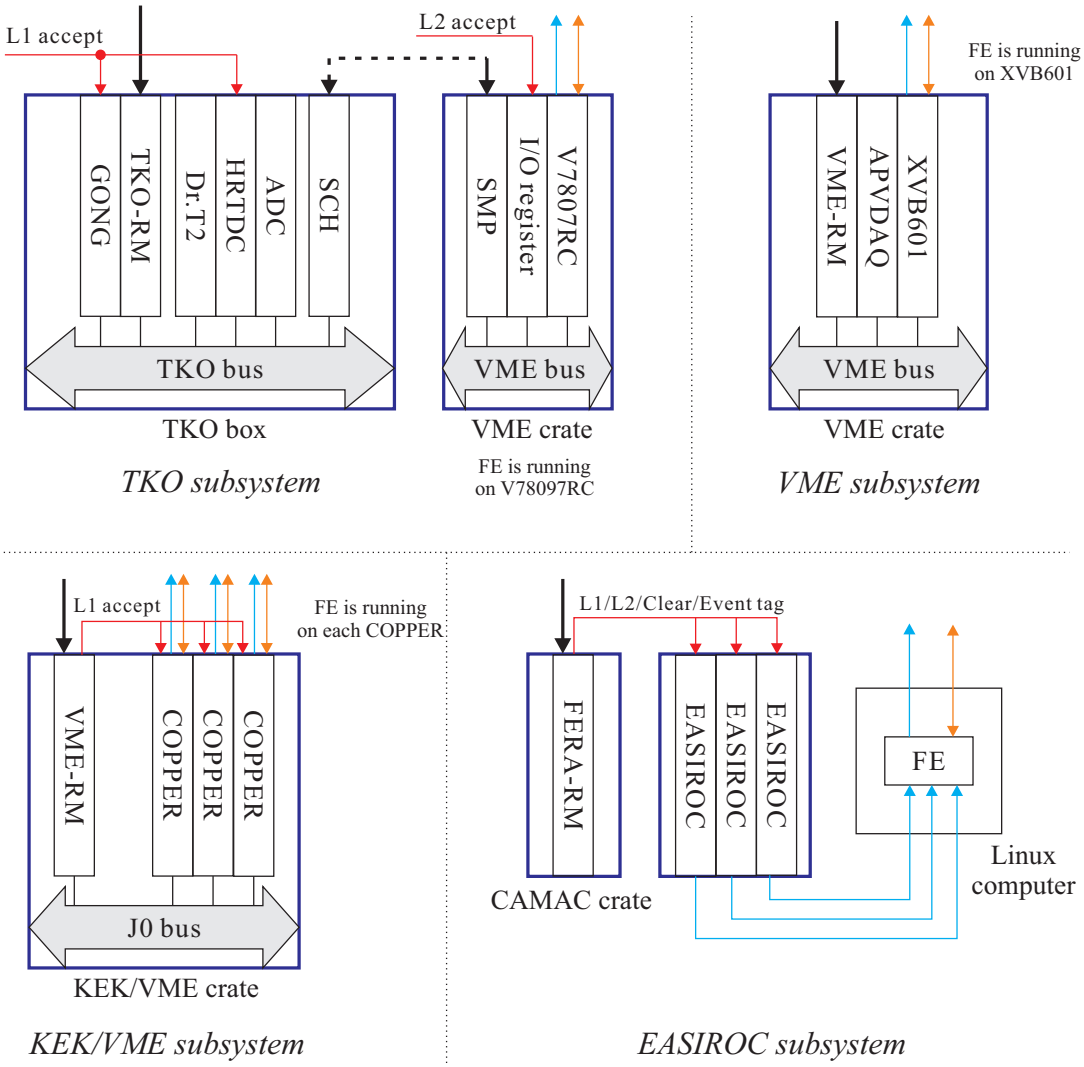

Figure 2.17: *The schema of each subsystem.*

collects data and transmits them via the network.

KEK-VME/COPPER

The network oriented readout system, COmmon Pipelined Platform for Electronics Readout (COPPER), is adopted to readout MWDCs. COPPER is a platform module of the 9U KEK-VME create, which is an extended VME bus standard with an extra bus using the "J0" connector. Trigger information received by RM is distributed through this extra bus. The COPPER platform has four slots to mount a daughter card called as FINESSE (Front-end INstrumentation Entity for Sub-detector Specific Electronics). In the present experiment, multi-hit FPGA TDCs are mounted. Although the COPPER platform is a slave modules of KEK-VME, the standalone operation is realized without any additional module because each platform has network interfaces for control and data transfer.

MPPC readout system with EASIROC

The multi-MPPC readout system with the EASIROC chip was developed to operate and read the scintillation fiber tracker. EASIROC is an ASIC, which has all essential functions

to operate and read the Pixelated Photon Detector (PPD). It was developed by Omega group in IN2P3 [56]. The readout module with EASIROC has DAQ functions such as ADC, FPGA multi-hit (MH) TDC and the network interface. Therefore, this is an all-in-one module for MPPC DAQ. Since this module does not belong to any standard, the FERA RM is used alternatively. The details of this system are described in Chapter 3.

Hadron DAQ

Hadron DAQ (HDDAQ) is a network based DAQ software consisting of several DAQ components, i.e. Front-end (FE), Event Builder (EB), Event Distributor (ED), and Recorder (RD). These components have two different paths, namely, DATA PATH and MESSAGE PATH, with the TCP/IP protocol. DATA PATH is a pathway to individual each detector data. On the other hand, all components are controlled by Controller via MESSAGE PATH. The front-end process reads data from each readout electronics and transmits them to the Event Builder process. The Event Builder process collects data fragments from FEs and builds an event packet event by event. This packet is sent to the Event Distributor process. The role of the Event Distributor process is to distribute the event packet to downstream processes such as Recorders and on-line monitors. ED gives all event packets to Recorders while it is not guaranteed that all packet is sent to on-line monitors because Recorder has the first priority. Recorder reads data from ED and stores them to the storage devices with compression by using "zlib".

FEs are running on each front-end server computer while other components are running on the control DAQ server.

Table 2.4: *The data summary. Momentum and Intensity mean the beam momentum and the beam intensity, respectively.* N_{pion} *means the total number of* π^- *beam injected.*

Data	Momentum (GeV/c)	Reaction	Target	Intensity (10^6/spill)	N_{pion}
${}^{6}_{\Lambda}$H	1.2	(π^-, K^+)	^{6}Li	12	1.7×10^{12}
${}^{12}_{\Lambda}$C	1.2	(π^+, K^+)	graphite	4	5.4×10^{10}
Σ^-	1.37	(π^-, K^+)	polyethylene	10	4.1×10^{10}
Σ^+	1.37	(π^+, K^+)	polyethylene	3.5	3.1×10^{9}
beam through	0.8, 0.9, 1.0, 1.2		none		

2.5 Targets

An enriched ^{6}Li (95.54%) block, which is 3.5 g/cm^2 in thickness, is used as the experimental target. The size of the target is 70×40 mm^2. The target is doubly packaged by the Z-86 bag [60], of which thickness is 55 μm, to suppress an oxidization of Lithium in the Argon gas grove box. The Z-86 bag is transparent, and that is an advantage compared to other non-transparent material that cannot be easily inspected. In addition, Z-86 has a low oxygen gas permeability of 80 ml/m$^2 \cdot$ d $\cdot$ MPa at 20 C°. Owing to this property, no oxidization of Lithium was visually observed.

Other targets, the carbon and the polyethylene target, are used to take calibration data. The carbon target is a graphite block which is 3.6 g/cm^2 in thickness. Its size is 80×88 mm^2. The size of polyethylene target, which is 3.4 g/cm^2, is 80×40 mm^2.

2.6 Data summary

We took data in two separate experimental cycles, in December of 2012 and in January of 2013. The data summary is listed in Table2.4. The total number of π^- beams injected on the ^{6}Li target is 1.7×10^{12}.

Chapter 3

Scintillation fiber tracker system

3.1 Overview

For the success of the present experiment, it is essential to handle the high intensity pion beams. The scintillation fiber detector, which achieves both a good timing resolution of better than 1 ns (σ) and a position resolution of better than 200 μm, is ideal for this purpose. Therefore, pions involved in the reaction can be identified with a better signal-to-noise ratio than when using wire chambers. The fiber detector consists of scintillation fibers, MPPCs mounted on printed circuit boards (PCB), and the readout electronics for a large number of MPPCs. In this chapter, this systems is described.

3.2 Beamline fiber tracker

The beamline fiber tracker (BFT) is a finely segmented scintillation hodoscope installed at just upstream of the Q10 magnet in the K1.8 spectrometer. BFT has one plane only and measures the x position of each particle. Method to reconstruct beam momenta using BFT hit information is described in Chapter 4.

Fiber detector

The effective region of BFT is comprised of 320 cylindrical scintillation fibers, the Kuraray SCSF-78MJ [61] fiber with diameter of 1 mm. The scintillation fibers are arranged in a staggered position with an overlap of 0.5 mm as shown in Figure 3.1. These fibers are fixed to the fixing bar shown in Figure 3.1 with epoxy adhesive. On the other hand, no adhesive is applied on surfaces of the fibers in the effective area. The size of the effective area is designed to be 160×80 mm^2 by considering the maximum beam size at the BFT position.

One of the two ends of each fiber is brought into contact with a MPPC sensor as shown in Figure 3.1 to readout scintillation light. The readout end of the fiber is inserted into holes bored in the readout frame. Precision of each fiber position at the readout frame is determined by these holes. Scintillation light is collected into a MPPC mounted on a MPPC card assembly, which is described in section 3.3.1. On the other hand, the other end is only attached to the fixing frame position and open.

The detector frame of BFT shown in Figure 3.1 is made from several aluminum parts except for the readout frame made of an acrylic bar. Metal plates are attached to the frame for light shielding except for the beam window; the window is covered by a black sheet.

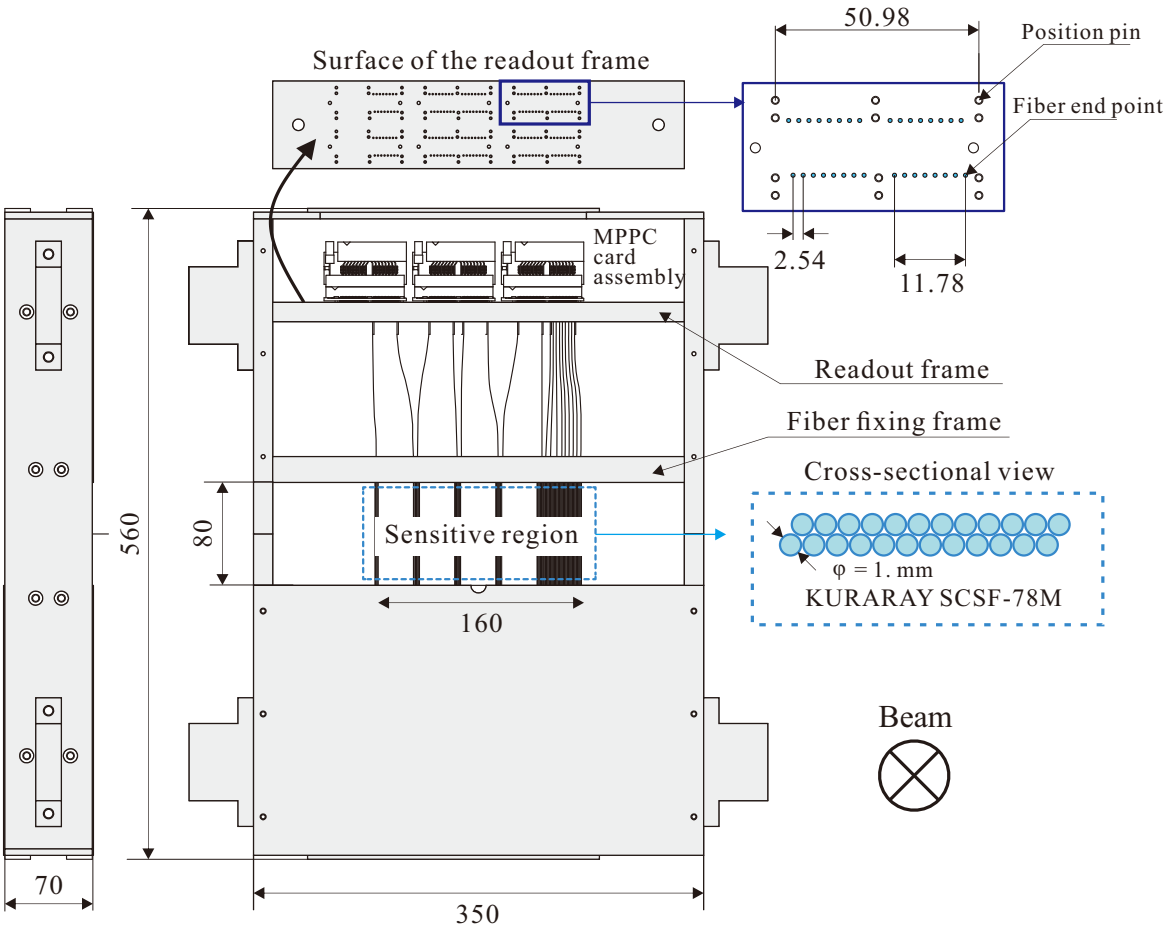

Figure 3.1: *The drawing of the detector frame of BFT.*

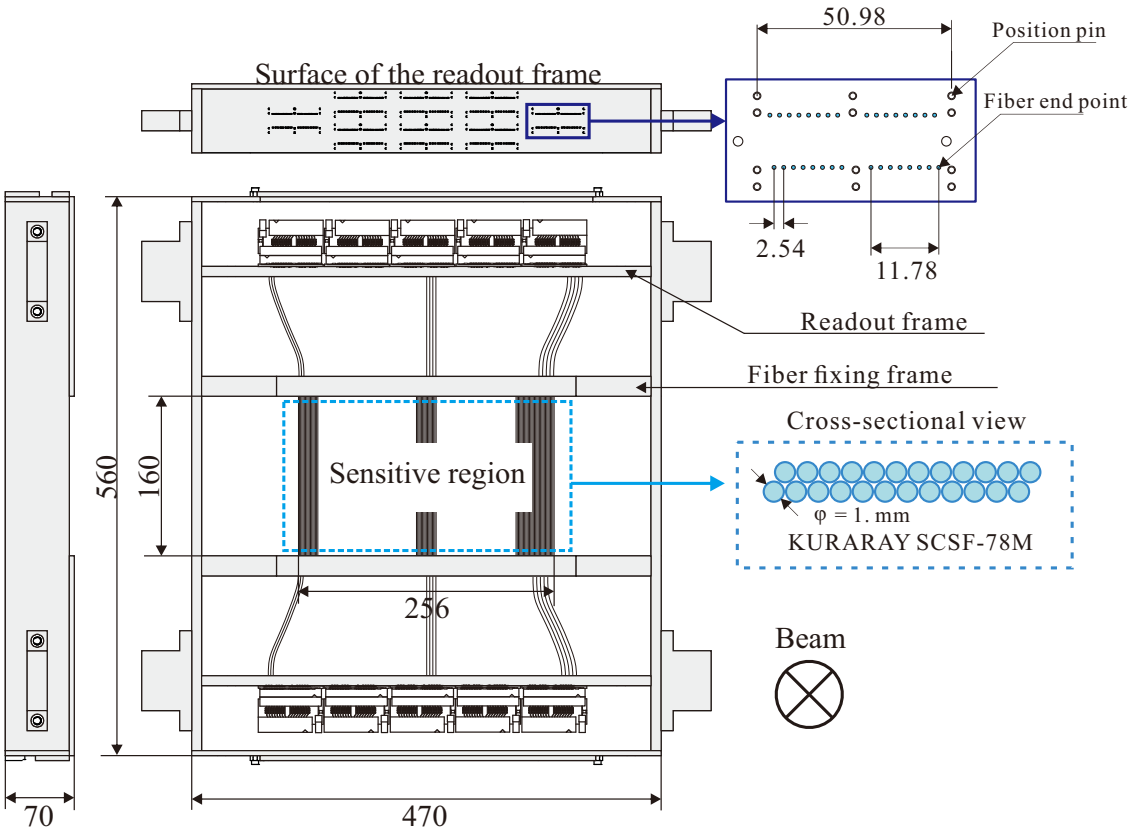

Figure 3.2: *The drawing of the x frame of SFT.*

3.3 Scattered fiber tracker

The scattered fiber tracker (SFT) is a tracking detector located upstream of SDC2 in the SKS system. It is comprised of two independent frames, a x frame and a u-v frame, and used for a three dimensional tracking.

Detector frame of the x plane

The x frame of SFT shown in Figure 3.2 is basically the same as that of BFT. However, the size of the effective area and the total number of fibers used are different because SFT has to detect scattered particles with scattering angles up to 20°. A beam window size is 450×160 mm^2 and the size of the effective area consisting of 512 fibers is 256×160 mm^2.

Detector frame of the u-v plane

The detector frame of the u-v plane, which fixes fibers in both of the u and v planes, is shown in Figure 3.3. Although the same scintillation fibers, Kuraray SCSF-78MJ, are used, its diameter is smaller in order to reduce the energy loss straggling. Scintillation fibers with diameter of 0.5 mm are arranged in a staggered relation with an overlap of 0.25 mm. Fibers in the u and v planes are tilted by 45° and $-45°$ with respected to those in the x frame. These fibers are fixed at the horizontal and vertical fixing frames shown in Figure 3.3. The beam window size of 280×160 mm^2 corresponds to the size of the effective area.

The number of fibers used is 960. However, the number of MPPCs is reduced to 320 in each plane by combining three fibers to read them out with one MPPC sensor as shown

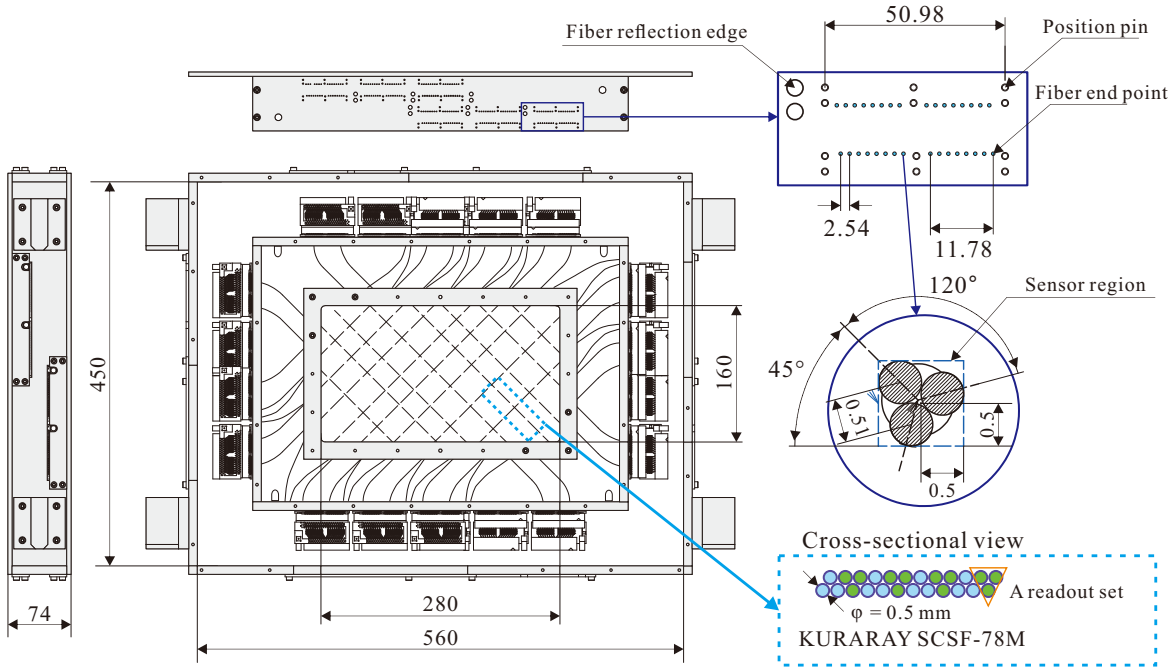

Figure 3.3: *The drawing of the u-v frame of SFT.*

in Figure 3.3. In order to guarantee good contact between three fibers and the sensor, three holes adjoining each other are made and three fibers are fixed in the holes as shown in Figure 3.3. Although each fiber in the *u-v* frame is also read from one end, aluminized mylar is put on the other end to reflect light and gain the light yield.

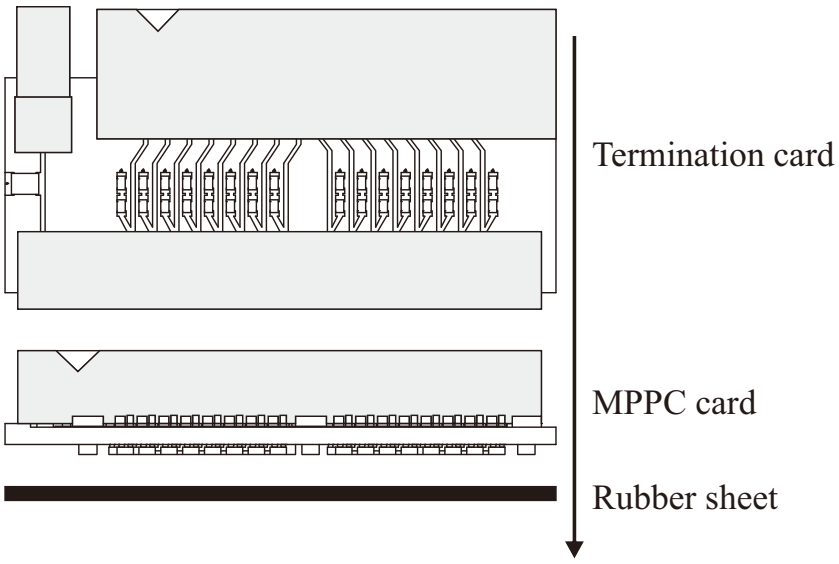

Figure 3.4: *The structure of the MPPC card assembly. Each card is connected to the other as shown.*

3.3.1 MPPC card assembly

Scintillation light from each fiber (or three fibers) is collected by a MPPC whose sensor is a square of 1 mm × 1 mm. The MPPC is a kind of avalanche photo diodes and well suited for a finely segmented counter because of its small size. Furthermore, both a good timing resolution and a high photon detection efficiency (PDE) are achieved. The type HPK S10362-11-100P, which has the highest PDE in the HPK products [62], is selected as a photon detector to obtain a sufficient detection efficiency for minimum ionizing particles. Since S10362-11-100P is a surface mount type detector, we can make a compact MPPC card assembly using PCB.

The MPPC card assembly consists of two cards, namely, a MPPC card and a termination card. These cards are connected with each other as shown in Figure 3.4.

MPPC card

The MPPC card mounts 32 MPPCs as shown in Figure 3.5 with several protection registers and filter capacitors. The positions of MPPCs on the MPPC card correspond to those of holes in the readout frame, in which fiber are inserted. The sensor is coupled to the end surface of the fiber by air contact by just attaching the MPPC cards with screws. A precise alignment of MPPC is necessary in order to achieve a uniform light collection efficiency because the sensor size and diameter of the fiber are equal. A position precision of each MPPC better than 100 μm is guaranteed by a special designed tool used in the soldering process. The rubber sheet with the thickness same as the height of MPPC is inserted between the readout frame and the MPPC card to fill the gap.

Termination card

A schematic drawing of the termination card is illustrated in Figure 3.4. As shown in Figure 3.6, a role of the termination card is to terminate signals near the sensor and to supply bias voltage to the MPPC card via a connector. By the termination registers on this

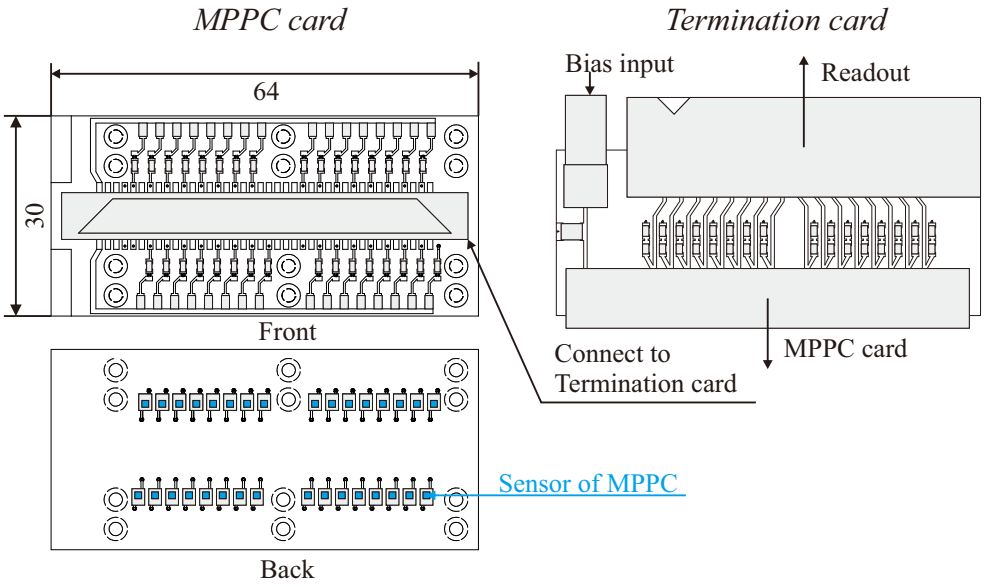

Figure 3.5: *The schematic drawing of the MPPC card.*

card, a reflected signal is absorbed. The common bias voltages is given to all the MPPCs while a bias of each MPPC is adjusted by EASIROC described in the next section.

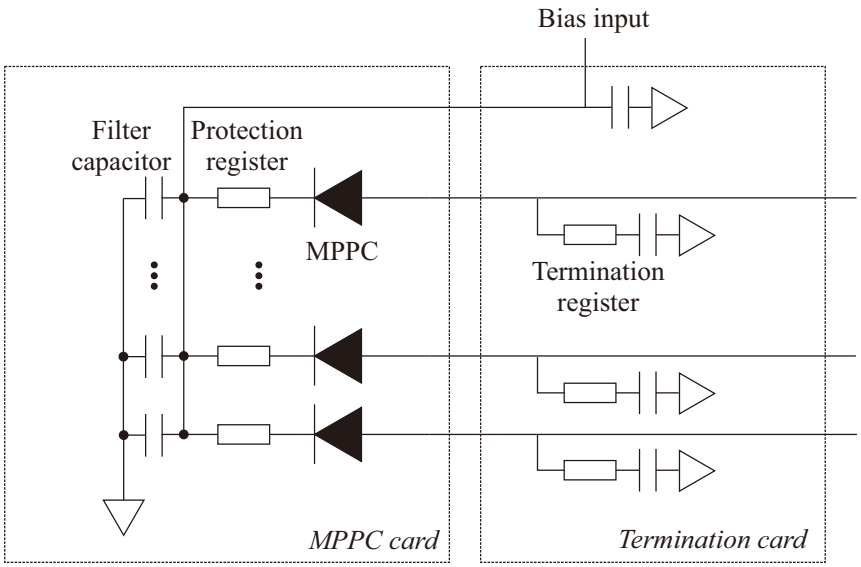

Figure 3.6: *The schematic circuit of the MPPC card assembly.*

3.3.2 Multi-MPPC readout electronics with EASIROC

MPPC has excellent properties such as a fast time response, magnetic field tolerance or high PDE while several difficulties in operation should be overcome. An amplifier and bias adjustment are necessary sensor by sensor. Especially, these problems become serious in the case of multi-MPPC operation such as the fiber tracker. A readout electronics dedicated to the multi-MPPC operation is required. Thus, the multi-MPPC readout electronics [63] is developed using EASIROC.

EASIROC

For such an integrated system as the multi-MPPC electronics, a front-end ASIC plays an essential role. Extended Analogue SiPM Integrated ReadOut Chip (EASIROC) developed by the Omega group in IN2P3 in France [56] has all necessary functions to read out MPPCs such as Digital to Analog Converter (DAC) for bias adjustment, amplifiers, shapers, and discriminators. One EASIROC chip can operate and read out 32 MPPCs. The circuit scheme of EASIROC is illustrated in Figure 3.7. The bias of each MPPC is adjusted by DAC, which is located in front of the input capacitor, with 20 mV step within a range of 0-4.5 V. An incoming analog signal is divided into a high gain (HG) and a low gain (LG) signal according to the ratio of the input captaincies. Each analog signal is amplified by a pre-amplifier with a typical gain of 75 and shaped by a slow shaper with a typical shaping time of 50 ns for a charge measurement. On the other hand, a fast shaper with shaping time of 15 ns is implemented only in the HG line for a timing measurement. Parameters in red rectangles in Figure 3.7 are programmable and can be accessed by a slow control method.

For the charge measurement, analog signals shaped by the slow shaper are sent to a charge measurement part shown in Figure 3.7; this part is independently connected to each analog line. Each analog signal is stored in a buffer at the hold signal timing in the ADC measurement. Since EASIROC has only two analog lines, namely, the high gain output and the low gain output, analog signals are multiplexed at this part. Signals held in the analog buffer are transferred to the ADC synchronized to the ADC clock cycle.

For the timing measurement, an update type discriminator is implemented into each analog part. Then, the discriminated signal width depends on the pulse height. A common voltage threshold is given to all the discriminators from 10-bit DAC. Analog signals are multiplexed while the discriminated signals are output in parallel. The timing resolution of EASIROC is 270 ps (σ) for a small pulse corresponding to 1 photo electron.

EASIROC readout board

A picture of the developed EASIROC readout board and its scheme are shown in Figure 3.8 (a) and (b), respectively. It is comprised of EASIROC, ADC, FPGA (SPARTAN6), and several analog and digital I/Os. Analog and digital signals from EASIROC are sent to ADC and FPGA, respectively. The role of FPGA is to control EASIROC and ADC, data processing, and the timing measurement with FPGA MHTDC. This module communicates with a server computer with the TCP/IP protocol realized by SiTCP [64], which is a hardware implementation of the TCP protocol without CPU. SiTCP functions are outsourced to the other sub-card, 100BASE-Tx SiTCP On Your circuit (SOY) [65].

The timing of the discriminated signal is digitized by MHTDC in FPGA, which can measure the timing of both the leading and trailing edges with a timing precision of 1 ns. To achieve the 1 ns precision, four free-run counters driven by four 250 MHz clocks with

Table 3.1: *The specification of MHTDC in FPGA.*

Timing precision	1 ns
Time window	1 μs
L1 buffer depth	16 per channel
L2 buffer depth	512 per event
Double hit resolution	$\sim$ 30 ns
Dead time	$\sim$10 μs ns
Timing resolution	530 ps (r.m.s)

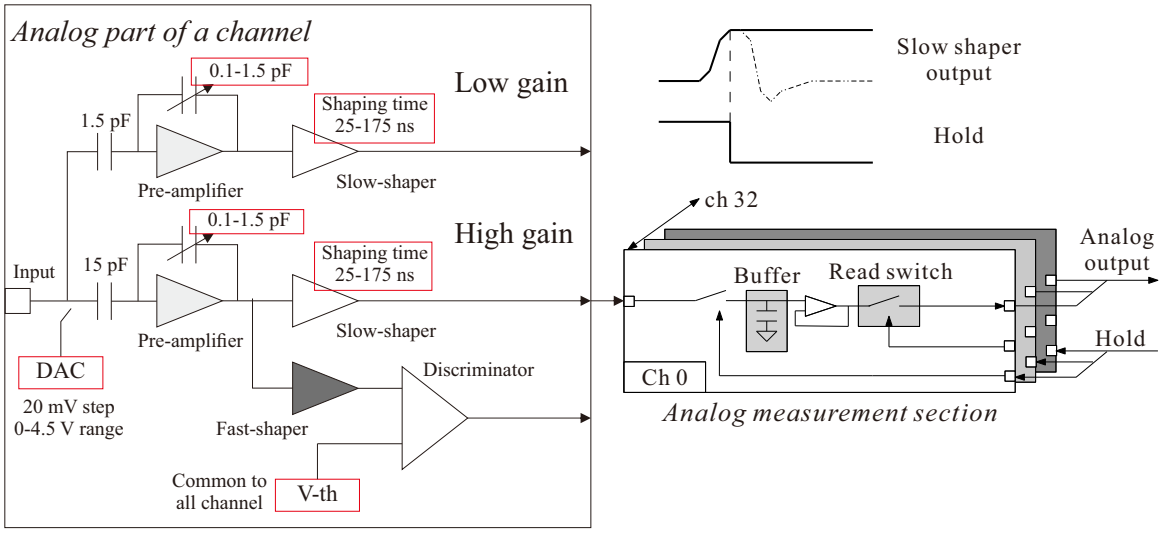

Figure 3.7: *The circuit scheme of EASIROC. EASIROC has DAC for bias adjustment, amplifiers, shapers, and discriminators for each channel. The programmable parameters such as DAC output, AMP gain, shaping time, or V-Th are accessed by the slow control method. The shaped analog signal is stored in a buffer at the signal hold timing and multiplexed to the analog output line.*

different phases are implemented. In each channel, a ring buffer which can store data for 1 μs is prepared and hit data are transferred to the level 1 (L1) buffer at the common stop timing. All data are collected from the L1 buffers to the level 2 (L2) buffer. These data transfer time, which corresponds to a dead time, is $\sim$10 μs. The specification of MHTDC is summarized in Table 3.1.

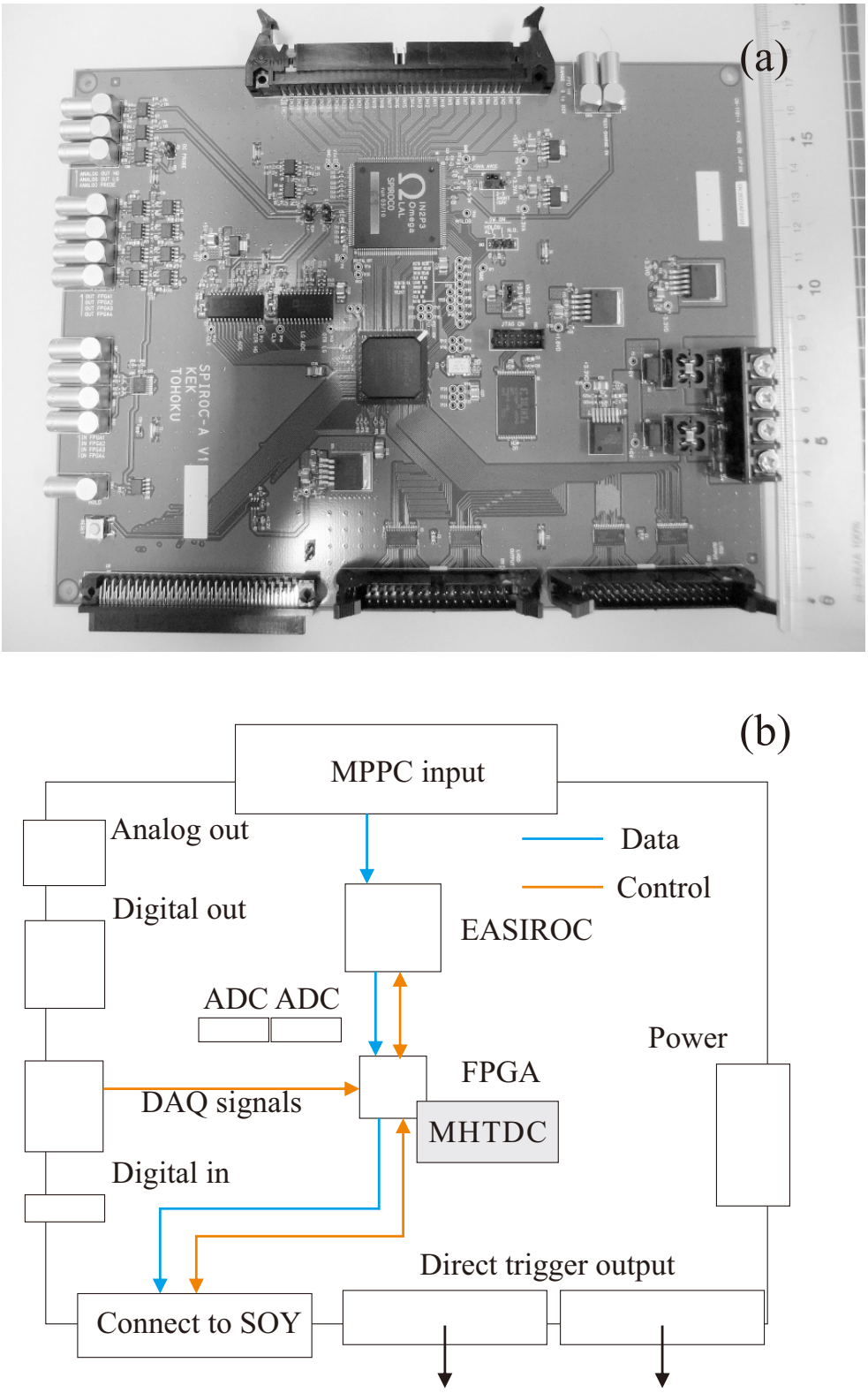

Figure 3.8: *The picture and the scheme of the EASIROC readout board. (a) The picture of the board. (b) The scheme of the readout board. Arrows in the figure show the data flow.*

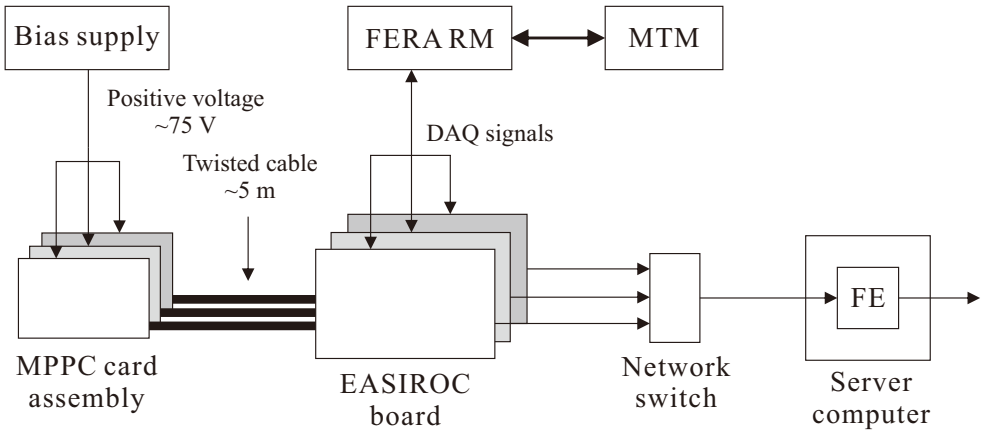

Figure 3.9: *The operation scheme of the BFT system.*

Operation

The operation scheme of BFT is illustrated in Figure 3.9 as an example for an operation method of the fiber tracker system. A common positive bias voltage is provided to a cathode of MPPC from a DC power supply, which is a series regulator (TAKASAGO TP/D model). On the other hand, the positive voltage from DAC in EASIROC is put on an anode of MPPC via the signal line. Therefore, the actual bias voltage for MPPC is determined channel by channel as the difference between the common voltage and the DAC voltage. Owing to the fine step of DAC in EASIROC, a gain curve of MPPC as a function of the bias voltage is easily obtained as shown in Figure 3.10 by changing the DAC voltage. According to the gain curve, each DAC voltage is determined to make all the gain of MPPC equal. Finally, each gain of MPPC is checked using ADC and tuned finely.

Analog signals from MPPC are transmitted via a 5 m twisted cable to the EASIROC readout board and dealt with 10 EASIROC boards. A server computer, on which the front-end process is running, collects data from each board via a network switch.

During the beamline operation, the TDC data only are taken because the slow shaper signals are piled-up under the high intensity beam condition. Hence, the internal power supply for the slow shapers is turned off. Basically, ADC information is necessary to correct time walk. However, the Time Over Threshold (TOT) having charge information is obtained by the update type discriminator of EASIROC and used instead of ADC. A time walk correction using TOT is described in Appendix A.

3.3.3 Basic performance

Basic performances of BFT such as a most probable number of photo electrons and a uniformity of light yield were obtained using a β-ray source. In addition, the position resolution was measured in the previous beam experiment.

Data for β rays were taken by setting a source over the sensitive area of BFT and a plastic scintillator with PMT below BFT. Figure 3.11 shows a typical ADC histogram of a fiber. By fitting a peak in such a histogram for each channel, the distribution of the most probable photoelectron number is obtained as shown in Figure 3.12. Owing to the good position precision of mounting MPPC, an excellent uniformity was obtained. Consequently, the light yield for MIP was $\sim$18 p.e..

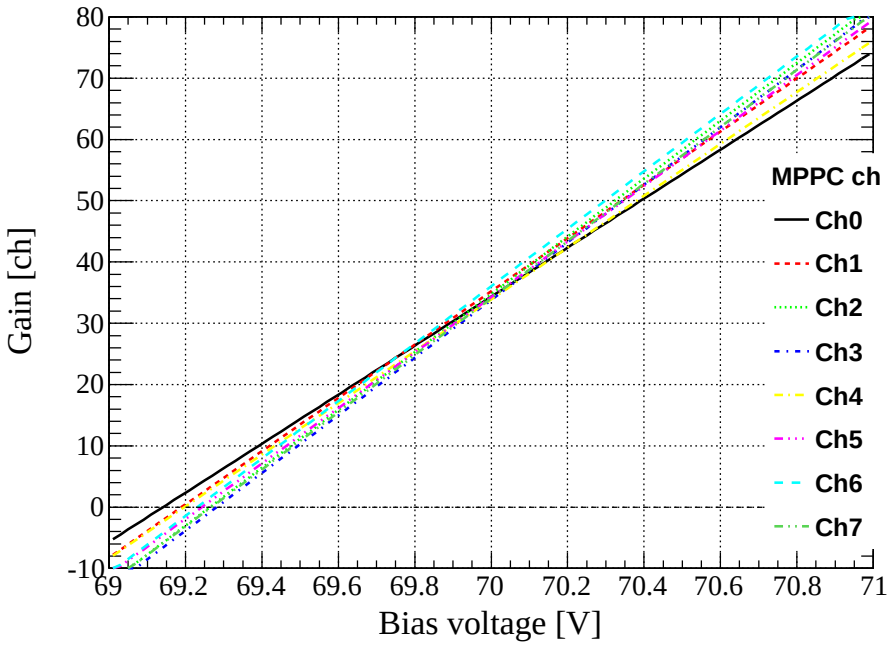

Figure 3.10: *A correlation between the MPPC gain and the bias voltage.*

In the previous experiment at the K1.8 beamline, performances of BFT were evaluated by installing BFT between two multi-wire proportional chamber (MWPC) whose anode-anode spacing is 1 mm. The position resolution was estimated as 192 μm (σ) from a residual distribution, which is a difference between a BFT hit position and a trajectory reconstructed by the two MWPCs.

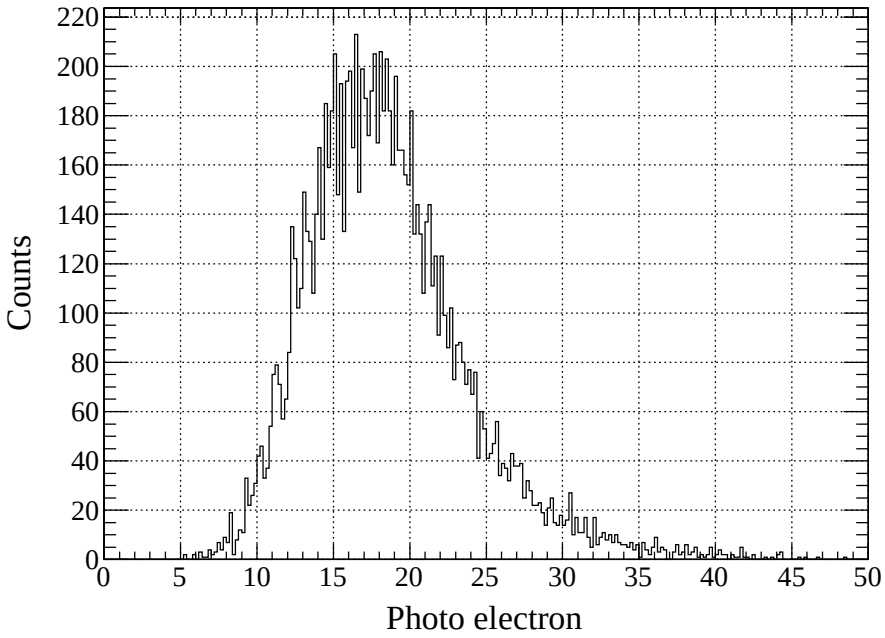

Figure 3.11: *A typical ADC histogram of a fiber for β rays.*

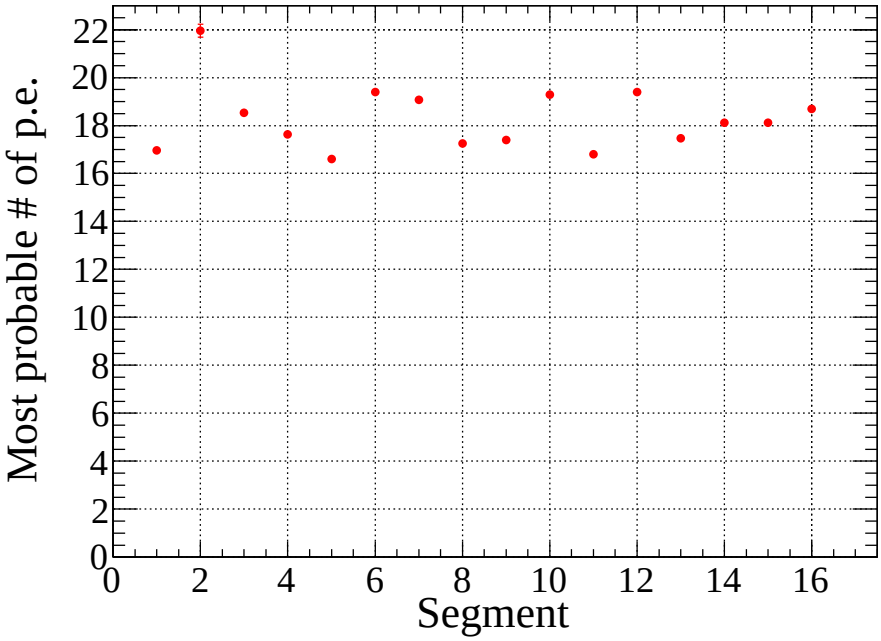

Figure 3.12: *The distribution of a mean number of photoelectrons for β rays.*

Chapter 4

Analysis

4.1 Overview

The purpose of our analysis is to derive the production cross section for the ^{6}Li(π^-, K^+)X reaction for every 2 degree of the reaction angle. This is achieved by two stages of analysis procedures, i.e. the missing mass analysis and the cross section analysis. In what follows, the overview of these procedures is introduced.

Here, we define some terminologies which are used in this chapter.

- Multi-hit event: An event with several hits or tracks in each analysis stage.
- Detection efficiency: A ratio that at least one hit or track exists after placing several gates.
- Analysis efficiency: A ratio that only one hit or track exists after placing several gates.

Missing mass analysis

The missing mass spectroscopy is to obtain the mass, which is not directly measured, from the conservation of the four momentum based on kinematics of incident and outgoing particles analyzed by spectrometers. Here, we define the four momenta of the beam π, the target, the outgoing K, and the reaction product as P_π, $\mathrm{P}_{\mathrm{tgt}}$, P_K, and P_X, respectively. These four momenta on the two-body kinematics satisfy the following relation:

$$\mathrm{P}_\mathrm{X} = \mathrm{P}_\pi + \mathrm{P}_{\mathrm{tgt}} - \mathrm{P}_\mathrm{K}. \tag{4.1}$$

The three momentum of the beam π ($\boldsymbol{p_\pi}$) and the outgoing K ($\boldsymbol{p_K}$) are measured while the target is at rest. Consequently, the mass of P_X, namely the missing mass, can be written as

$$M_X = \sqrt{(E_\pi + M_{tgt} - E_K)^2 - ({p_\pi}^2 + {p_K}^2 - 2p_\pi p_K cos(\theta_{\pi K}))}, \tag{4.2}$$

where E_π and E_K are the total energy of a pion and a kaon, M_{tgt}: the mass of the target, and $\theta_{\pi K}$: the reaction angle. Therefore, the main part of the missing mass analysis is the momentum reconstruction of the incident and outgoing particles from each spectrometer. In addition, since the mass of the incident and the outgoing particle are assumed to be the charged pion and kaon for determining their four momenta, the particle must be identified before calculating the missing mass. The actual analysis procedures are described in the following sections.

1. **Determination of a beam momentum**
   Hit position data in BFT, BC3, and BC4 are selected by applying a timing and position gate. At this stage, the single value of the beam momentum is reconstructed by these information using a third-order transfer matrix.

2. **Determination of a scattered particle momentum and kaon selection**
   The momentum of a scattered particle is determined from trajectories at the entrance and the exit of the SKS magnet measured by SFT, SDC2, SDC3, and SDC4, and with a calculated magnetic field. Kaon is selected using a scattered particle mass obtained from the time-of-flight and its momentum.

3. **Reconstruction of a reaction vertex**
   The reaction vertex is defined as the closest distance point between the pion and the kaon trajectories.

The method introduced above is used in the past KEK experiment analyses; however, in the present experiment, additional improvements to select a true hit in a multi-hit event are essential under a high multiplicity condition. Thus, the missing mass analysis section focuses on such the technique for high analysis efficiencies.

Cross section analysis

In this section, momentum correction and efficiency estimation are described to obtain the cross section via the $^{6}\mathrm{Li}(\pi^{-}, K^{+})\mathrm{X}$ reaction. First, correction parameters to calculate an absolute momentum in each spectrometer are extracted by studying beam-through data and $\Sigma^{\pm}$ missing mass spectra. Secondly, various efficiencies such as analysis efficiency of each detector, decay factor of kaon, and the acceptance of the SKS system are estimated for the cross section calculation. Finally, our analysis procedures are confirmed by extracting the differential cross section of the $\Sigma^{\pm}$ production.

Analysis procedures

The procedure routine of the missing mass analysis and the cross section analysis are shown in Figure 4.1. The missing mass analysis is divided into two stages. In the first stage, the momentum of each spectrometer system is reconstructed and stored in the data summary table (DST). Since tracking processes, especially, the Runge-Kutta method, require a large amount of computer resources, they are separated from the other analyses. The routine starts from the upstream counter. A single beam momentum is required before going to the next step to analyze SSD using the beam track information. The momentum in each spectrometer is uniquely reconstructed in the first stage. Other analyses such as the momentum correction and the missing mass calculation are performed in the second stage.

By using the 2nd DST created in the second stage of the missing mass analysis, the cross sections is calculated after selecting the $^{6}\mathrm{Li}(\pi^{-}, K^{+})\mathrm{X}$ reaction.

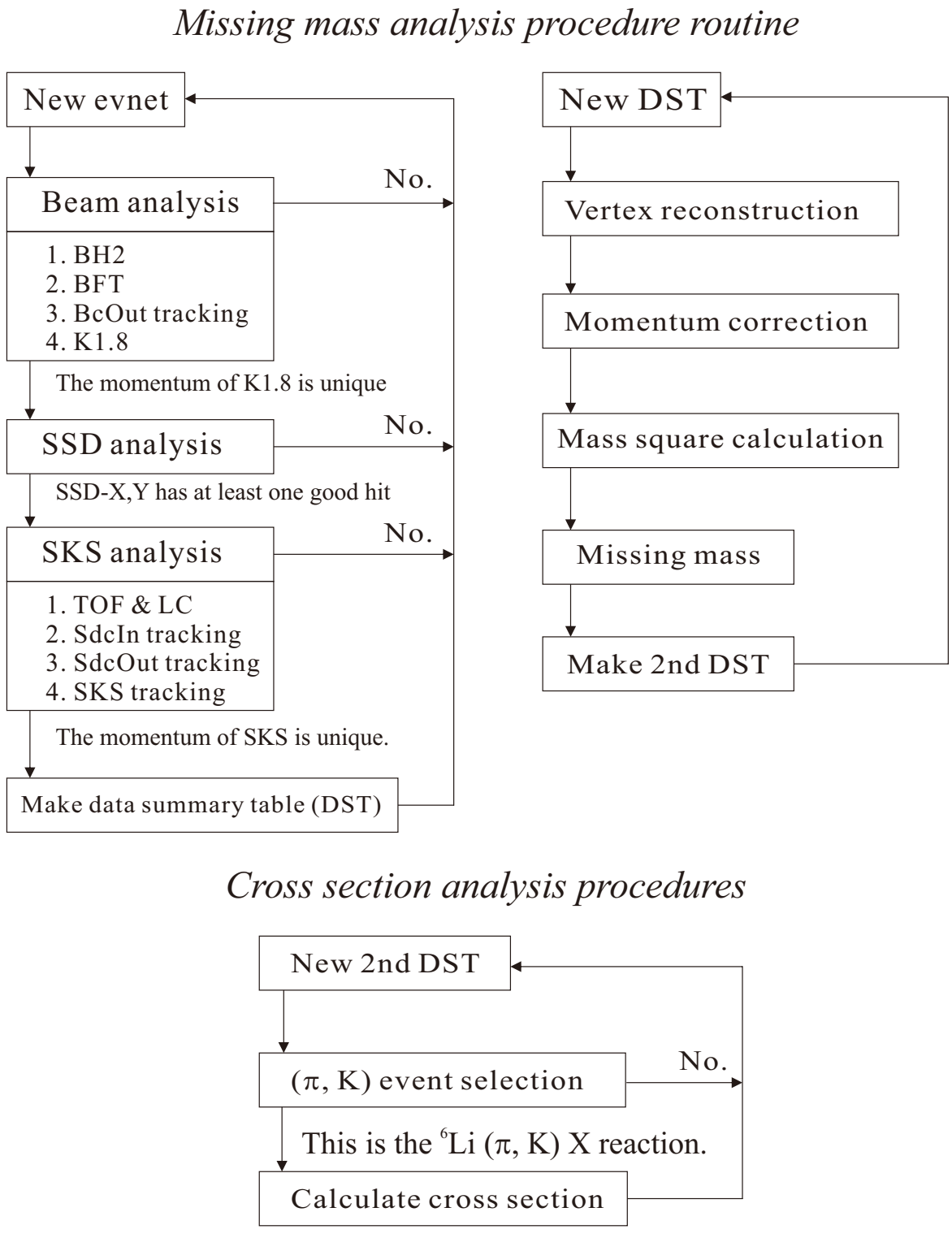

Figure 4.1: *Procedures of the missing mass analysis and the cross section analysis.*

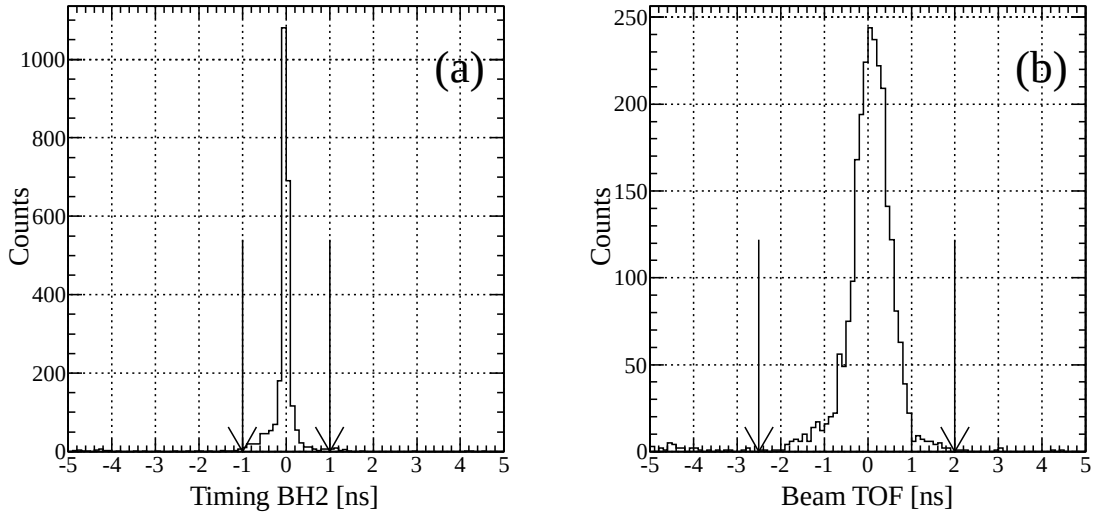

Figure 4.2: *(a) The timing distribution of the t0 segment in BH2. (b) The beam TOF distribution between t0 segments of BH1 and BH2.*

4.2 π^- beam analysis

4.2.1 Identification of the time zero segment

Timing information is the most basic and effective way to identify a true hit in a multi-hit event. Especially, BH1·2 information helps analyses of other beamline detectors because they have the best timing resolution in the present experimental system. The time zero (t0) segment, which is a segment of BH1·2 with the hit timing nearest to 0, is defined. The timing distribution of the t0 segment in BH2 and the time-of-flight distribution between the t0 segments of BH1 and BH2 are shown in Figure 4.2. Since the BH2 timing serves as the start/stop timing of the DAQ system, the timing distribution of BH2 has almost no spread. Therefore, the t0 segment of BH2 is identified with an analysis efficiency of 95.0% by applying a symmetric gate of ± 1 ns. On the other hand, the beam TOF distribution is gated asymmetrically from -2.5 to 2.0 ns covering a time walk of BH1·2. In principle, the time walk should be corrected by ADC information; however, the correction is impossible under the high intensity condition because several particles hit the same segment within an ADC gate of 100 ns.

Time zero segments of both BH1·2 are identified and used for the analyses of BFT and MWDC. However, there is a problem. The analysis efficiency of BH1 is 85% under the high intensity condition due to a dead time of electronics because BH1 does not perticipate in the triggers. Since the loss of 15% events at this stage cannot be tolerated, the analysis is continued if the t0 segment, of which timing lies within the gate, is not found. The condition for rejecting events is described in the BFT analysis section.

As described earlier, the contamination from anti protons are negligible owing to the double ESS system.

4.2.2 BFT analysis

The purpose of BFT is to obtain a single x position at the entrance of the $QQDQQ$ system in the multi-hit event with the good timing resolution. For this purpose, we attempted

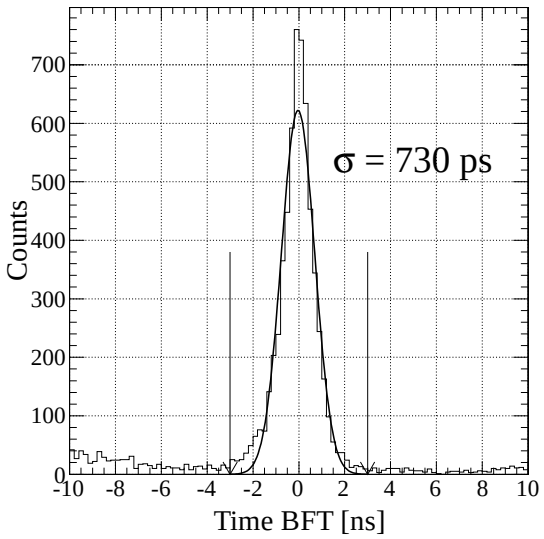

Figure 4.3: *The timing distribution of BFT.*

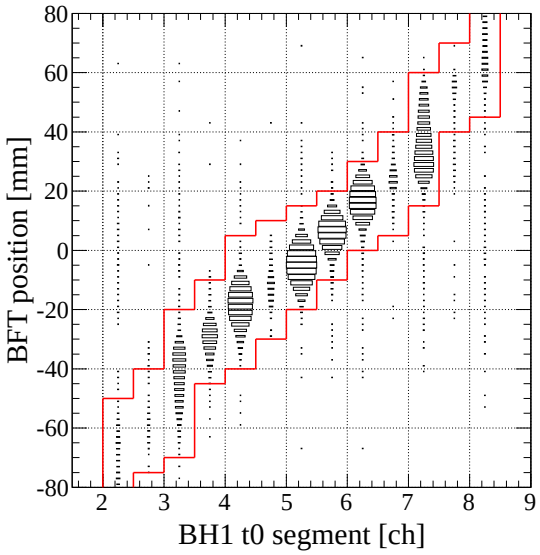

Figure 4.4: *A correlation between the t0 segment of BH1 and hit pattern of BFT. Events lying within red lines are accepted.*

various analysis procedures to improve the timing resolution and a signal-to-noise ratio; they are described in the Appendix A. The timing resolution of BFT is 730 ps (σ) by fitting the histogram in Figure 4.3 with a Gaussian. The detection and analysis efficiencies of BFT when gating with a timing range of $\pm$2.5 ns are 98.3% and 88.5%, respectively. These values are affected by accidental hits between the two detectors. The correlation between the t0 segment of BH1 and a hit pattern of BFT (BH1 matching), which is shown in Figure 4.4, is used to remove the effect of accidental background. By applying the BH1 matching, redundant BFT hits outside red lines are rejected. However, since the t0 segment of BH1 may not be always defined as described earlier, the different analysis procedures are followed according to the following cases.

Case1

- A single BFT hit is identified only by placing the timing gate.
The hit selected is unconditionally used to reconstruct a beam momentum. BH1 matching is not used.

Case2

- Several BFT hits remain with application of the timing gate, and finding the t0 segment of BH1 of which timing falls within the timing gate.
BH1 matching is used to reject the redundant BFT hits.

Case3

- Several BFT hits remain with application of the timing gate, but **NOT** finding the t0 segment of BH1 of which timing falls within the timing gate.
This event is rejected.

In Case1, the single hit can participate in the momentum reconstruction with or without the t0 segment of BH1 because it is confirmed that this analysis method is valid using data on a low beam rate. The detection and analysis efficiencies after going through these procedures become 97.6% and 92.8%, respectively.

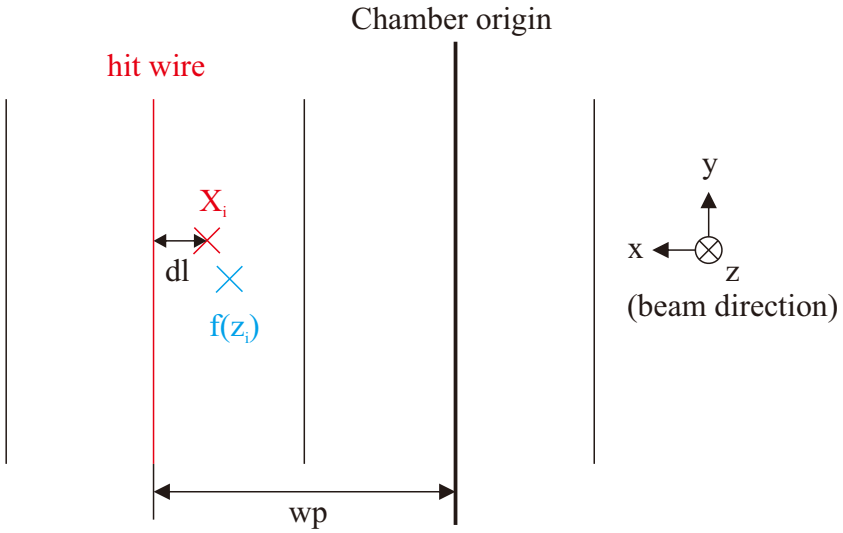

Figure 4.5: *Definition of the local chamber coordinate.*

4.2.3 MWDC analysis

Three-dimensional trajectories at the exit of the *QQDQQ* system are reconstructed using hit positions on BC3·4 with the least square method. This is called the BcOut tracking. All combinations are examined to find tracks, where combinations of at least 9 planes are accepted as track candidates. These candidates are sorted according to χ^2 defined as

$$\chi^2 = \frac{1}{n-4}\sum_{i=1}^{12} H_i \left(\frac{X_i - f(z_i)}{\sigma_i}\right)^2, \tag{4.3}$$

$$n = \sum_{i=1}^{12} H_i,$$

$$H_i = \begin{cases} 1 & \text{if i-th plane has a hit} \\ 0 & \text{if i-th plane has no hit} \end{cases}$$

$$\begin{aligned} X_i &= wp \pm dl_i(t), \\ f(z_i) &= x(z_i)cos(\theta) + y(z_i)sin(\theta), \\ x(z_i) &= x_0 + u_0 z_i, \\ y(z_i) &= y_0 + v_0 z_i, \end{aligned}$$

where X_i is a local hit position in each plane represented by wp: a wire position defined as shown in Figure 4.5 and dl: a drift length, and $f(z_i)$ is a position calculated from a tracking result at the z position of each plane. The local straight track is expressed by a wire tilt angle, θ, and four parameters, i.e. x_0, y_0, u_0, and v_0, which respectively denote x and y position at the origin of a local tracking coordinate and its slope, dx/dz and dy/dz.

Reducing the number of hit combinations under the high rate condition is crucial to their analysis with a reasonable amount of computer resources required. Since the beam particles are incident almost perpendicular to the chamber planes, in the BcOut analysis

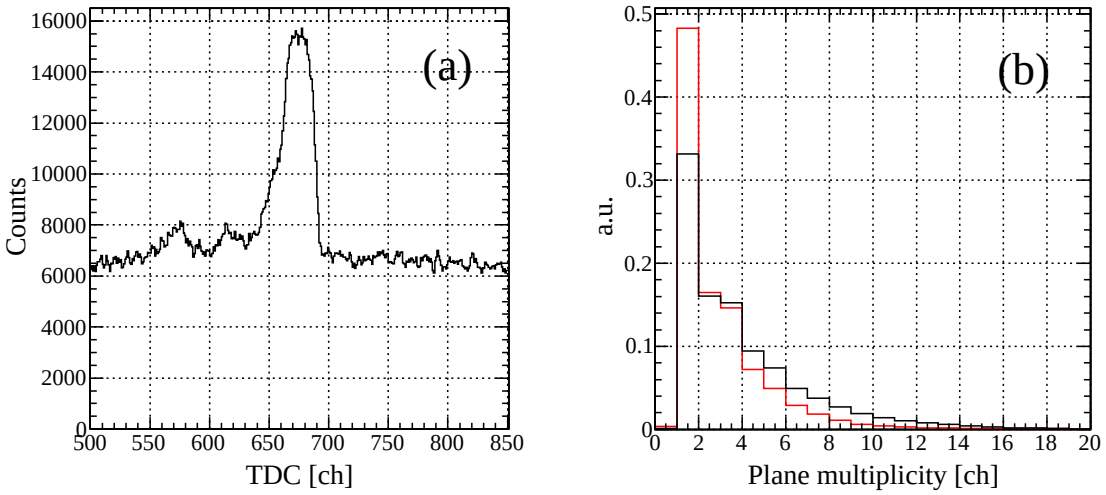

Figure 4.6: *(a) Raw TDC distribution of a plane of BC3. (b) Plane multiplicity distribution. In Figure (b), black lines and red lines show the multiplicity without and with the BH2 filter, respectively .*

the pair plane analysis method is adopted to solve a left/right ambiguity; the method treats a set of pair planes such as xx', uu', and vv' as one apparent plane. Therefore, combinations of hits on BC3·4 are made from six apparent planes. This method has been successfully applied; however, the number of combinations in the present experiment is still too high because of a high multiplicity of each pair plane as shown by black lines in Figure 4.6 (b). This is caused by accidental hits as seen in a raw TDC histogram in Figure 4.6 (a). An additional way to reduce the multiplicity is necessary. Thus, a correlation between hits on each plane and the t0 segment of BH2 (the BH2 filter) is applied to limit the number of hits participating in the track search. For instance, only hits within red lines in Figure 4.7 are used to make the combinations. The reduced multiplicity by applying the BH2 filter is presented with the red lines in Figure 4.6 (b). Owing to the BH2 filter, the detection efficiency of the BcOut tracking is improved from 93.6% to 98.7% by recovering some of events with too many combinations.

Since tracks made from the accidental hits give a flat reduced χ^2 distribution as shown in Figure 4.8, those fake tracks are almost removed by applying a reduced χ^2 gate less than 7, which is an optimal value to obtain the maximum analysis efficiency. Consequently, the detection and analysis efficiency of the BcOut tracking become 98.5% and 97.1%, respectively.

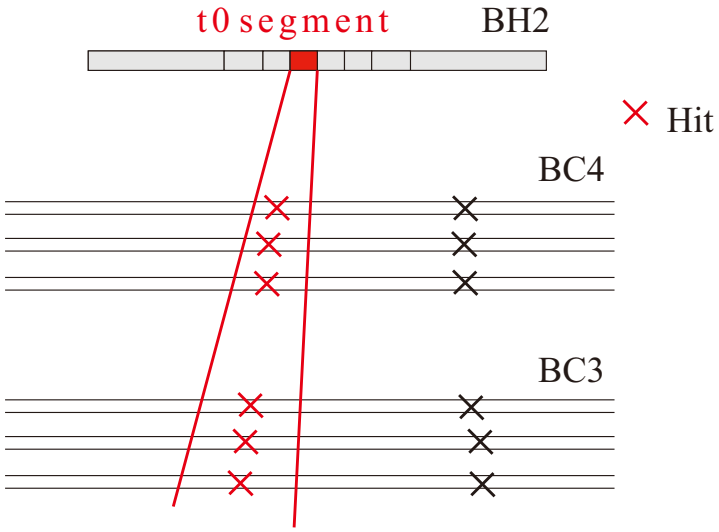

Figure 4.7: *Scheme of the BH2 filter. Hits correlated with the t0 segment of BH2 only are used to make combinations.*

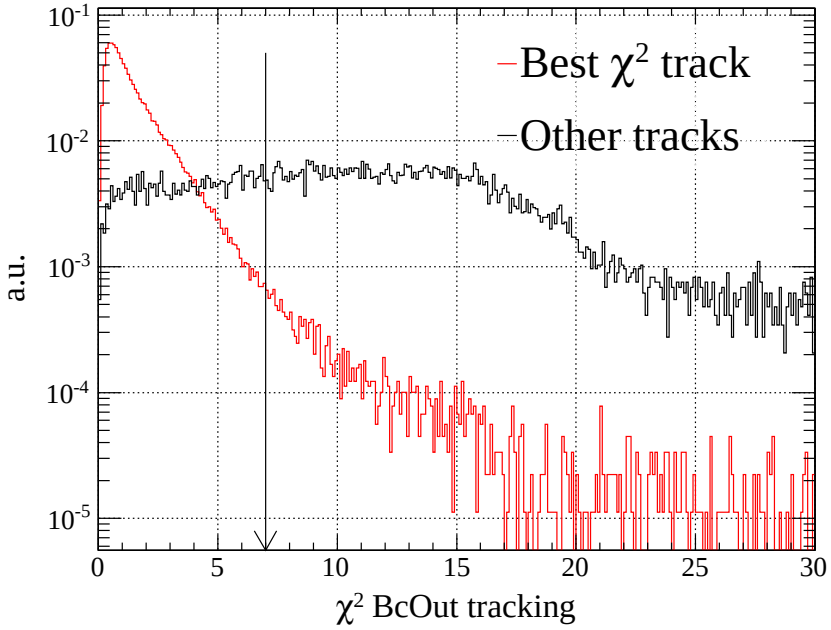

Figure 4.8: *The reduced χ^2 distribution of BcOut tracks.*

4.2.4 Beam momentum reconstruction

Momenta of beam particles are reconstructed using information on BFT and BcOut with a third-order transfer matrix calculated by ORBIT [66]. In this section, a method to determine beam momenta is described.

In general, a beamline is comprised of a series of components such as dipole, quadrupole, higher multipole magnets, or just intervals; components are placed along with the reference trajectory. The reference trajectory is a path of a charged particle with a designed central momentum in ideal magnets. An arbitrary charged particle passing magnets is represented by a vector defined as

$$\boldsymbol{X} = \begin{pmatrix} x \\ u \\ y \\ v \\ \delta \end{pmatrix}.$$

Definition of these variables are

- x = Horizontal position with respect to the central trajectory.
- u = Angle in the horizontal plane with respect to the central trajectory.
- y = Vertical position with respect to the central trajectory.
- v = Angle in the vertical plane with respect to the central trajectory.
- δ = Momentum deviation from the central momentum.

On the other hand, a first-order matrix of a magnetic component is described by a square matrix, R. The series of magnetic components are represented by a product of each matrix as

$$R(t) = R(n) \cdots R(3)R(2)R(1). \tag{4.4}$$

Therefore, a final vector $(X(1))$ representing an arbitrary particle after passing through the magnetic components is defined by an initial vector $(X(0))$ as

$$X(1) = R(t)X(0). \tag{4.5}$$

As an extension of this equation, the final vector component including a second-order and third-order matrices, T and U, becomes

$$X_i(1) = \sum_j R_{ij}X_j(0) + \sum_{jk} T_{ijk}X_j(0)X_k(0) + \sum_{jkl} U_{ijkl}X_j(0)X_k(0)X_l(0). \tag{4.6}$$

In the present experiment, the components of the final vector at the exit of the $QQDQQ$ system are known from the BcOut tracking except for δ, whereas only the x position of the initial vector is measured by BFT. Then, the x component of the initial vector is described using inverse transfer matrices, $R^{'}, T^{'}$, and $U^{'}$ as

$$x(0) = \sum_j R^{'}_{0j}X_j(1) + \sum_{jk} T^{'}_{0jk}X_j(1)X_k(1) + \sum_{jkl} U^{'}_{0jkl}X_j(1)X_k(1)X_l(1). \tag{4.7}$$

By solving this equation for δ, the beam momentum is obtained as a general solution of a cubic equation.

Table 4.1: *The list of a position resolution of detectors used in the K1.8 spectrometer.*

Name	Resolution μm (σ)
BFT	190
BC3	180
BC4	180
BC1	300
BC2	300

The performance of this momentum reconstruction method was evaluated by comparing with the conventional method using a set of wire chambers placed at the entrance of the beamline spectrometer in an other experiment. In that case, BFT was installed between the wire chambers (BC1 and 2). The position resolution of the detectors used in this spectrometer are listed in Table 4.1. As the result, the difference in δ by both reconstruction methods is found to be $\sim 2 \times 10^{-1}$ MeV/c (σ). Therefore, it is confirmed that this momentum reconstruction method works well.

By using this method, beam momenta can be determined for all possible combinations between BFT hits and BcOut tracks. Hence, we select events in which a beam momentum is uniquely reconstructed at this stage. The probability that the single value of the beam momentum (Both BcOut and BFT have single hit) is determined in an event (f_{K18}) is 95.2%. Consequently, the analysis efficiency of the beam momentum is given by

$$eff_{analysisbeam} = eff_{BH2} \times eff_{BcOut} \times eff_{BFT} \times f_{K18}, \tag{4.8}$$

where eff_{BH2}, eff_{BcOut} and eff_{BFT} are detection efficiency of each detector, and $eff_{analysisbeam}$ is 86.5%. Finally, the beam momentum distribution of 1.2 and 1.37 GeV/c in the present experiment are shown in Figure 4.9.

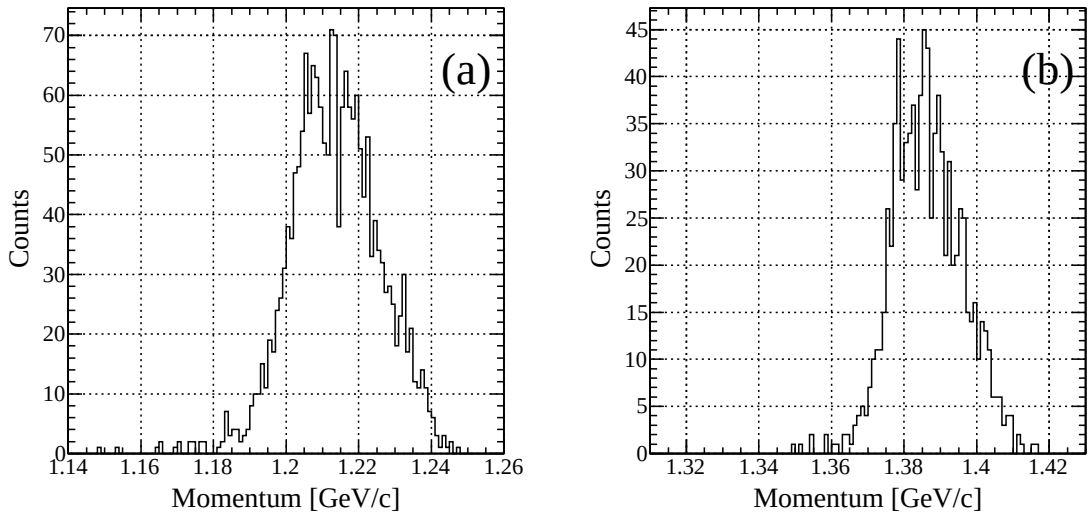

Figure 4.9: *A beam momentum distribution of 1.2 and 1.37 GeV/c in Figure (a) and (b), respectively.*

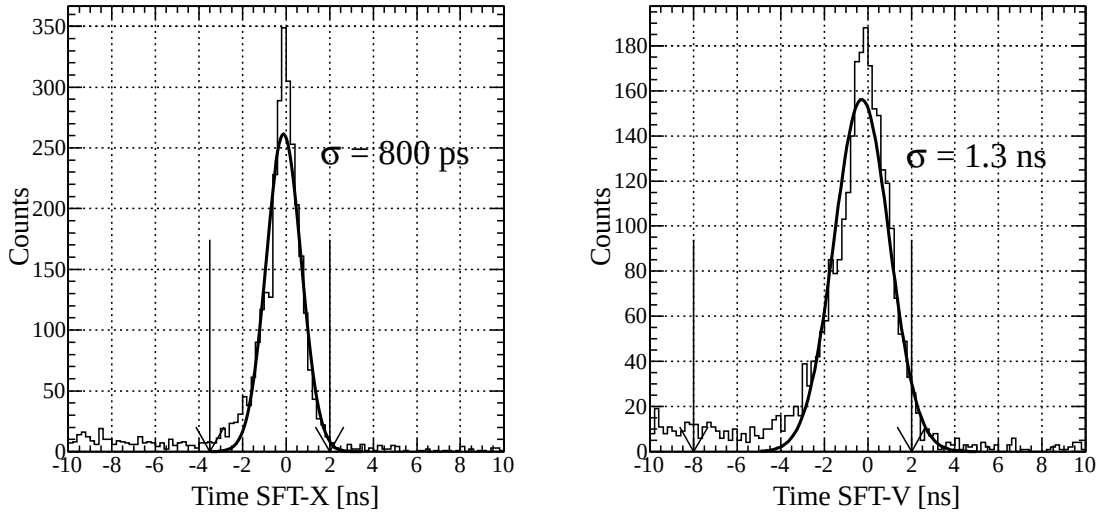

Figure 4.10: *Timing distributions of SFT-X (a) and SFT-V (b).*

4.3 Outgoing K^+ analysis

4.3.1 SFT-SDC2 analysis

The local tracking at the entrance of the SKS magnet is called the SdcIn tracking. Although the plane multiplicity of SDC2 is also high, there is no method to reduce the multiplicity such as the BH2 filter for devices detecting outgoing particles. Therefore, SFT plays an essential role to reduce the number of combinations owing to the good timing resolution as shown in Figure 4.10. Details of the SFT analyses are the same as those of BFT described in Appendix A.

Unlike the beamline detectors, outgoing particles with large scattering angles are no longer incident perpendicularly to each plane. Hence, the pair plane analysis is no longer available and all possible hit combinations including the left/right ambiguity of a drift length must be examined. In this case, two dimensional pre-tracking in each coordinate (x, u, v) is conventionally performed before the three-dimensional tracking in order to reduce the number of combinations. However, the pre-tracking is impossible in the present experimental setup because wire tilt angles between SFT and SDC2 are different. Since the pair plane analysis is alternatively used, χ^2 values for tracks with a large scattering angle become large due to miss-solving of left/right. Therefore, left/right of each hit which participates in a reconstructed straight track is re-analyzed to find the best left/right combination, which minimizes its χ^2 value. Figure 4.11 shows reduced χ^2 distribution of a SdcIn track with the best χ^2 before and after re-analysis. In our analysis, tracks in which at least seven hits participate with the reduced χ^2 value of less than 10 are accepted.

4.3.2 SDC3 and 4 analysis

The local track search at the exit of the SKS magnet is called the SdcOut tracking. The plane multiplicity of SDC3·4 is quite low comparing to that of BC3·4 and SDC2 owing to the DCX reaction. The total rate at the TOF wall position is ∼50 kHz. Since SDC3 and 4 has the same plane structure, two dimensional pre-tracking to decide left/right of the drift length is performed before the three-dimensional tracking. The reduced χ^2 distribution of

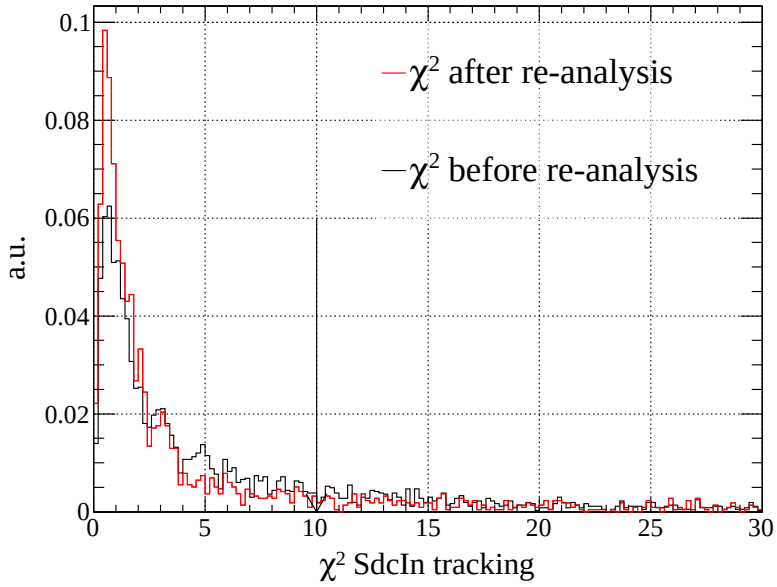

Figure 4.11: *The reduced χ^2 distributions of the SdcIn tracking.*

Table 4.2: *The list of a position resolution of detectors used in the SKS system.*

Name	Resolution μm (σ)
SFT-X	190
SFT-UV	270
SDC2	150
SDC3	300
SDC4	300

a track with the best χ^2 value is shown in Figure 4.12. Tracks in which at least nine hits participate with the reduced χ^2 value of less than 10 are accepted.

Position resolutions of detectors in the SKS system are summarized in Table 4.2.

4.3.3 Momentum reconstruction of outgoing particle

In order to determine momenta of outgoing particles, trajectories inside the SKS magnet connecting the SdcIn track and the SdcOut track are reconstructed by numerically solving the equation of motion inside the magnetic field calculated by ANSYS [68] using the fourth-order Runge-Kutta method [67]. In our analysis, this reconstructing procedure is called the SKS tracking. The SKS tracking starts from the TOF position to the target position with five parameters defined as follows:

- x : x position on the TOF plane,
- y : y position on the TOF plane,
- u : slope in the horizontal plane (dx/dz) at TOF,
- v : slope in the vertical plane (dy/dz) at TOF,
- q : charge divided by momentum.

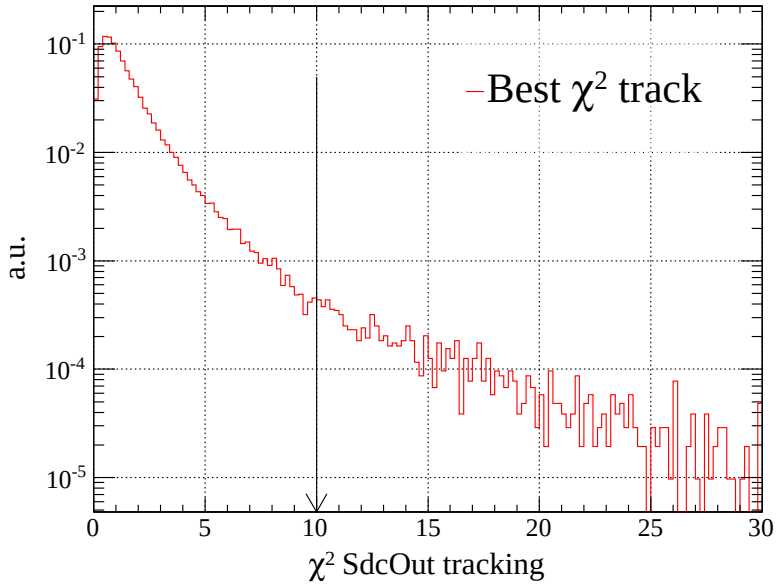

Figure 4.12: *The reduced χ^2 distributions of the SdcOut tracking.*

Optimal parameters minimizing the χ^2 value defined below are searched for by a numerical iteration according to the following criterion, $\delta_{\chi^2} = (\chi^2_{k+1} - \chi^2_k)/\chi^2_k < 10^{-3}$, where χ^2_k is the χ^2 value for the k-th iteration. The definition of χ^2_{SKS} is as

$$\chi^2_{SKS} = \frac{1}{n-5}\sum_{i=1}^{21} H_i \left(\frac{X_i^{hit} - X_i^{track}}{\sigma_i}\right)^2 \tag{4.9}$$

$$n = \sum_{i=1}^{21} H_i$$

$$H_i = \begin{cases} 1 & \text{if i-th plane has a hit} \\ 0 & \text{if i-th plane has no hit} \end{cases}$$

where X_i^{hit} and X_i^{track} respectively mean a local position obtained from the SKS tracking and each detector hit, and σ_i is a position resolution of each plane. For the multi-hit events, all combinations between the SdcIn tracks and the SdcOut tracks are examined and sorted by χ^2 values.

Initial parameters of x, y, u, and v are given by the SdcOut tracks while the initial momentum is constant; nevertheless, the present SKS system has the large momentum acceptance. Since it is customary to select a little higher initial momentum than the actual momentum of an outgoing particle, the initial momentum, which is expected by $u(dx/dz)$ of the SdcOut track, is set event by event according to the red line in Figure 4.13.

The reduced χ^2 distribution of the SKS tracking is shown in Figure 4.14. Good tracks with reduced χ^2 value less than 20 are accepted. The multi-track ratio of the SKS tracking is negligible because all tracks found are of single track in the SdcOut tracking for an event.

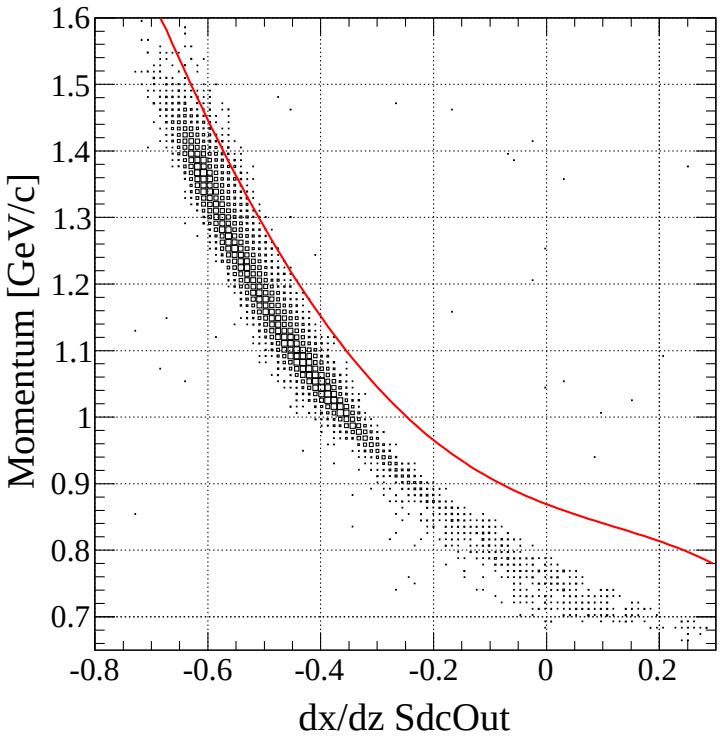

Figure 4.13: *A correlation between momenta and u (dx/dz) of SdcOut tracks. A red line shows an initial momentum function.*

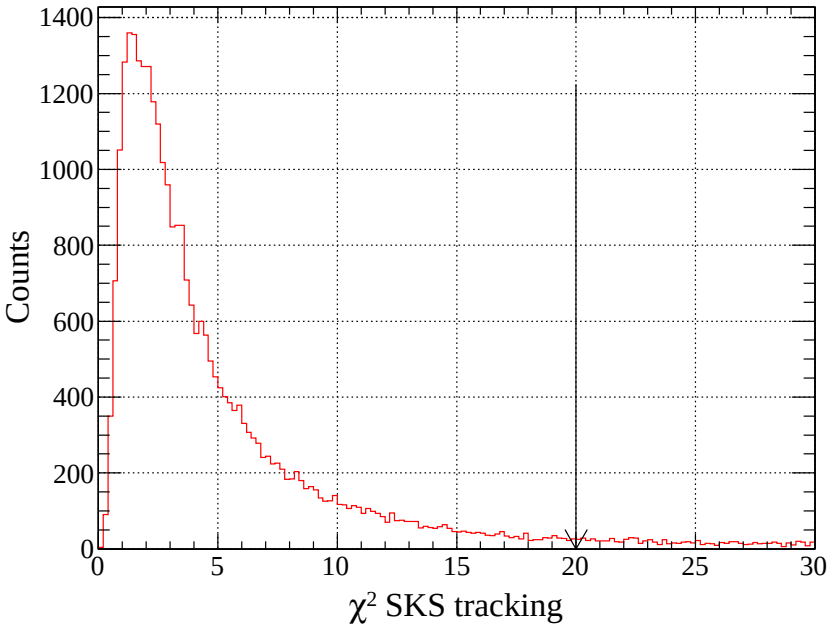

Figure 4.14: *The reduced χ^2 distribution of the SKS tracking.*

4.4 Kaon identification

In the off-line analysis, kaons are identified by momenta of the outgoing particles and the time-of-flight information from BH2 to TOF. Since the flight path length from BH2 to TOF is already known from the SKS tracking, β of each particle can be calculated by the flight path length and the momentum. Therefore, the mass square of an outgoing particle is reconstructed as

$$M^2 = \left(\frac{p}{\beta}\right)^2 (1 - \beta^2), \tag{4.10}$$

where p is the momentum of the outgoing particle. The mass square distributions for the beam momentum of 1.2 and 1.37 GeV/c are shown in Figure 4.15 and Figure 4.16, respectively. Events with momenta of range between 0.7-1.0 GeV/c are plotted in the figures because no kaon event exists with the momentum over 1.0 GeV/c. In the present experiment, it is necessary to estimate the kaon identification efficiency within the range of 0.7-0.9 GeV/c. However, the statistics around the momentum region of 0.9 GeV/c is poor due to small cross sections. On the other hand, a typical kaon momentum of the Σ^- production at the beam momentum of 1.37 GeV/c is 0.9 GeV/c. Hence, the kaon identification efficiency is estimated using both data sets with the beam momentum of 1.2 and 1.37 GeV/c.

In Figure 4.15 and 4.16, one can find tail structure in the mass square distribution of each particle. Therefore, it is impossible to represent this distributions with a simple Gaussian. In order to extract a shape of the mass square distribution for kaon and to estimate the background contamination, the distribution is fitted with three components, that is, pion, kaon, and proton and unknown constant background. Double Gaussian is used to fit the kaon distribution. The pion distribution is represented by double Gaussian and an exponential function, which reproduces the tail structure on the right-hand side of Gaussian. The proton contamination is represented by an exponential function. Fitting results with these functions are shown in the same figures. The shape of the kaon distribution for the beam momentum of 1.2 (red) and 1.37 GeV (black) are extracted as shown in Figure 4.17. The mass square distribution is gated with a wide range of 0.17 to 0.4 GeV/c^2. Gating efficiencies are 99.0% and 99.3% for the beam momentum of 1.2 and 1.37 GeV/c, respectively. Thus, the kaon identification efficiency is independent of the kaon momentum and results in 99.1%$\pm$0.4%.

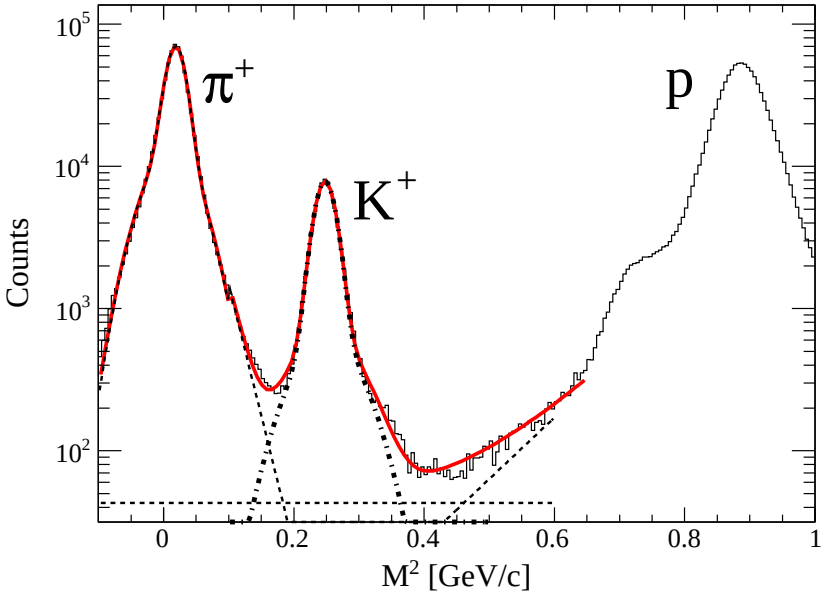

Figure 4.15: *The mass square distribution obtained from data on the production run.*

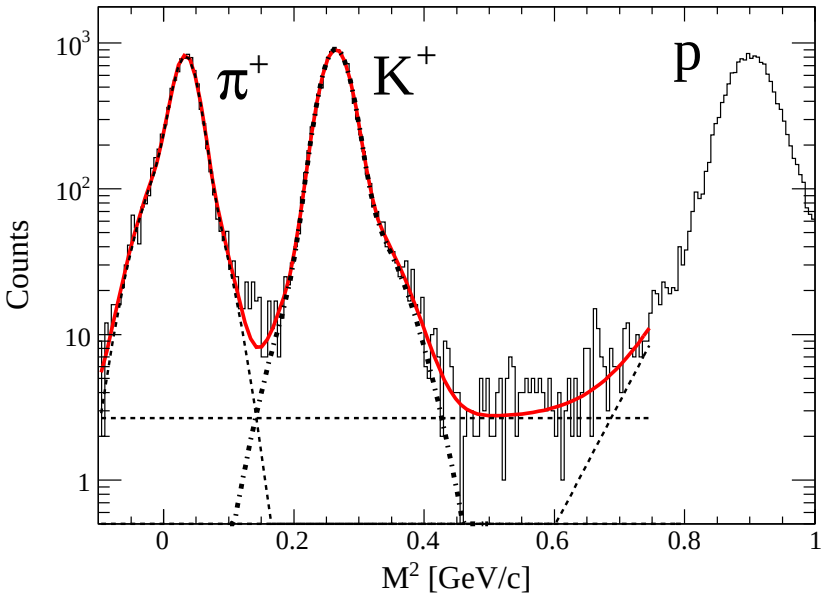

Figure 4.16: *The mass square distribution obtained using the data set for the Σ^- production.*

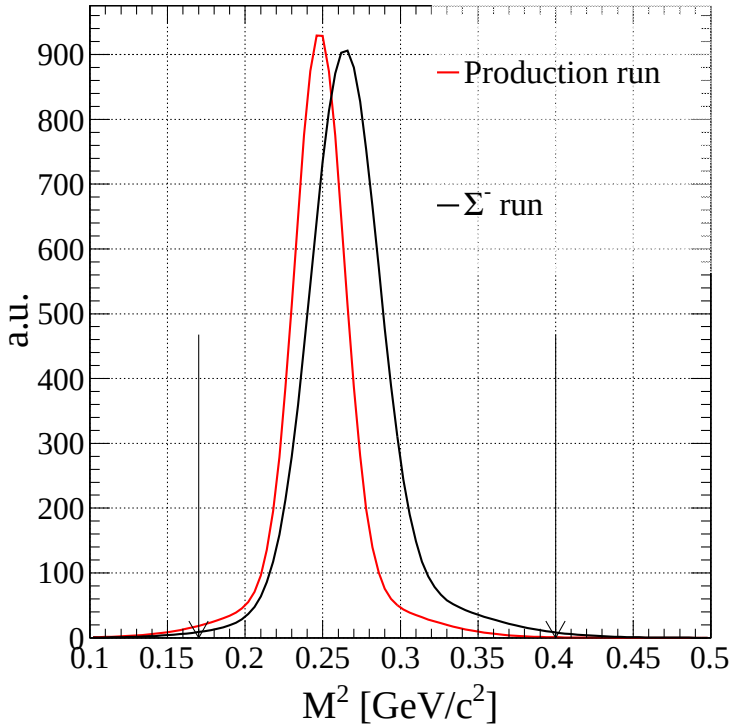

Figure 4.17: *The kaon distribution obtained from data of the production run (red line) and the data set for the Σ^- production (black line).*

4.5 Vertex reconstruction

There are two kinds of purposes to reconstruct the reaction vertex. The first is to reject the contamination from other than the target materials, for example, SSD or SFT. The second is to correct the energy loss of π^- and K^+ in the target event by event using the vertex information in order to obtain the best missing mass resolution. For the second purpose, the sufficient z-vertex resolution is necessary to correct the energy loss when the target thickness is of a few cm. Therefore, SSDs are installed to correct the BcOut track to obtain the better vertex resolution. However, the analysis efficiency of SSD is low as described below. For the shape analysis of the spectrum, the statistics of each missing mass bin is more important than the missing mass resolution. In the present analysis, the use of SSD is limited to separate the SFT originated contamination from events taken place in the ^{6}Li target to keep the analysis efficiency. Hence, the dynamical energy loss correction is abandoned.

In this section, the reason for the low analysis efficiency is described. Furthermore, the reconstructed reaction vertex is shown.

4.5.1 SSD analysis

Two sets of SSD-X and Y are installed at the distance of 140 mm from the target and the distance of 1500 mm from the BC3·4. Since the role of SSDs to compensate a reaction vertex affected by the multiple scattering between BC3·4 and the target, the SSD information are not used to determine the beam momenta. The BcOut track is corrected using the position projected at BH2 and SSD hit information as shown in Figure 4.19. The corrected track is defined as a line connecting these two positions. Therefore, parameters representing the local straight track, namely, x_0, y_0, u_0, and v_0, obtained from the BcOut tracking are changed to $x_0^{'}$, $y_0^{'}$, $u_0^{'}$, and $v_0^{'}$.

Here, we describe details of the SSD analysis. At first, SSD analog signals are sampled five times by APV25 chips with a 40 MHz clock. Second, signals multiplexed by APV chips are digitized by FADC and checked whether each sampling point is larger than the threshold to suppress pedestal in the hardware level. Then, a typical SSD wave form is represented by five points as shown in Figure 4.18. Valid hits are distinguished from the accidental background according to the following algorithm.

- A wave form has at least four sampling points.
- A second or third sampling point is at the maximum.
- Sum of the second and the third sampling points are lager than that of the first and the fourth one.

After rejecting the background, the clustering method is applied; the method is to combine valid hits adjacent to each other. Consequently, the number of clusters is counted as the hit multiplicity of SSD. The hit multiplicity at this stage is shown in Figure 4.20 with black lines showing high multiplicity. This situation is caused by the insufficient timing resolution of SSD because the wave form analysis to obtain the best timing resolution is not performed. However, the wave form analysis for all hits is impractical. Thus, we limit the track correction to the range of $|u_0 - u_0^{'}| < 0.004$ rad and $|v_0 - v_0^{'}| < 0.008$ rad to decrease the multiplicity. The difference of u_0-$u_0^{'}$ and v_0-$v_0^{'}$ are shown in Figure 4.21. The gate ranges are determined using data taken under the low intensity condition. The final multiplicity for each SSD is shown in Figure 4.20 with red lines. The multiplicity for SSD-Y

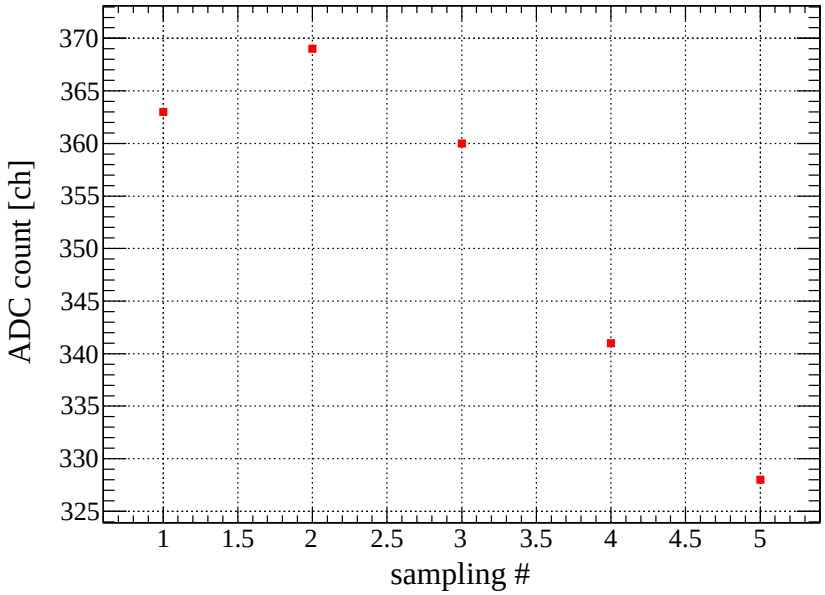

Figure 4.18: *A typical wave form of SSD.*

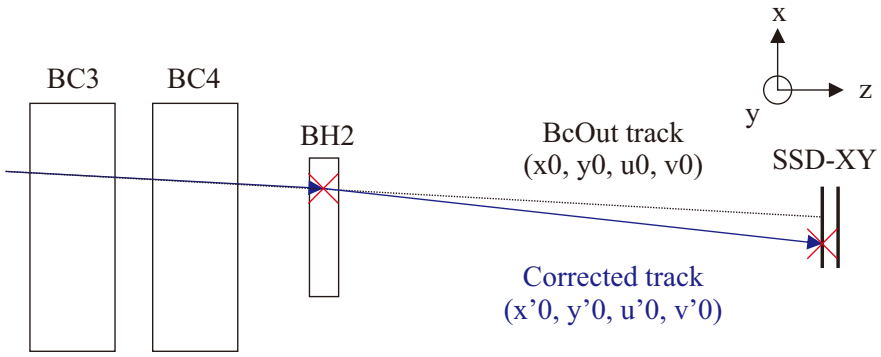

Figure 4.19: *The correction method for the BcOut track. The corrected track is defined as a line connecting the projected position on BH2 and the SSD hit position.*

is still high because the position resolution for the y direction of BcOut is worse than that for the x direction due to the small tilt angle of wires in the u-v planes. The detection efficiency of SSD is 84.1%. However, the analysis efficiency of SSD is rather low due to the high multiplicity of SSD-Y. Therefore, SSD-X only is used to distinguish event in the ^{6}Li target from the SFT contamination. The method is described in the next.

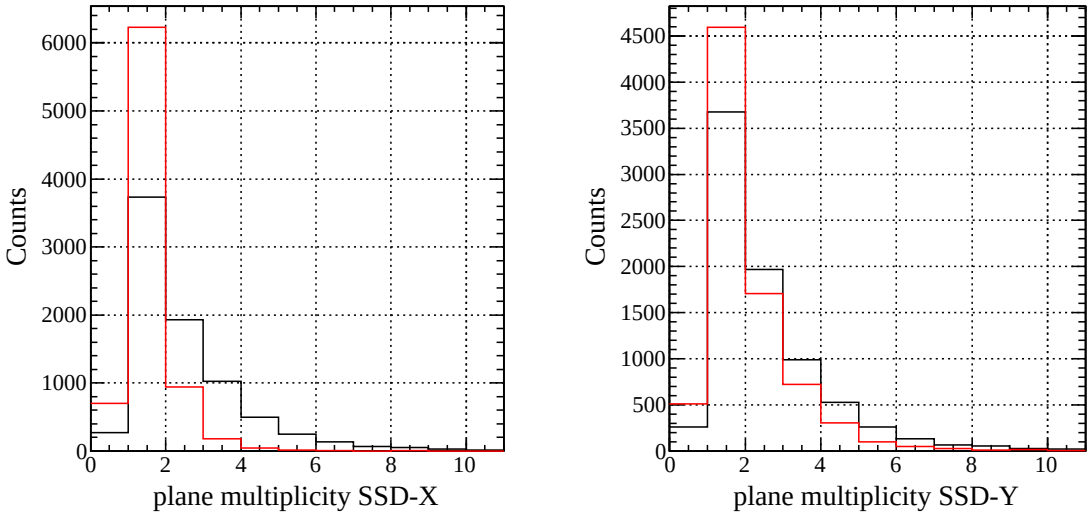

Figure 4.20: *The plane multiplicity of SSD-X and SSD-Y.*

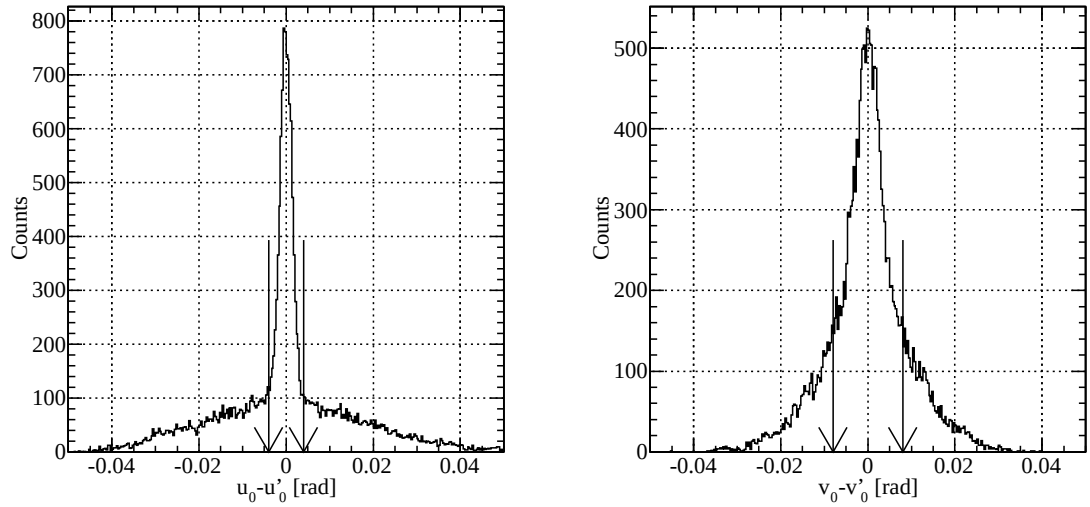

Figure 4.21: *The difference between* u_0-u'_0 *and* v_0-v'_0.

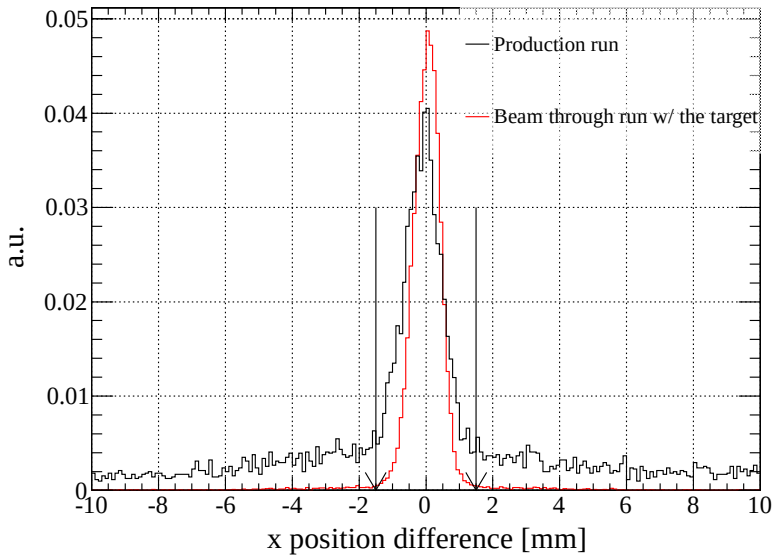

Figure 4.22: *The x-position difference between corrected BcOut tracks and hits on SFT-X. Black lines and red lines are data taken in the production run and the beam through run with the target, respectively.*

4.5.2 Separation of the ^{6}Li target and SFT

SFT is installed behind the target at the distance of 180 mm; the amount of material of SFT is 8% of the target. The z-vertex contamination from SFT to the target region is not negligible. Therefore, the method to separate the ^{6}Li target from SFT using the x position difference between the BcOut track and hits on SFT-X instead of the z vertex is adopted. For this purpose, only x_0 and u_0 of the BcOut track are corrected by SSD-X.

The x-position difference between the corrected BcOut track and hits on SFT-X at the z-position of SFT-X is shown in Figure 4.22. Black lines and red lines are data taken in the production run and the beam through run with the target, respectively. The standard deviation for the red lines is 400 μm. Thus, events lying within the 3σ range are recognized as the reaction in SFT. With respect to the distance from the surface of the target and SFT-X, the contamination from SFT is rejected with the efficiency of over 99% by selecting the reaction angle of over 2 degree.

4.5.3 Reaction vertex

The reaction vertex is determined from the closest distance between the BcOut track and the SKS track. Vertices for the (π^-, K^+) reaction and the closest distance distribution for reaction angle between 2° to 14° are shown in Figure 4.23. The figure (a), (b) and (c) show the x, y and z-vertex distribution, respectively. From the x and y-vertex distribution, it is clear that there is no contribution from other materials except for the target. In the figure (c), the black line shows all events while the red line represents the distribution recognized as coming from the ^{6}Li target. The contamination from SFT is well separated. On the other hand, the contribution from SSD is seen in Figure 4.23 (c). However, there is no way to separate them from the ^{6}Li target except for the z-vertex distribution. The figure (d) shows the closest distance distribution between the BcOut track and the SKS track. Events of which the closest distance is smaller than 8 mm are selected as good events.

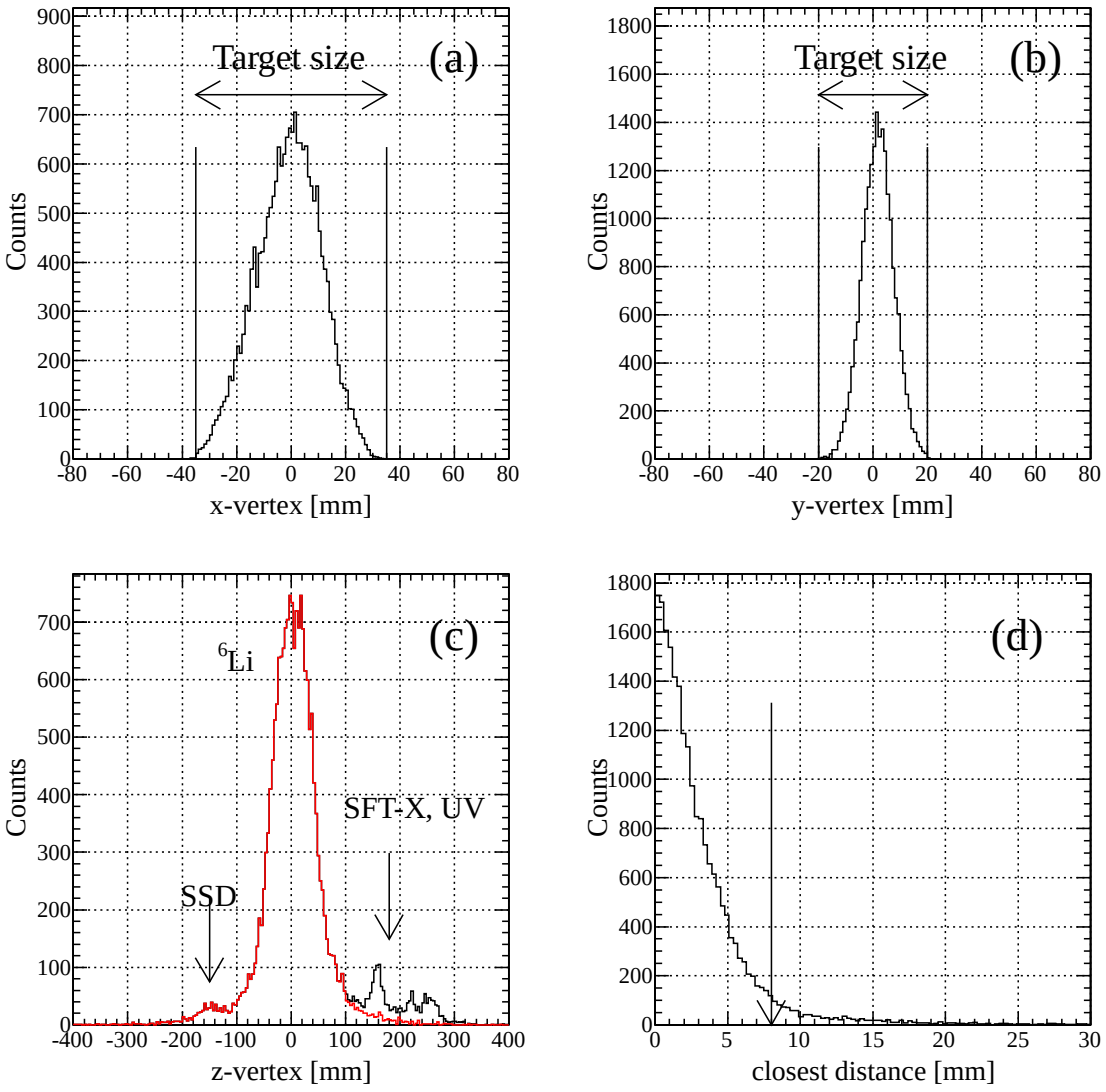

Figure 4.23: *Figure (a), (b), and (c) show the x, y, and z-vertex distribution, respectively. Figure (d) show the distribution of the closest distance. In the figure (c), the black line means all events and the red line means the distribution recognized as events come from the ^6Li target.*

Table 4.3: *Data summary used for the momentum calibration.*

Label	Data	SKS Mom. (GeV/c)	K18 Mom. (GeV/c)	Particle	target
A	Σ^-	0.7	1.20	π^-	SFT
B	Σ^-	0.9	1.37	π^-	Polyethylene
C	Σ^+	0.9	1.37	π^+	Polyethylene
D	Beam through		0.8, 0.9, 1.0, 1.2	π^+	none
E	Beam through		0.8, 0.9, 1.0, 1.2	π^+	^{6}Li

4.6 Momentum correction

There are two types of set of momentum correction parameters. One is a set of parameters to obtain the absolute momentum of the beam pion and the outgoing kaon at the reaction position. The other set is for correcting the correlation between the momentum of the SKS system and a scattering angle in order to improve the momentum resolution of the SKS system. In this section, the procedures to obtain momentum correction parameters are described.

4.6.1 Absolute momentum

In the present experiment, momenta of outgoing kaons produced are distributed within the range of 0.7-0.9 GeV/c at the beam momentum of 1.2 GeV/c. The lower end point is determined by the acceptance of the SKS system. Thus, the purpose of this analysis is to obtain absolute momenta in this momentum range. We already know the reconstructed momentum measured by each spectrometer, that is, p_{K18} and p_{SKS}. From these momenta, momenta at the reaction position, namely, p'_{K18} and p'_{SKS}, are derived as

$$p'_{K18} = f(p_{K18}) - dE_{K18}, \tag{4.11}$$
$$p'_{SKS} = g(p_{SKS}) + dE_{SKS}, \tag{4.12}$$

where f and g are correction functions, and dE_{K18} and dE_{SKS} are the energy loss of π and K, respectively. In order to obtain appropriate f and g, four sets of beam through data and masses of $\Sigma^\pm$ are used as summarized in Table 4.3. The label in Table 4.3 is used to indicate each data. SKS Mom. and K18 Mom. denote the typical momentum of outgoing kaon and the beam momentum, respectively. Data set A is a byproduct of the production run: the Σ^- production in SFT, that is, $\pi^- p \to K^+\Sigma^-$. Data set B and C are the $\Sigma^\pm$ production using the polyethylene target. Data set D and E are the beam through run measuring the beam momentum by each spectrometer. By using these data sets, f, g, dE_{K18}, and dE_{SKS} are determined by the following procedures. Firstly, the energy loss in each material is estimated. Secondly, the relative momentum difference, namely, $dP = p'_{K18} - p'_{SKS}$ is obtained using data set D. Finally, the absolute momenta are determined using the data sets B and C and checked using the data set A.

Energy loss

dE_{K18} contains the energy loss in BH2, the chambers, air, and targets. We ignore contributions from chambers and air because of their small amount of material. The energy loss in material is estimated using the Geant4 simulation and the Bethe-Bloch formula except for

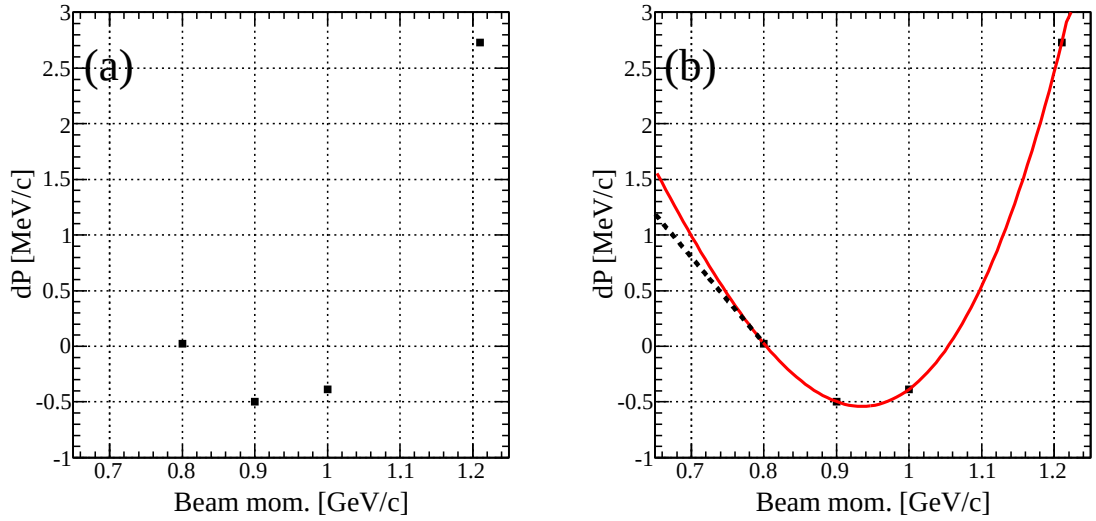

Figure 4.24: *(a) The momentum difference for each beam momentum obtained from data set D. (b) The fitting with a third-order polynomial and a tangential line.*

the case of pion in the ^{6}Li target. The energy loss of pion in the ^{6}Li target is determined using the data set D and E; the energy loss is defined as the difference of p_{SKS} obtained from each data set.

On the other hand, dE_{SKS} contains the energy loss in the target, SFT, the chambers, and air. However, contributions from the chambers and air are also ignored. All energy losses in material are estimated using the Geant4 simulation and the Bethe-Bloch formula.

Beam through analysis

After correcting dE, the relative momentum difference, namely, $dP = p'_{K18} - p'_{SKS}$ is obtained from the data set D. At this stage, the parameters for dP to be zero are determined. The momentum difference for each beam momentum is plotted in Figure 4.24 (a). It is clear that the distribution cannot be explained with a simple linear function. Thus, we define f and g as a linear and third-order functions, respectively. For the reason to select a third-order and linear functions, see Appendix B. The definition of f and g are given by

$$f(p) = \alpha p + \beta, \tag{4.13}$$
$$g(p) = Ap^3 + Bp^2 + Cp + D. \tag{4.14}$$

The momentum difference is represented as

$$\begin{aligned} dP &= h(p) \\ &= g(p) - f(p) \\ &= Ap^3 + Bp^2 + (C - \alpha)p + D - \beta. \end{aligned} \tag{4.15}$$

The fit to the plot in Figure 4.24 (a) with the function described above is shown in Figure 4.24 (b). Since the lowest beam momentum in the data set D is 0.8 GeV/c, an extrapolation to the momentum region of 0.7 GeV/c is necessary. A tangential line at $p = 0.8$ GeV/c shown in Figure 4.24 (b) with a dashed line is used as the correction function below $p = 0.8$ GeV/c.

Table 4.4: *Data summary used for the momentum calibration.*

Parameters	3rd order	2nd order	1st order	offset
				Unit [MeV/c]
f			0.0064	0.0
g	-0.026	0.038	-0.0041	-8.9
PO				2.15

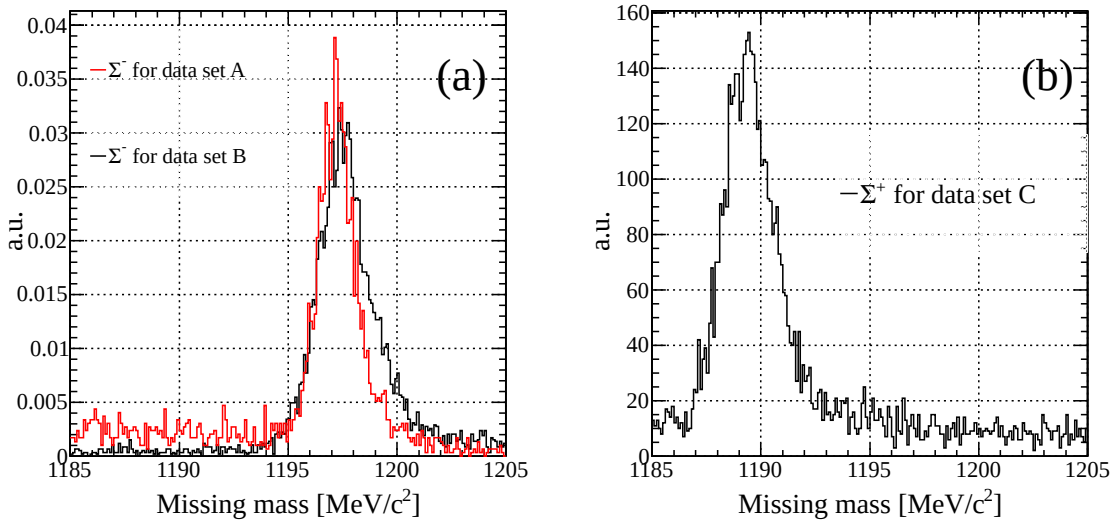

Figure 4.25: *The missing mass spectra of* Σ^- *obtained from the data set A (red lines) and B (black lines). (b) The missing mass spectrum of* Σ^+.

Missing mass analysis

To determine C, D, α, and β, optimal values are searched by comparing with the missing mass of $\Sigma^\pm$ and the mass in the Particle Data Group (PDG) table [69]. Here, we introduce an additional offset in the K1.8 spectrometer analysis; it is called as the polarity offset (PO). It is known that there is an offset between opposite polarities of the D4 magnet in the K1.8 spectrometer. As the result of numerical iteration, all correction parameters are determined as summarized in Table 4.4. The missing mass spectra shown in Figure 4.25 of $\Sigma^\pm$ for the data set A, B, and C are use these parameters. The data set A does not participate in the calibration process; however, the Σ^- peak position at 1197.22 ± 0.03 MeV/c^2 is consistent with the mass in the PDG table.

4.6.2 Correction for the SKS system

In the SKS system, it is known that there is a correlation between the momentum and the scattering angles, which should not exist in principle. To account for the correlation, we introduce a function $k(u)$ and $l(v)$ where u and v are a horizontal and vertical angles of the SKS track, namely, dx/dz and dy/dz. The corrected momentum of the SKS track is defined as

$$p'_{SKS} = p_{SKS} + k(u) + l(v). \tag{4.16}$$

These functions are determined by using the ground-state peak of ${}^{12}_{\Lambda}\mathrm{C}$ via the (π^+, K^+) reaction.

The correlation appears in the momentum difference, that is, $dp_{SKS} = p_{SKS}^{measured} - p_{SKS}^{calculated}$, where $p_{SKS}^{measured}$ is a reconstructed momentum by the SKS tracking and $p_{SKS}^{calculated}$ is a kaon momentum calculated by assuming the kinematics of the ${}^{12}\mathrm{C}(\pi^+, K^+){}^{12}_{\Lambda}\mathrm{C}$ (g.s.) reaction. $p_{SKS}^{calculated}$ is extracted by back calculation the missing mass formula using the beam momentum, the reaction angle and the mass of the ground-state of ${}^{12}_{\Lambda}\mathrm{C}$ [70]. Correlation plots between dp_{SKS} and the horizontal and vertical angle of the SKS track are shown in Figure 4.26 (a) and (b), respectively. Figure (a) and (b) are respectively fitted with a fourth-order and second-order polynomials. These fitting functions have no offset parameter because the absolute momentum is already obtained. Correlation plots after the correction are shown in Figure 4.26 (c) and (d).

These correction parameters obtained are applied to the analysis of the production run.

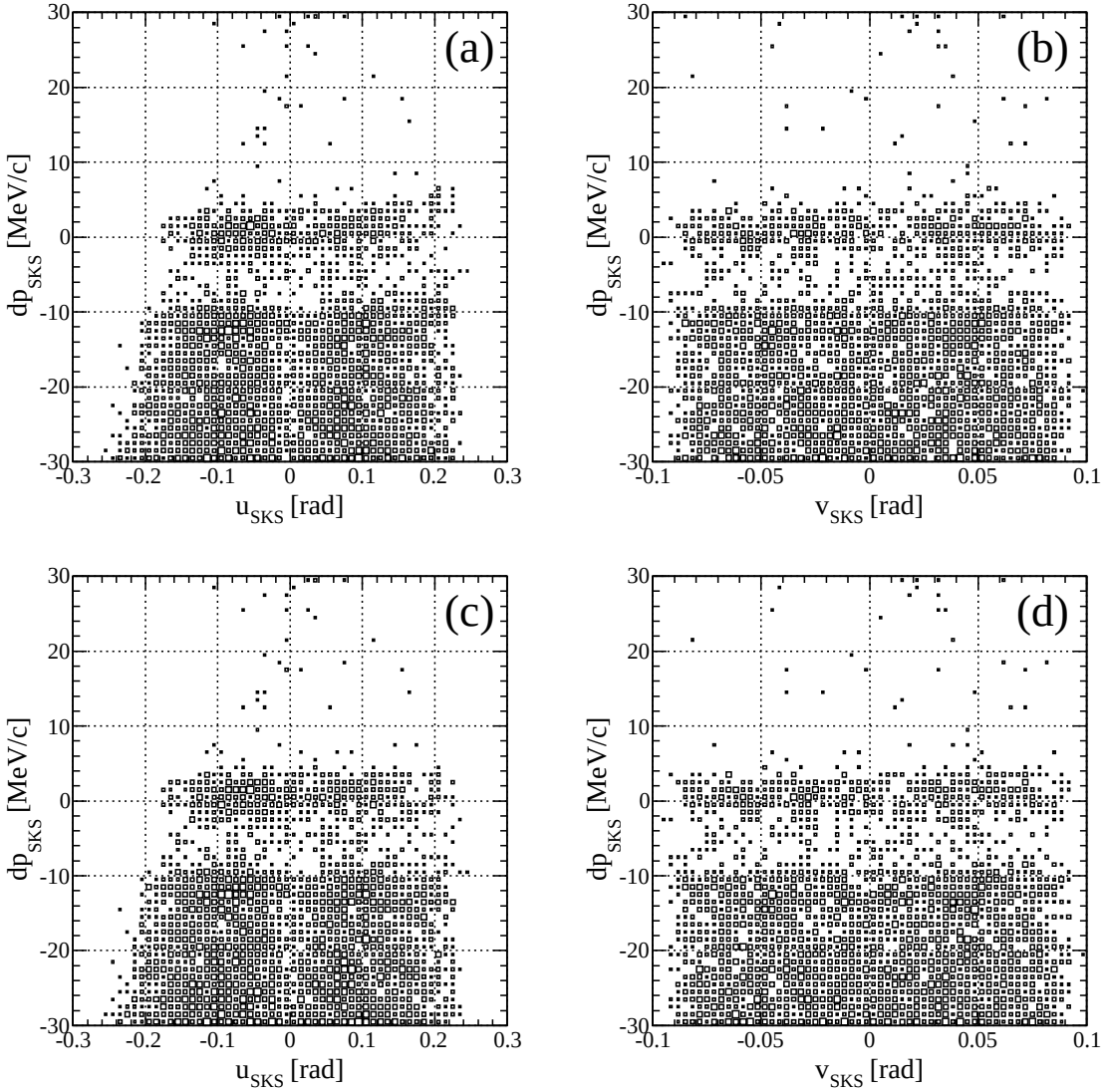

Figure 4.26: *Correlation plots between dp_{SKS} and a horizontal and vertical angles of the SKS track. Figure (a) and (b) show the correlation before the correction. Figure (c) and (c) show the correlation after the correction.*

4.7 Cross section analysis

After the missing mass analysis, the production cross section for the ^{6}Li(π^-, K^+)X reaction is calculated using an experimental yield and several correction factors such as the detector efficiency, decay factor of kaon, and the acceptance of the SKS system. In the present experiment, the differential cross section is defined as

$$\left(\frac{d\sigma_{\theta_1-\theta_2}}{d\Omega}\right) = \frac{1}{N_{target}} \cdot \frac{1}{N_{beam} \cdot f_\pi \cdot \epsilon_{K1.8}} \cdot \frac{N_{kaon}}{\epsilon_{SKS} \cdot f_{decay} \cdot f_{abs}} \cdot \frac{1}{\epsilon_{vertex} \cdot \epsilon_{DAQ} \cdot \epsilon_{MsT}} \cdot \frac{1}{\Delta\Omega_{\theta_1-\theta_2}}, \tag{4.17}$$

$$\begin{aligned} N_{target} &= f_{enrich} \cdot \frac{(\rho x) \cdot N_A}{6}, \\ \epsilon_{K1.8} &= \epsilon_{BH2} \cdot \epsilon_{BFT} \cdot \epsilon_{BcOut} \cdot \epsilon_{K1.8} \cdot \epsilon_{SSD}, \\ \epsilon_{SKS} &= \epsilon_{TOF} \cdot \epsilon_{LC} \cdot f_{LAC} \cdot \epsilon_{SdcIn} \cdot \epsilon_{SdcOut} \cdot \epsilon_{SKS} \cdot \epsilon_{PID}. \end{aligned}$$

Here, N_{target}, N_{beam} and N_{kaon} represent the number of ^{6}Li nuclei in the target, beam particles counted by the DAQ scaler, and kaons identified in the previous analysis, respectively. N_{target} is determined by f_{enrich}, which is ratio of ^{6}Li nuclei to the Li target, ρx (target thickness), and N_A (Avogadro's number). The solid angle corresponding to the reaction angle between θ_1 and θ_2 is expressed by $\Delta\Omega_{\theta_1-\theta_2}$. Other ϵ's and f's are the experimental efficiencies and correction factors, respectively. These efficiencies and factors are divided into two different groups. One group contains common factors to all events, and the other has efficiencies/factors correcting event by event with different values. Furthermore, the present experiment is divided to five periods according to the experimental conditions. Several efficiencies are estimated in each period. Their typical values at the reaction angle of 4°-6° in the second period are summarized in Table 4.5. In this section, we describe procedures to estimate them.

Table 4.5: *The list of efficiencies and factors at the reaction angle of* 4°-6° *in the period 4.*

Factors	Meaning	Values (%)
	Common values	
f_π	Beam normalization factor	86.8±0.2
ϵ_{BH2}	BH2 analysis efficiency	95.0±0.6
ϵ_{BFT}	BFT detection efficiency	97.5±0.4
ϵ_{BcOut}	BcOut tracking efficiency	98.3±0.3
$\epsilon_{K1.8}$	Analysis efficiency of K1.8	95.0±0.5
ϵ_{SSD}	SSD detection efficiency	84.1±0.8
ϵ_{TOF}	TOF detection efficiency	100
ϵ_{LC}	LC detection efficiency	97.8±0.1
f_{LAC}	LAC accidental kill factor	86.3±1.4
ϵ_{SdcOut}	SdcOut tracking efficiency	99.1±0.5
ϵ_{PID}	K^+ identification efficiency	99.1±0.4
f_{abs}	K^+ absorption factor	96.9±0.5
ϵ_{cdist}	Closest distance efficiency	96.5±0.5
ϵ_{DAQ}	DAQ efficiency	79.0±0.8
ϵ_{MsT}	Mass trigger efficiency	97.2±0.1
	Event by event correction	
ϵ_{SdcIn}	SdcIn tracking efficiency	82.4±2.0
ϵ_{SKS}	SKS tracking efficiency	95.5±0.5
ϵ_{vertex}	Vertex gating efficiency	93.1±0.6
f_{decay}	K^+ decay factor	42.2±0.8

4.7.1 Beam normalization factor

The beam normalization factor, that is, f_π represents the ratio of π^- to the number of beam particles, namely, N_{beam}. We should consider the electron and anti-proton contamination. The anti-proton contamination is negligibly small owing to the double-separator system. On the other hand, the electron contamination should be subtracted from N_{target} because GC, which is installed to reject electrons, does not participate in the trigger. The ratio of electron is estimated using the GC information in the off-line analysis using data taken with the BEAM trigger. However, GC is overloaded under the high intensity condition because GC is not segmented. In addition, in order to decrease the secondary beam intensity, the slit condition in the secondary beamline must be changed from that of the production run. Therefore, special calibration data are taken by decreasing the primary accelerator power by keeping the slit condition the same. The TDC distribution of GC obtained from this data is shown in Figure 4.27. By gating around the prominent peak corresponding to electron events, the electron contamination is measured to be 11.3±0.2%.

Furthermore, we should consider the decay of pions, that is, $\pi \to \mu\nu$. The μ contamination on the target position is estimated to be 2.2% using Decay-TURTLE [71]. The contamination mainly comes from the decays in the $QQDQQ$ system. Consequently, the beam normalization factor is determined as

$$f_\pi = (1 - f_e) \cdot (1 - f_\mu), \tag{4.18}$$

where f_e and f_μ are the ratio of the electron and μ contamination to N_{beam}, respectively. The value of f_π is 86.8±0.2%.

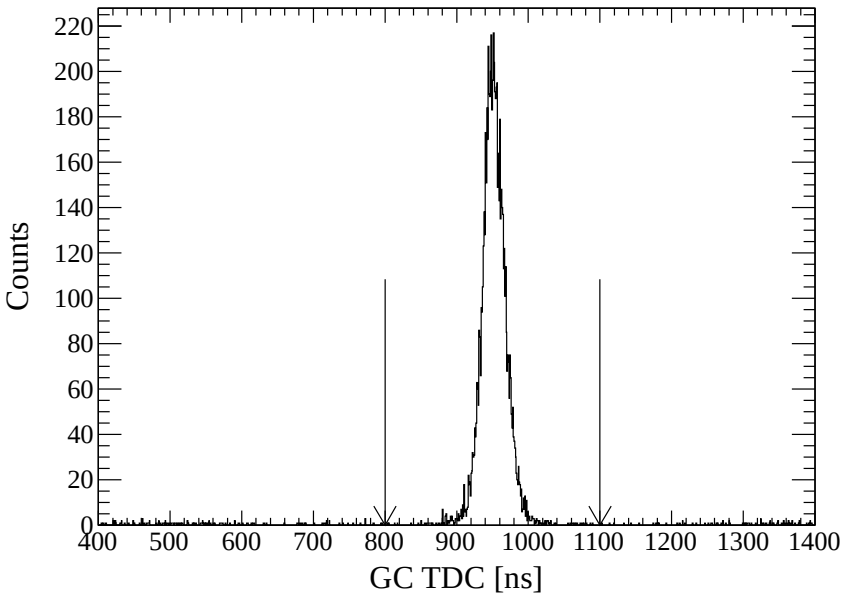

Figure 4.27: *The TDC distribution of GC obtained from the special calibration data.*

4.7.2 Efficiencies of beam detectors

The method to estimate efficiencies of the detectors exposed to the beam is different from that of detectors which are not. Presently, it is known that the slow-extracted beam in J-PARC has a time structure with non-uniform beam intensity in the order of μs, due to the unstable primary beam orbit in MR. Therefore, the intensity of the secondary beam instantaneously increases up to 10 times higher, which in turn makes detectors inefficient. The inefficiency caused to the beam exposed detectors are not entirely independent of each other. Then, an over correction results from the fact that the total efficiency is a product of these efficiencies assumed independent. Hence, the efficiencies are estimated based on the analysis procedure shown in Figure 4.1 by using data taken with the BEAM trigger. At first, when the efficiency of a certain detector is estimated, the number of events satisfying the previous analysis stage is taken as a denominator (N_1). Nextly, the number of events meeting this analysis stage is taken as a numerator (N_2). Then, the efficiency of that detector is determined by the ratio between N_1 and N_2, that is, N_2/N_1.

Analysis methods and efficiencies of BH2, BFT, BcOut, K1.8, and SSD are already described in the previous section. Their efficiencies are listed in Table 4.5 with a systematic error, which is estimated from the fluctuation of the efficiency during the experiment.

SdcIn tracking efficiency

SFT and SDC2 are the most downstream detectors exposed to the beam. A denominator in estimating the detection efficiency of the SdcIn tracking is defined as the number of events satisfying the SSD analysis. The condition going through the SdcIn analysis is that there is at least one track after applying the χ^2 gate. A track with the reduced χ^2 value of less than 10 is recognized as a good track. In this subsection, we describe the horizontal position dependence of the tracking efficiency at first, and then, its time stability is discussed.

As the beam is focused on the target, the counting rate of each fiber or wire in SFT and SDC2 is the highest among all detectors; SFT and SDC2 are placed nearest to the target. The tracking efficiency is decreased around the region in which the beam passes through. The horizontal position dependence of the efficiency is shown in Figure 4.28 at the SFT-X position. This plot is obtained by extrapolating the BcOut track to the SFT-X position. Since it is clear that there is a strong position dependence, the efficiency is changed track by track according to the plot in Figure 4.28.

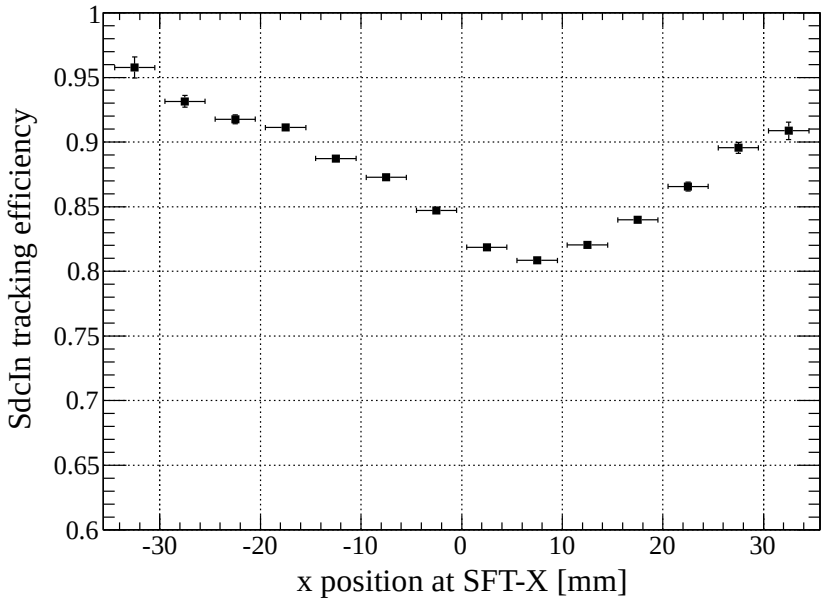

Figure 4.28: *The horizontal dependence of the SdcIn tracking efficiency at the SFT-X position.*

In order to check the stability over time, we introduce the averaged efficiency with respect to the horizontal position. The averaged efficiencies are plotted in Figure 4.29 as a function of the run number for all the experimental periods. This time instability is understood to related to the instability of the SFT system. However, details are still unknown. In order to correct this instability, position-dependent efficiency tables corresponding to six different averaged efficiency regions are set. Six regions are defined as follows.

- Region 1 : Averaged efficiency is over 84%;
- Region 2 : Averaged efficiency is within 82-84%
- Region 3 : Averaged efficiency is within 80-82%
- Region 4 : Averaged efficiency is within 78-80%
- Region 5 : Averaged efficiency is within 76-78%
- Region 6 : Averaged efficiency is below 76%

Consequently, the SdcIn efficiency is corrected track by track using the six position-dependent efficiency tables. The systematic error of $\pm 2\%$ is determined; it corresponds to the size of each reagion.

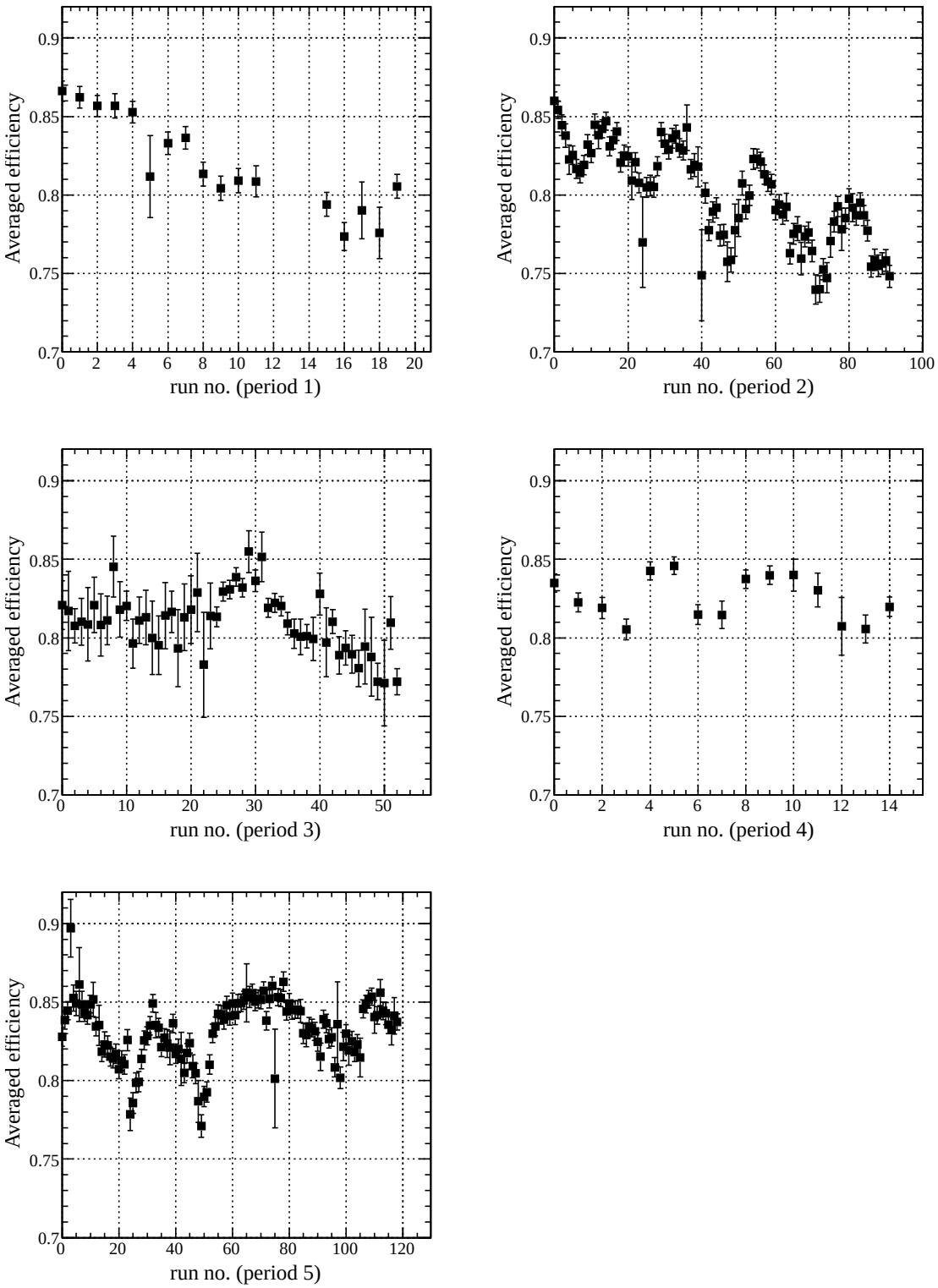

Figure 4.29: *The time dependence of the averaged SdcIn tracking efficiency.*

4.7.3 Efficiency of TOF and LC

In the present experiment, we do not have data to estimate the TOF efficiency. Then, the TOF efficiency is assumed to be 100%.

The LC detection efficiency is estimated using the beam-through data with the beam momentum of 0.8, 0.9, and 1.0 GeV/c. The beam-through data are taken with the TOF trigger defined as

$$TOF\ trigger \equiv BEAM \times TOF.$$

By selecting the pion events using the mass square distribution of the scattered particles, the detection efficiency of LC is obtained as

$$\epsilon_{LC} = \frac{N(LC\ hit \times pion)}{N(pion)}, \tag{4.19}$$

where $N(pion)$ is the number of pion events identified by the mass of the scattered particles and $N(LChit \times pion)$ is the number of events satisfying the condition that there is at least one LC hit. The multi-hit event on TOF is rejected from $N(pion)$ in order to suppress the background. Consequently, the averaged detection efficiency of LC is 97.8±0.1%. We apply the same efficiency to kaon events because the sufficient yield of Čerenkov lights is obtained for kaons with the momentum range of 0.7-0.9 GeV/c.

4.7.4 LAC accidental veto factor

The accidental kaon veto is estimated using data taken with the controlled trigger, that is, the PIPI trigger defined as

$$PIPI \equiv BEAM \times TOF \times LC.$$

LAC does not participate in this trigger. To estimate the accidental veto factor, proton events, which should not be detected by LAC, are used. The accidental veto factor is obtained as,

$$f_{LAC} = 1 - \frac{N(LAC\ hit \times proton)}{N(proton)}. \tag{4.20}$$

Here, $N(proton)$ is the number of proton events selected using the mass square distribution of the scattered particles. In addition, it is required that pions pass through the sensitive region of LAC using the SdcOut track and LC hit information. $N(LAC\ hit \times proton)$ is the number of events meeting the condition that there is at least one LAC hit. To identify accidental coincidence, we should determine the coincidence gate of LAC using the timing distribution of LAC for proton events in data taken with the PIK trigger; the distribution is shown in Figure 4.30 (a). Since the coincidence width of LAC was set to be 30 ns, we assume that the coincidence gate is from -10 ns to 20 ns. Events lying within this region are recognized an accidental coincidence. Figure 4.30 (b) shows the timing distribution for proton events in data taken with the PIPI trigger. From this figure, the accidental veto factor is 86.3±1.4%. The error is estimated by changing the gate region.

The accidental veto caused by δ ray produced by protons is already taken into account. The production cross section of δ ray as a function of a energy transfer is parametrized by β of a incident particle. In the present experiment, since mean momenta of kaons and protons are 0.74 and 1.2 GeV/c, respectively, mean β of kaons and protons are almost the same. Then, we consider that the accidental veto caused by δ ray produced by kaons and protons are the same.

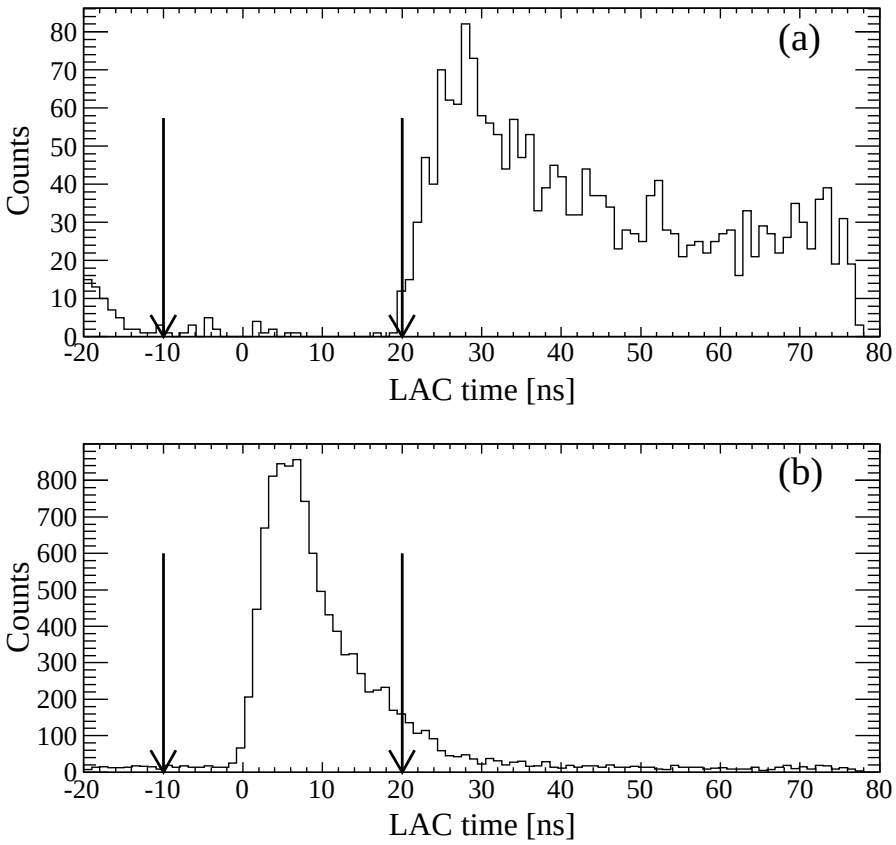

Figure 4.30: *The timing distribution of LAC for proton evens for the PIK trigger (a) and the PIPI trigger (b).*

4.7.5 SdcOut tracking efficiency

The SdcOut tracking efficiency is defined as the probability that the SdcOut tracking succeeds when a single hit and track respectively exist on TOF and the SdcIn analysis. In order to estimate this efficiency, protons which do not decay are selected using the correlation between the horizontal angle of the SdcIn track, that is, $u(dx/dz)$ and the time-of-flight from BH2 to TOF. The correlation plot is shown in Figure 4.35 with black points. In the figure, we can see three bands, which respectively represent protons, kaons, and pions from top to bottom. One can find a unrelated line around $u = 0$; the line corresponds to the accidental beam background. Therefore, proton events represented by red points are selected and used to estimate the tracking efficiency.

The horizontal angle and the x-position dependencies at the midpoint between SDC3 and 4 of the SdcOut tracking efficiency are shown in Figure 4.32 (a) and (b), respectively. The horizontal angle and the x position are determined by the hit combination of TOF and LC. Since there is almost no dependence, the averaged tracking efficiency of 99.1±0.1% is used for all events.

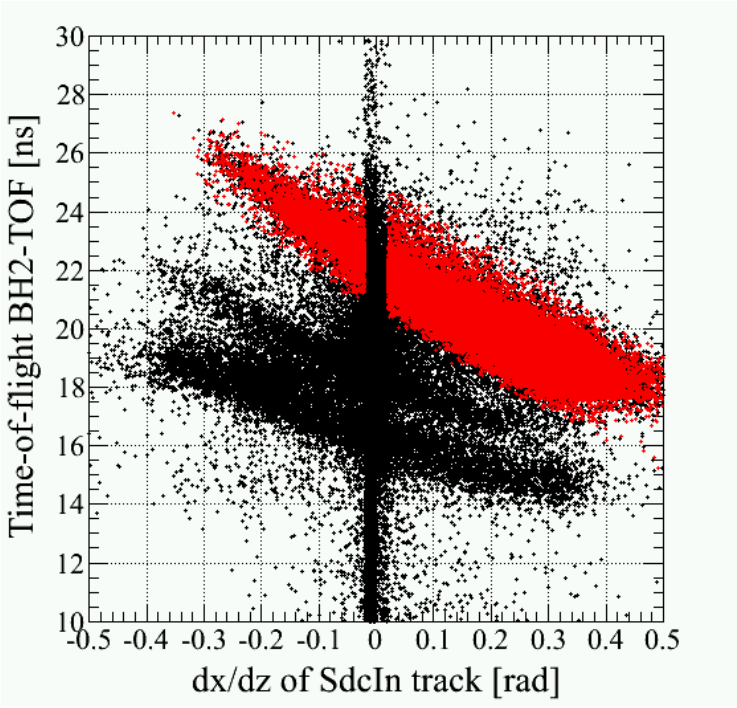

Figure 4.31: *The correlation plot between the horizontal angle of the SdcIn track and the time-of-flight from BH2 to TOF. Black marker and red markers show all events and proton events, respectively.*

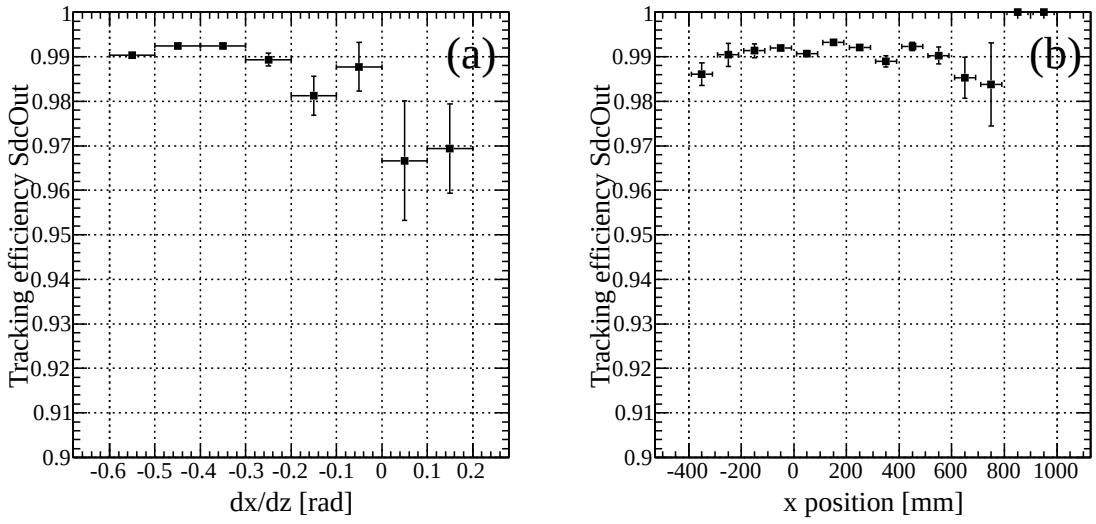

Figure 4.32: *(a) The horizontal angle dependence. (b) The x-position dependence of the SdcOut tracking efficiency.*

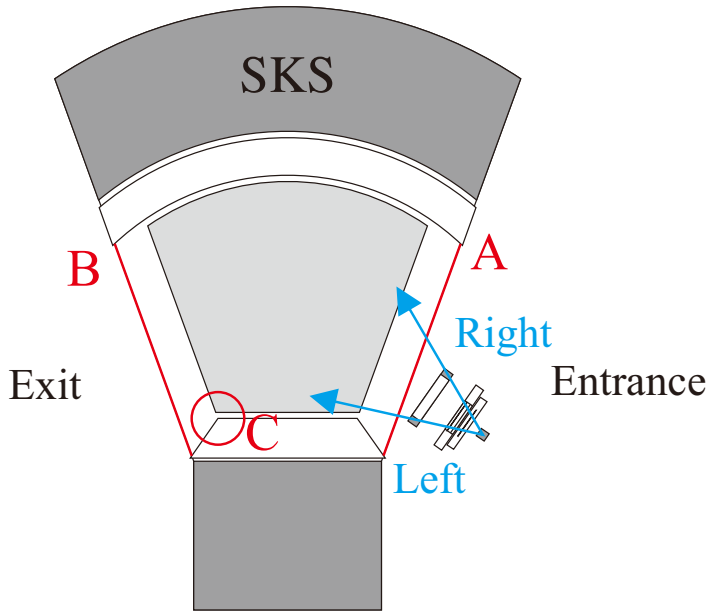

Figure 4.33: *The red lines A and B represent the entrance and exit of the magnet. The red circle C shows the horizontal edge of the coil vessel. Blue arrows express the definition of scattering to the left and right.*

4.7.6 Fiducial volume of the SKS magnet

Before estimating the SKS tracking efficiency, we introduce the fiducial volume of the SKS magnet because there are several ambiguities such as the structure of the magnet itself and the calculated magnetic field near the magnet. Two types of different gates are applied to the SKS tracking result. One is a vertical angle gate at the entrance of the SKS magnet. The other is a vertical position gate at the exit of the SKS magnet.

Figure 4.34 shows the correlation plot between the vertical angle of the SdcIn track, that is, $v(dy/dz)$ and the y position at TOF obtained from the SdcOut track. Red points represent events that the SKS tracking succeeds. On the other hand, black points are events that the SKS tracking fails. From the distribution the red points, it is understood that there is a good correlation between the vertical angle at the entrance and the vertical position at the exit. However, one can find unrelated events, which represented by black points, distributed around $v = 0$ and $v = \pm 0.1$. The distribution around $v = 0$ comes from the accidental beam background while the distribution around $v = \pm 0.1$ are particles scattered by the SKS magnet at the entrance, which is shown in Figure 4.33 by the red line A. Therefore, the vertical angle gate at the entrance is set to be $-0.09 < v < 0.09$.

On the other hand, the vertical position distributions of the SKS track at the exit, which is shown in Figure 4.33 by the red line B, are shown in Figure 4.35. Figure 4.35 (a) and (b) represent distributions with the χ^2_{SKS} values of less than 10 and lager than 20, respectively. In Figure 4.35 (b), one can find two peaks around $y = \pm 250$ mm; they correspond to particles scattered by the SKS magnet at the exit. Hence, the vertical position gate at the exit of the magnet is taken to be ± 235 mm.

The estimation of the SKS tracking efficiency and the acceptance of the SKS system are obtained within these gate ranges.

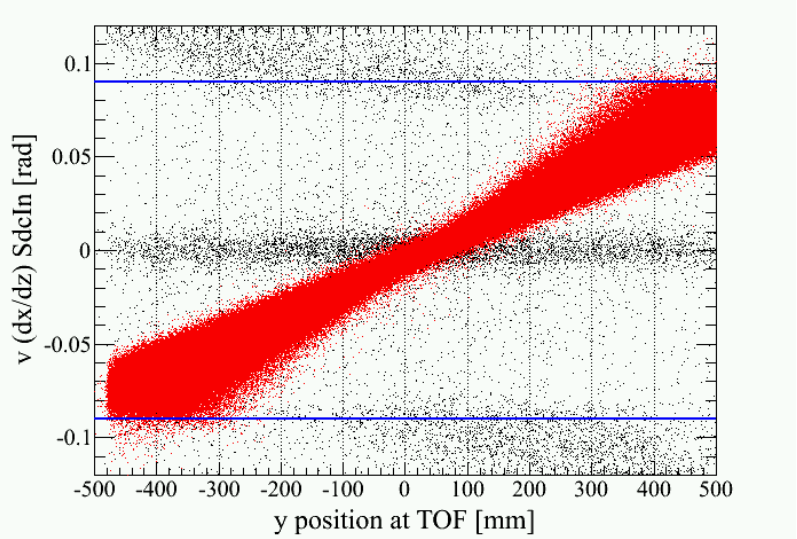

Figure 4.34: *The correlation plot between the vertical angle of the SdcIn track and the vertical position at TOF obtained from the SdcOut track. Black and red points represent events that the SKS tracking are failed and succeeded, respectively.*

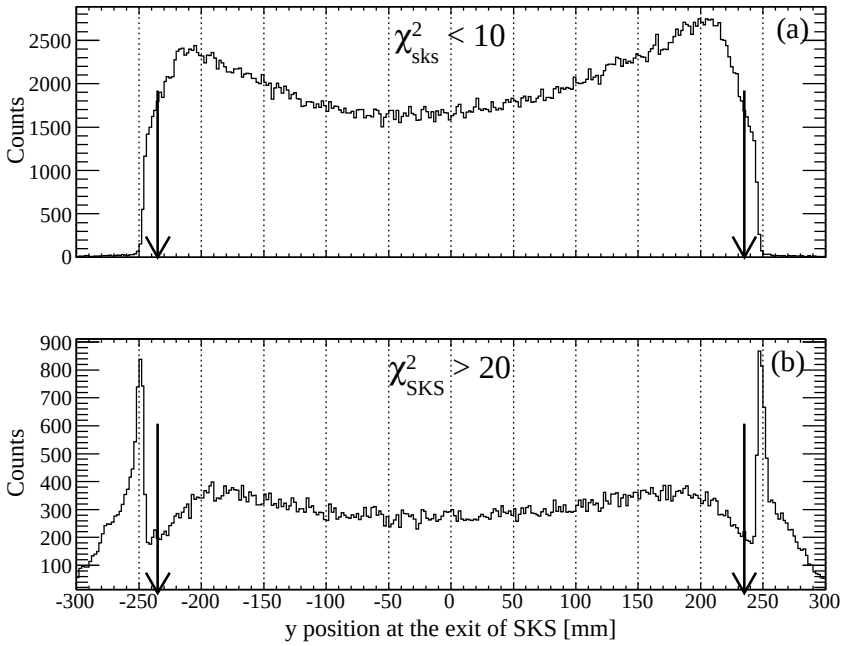

Figure 4.35: *Vertical position distributions obtained from the SKS track at the exit of the magnet with different χ^2_{SKS} gating.*

4.7.7 SKS tracking efficiency

In the present experiment, the SKS tracking efficiency is defined as the probability that the χ^2_{SKS} value converges to below 20 when there is one track only at the entrance and the exit of the SKS system. In order to estimate the SKS tracking efficiency, proton events as selected in Figure 4.31 are also used. Here, we introduce the scattering direction as represented by blue arrows in Figure 4.33, that is, scattering to the left and right in the horizontal plane. The SKS tracking efficiency for scattering to the left and right is separately estimated because their flight path lengths are different. They are obtained as shown in Figure 4.36 and Figure 4.37 as a function of the reaction angle. The typical value at the reaction angle of 4°-6° for the scattering to the right is 95.5±0.5%.

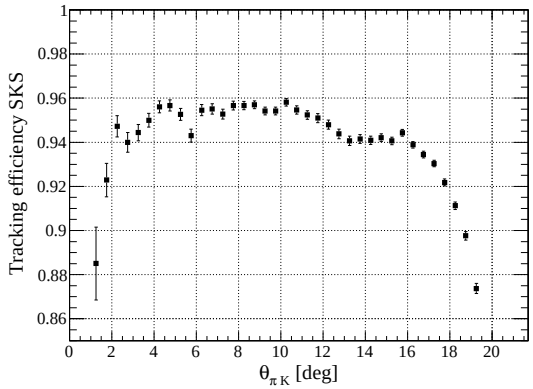

Figure 4.36: *The SKS tracking efficiency for scatterings to the left.*

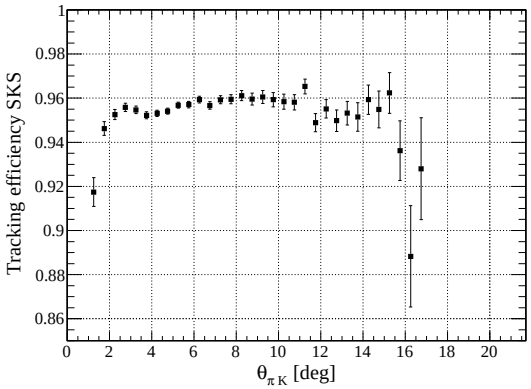

Figure 4.37: *The SKS tracking efficiency for scatterings to the right.*

4.7.8 Event vertex selection

Closest distance selection

As described earlier, the vertex is reconstructed using the closest distance between the beam track and the SKS track. In the present analysis, the vertex with the closest distance of less than 8 mm is recognized as a good vertex. Since this gating efficiency does not depend on the reaction angle, an averaged closest distance selection efficiency, namely, ϵ_{cdist} is used, and it is 96.5±0.5%. The errors is the root mean square of the averaged efficiency.

Z-vertex selection

In the present analysis, the vertex selection for the x and y planes are not required because the horizontal size of SSD-X is smaller. Thus, the x-vertex selection is included into the SSD efficiency. In addition, since the beam is vertically well focused, there is no contribution from other materials such as the target stand. Therefore, only the z-vertex selection is considered.

The z-vertex distribution for the (π^-, K^+) events for each reaction angle is shown in Figure 4.39. These distributions are gated with the range of ±30 mm from the two sides of the target, namely, ±68.5 mm. Events lying within this range are recognized as the ^{6}Li(π^-, K^+)X reaction. The z-vertex selection efficiency as a function of the reaction angle is obtained as shown in Figure 4.38. The error of efficiency at different angles is estimated by the statistical error. However, a contamination from SSD in the distribution for the

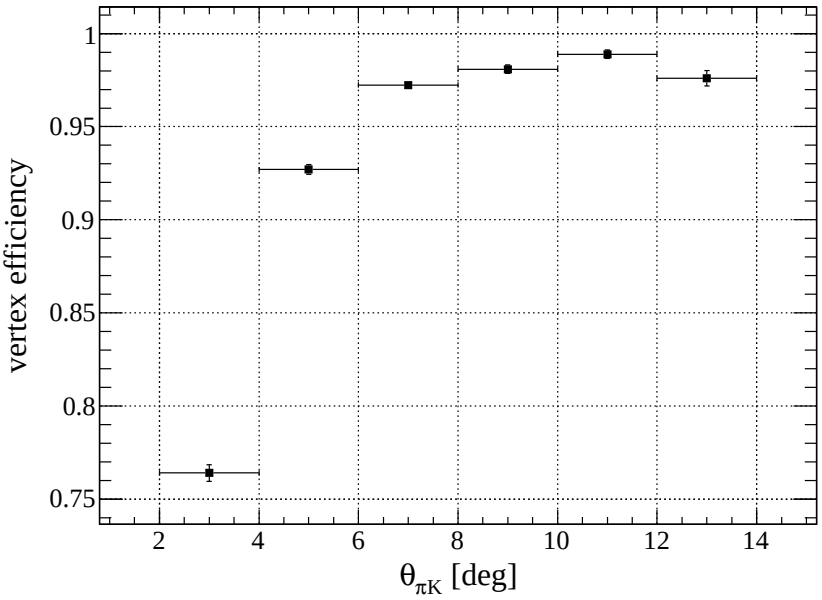

Figure 4.38: *The z-vertex selection efficiency as a function of the reaction angle.*

reaction angle of 2°-4° cannot be separated due to the insufficient vertex resolution. Hence, the contribution from SSD is estimated from using other distributions, in which SSD is well separated, and it is 3%. Consequently, the vertex selection efficiency for the reaction angle of 2°-4° is $76.4^{+3.0}_{-0.5}$%.

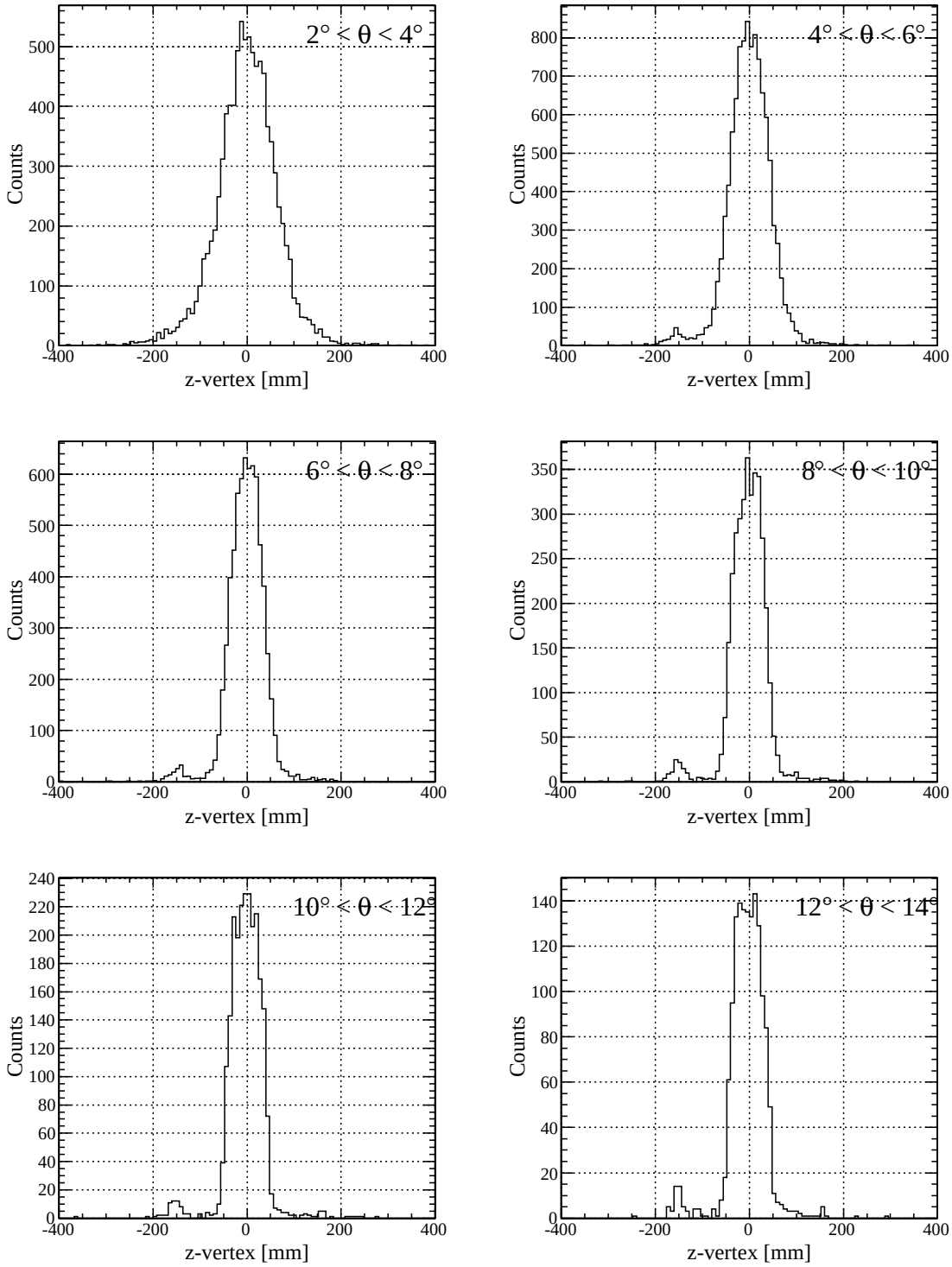

Figure 4.39: *Z-vertex distributions for the (π^-, K^+) events for each reaction angle.*

4.7.9 K^+ absorption factor

A part of produced kaons are absorbed by materials between the target and LC. The absorption rate is estimated using the Geant4 simulation by considering the electro-magnetic interaction and the hadronic interaction. The K^+ absorption factor, that is, f_{abs} is defined as

$$f_{abs} = 1 - \frac{N_{K\ on\ LC}}{N_{K\ generated}}, \tag{4.21}$$

where $N_{K\ on\ LC}$ is the number of kaons detected by LC and $N_{K\ generated}$ is the number of kaons generated at the target position. In the simulation, kaons are generated with the angle of zero degree within the momentum range of 0.7-0.9 GeV/c because such kaons must be detected by the downstream counters of the SKS system if kaons do not react. The K^+ absorption factor is 96.9±0.5. The error is determined by the difference caused by the change in the momentum condition.

4.7.10 K^+ decay factor

A part of kaons produced in the target decays before reaching the downstream detectors. All kaons that decay before passing through LAC are rejected in the trigger level because the decay products can be detected by LAC. In order to correct the number of kaons decayed, the decay factor is introduced; the factor is calculated event by event. The decay factor, namely, f_{decay} is expressed using the flight path length (L_K) of the kaon and its $\beta\gamma c\tau$ as

$$f_{decay} = \exp(-L_K/\beta\gamma c\tau). \tag{4.22}$$

The decay factor for the reaction angle of 4°-6° is 42.2% typically. The systematic error is estimated by taking into account the radiator size of LAC. The value of ±0.8% is obtained, and it is common to all reaction angle.

4.7.11 Acceptance of the SKS system

The effective solid angle of the SKS system ($\Delta\Omega_{\theta 1-\theta 2}$) is calculated using the Monte-Carlo simulation, in which the realistic SKS system is reproduced. This solid angle for an arbitrary event with the momentum of scattered particle (p) and the reaction angle (θ) is defined as

$$\Delta\Omega(p,\theta) = 2\pi \int_{\theta 1}^{\theta 2} dcos(\theta) \times \frac{N_a(p,\theta)}{N_g(p,\theta)}, \tag{4.23}$$

where $\theta 1$ and $\theta 2$ are expressed as $\theta - \frac{1}{2}\Delta\theta$ and $\theta + \frac{1}{2}\Delta\theta$ using a fixed interval ($\Delta\theta$), and N_a and N_g are the number of kaons accepted and the number of kaons generated, respectively. A table of the N_a/N_g ratio is called as the acceptance table of the SKS system.

In the simulation, the multiple-scattering effect and the energy loss are taken into account. In order to estimate the effective solid angle as a function of the reaction angle, the realistic beam profile is reproduced in the event generator. The beam profile is represented by the function of (x, y, u, v) at the target position. Kaons of a certain momentum are uniformly generated from the target position between 0 to 30 degree in the polar angle, and from 0 to 2π in the azimuthal angle. By changing the momentum of kaon, the acceptance table representing the N_a/N_g ratio for each momentum and the reaction angle is created. In the present analysis, a mesh size of the table is 1 MeV/c in the momentum axis and 0.2 degree in the angle axis.

The obtained acceptance tables for scattering to the left and right are shown in Figure 4.40 and Figure 4.41, respectively. In the figure, the N_a/N_g ratio in percentage is represented by colors. In the table for scattering to the left, one can find a line along which the acceptance value is drastically changed. This is caused by the structure of the SKS magnet. Scattered particles with a particular momentum and reaction angle hit the edge of the coil vessel, which is shown in Figure 4.33 by a red circle C, and cannot reach the downstream detectors. In the present analysis, since the entire shape of the spectrum is quite important, such drastic acceptance change is not suitable. Therefore, we do no analyze events scattering to the left. In this paper, only events of scattering to the right are analyzed and discussed.

Furthermore, the lower limit of the kaon momentum is set to be 730 MeV/c to avoid to use the region, in which the acceptance values are drastically changed. This kaon momentum corresponds to the mass of 5920 MeV/c^2 in the case of the ^{6}Li(π^-, K^+)X reaction at the beam momentum of 1.2 GeV/c.

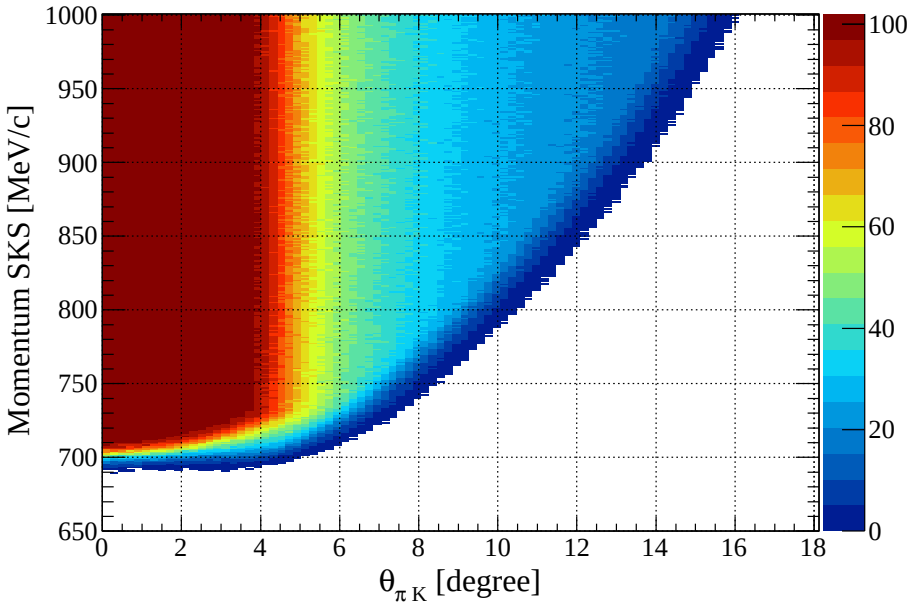

Figure 4.40: *The acceptance table of the SKS system for scattering to the left.*

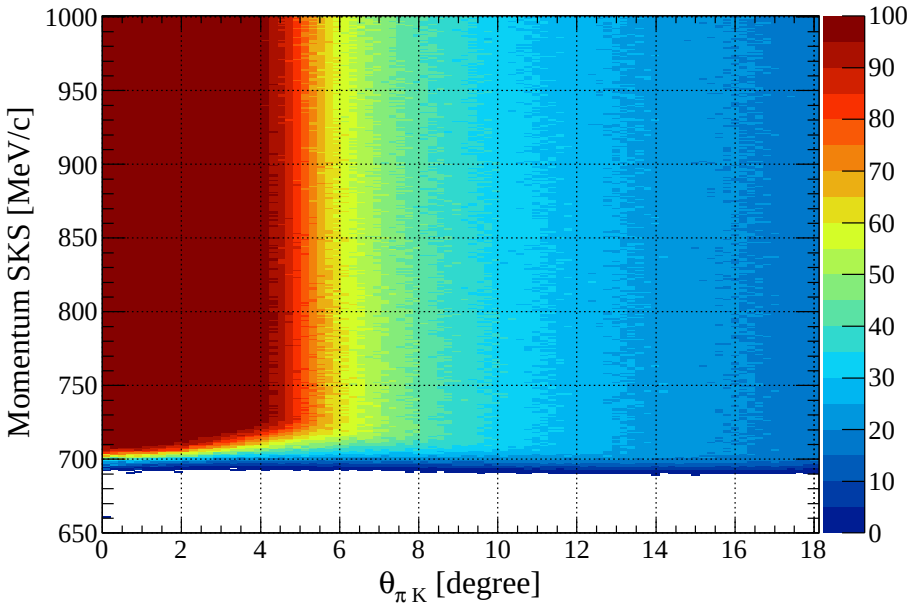

Figure 4.41: *The acceptance table of the SKS system for scattering to the right.*

4.7.12 DAQ efficiency

Main DAQ efficiency

The DAQ efficiency, ϵ_{DAQ}, is defined as the ratio of the number of events accepted against that of triggered with the L1 trigger because the L2 trigger does not suffer from the dead time of the DAQ system. A typical value is 79.0±0.8%. The dead time of the DAQ system in the present system is mainly caused by the TKO subsystem. The error comes from the stability of the DAQ system.

Mass trigger efficiency

The purpose of the mass trigger system is to reject a large proton background using the hit combination of TOF and LC and time-of-flight information. However, the (π, K) events are sometimes rejected due to miss identification. In order to estimate ϵ_{MsT}, pre-scaled rejected events are additionally taken with the pre-scale factor of 10 using the same DAQ system. The mass trigger efficiency ϵ_{MsT} is represented as

$$\epsilon_{MsT} = 1 - \frac{10 \times N_{K\ rejected}}{N_{K\ triggered}}, \tag{4.24}$$

where $N_{K\ triggered}$ and $N_{K\ rejected}$ are the number of kaon events triggered by the L1 trigger and rejected by the mass trigger. The mass square distribution of the kaon obtained from data taken with the normal L2 trigger and the pre-scaled special trigger are shown in Figure 4.42. By assuming that all events lying in the figure are kaons, the mass trigger efficiency is 97.2±0.1%. The error considers only the statistical error one.

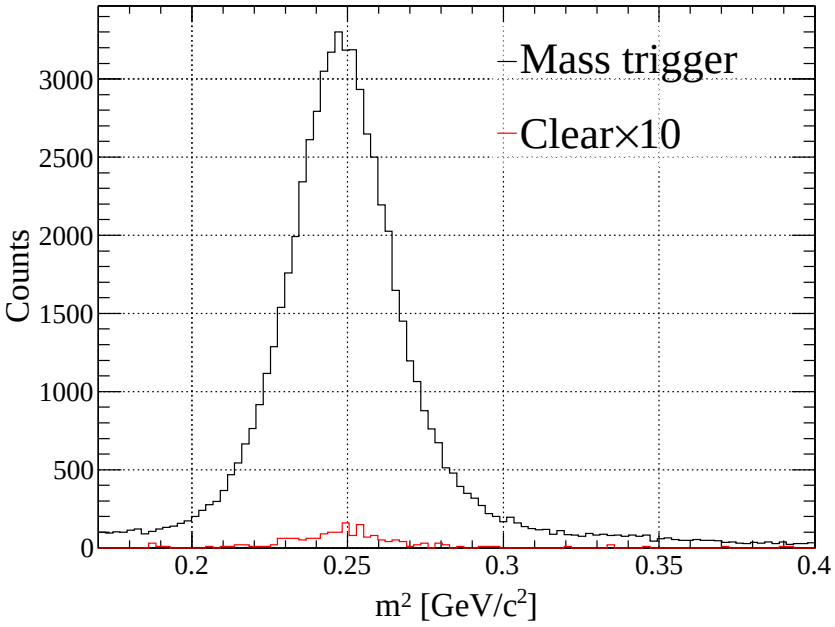

Figure 4.42: *The mass square distribution of kaon obtained from data taken with the normal L2 trigger and the pre-scaled trigger.*

Table 4.6: *Summary of systematic errors.*

Systematic errors (%)						
2°-4°	4°-6°	6°-8°	8°-10°	10°-12°	12°-14°	14°-16°
^{6}Li(π^-, K^+)X run						
$^{+4.1}_{-6.1}$	±4.7	±4.4	±4.4	±4.3	±4.3	-
$\Sigma^\pm$ production run						
±4.6	±4.9	±4.4	±4.4	±4.3	±4.3	±4.4

4.7.13 Systematic error of the cross section

The systematic error of the cross section is estimated for every 2 degree. Errors of the common factors and efficiencies are summed up according to the propagation of error. Errors for efficiencies used with event by event correction are individually considered. The SKS tracking efficiency and the vertex selection efficiency are represented as a function of the reaction angle. Therefore, the errors for each reaction angle range are summed up according to the propagation of error. The error of the SdcIn tracking and the decay factor are common to all events.

On the error of the acceptance table of the SKS system, we can estimate two types of errors. One comes from the statistics of the simulation. However, it is negligibly small owing to a significant number of events generated. Second one is caused by the mesh size dependence. In order to estimate this, we prepare six acceptance tables with different mesh sizes as

- type0 : $\Delta P = 1$ MeV/, $\Delta\theta = 0.2$ deg. (used in the present analysis)
- type1 : $\Delta P = 1$ MeV/, $\Delta\theta = 0.4$ deg.
- type2 : $\Delta P = 1$ MeV/, $\Delta\theta = 0.1$ deg.
- type3 : $\Delta P = 2$ MeV/, $\Delta\theta = 0.2$ deg.
- type4 : $\Delta P = 2$ MeV/, $\Delta\theta = 0.4$ deg.
- type5 : $\Delta P = 2$ MeV/, $\Delta\theta = 0.1$ deg.

The mesh-size dependence appears as the difference between averaged acceptance values in each missing mass bin. The obtained errors, which are a deviation from the averaged acceptance value in each missing mass bin, are shown in Figure 4.43. From this distribution, the total systematic error in each missing mass bin can be calculated according to the propagation of errors. In the present experiment, the maximum value in the missing mass spectrum is adopted as the total systematic error for a certain reaction angle.

In addition, an extra error coming from the difference of left/right of the SKS system except for the acceptance has to be estimated because the events for scattering to the right only are used in the present analysis. For the estimation, the cross section of the ^{6}Li(π^-, K^+)X reaction between 2-4 degree are used because there is no difference between the acceptance of the SKS system for scattering to the left and right as shown in Figure 4.40 and Figure 4.41. The difference between those cross section for scattering to the left and right is shown in Figure 4.44 (a) and its projection to the y axis is also shown in Figure 4.44 (b). From these figures, we conclude the extra error coming from the difference of left/right of the SKS system except for the acceptance is negligibly small.

Finally, systematic errors for the ^{6}Li(π^-, K^+)X run and the $\Sigma^\pm$ production run are summarized in Table 4.6.

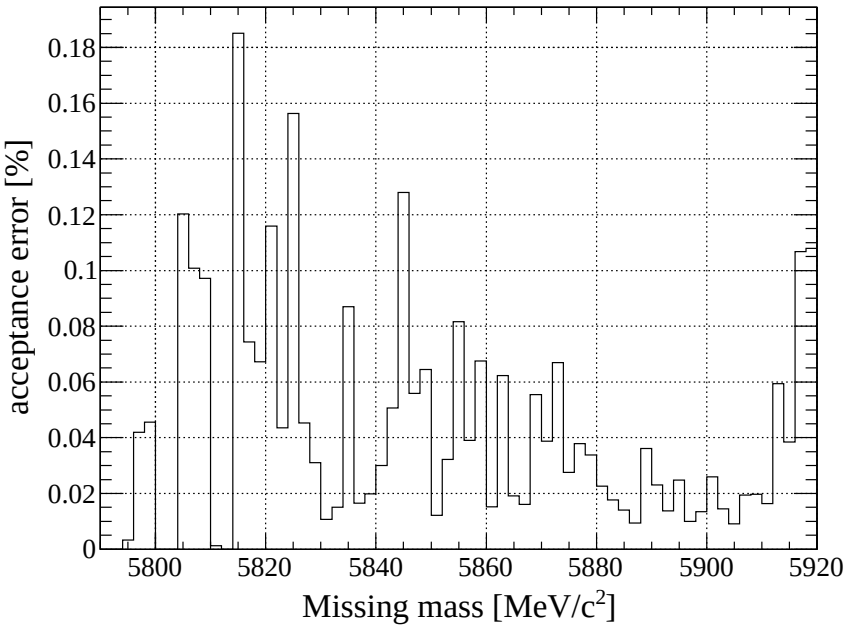

Figure 4.43: *The error of the acceptance table in each missing mass bin for the reaction angle of* 2°-4°.

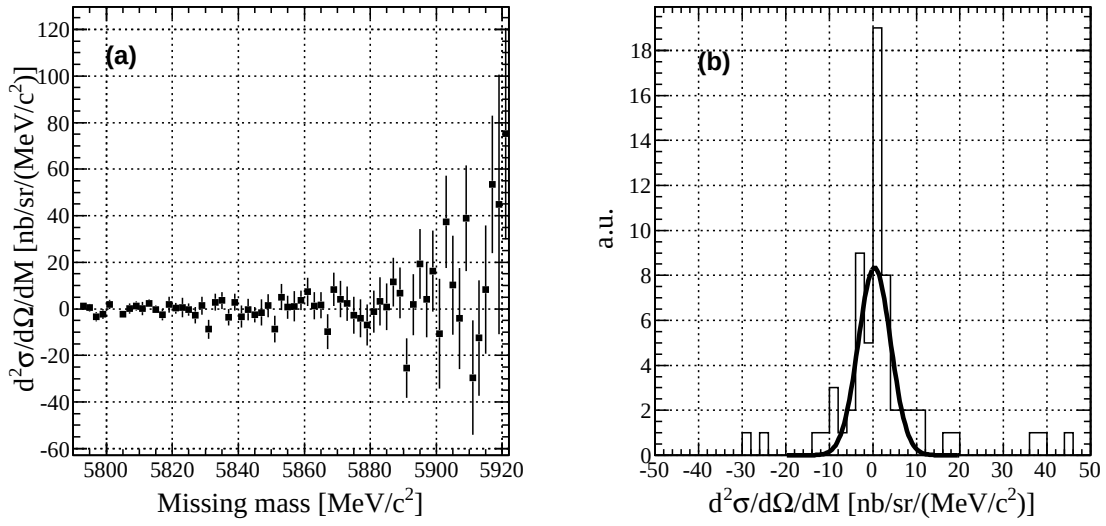

Figure 4.44: *(a) The difference between the cross section of the* $^6Li(\pi^-, K^+)X$ *reaction for scattering to the left and right between 2-4 degree. (b) Its production to the y axis.*

Table 4.7: *The summary of the background level.*

Background [nb/sr/(MeV/c^2)]					
2°-4°	4°-6°	6°-8°	8°-10°	10°-12°	12°-14°
0.9±0.2	0.5±0.1	0.7±0.1	0.7±0.1	0.7±0.1	0.6±0.1

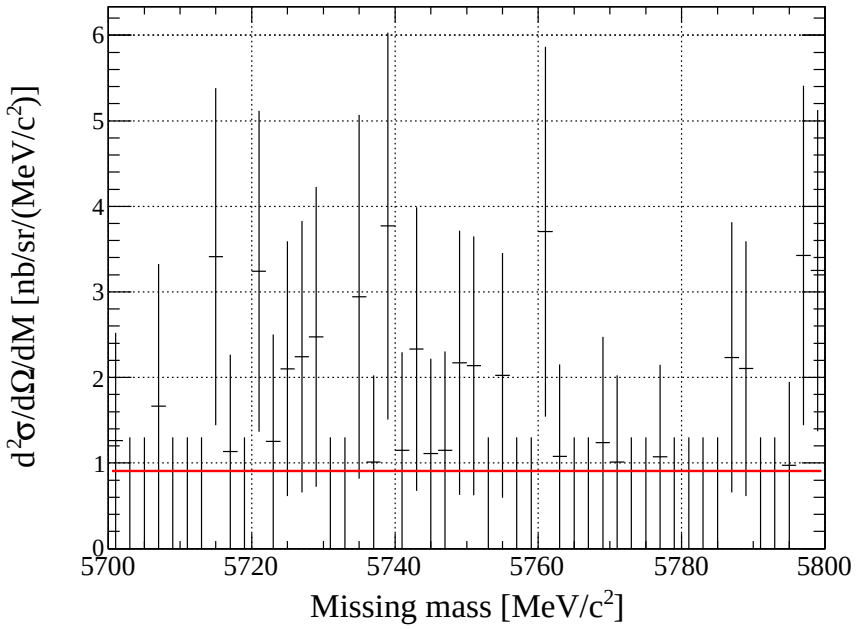

Figure 4.45: *The spectrum corresponding to the over bound region with respect to the expected mass of* ${}^{6}_{\Lambda}H$ *at the reaction angle of* 2-4 *degree.*

4.7.14 Background

As described in the section 4.4, there is the unknown constant background in the mass square distribution. It is difficult to extract the realistic shape of the background. Therefore, the background is estimated using the spectrum in the over bound region with respect to the expected mass of ${}^{6}_{\Lambda}$H by assuming that the background is constant in all the missing mass region. Figure 4.45 shows the missing mass spectrum corresponding to the over bound region for the reaction angle of 2°-4°. The background is ∼0.7 nb/sr/(MeV/c^2) typically by fitting the spectrum with a constant function. Background levels are summarized in Table 4.7. The error comes from the fitting error.

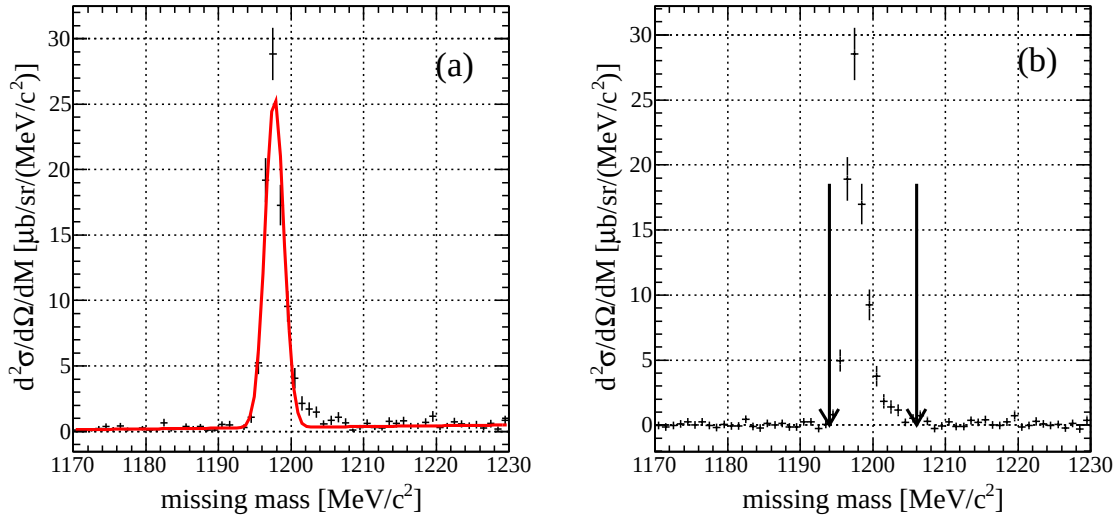

Figure 4.46: *The spectrum for the $\pi^- p \to K^+\Sigma^-$ reaction fitted with a Gaussian and the background function (a). The spectrum after subtracting the background (b).*

4.7.15 The production cross section of $\Sigma^{\pm}$

In order to confirm the validity of our experiment and the analysis method, the production cross section of $\Sigma^{\pm}$ is derived and compared with the past experimental data. The present experimental data are taken with the beam momentum of 1.37 GeV/c using the polyethylene target. A contribution from carbon, which exists in the polyethylene target, becomes a background in the missing spectrum. By fitting the spectrum with a Gaussian and the background function, the background component is subtracted as shown in Figure 4.46. The differential cross section for each reaction angle is obtained by integrating the spectrum. The production cross section of Σ^- via $\pi^- p \to K^+\Sigma^-$ at the beam momentum of 1.37 GeV/c in the CM system is shown in Figure 4.47 with other experimental data [73] [74]. In the Figure 4.47, the past experimental data taken with the beam momentum of 1.275 and 1.325 GeV/c are shown with open triangles and closed triangles, respectively. In addition, another experimental data taken with the momentum of 1.5 GeV/c is shown with open circles. On the other hand, the production cross section of Σ^+ via $\pi^+ p \to K^+\Sigma^+$ at 1.37 GeV/c in the CM system is shown in Figure 4.48. Past experimental data taken with the beam momentum of 1.37 GeV/c [72] are also plotted in Figure 4.48. The production cross section of Σ^+ obtained in the present experiment is well consistent with the past experiment [72]. On the other hand, it is obvious that the quite highly precise data on the production of Σ^- is obtained comparing to those of past experiments.

The production cross section of $\Sigma^{\pm}$ in the Lab. system is shown in Chapter 5.

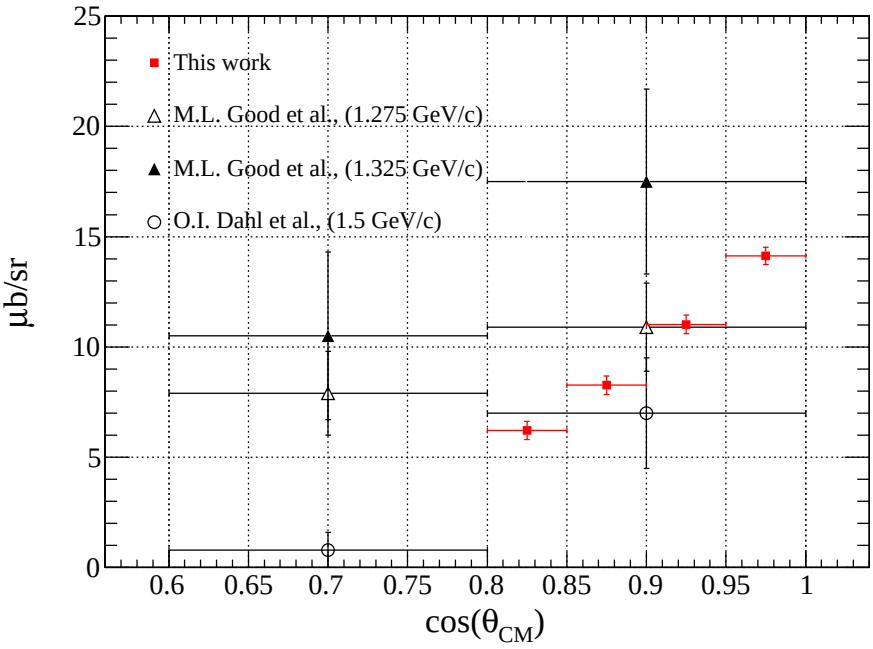

Figure 4.47: *The production cross section of Σ^- via $\pi^- p \to K^+\Sigma^-$ in the CM system at 1.37 GeV/c. Data in the reference [73] are shown with open triangles and closed triangles. Data in the reference [74] is shown with open circles.*

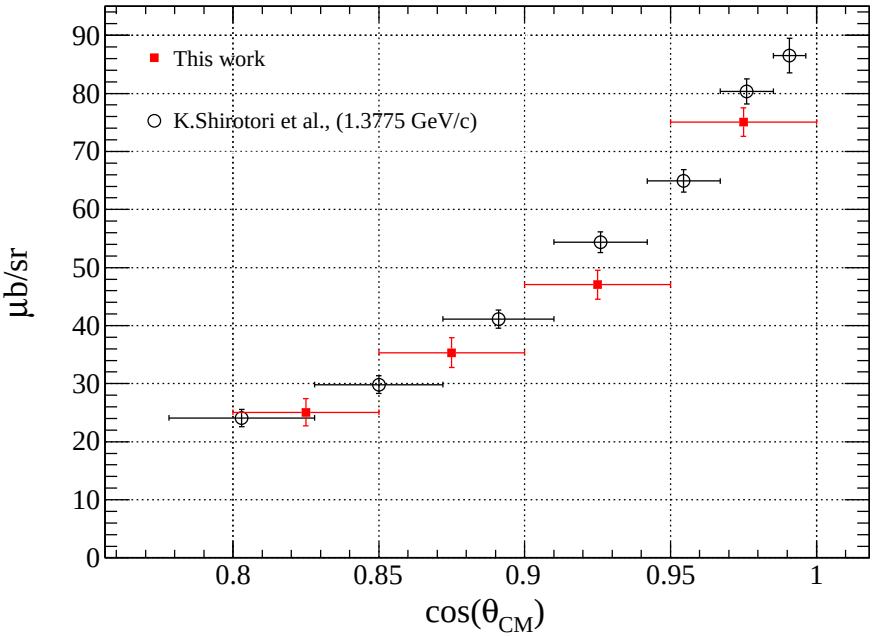

Figure 4.48: *The production cross section of Σ^+ via $\pi^- p \to K^+\Sigma^-$ in the CM system at 1.37 GeV/c. Data in the reference [72] are shown with open circles.*

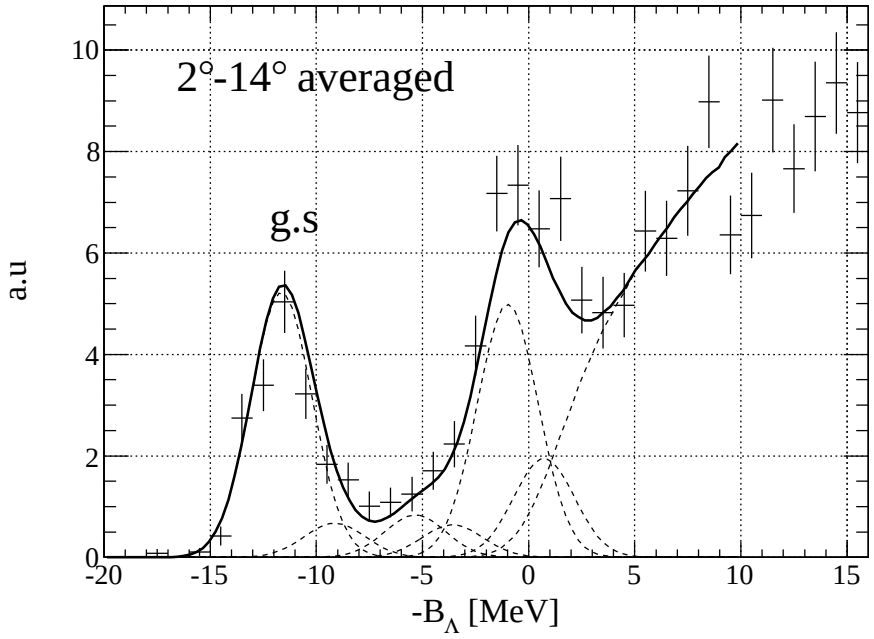

Figure 4.49: *The spectrum for the* ^{12}C(π^+, K^+) *reaction and fitting functions.*

4.7.16 Ambiguity of the absolute mass

In this section, an error of the absolute missing mass is estimated using the spectrum of $^{12}_{\Lambda}$C, which does not participate in the calibration process. This data is taken with the beam momentum of 1.2 GeV/c via the (π^+, K^+) reaction using the graphite target. The error includes all ambiguities such as the energy loss estimation and momentum calibration functions. The spectrum averaged over the reaction angle of 2°-14° is prepared to be fitted. The fitting is performed by using six Gaussian and the convoluted $\sqrt{E}$ function, which represents the quasi-free production. Relative height and relative peak position of Gaussian are fixed according to the past experimental data [42]. Hence, there are four free parameters, that is, height, mean, and σ of the first Gaussian, and a scale factor of the $\sqrt{E}$ function. The fitting result is shown in Figure 4.49. The peak position of the first Gaussian is determined to be -11.6 MeV. Since the binding energy of the ground state of $^{12}_{\Lambda}$C is -10.76 MeV [70], the total error of the missing mass is ±0.9 MeV.

4.7.17 Missing mass resolution

The missing mass resolution for the g.s. peak of $^{12}_{\Lambda}$C is simultaneously obtained from the fitting result described in the section 4.7.16. The obtained missing mass resolution is 3.4 MeV/c^2 (FWHM). Since the purpose of this analysis is not a peak search, the precise estimation of the mass resolution is unnecessary. Furthermore, we will discuss the Σ-nucleus potential with an order of 10 MeV. The obtained value of 3.4 MeV/c^2 (FWHM) is sufficient for the present discussion; therefore, it is adopted as the missing mass resolution for the ^{6}Li(π^-, K^+)X reaction for every reaction angle in the present analysis.

Chapter 5

Experimental result

5.1 Spectra of the ^{6}Li(π^-, K^+)X reaction

In the present experiment, the total number of pions injected is 1.7×10^{12}. The number of kaons analyzed to derive the cross section is 2.5×10^4. In this chapter, the experimental results obtained from all the data taken in the experimental period are reported.

5.1.1 Spectra for every 2 degree

The ^{6}Li(π^-, K^+)X missing mass spectra obtained for every 2 degree between 2 to 14 degree are shown in Figure 5.1 in the double-differential cross section in the mass range of 5790-5920 MeV/c^2. The enlarged view of them below the Σ-binding threshold are also shown in Figure 5.2 with the background function. The dashed line in each spectrum represents the background level obtained in Section 4.7.14. The qualities of spectra are summarized in Table 5.1.

Table 5.1: *The summary of qualities of spectra.*

Angle (deg)	Cross section err.(%)	Energy err. (MeV)	Mass resolution FWHM (MeV/c^2)	Background (nb/sr/(MeV/c^2))
2-4	$^{+4.1}_{-6.1}$	±0.9	3.4	0.9±0.2
4-6	±4.7	±0.9	3.4	0.5±0.1
6-8	±4.4	±0.9	3.4	0.7±0.1
8-10	±4.4	±0.9	3.4	0.7±0.1
10-12	±4.3	±0.9	3.4	0.7±0.1
12-14	±4.3	±0.9	3.4	0.6±0.1
2-14	±4.5	±0.9	3.4	0.43±0.04

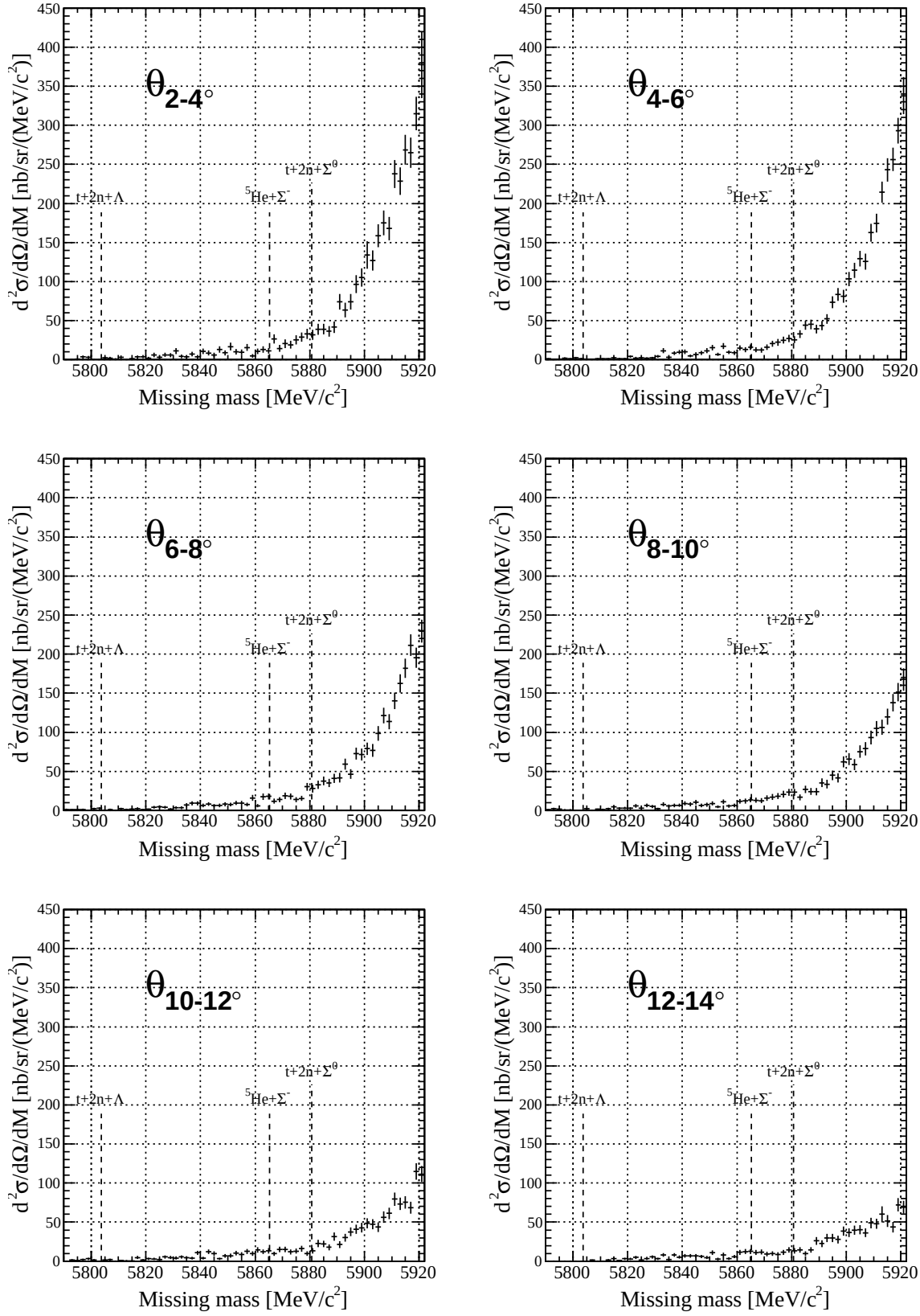

Figure 5.1: *Spectra for the* $^6\mathrm{Li}(\pi^-, K^+)X$ *reaction in the mass range of 5790-5920 MeV/c*^{2}.

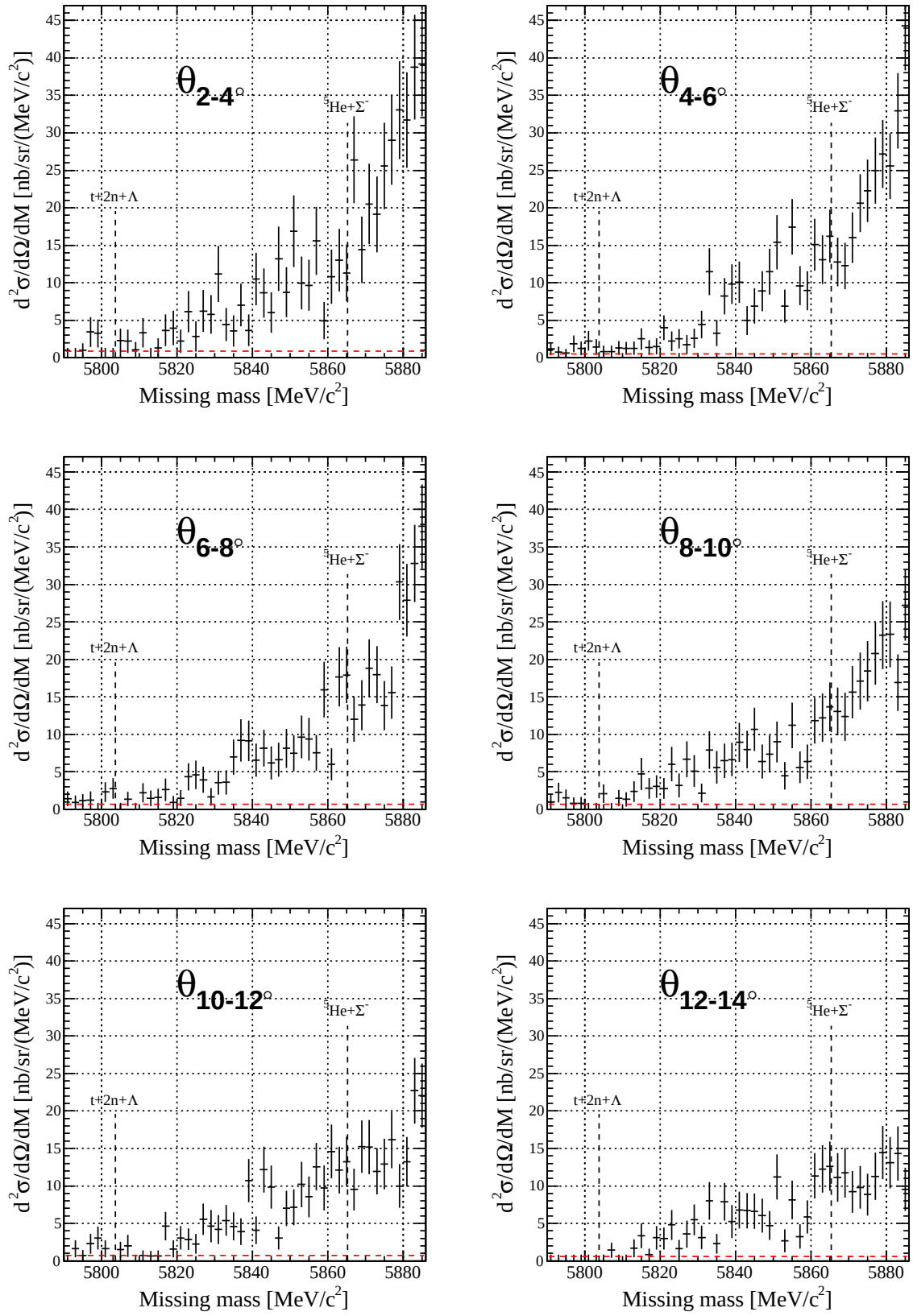

Figure 5.2: *The enlarged view of spectra for the* ^{6}Li$(\pi^-, K^+)X$ *reaction below the* Σ*-binding threshold.*

5.1.2 Angle-averaged spectrum

The spectrum averaged over the reaction angle of 2-14 degree and its enlarged view below the Σ-binding threshold are shown in Figure 5.3 (a) and Figure 5.3 (b), respectively. The qualities of the averaged spectrum are also summarized in Table 5.1.

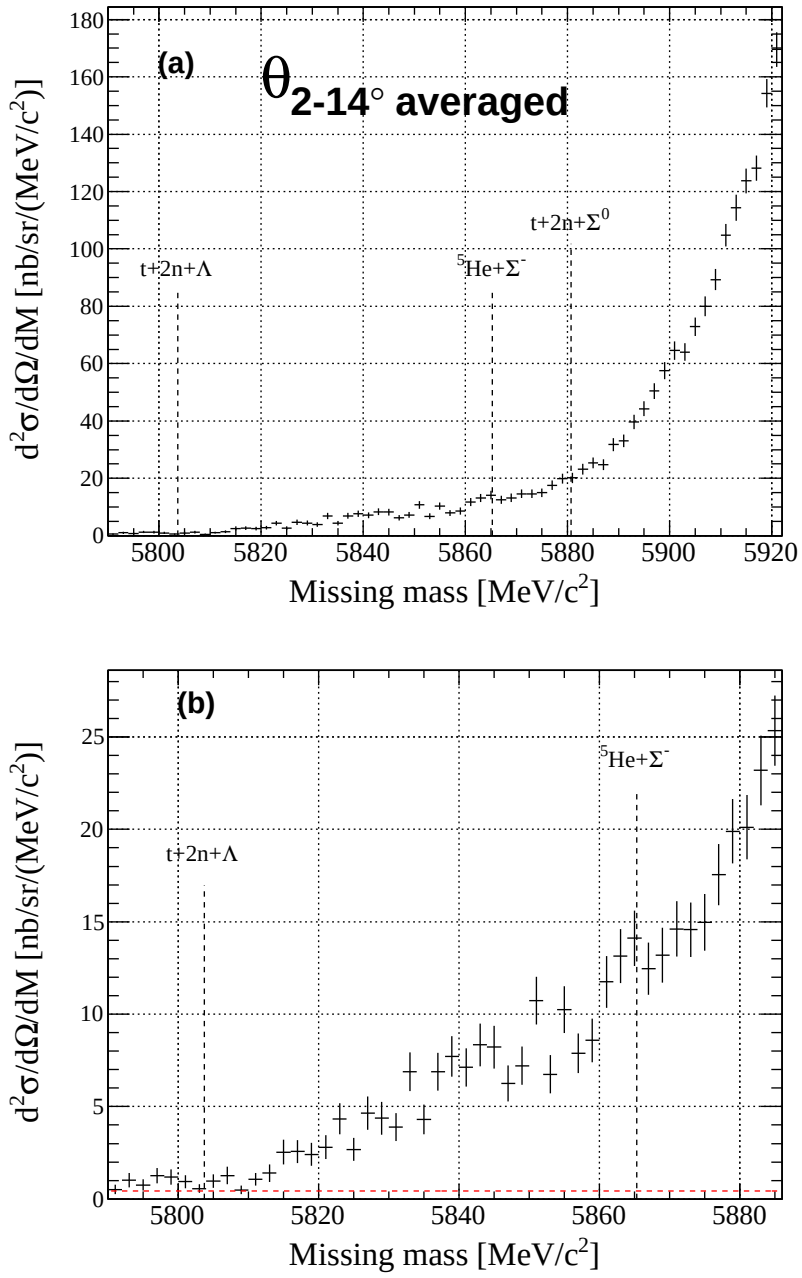

Figure 5.3: *(a) The angle-averaged spectrum for the* ^{6}Li$(\pi^-, K^+)X$ *reaction. (b) Its enlarged view below the Σ-binding threshold.*

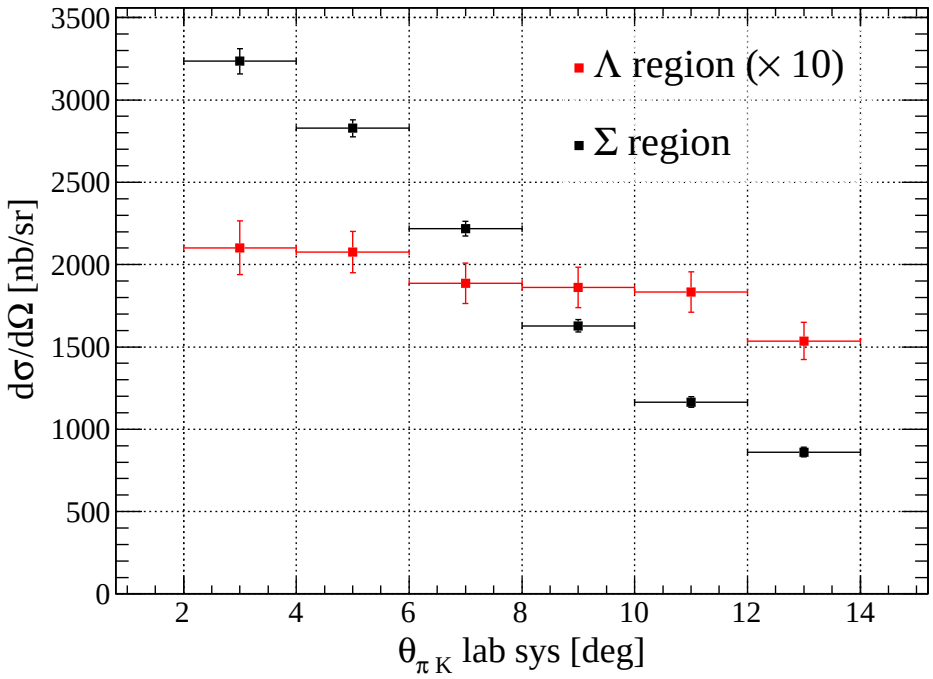

Figure 5.4: *The angular distribution of the production cross section of the* $^{6}\mathrm{Li}(\pi^{-}, K^{+})X$ *reaction in the* Λ *region and the* Σ *region.*

5.1.3 Integrated production cross section

The production cross sections, which integrate events lying in the Λ region and the Σ region, are shown in Figure 5.4 as a function of the reaction angle. The Λ and Σ region are defined as follows.

Λ region
The region between the mass of $t + 2n + \Lambda$ and $^{5}\mathrm{He} + \Sigma^{-}$.

Σ region
The region between the mass of $^{5}\mathrm{He} + \Sigma^{-}$ and 5920 MeV/c^2.

The cross section in the Λ region are multiplied by 10.

5.2 Production cross section of $\Sigma^{\pm}$

The production cross section of $\Sigma^{\pm}$ via $\pi^{\pm}p \to K^{+}\Sigma^{\pm}$ at the beam momentum of 1.37 GeV/c in the Lab. system are shown in Figure 5.5 as a function of the reaction angle.

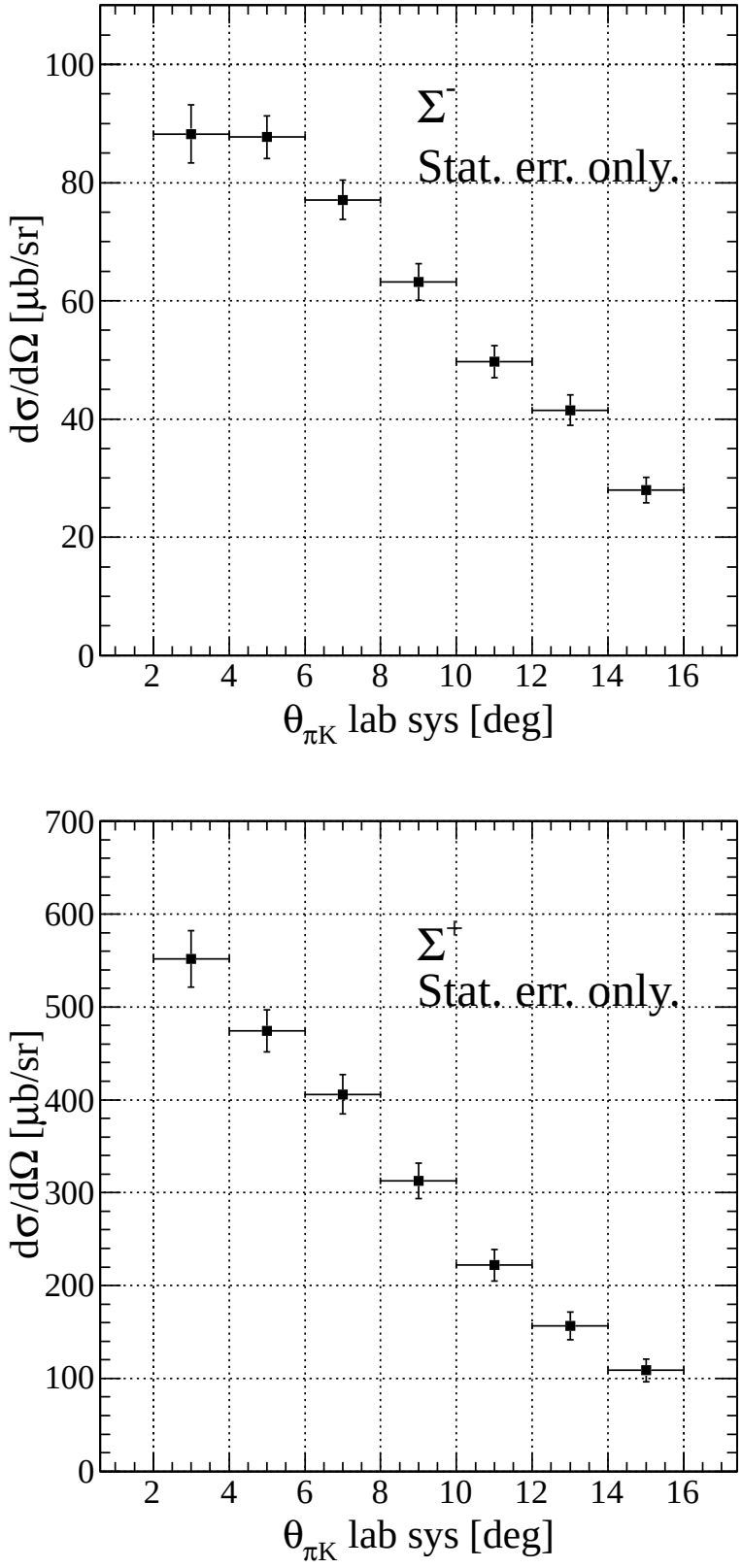

Figure 5.5: *The production cross section of* $\Sigma^{\pm}$ *via* $\pi^{\pm}p \to K^{+}\Sigma^{\pm}$ *in the lab. system at the beam momentum of 1.37 GeV/c.*

Chapter 6

Discussion

As described in Chapter 5, we obtained the double-differential cross section of the ^{6}Li(π^-, K^+)X reaction between the mass range of 5790-5920 MeV/c^2 at the beam momentum of 1.2 GeV/c, together with the production cross section of $\Sigma^\pm$ via $\pi^\pm p \to K^+\Sigma^\pm$ at the beam momentum of 1.37 GeV/c. The quality of our spectra of the ^{6}Li(π^-, K^+)X reaction is quite high because of the good missing mass resolution of 3.4 MeV/c^2, the wide momentum acceptance of the SKS system, and the high statistics. Especially, the number of pions irradiated (1.7×10^{12}) is larger than that of any past experiments at present. Then, two types of spectra for the ^{6}Li(π^-, K^+)X reaction, that is, six spectra for every 2 degree and the angle-averaged spectrum were able to be made owing to the high statistics. This is the first data to lead to the precise analysis, which simultaneously discuss the real and imaginary part of the ΣN interaction in nuclei. The obtained spectra have no narrow structure in the entire mass region. This is natural because the bound states of Σ-hypernuclei have already been excluded for various mass numbers except for $^4_\Sigma$He by past experimental and theoretical studies [21] [75]. In addition, any peak structure has not been observed around the Λ-binding threshold either.

In order to extract information on the ΣN interaction from such continuum spectra without a peak structure, theoretical help is essential to analyze the shape of the spectra. We analyze our spectra using the theoretical calculation by T. Harada [76]. The production cross sections are calculated in the framework of DWIA using the Green's function method describing all the Σ-nucleus states [78]. In the present calculation, the one-step process only is considered as the production process of the Λ continuum and the Λ hypernucleus. The meson-distorted waves are given by the eikonal approximation. The details of this calculation is explained in Appendix C. In the calculation, the Σ-nucleus potential is assumed to have the WS form as

$$U^\Sigma = (V_0^\Sigma + iW_0^\Sigma \cdot g(E_{ex}))/[1 + \exp(r - R)/a]. \tag{6.1}$$

Here, V_0^Σ and W_0^Σ represent the strengths of the real and imaginary parts of the potential; the imaginary potential describes the absorption of a Σ particle in nuclei due to the $\Sigma N \to \Lambda N$ conversion. Since the spreading imaginary potential represents the exited states of Λ-hypernuclei, the energy-dependent function, $g(E_{ex})$, which linearly increases from the Λ-binding threshold to the Σ-binding threshold, is multiplied in order to describe the state width. The parameters R and a are chosen to be $R = 1.1(A-1)^{1/3}$ fm $= 1.9$ fm and $a = 0.67$ fm, respectively. Although it is known that the ^{6}Li nucleus is well described by α-d clusters, the core nucleus wave function is assumed to be spherical for the sake of simplicity.

We describe shape analysis of our spectra using the DWIA calculation results in this

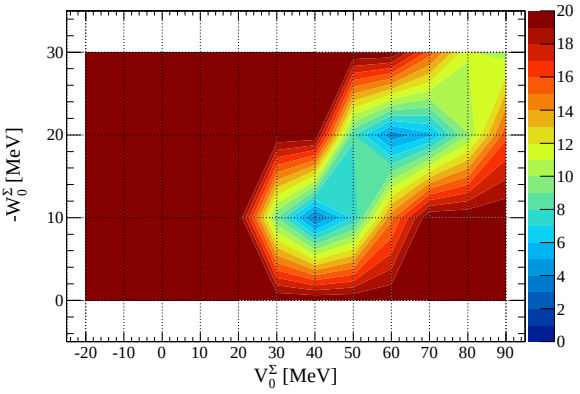

Figure 6.1: *The reduced χ^2 distribution for the fitting of the angle-averaged spectrum with the DWIA calculation results.*

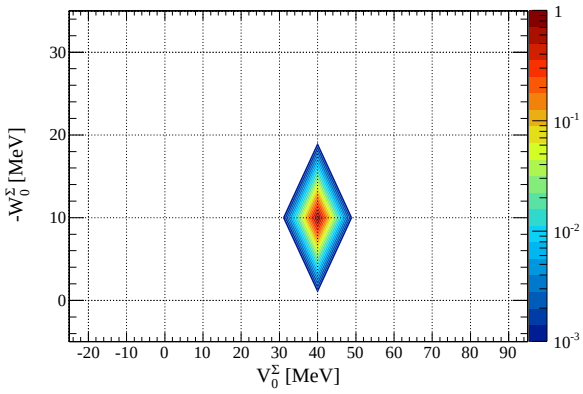

Figure 6.2: *The distribution of the relative goodness of fit for the angle-averaged spectrum.*

chapter. The determination of the strengths of the Σ-nucleus potential and the reaction mechanism of the neutron-rich hypernucleus via the (π^-, K^+) reaction will be discussed. In addition, the outlook for the future analyses and the future experiments are described.

6.1 Σ-nucleus potential

The best combination of $(V_0^\Sigma, -W_0^\Sigma)$ is searched for by the χ^2 fitting method using the cross section tables as a function of the missing mass calculated with several potential strengths. The strengths of $(V_0^\Sigma, -W_0^\Sigma)$ are changed by a 10 MeV step in the range of V_0^Σ from -20 to $+90$ MeV, and $-W_0^\Sigma$ from 0 to 30 MeV, respectively. In addition, the cross section tables of the missing mass spectra are made for every 2 degree of the reaction angle between 3 to 13 degree. In order to determine the optimal V_0^Σ and W_0^Σ values, our experimental spectra are fitted with calculation results with different V_0^Σ and W_0^Σ values. We consider V_0^Σ and W_0^Σ as fitting parameters while the absolute scale of the calculated cross section is not adjusted to fit the data because it is known that the DWIA calculation using the eikonal approximation can reproduce the absolute values of the production cross section of the Λ hypernuclei via the (π^+, K^+) reaction well [79].

6.1.1 Fitting the angle-averaged spectrum

In order to fit the angle-averaged spectrum, the cross section tables calculated every 2 degree are averaged by considering weight of the solid angle. The best-fit potential strengths for the angle-averaged spectrum are determined to be $(V_0^\Sigma, -W_0^\Sigma) = (40 \text{ MeV}, 10 \text{ MeV})$ as the result of the χ^2 fitting, where the reduced chi-square (χ^2/ndf) value is 3.58. Here, several calculation results with different potential strengths are simultaneously illustrated in Figure 6.3 and Figure 6.4. The five results calculated with different real potential strengths by fixing the imaginary part strength $(-W_0^\Sigma = 10 \text{ MeV})$ are shown in Figure 6.3. On the other hand, the imaginary part dependence is shown in Figure 6.4 at the real part strength $(V_0^\Sigma = +40 \text{ MeV})$. From these figures, it is understood that our experimental data have sensitivity to constraint to the real and imaginary parts of the potential and can exclude unfavored potentials with the present statistical error.

However, we can find another local minimum in the reduced χ^2 map shown in Figure 6.1, where χ^2/ndf values are represented with colors. The potential at the second local

minimum is $(V_0^\Sigma, -W_0^\Sigma) = (60 \text{ MeV}, 20 \text{ MeV})$ with $\chi^2/ndf = 4.29$. The probability at the second local minimum, $P(\chi^2/ndf \geq 4.29))$, is at least three-order of magnitude smaller than that of the best fit. Then, we adopt the potential $(V_0^\Sigma, -W_0^\Sigma) = (40 \text{ MeV}, 10 \text{ MeV})$ only as the result of the fitting.

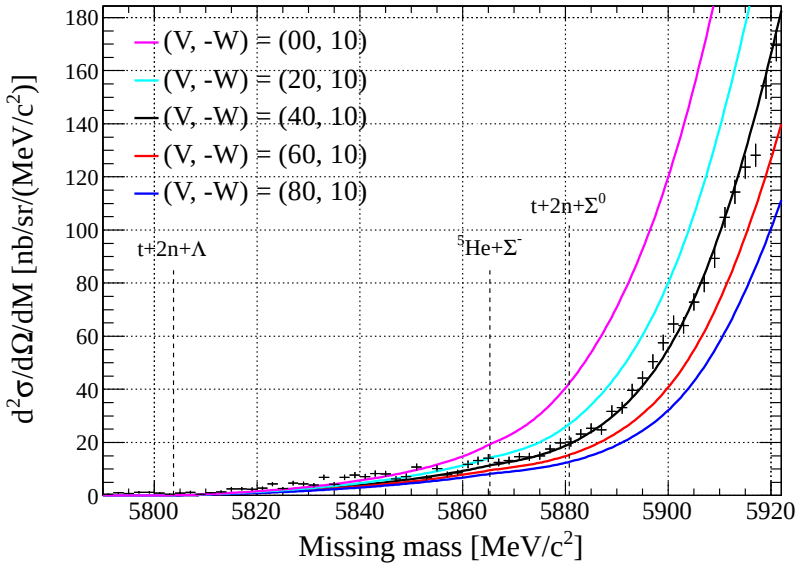

Figure 6.3: *The dependence on the real-part strength V_0^Σ for the calculated cross sections. [76]*

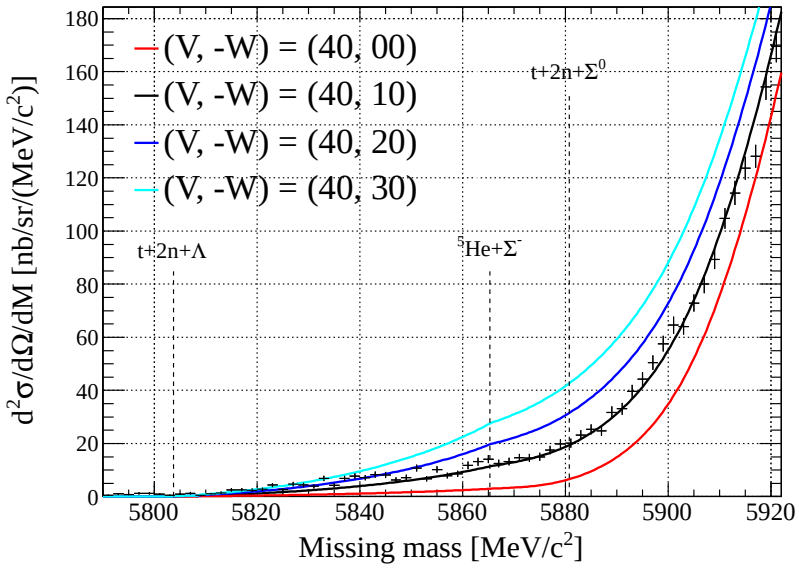

Figure 6.4: *The dependence on the imaginary-part strength W_0^Σ for the calculated cross sections. [76]*

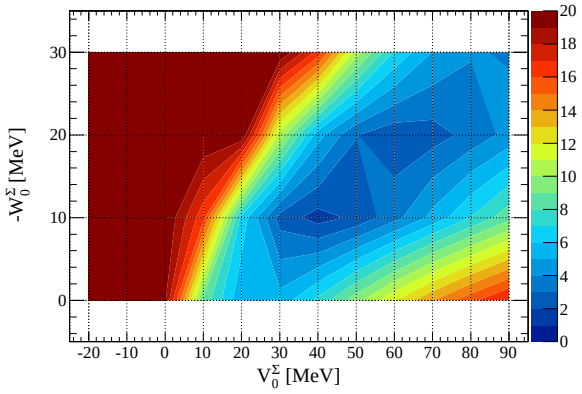

Figure 6.5: *The reduced χ^2 distribution for the fitting of six spectra obtained for every 2 degree.*

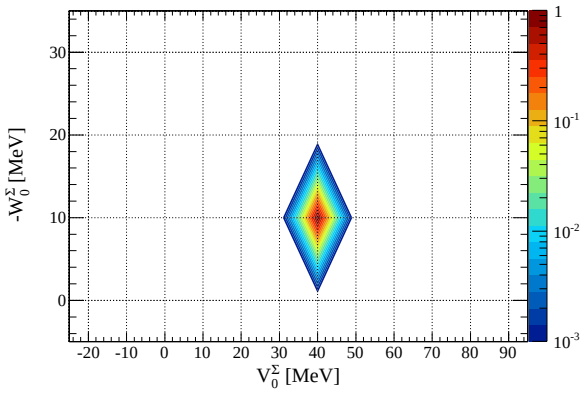

Figure 6.6: *The distribution of the relative goodness of fit for the fitting of six spectra obtained every for 2 degree.*

6.1.2 Fitting spectra for every two degree

A set of the six spectra for every 2 degree is one of the most important result in the present experiment. The optimal potential strengths are searched for by simultaneously fitting these spectra with the chi-square as the sum of contributions from all the spectra. The χ^2/ndf distribution is shown in Figure 6.5. Since the statistical error of each missing mass bin becomes larger than that of the angle-averaged spectrum, the reduced chi-square value is $\chi^2/ndf = 1.57$, being smaller than those shown in Figure 6.1. The position of the local minimum is not changed; the best-fit values are determined to be the same $(V_0^\Sigma, -W_0^\Sigma) = (40 \text{ MeV}, 10 \text{ MeV})$ as those obtained by the fitting of the angle-averaged spectrum. Although the second local minimum is still located at $(V_0^\Sigma, -W_0^\Sigma) = (60 \text{ MeV}, 20 \text{ MeV})$, this is also excluded because the relative goodness of fit is at least three order of magnitude smaller. Then, we can uniquely determine the optimal potential strengths as $(V_0^\Sigma, -W_0^\Sigma) = (40 \text{ MeV}, 10 \text{ MeV})$.

The calculation results with the potential of $(V_0^\Sigma, -W_0^\Sigma) = (40 \text{ MeV}, 10 \text{ MeV})$ are illustrated with the experimental data in Figure 6.7.

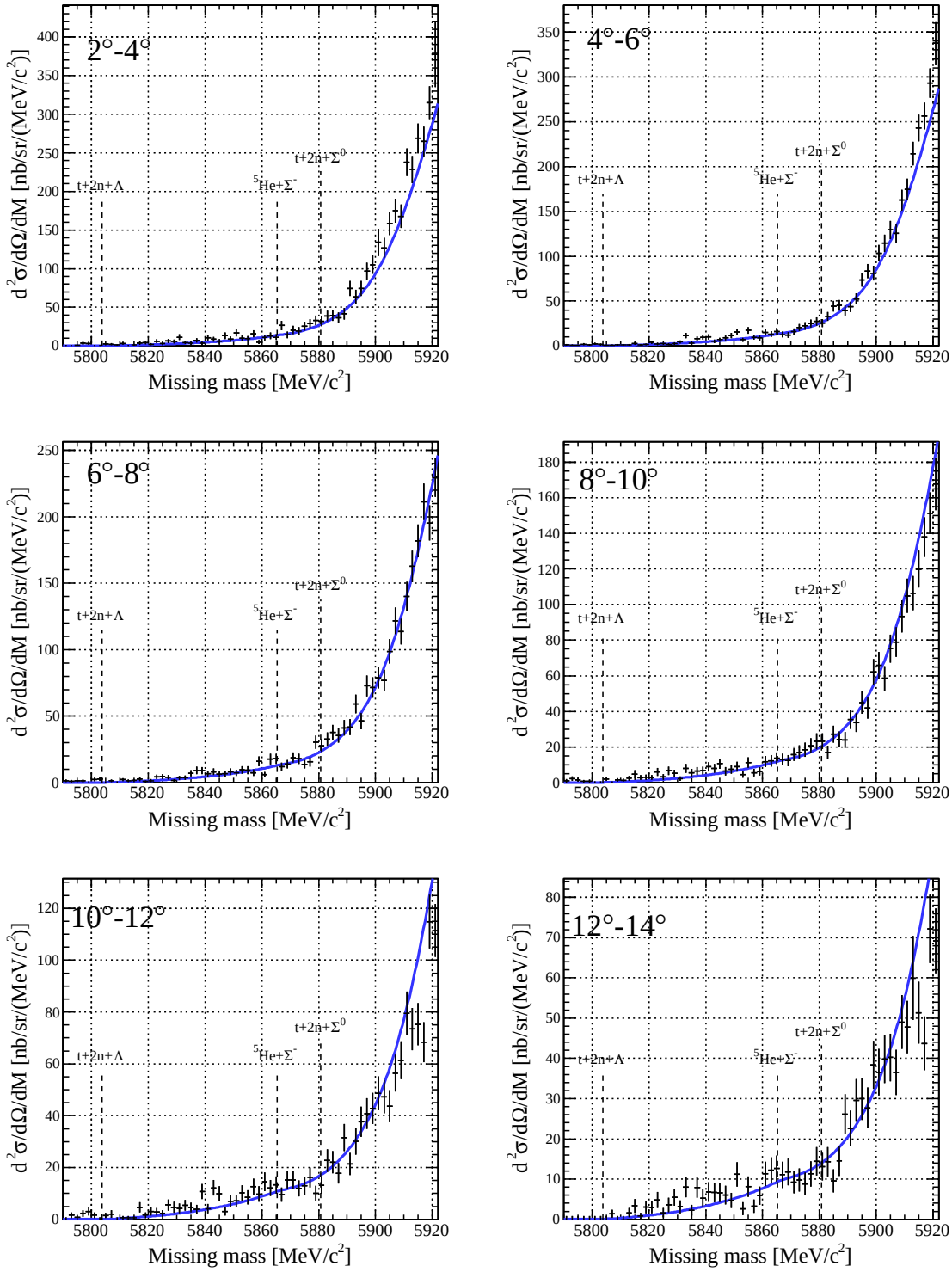

Figure 6.7: *Experimental results with the mass range of 5790-5920 MeV/c^2 with the theoretical calculation results with the potential of* $(V_0^\Sigma, -W_0^\Sigma)$ *= (40 MeV, 10 MeV).*

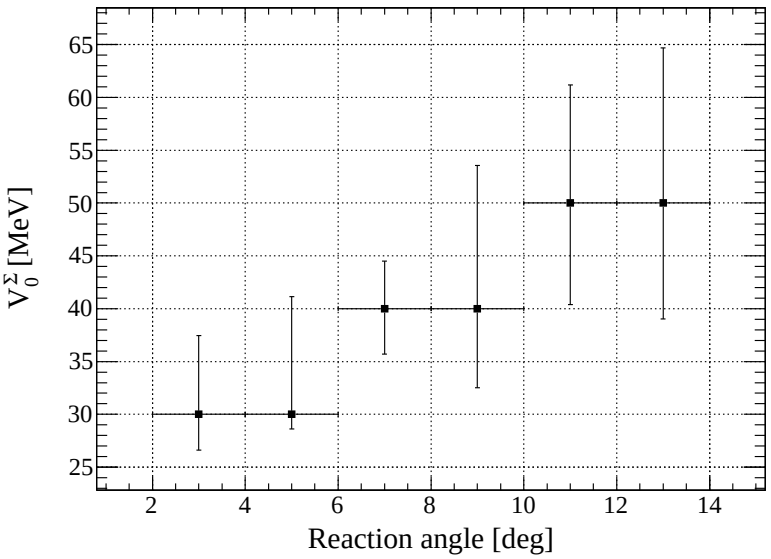

Figure 6.8: *The best-fit real-part potential strength as a function of the reaction angle. The "error" bars denote the range of* $\chi^2_{best}/ndf \pm 0.5$.

6.1.3 Individual fitting

The χ^2/ndf was defined as the sum of all contributions from spectra in the previous section. In contrast, we fit individually each spectrum in the next analysis. We find a tendency to favor more repulsive potential for the larger reaction angles from the χ^2/ndf distributions shown in Figure 6.9. Furthermore, the curvature of the chi-square valley in the large reaction angles is loose because of the statistical error larger than that of the spectrum for the forward angles. Then, several potential strengths, which cannot be excluded by relative goodness of fit shown in Figure 6.10, remain. However, we do not allow repulsion of the real part and absorption of the imaginary part stronger than $(V_0^\Sigma, -W_0^\Sigma) = (40$ MeV, 10 MeV) because this is unphysical. If the real part potential is more repulsive, the wave function of a Σ particle is pushed out from the core nucleus. Since the overlap between the Σ particle and the core nucleus should be decreased, the absorption cannot be stronger in such the situation.

If we fix the real part strength to +40 MeV, the imaginary part strengths are determined to be $-W_0^\Sigma = 10$ MeV for all the reaction angles. Then, we discuss the angle dependence of the real part strength in this section. In the present discussion, we set the "error" of the real part strength as the range of $\chi^2/ndf \pm 0.5$. Since this range corresponds to the case, in which the fitted curve leaves from the data by 1σ for a half of data points, we can clearly see a difference between the fitting curves and the data.

The best-fit curve and others are illustrated by the black lines and colored lines in Figure 6.11, respectively. In the present discussion, the best-fit potential strengths and its "errors" are obtained as shown in Figure 6.8 as a function of the reaction angle. It is found that the more repulsive potentials are favored in the larger reaction angles. The interpretation of these fitting results are given in the next section.

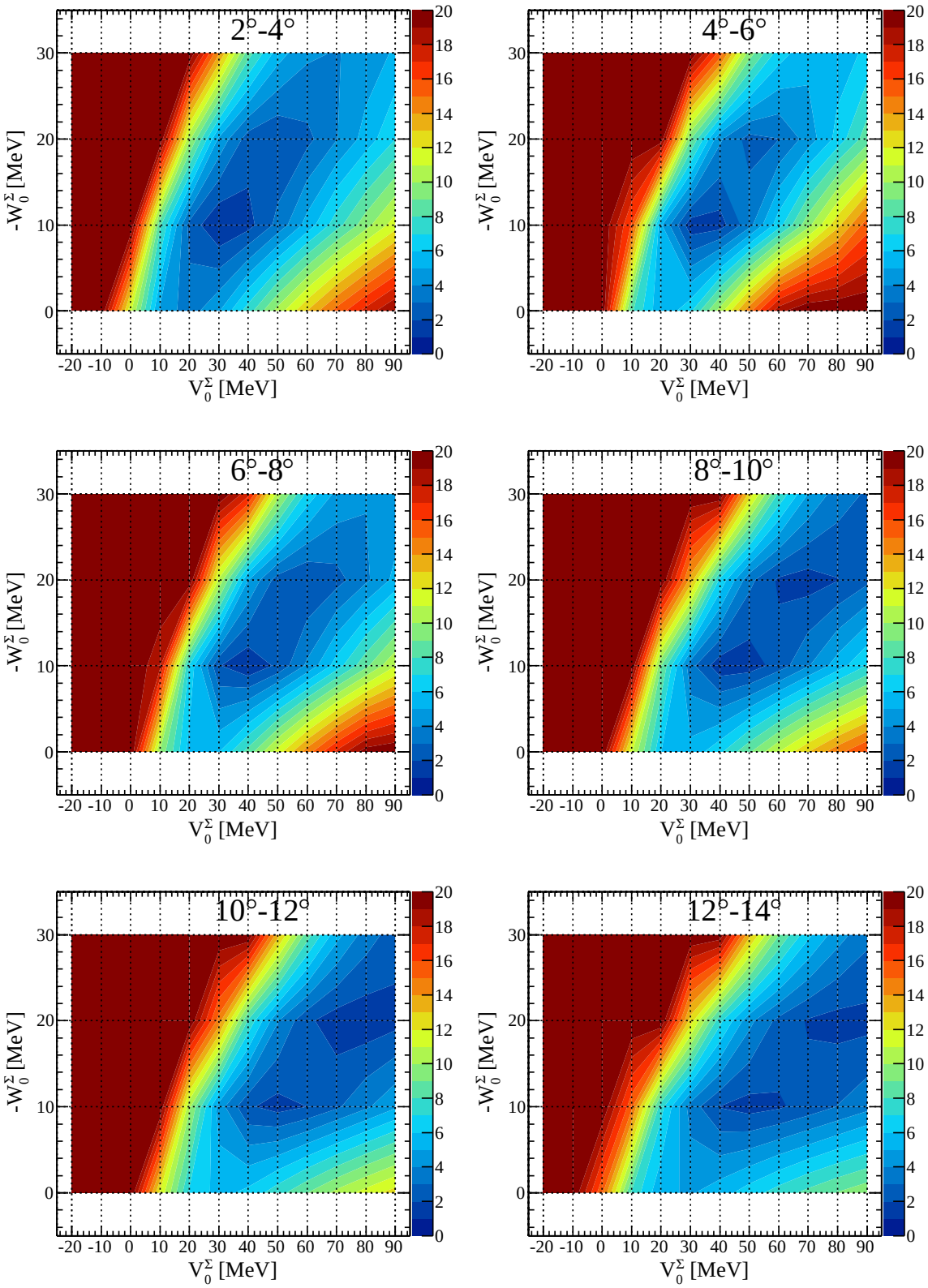

Figure 6.9: χ^2/ndf *distributions obtained from the fitting for each spectrum.*

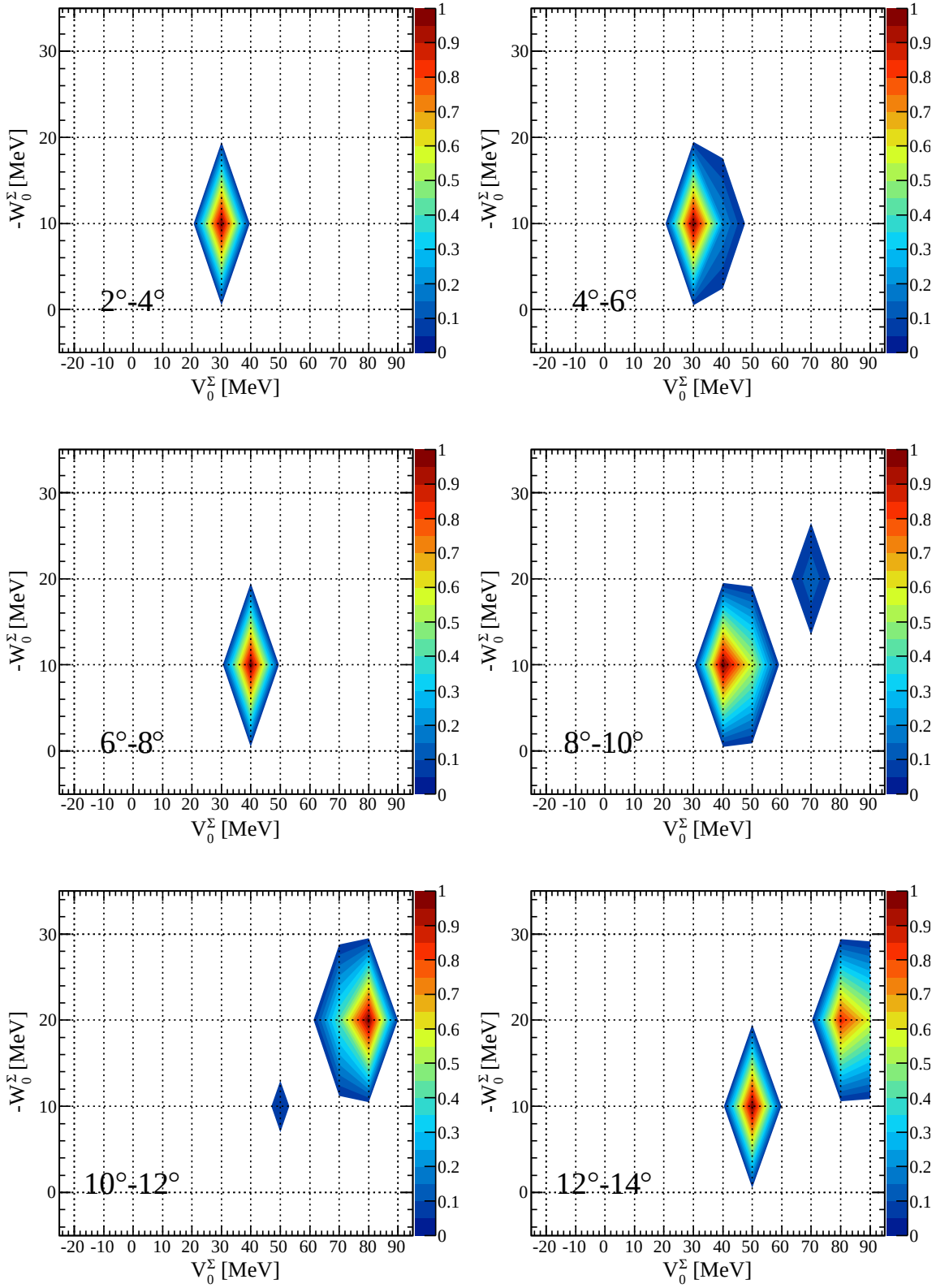

Figure 6.10: *Relative goodness of fit distributions obtained from the fitting for each spectrum.*

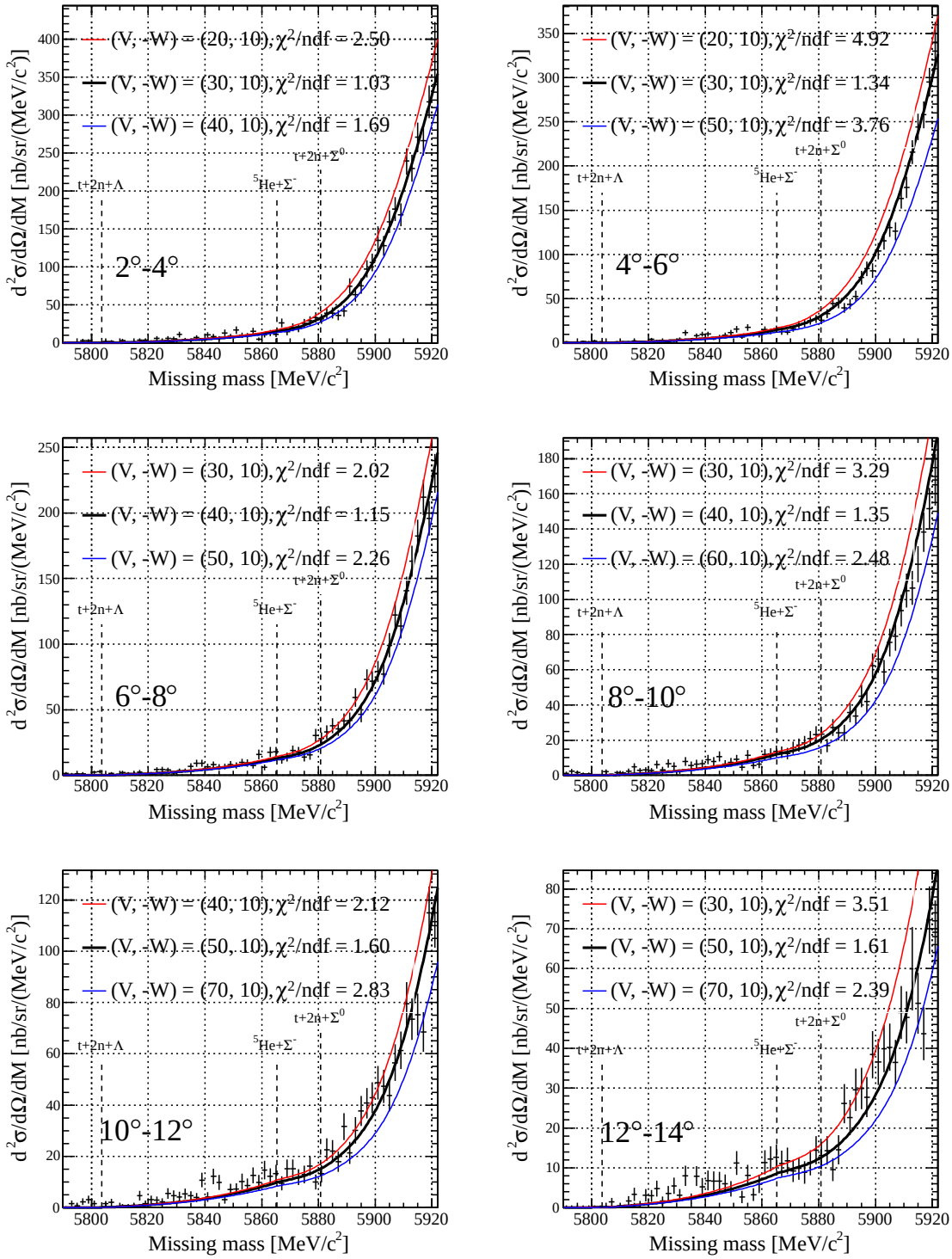

Figure 6.11: *The best-fit curves obtained by the fitting.*

6.1.4 Interpretation and outlook

The fitting of the angle-averaged spectrum

In the present discussion, the Σ-nucleus potential strength is determined to be $(V_0^\Sigma, -W_0^\Sigma)$ = (40 MeV, 10 MeV). The extracted strongly repulsive potential ($V_0^\Sigma = +40$ MeV) supports the recent two-body interaction model, ESC08 and fss2, summarized in the 1.2; the models give the repulsive Σ-nucleus potential as the result of the G-matrix calculation. In addition, the previous experimental data on the ^{28}Si(π^-, K^+)X reaction obtained in KEK-PS E438 were theoretically analyzed by using several types of potentials [77], and its best-fit potential strength was determined to be $(V_0^\Sigma, -W_0^\Sigma)$ = (30 MeV, 40 MeV) in the case of the WS form. Our experimental result is consistent with the previous study. On the other hand, the imaginary potential is rather small comparing with the case of ^{28}Si. This is understood as follows. The imaginary potential in the two-body system exists in the isospin state of 1/2 only. By introducing a Σ^- particle in the ^{6}Li nucleus by the (π^-, K^+) reaction, there are only 2 protons in the $\Sigma^- + 3n + 2p$ system, while in the case of ^{28}Si, 13 protons remain after producing a Σ^- particle. In addition, the nuclear density of ^{6}Li is smaller than that of ^{28}Si. The difference of protons density appears in the strength of the imaginary potential.

However, the WS form potential for light nuclei is not realistic because the charge distribution of nuclei does not follow to the WS distribution. Then, the present discussion cannot give a definite constraint to the models of the two-body interaction. In order to do it, a DWIA calculation from a few-body microscopic calculation is essential.

The individual fitting

The tendency that the more repulsive potentials are favored in the large reaction angles is found as the fitting result. If this tendency reflects the property of the ΣN interaction in nuclei, we may be able to extract information on the momentum dependence of the ΣN interaction. The recoil momentum of a Σ particle is increased from 520 to 590 MeV/c between 2 to 14 degree of the reaction angle. In addition, it is expected that the phase shift of the $(s = 1, t = 3/2)$ state of the two-body ΣN system becomes lager as a function of the momentum of a Σ particle [8]. Hence, this tendency may be related to the recoil momentum dependence of the phase shift of the $(s = 1, t = 3/2)$ state of the two-body ΣN system.

On the other hand, this tendency implies a problem in the present theoretical treatment. In the present calculation, there are several points which should be improved. One is the description of the angle-dependent Fermi-averaged t-matrix, which is constructed for the first time in the present calculation [76]. (see Appendix C). Since the experimental data on $\pi^- p \to K^+\Sigma^-$ to make the Fermi-averaged t-matrix is still limited, and especially the angular distribution in the forward angles is never reported, the angle-dependent Fermi-averaged t-matrix has an ambiguity. The other is the wave function of the ^{6}Li nucleus. Although the core nucleus wave function is assumed to be spherical for the sake of simplicity, the ^{6}Li nucleus is known to be well described by $\alpha + d$ clusters. In addition, as described above, the WS form potential is not realistic in light nuclei. Such imperfections of the theoretical treatment may affect the tendency of the χ^2 distribution. Our experimental spectra obtained for every 2 degree could be a good test bench for theorists.

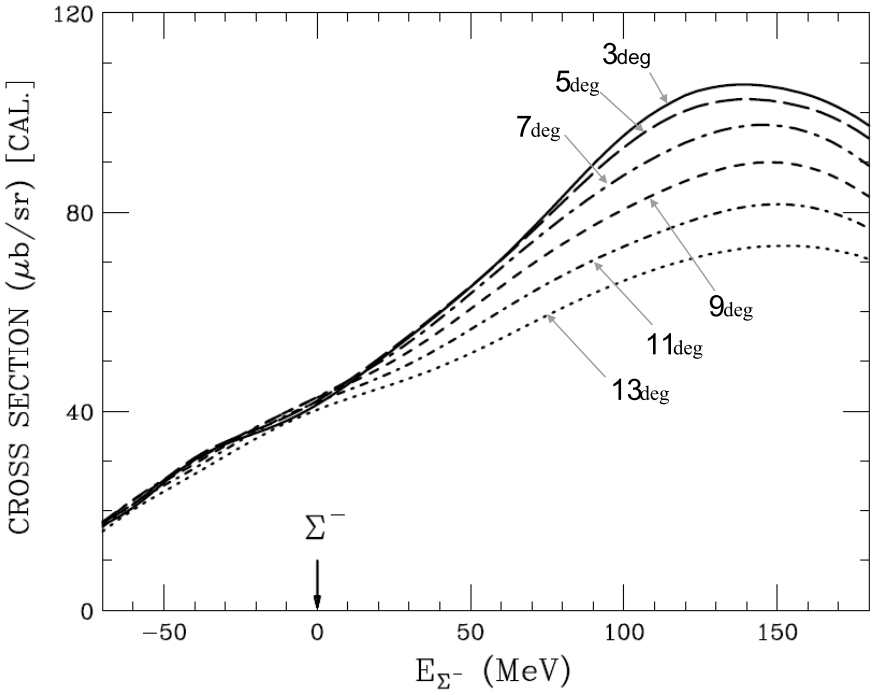

Figure 6.12: *The Fermi-averaged t-matrices as a function of the energy [76].*

6.2 Angular distribution of the integrated cross section

We reported the angular distribution of the integrated cross section for the Λ region and the Σ region in Chapter 5. The angular distribution of the Σ region is steep, which is similar to that of the elementary process $\pi^- p \to K^+\Sigma^-$ obtained in the present experiment. On the other hand, the angular distribution of the Λ region is flat. The difference of the angular distribution might be explained by the energy dependence of the Fermi-averaged t-matrix (see Appendix C) for each reaction angle. The amplitude of the Fermi-averaged t-matrices used in the present calculation are shown in Figure 6.12 as a function of the energy. The amplitude of every t-matrices has almost no difference below the Σ-binding threshold (at 0 MeV in the figure) while they have angle dependence over the threshold. We can consider that the angular distribution of the integrated cross section is originated from the property of the Fermi averaged t-matrices.

6.3 The production mechanism

In this section, we discuss the production mechanism of the neutron-rich Λ-hypernuclei via the (π^-, K^+) reaction. In the present understanding, we consider that the one-step process is favored in the production of neutron-rich hypernuclei via the (π^-, K^+) reaction because of the momentum dependence of the production cross section obtained in the KEK-PS E521 experiment [29]. The present spectrum seems to be well reproduced by the DWIA calculation via the one-step process. However, the Λ continuum region between 5810-5860 MeV/c^2 shown in the Figure 6.13 is underestimated by the result of the DWIA calculation through the one-step process. This implies that the contribution of the two-step process is

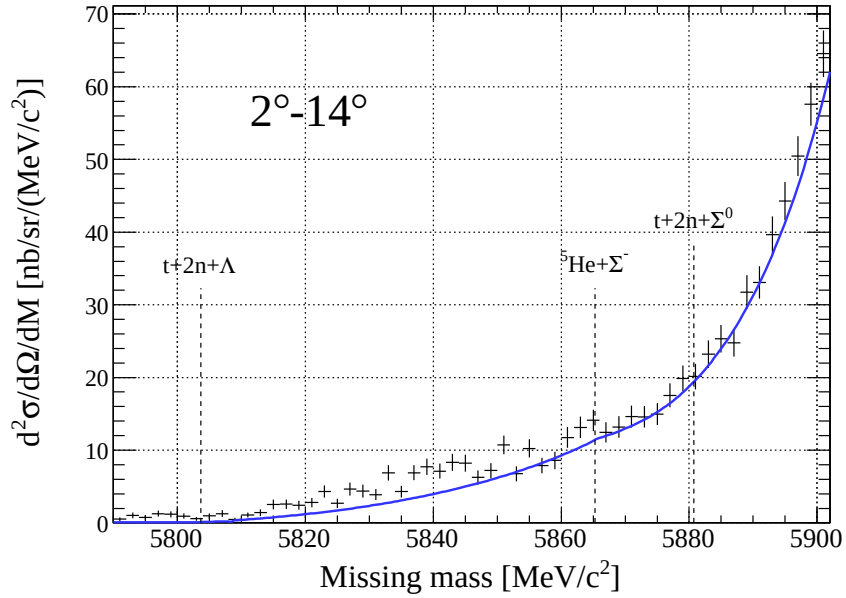

Figure 6.13: *The difference between the experimental data and the DWIA calculation [76] in the* Λ *continuum region.*

not negligible.

Here, it should be emphasized that we cannot conclude that the Λ-Σ coupling strength is small and inconsistent with the KEK-PS E521 result. In order to populate the hypernuclear state via the Σ^- doorway, a sufficient overlap between the wave functions of the nucleons and a Σ particle is important. In the present discussion, the Σ-nucleus potential in the case of the ^{6}Li target is repulsive. Therefore, the overlap should be decreased in the repulsive potential. In such a situation, the amplitude of the hypernuclear state disappears even if the coupling strength is sizable. Here, we conclude that the one-step process seems to be favored as well but the contribution from the two-step may be not negligible. On the other hand, the Λ-Σ coupling strength cannot be determined.

6.4 Outlook

Elementary cross section

The DWIA calculation of the hypernuclear cross section on nuclei is based on its elementary cross section such as $\pi^- p \to K^+\Sigma^-$. The cross sections for various beam momenta are necessary to construct the Fermi-averaged t-matrix as a function of the energy transfer. However, information on the elementary cross section of hyperon productions, especially, of $\pi^- p \to K^+\Sigma^-$, is limited. The measurement of its total and differential cross sections is a task for experimentalists using secondary meson beams.

Experiments via the (K^-, π) reaction

Since the momentum transfer of the (K^-, π) reaction strongly depends on the reaction angle, the data give us opportunities to investigate the s-wave Σ-nucleus potential and higher wave contributions separately by obtaining spectra for various reaction angles. In

the past experiments via the $(K^-_{stopped}, \pi)$, there is no angular dependence because the kaon is at rest. In addition, there is no experiments via the in-flight (K^-, π) reaction, which cover wide angles and give angular distribution of the cross section.

Recently, a γ-ray spectroscopy experiment using the in-flight (K^-, π^-) was proposed as the J-PARC E13 experiment. The experiment will be performed at the K1.8 experimental area using the SKS system and a liquid He target. Owing to the large acceptance of the SKS system, we can take data with the reaction angle up to 20 degree. Furthermore, a large amount of the reaction data will be obtained. Then, it is expected that this experiment will report angular dependence of the missing mass spectra for Σ production on ^{4}He by the (K^-, π^-) reaction.

Chapter 7

Summary

The understanding of the BB interaction in the flavor SU(3) symmetry is an important topic in hadron and nuclear physics. The study of the ΣN interaction is related to the quite strong repulsive core, which is suggested to appear in the ΣN ($s = 1, t = 3/2$) channel from Pauli blocking in the quark level by the quark cluster model [1].

Several models such as the Nijmegen models [7] and the Kyoto model [8] describing the BB interaction in $\mathrm{SU_f(3)}$ were proposed. However, there are large ambiguities in the parameters in those models because of lack of YN scattering data. Thus, the ΣN interaction was historically studied through the interaction between a Σ particle and nuclei. The two-body ΣN interactions are connected to the Σ-nucleus potential through the G-matrix calculation. The recent two-body interaction models suggest that the isospin-independent Σ-nucleus potential is strongly repulsive.

The Σ-nucleus potential is separated to the isospin independent term and the isospin dependent term (Lane's term) originated from the isospin dependence of the ΣN interaction. This term plays an essential role in light nuclei. The property of the Σ-nucleus potential in light nuclei strongly depends on the total isospin. On the other hand, the isospin independent potential is dominant in heavy nuclei. The theoretical analysis for the experiment using DWIA derived the strengths of the complex Σ-nucleus potential to be $(V_0^\Sigma, -W_0^\Sigma) = (30\ \mathrm{MeV}, 40\ \mathrm{MeV})$ by assuming the WS form.

The present experiment (J-PARC E10) was proposed to study the ΛN and ΣN interaction in the neutron excess environment in light nuclei. The purpose of this experiment is to obtain background-free missing mass spectra via the (π^-, K^+) reaction on ^{6}Li and ^{9}Be targets at the beam momentum of 1.2 GeV/c. As the first stage of this experiment, the ^{6}Li target run was carried out in 2012 to 2013. The experiment was performed at the K1.8 beamline in J-PARC with the SKS system. The π^- beams were analyzed by the K1.8 beamline spectrometer and outgoing kaons were measured by the SKS system. Owing to the wide momentum acceptance of the SKS system, we successfully obtained spectra not only for a part of the quasi-free Σ production region but also for the Λ continuum region. Since the production cross section below the Λ-binding threshold is small (order of nano barn), the large number of pion beam particles is essential in the present experiment. Hence, the new detector system, BFT and SFT, consisting of scintillation fibers and MPPCs are developed in order to handle high rate secondary beams. We succeeded in handling of the high intensity beam of 12 M pions/spill. In the present experiment, the total number of pions injected was 1.7×10^{12}. As the result, missing mass spectra of the $^6\mathrm{Li}(\pi^-, K^+)\mathrm{X}$ reaction with the mass range of 5790-5920 MeV/c^2 between 2-14 degree of the reaction angle were obtained with the missing mass resolution of 3.4 MeV/c^2 (FWHM). In addition, the $\Sigma^\pm$ production cross sections via $\pi^\pm p \to K^+\Sigma^\pm$ at the beam momentum

of 1.37 GeV/c between 2-16 degree were obtained. These are the first data that contains events of both of the Λ continuum and the quasi-free Σ production with small statistical errors. The number of pions irradiated on the target is much larger than that of past experiments. Our data leads to the precise analysis which simultaneously evaluates the real and imaginary parts of the Σ-nucleus potential.

The shape analysis is performed using the cross sections calculated in the DWIA framework by T. Harada [76]. The best-fit potential strengths are determined to be $(V_0^{\Sigma}, -W_0^{\Sigma})$ = (40 MeV, 10 MeV). The real part potential of $V_0^{\Sigma} = +40$ MeV is consistent with the past theoretical analysis of the KEK-PS E438 experiment [77]. The repulsive Σ-nucleus potential supports the results of the G-matrix calculation from the recent two-body interaction models. On the other hand, the strength of the imaginary potential (W_0^{Σ}) is small reflecting the density of protons in the core nucleus. As the result of the individual fitting for six spectra obtained for every 2 degree, the tendency that the more repulsive potentials are favored in the larger reaction angles is found. However, these analysis results are not conclusive because several points remain to be improved in the theoretical treatment, and then, further theoretical analysis is awaited.

Appendix A

Analysis of the fiber tracker

The basic analysis procedure routine for BFT and SFT are described in this appendix.

A.1 Time walk correction

In order to obtain the best timing resolution, the correction for a time walk is essential. In principle, the time walk is corrected using the correlation between ADC and TDC. However, the correction using ADC information is impossible in the present experiment because ADC cannot be used due to the pile-up of signals shaped by the slow shaper in EASIROC under the high counting rate condition. Fortunately, since the discriminator in EASIROC is an update type, the Time Over Threshold (TOT) information is alternatively used; TOT information is roughly related to the charge information. The correlation plot between TOT and the timing of one segment in BFT is shown in Figure A.1 (a). This distribution is fitted with a second-order polynomial and corrected as shown in Figure A.1 (b) segment by segment. The timing resolution of one segment before and after the correction are 1.5 and 1.0 ns (σ), respectively.

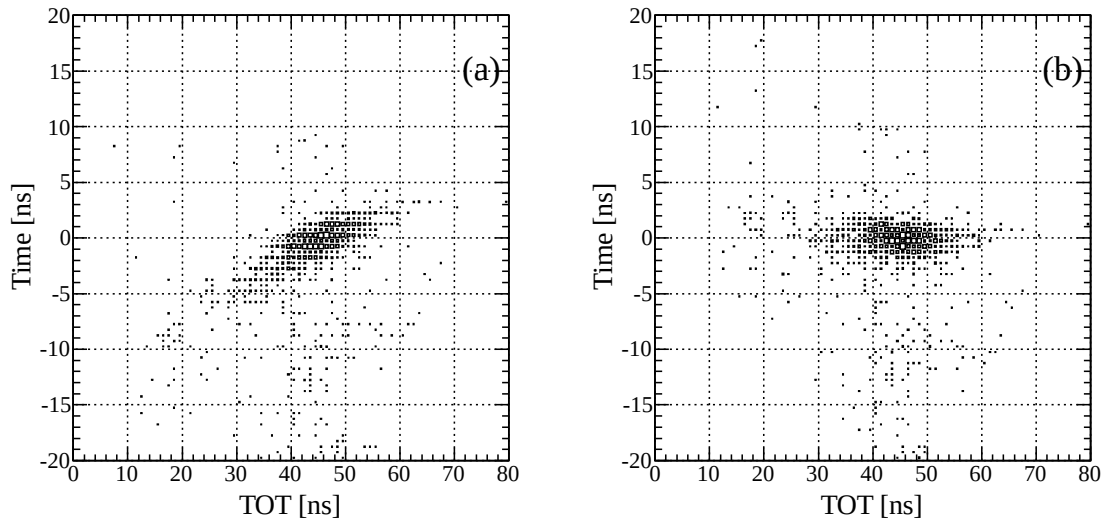

Figure A.1: *(a) The correlation between the timing and TOT of BFT before the correction. (b) The distribution after the correction.*

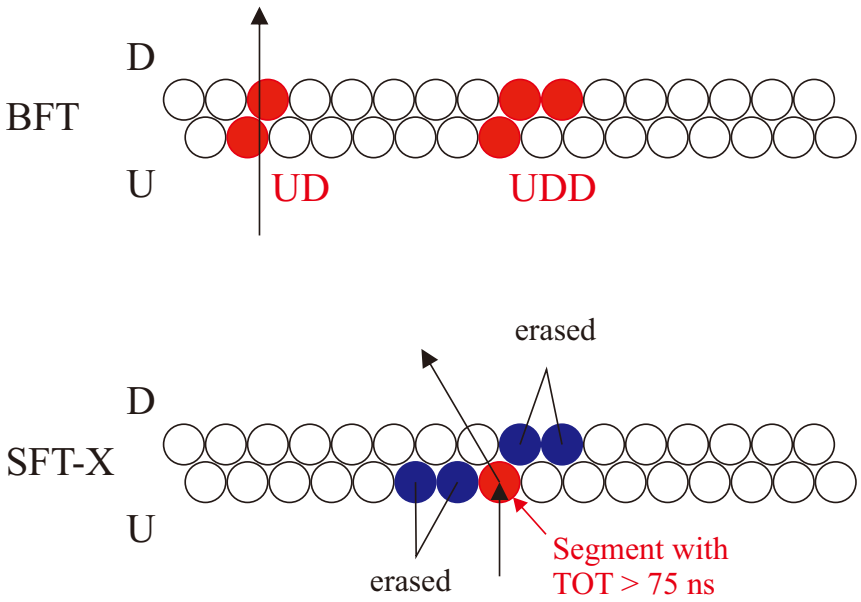

Figure A.2: *Clustering method for BFT and SFT-X. Red circles represent hit segment. Blue circles are erased when clustering for SFT-X.*

A.2 Clustering

Since scintillation fibers are arranged in a staggered position, a charged particle may pass through two fibers at the same time. In such the case, a hit is combined with neighbor hit, that is, the clustering. However, since the timing of each segment is measured by MHTDC, sometimes one segment has several hits. Then, a hit is recognized as belonging to a certain cluster when it is close to other hit not only spatially but also in terms of time. In order to check it, all possible combinations are examined. We describe the clustering method for BFT, SFT-X and SFT-UV.

BFT

There are two layers which are arranged in a staggered relation in BFT. These layers are labeled by U (up) and D (down). In an ideal case, the number of hits participating in a cluster should be 2 as shown in Figure A.2. Such a combination is represented using labels as UD or DU. However, since it is known that sometimes the number of hits becomes 3 or 4, the number of hits in a cluster is allowed up to 4. Then, unnatural combinations such as UDD, UDU or UDDD are allowed in the present analysis as shown in Figure A.2. The maximum timing difference allowed between hits to participate in a cluster is less than 8 ns.

SFT-X

Since the structure of SFT is the same as BFT, the clustering algorithm is similar to that of BFT. One difference is that reaction events occurred in SFT-X can be detected by the SKS system. In such the events, hits, whose TOT are quite large, exist with redundant hits around it as shown in Figure A.2. This situation is understood that the reaction is occurred in a segment with large TOT, and several charged particle are emitted. Then, if

such hit is found, redundant hits are erased as shown in Figure A.2.

The maximum timing difference allowed is the same as that of BFT.

SFT-UV

An clustering algorithm for SFT-UV is simple. Hits adjoining each other are combined when the timing difference between them is less than 10 ns.

A.3 Observable in a cluster

The calculation for the position and TOT in a cluster is simple. Positions of all hits are averaged, and a maximum TOT among hits is used as TOT of a cluster.

On the other hand, a timing which is most close to "zero" is selected as a timing of a cluster. The mean of timing "zero" is equivalent to the definition of the time zero of BH1·2. The purpose of the fiber tracker system is not to measure the time-of-flight but to identify particle causing a reaction with a better signal-to-noise ratio. Hence, not an averaged timing but the timing which is close to zero is adopted as the timing of a cluster in order to improve the timing resolution.

Finally, the timing resolution reported in Chapter 4 are obtained.

A.4 TOT gate

High noise rate is one of disadvantages of pixelated photon detectors comparing with that of PMT. In the case of MPPC, the dark noise rate is typically 0.5∼1 MHz. Noise type of MPPC are classified as follows.

Dark noise (thermal noise)
: An electron-hole pair created by a thermal excitation makes an avalanche. Since the thermal excitation is randomly occurred, amplitude of a noise signal should be equal to 1 photoelectron. Then, it is considered that dark noise of which amplitude is more than 1 p.e. are caused by the optical cross talk.

After pulse
: After pulse is an avalanche which is occurred after a several tens of nano-seconds from a previous avalanche in a same pixel or a neighbor pixel. Nowaday, the cause is understood as follows. By-product photons produced in the previous avalanche are absorbed and create e-h pairs in the bulk region of a semiconductor. These pairs are drifted by the electric field and make the after pulse when reaching a depletion layer.

Optical cross talk
: By-product photons produced in an avalanche reach to the other pixel and cause another avalanche at the same time.

Although a source of accidental background is mainly dark noise, a contribution from the after pulse becomes large under high counting-rate condition. Their amplitude should be 2∼3 p.e. at most by even concerning the optical cross talk. Then, we can reject contributions from these noise using TOT information. BFT TOT distributions are shown in Figure A.3. Events obtained between the timing of $|time| < 5$ ns are represented by black lines. On the other hand, red lines show events lying in the accidental timing region.

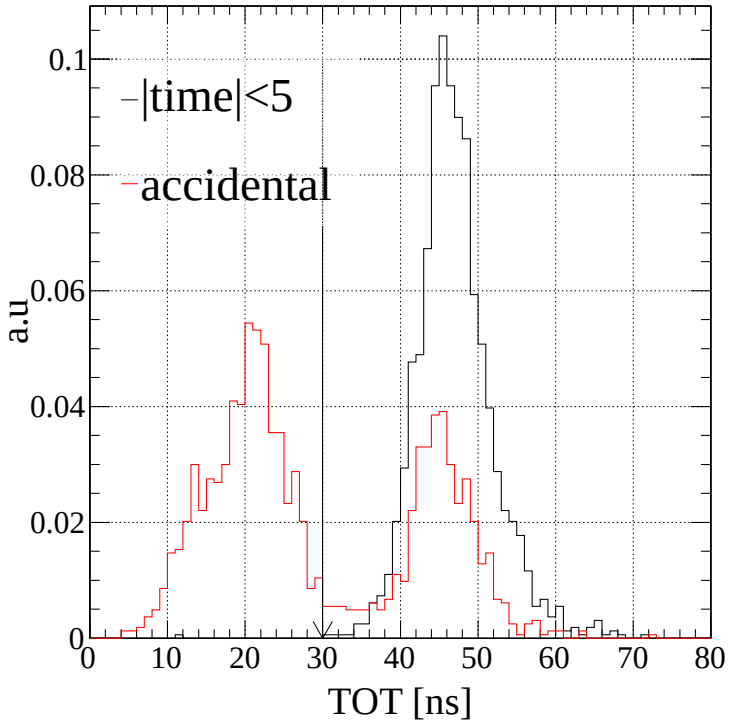

Figure A.3: *The BFT TOT distribution. Black and red lines show events lying within the timing of* $|time| < 5$ *ns and an accidental region, respectively.*

We can recognize the peak in the left-hand side as a contribution from noise. Then, clusters whose TOT is less than 30 ns are rejected.

Appendix B

Beam through analysis in E13

In this appendix, the reason is explained to select a third-order polynomial as a function for the absolute momentum correction of the SKS system. After the E10 experiment, we took a commissioning data for the E13 experiment. By analyzing beam-through data taken in both experiments, we find a bending angle dependence of SKS momenta. We introduce a setup of the E13 experiment and analysis results.

B.1 Introduction

The E13 experiment is a γ-ray spectroscopy using a germanium detector array, namely, hyperball-J; the experiment will be performed at the K1.8 beamline with the SKS system. The target proposed are a liquid ^{4}He with thickness of 3.0 g/cm^2 and a hydrogen fluoride with thickness of 20 g/cm^2. In this experiment, damages to germanium detectors must be suppress as small as possible. Then, the (K^-, π^-) reaction is adopted instead of the (π^+, K^+) reaction because we can decrease the beam intensity owing to the large hypernuclear production cross section of the (K^-, π^-) reaction.

In the case of the ^{4}He, the purpose is to observe the γ transition of M1 between the ground-state spin doublet, namely, $^4_\Lambda$He $(1^+ \to 0^+)$ in order to confirm the charge symmetry breaking effect in the ΛN interaction. Since the 1^+ must be populated to observe the γ transition between the ground-state doublet, the spin-flip amplitude of the Λ production cross section should be as large as possible. Thus, the (K^-, π^-) reaction at the beam momentum of 1.5 GeV/c is selected to produce the hypernucleus.

On the other hand, the purpose of an use of ^{19}F is a study of the ΛN interaction in the s-d shell hypernucleus. A large momentum transfer is necessary because excited states of $^{19}_\Lambda$F should be populated with different ΔL = 0, 1, 2 in order to observe various γ transitions. In addition, the non-spin-flip cross section is expected to be maximum at the beam momentum of 1.8 GeV/c. Therefore, the (K^-, π^-) reaction at the beam momentum of 1.8 GeV/c is selected.

B.2 Setup

The experimental setup is illustrated in Figure B.1. In the E13 experiment, we have to identify kaons in the beamline and pions in the SKS system. Then, an arrangement of PID counters are quite different from that of E10. In order to identify beam kaons, Beam Aerogel Čerenkov counter (BAC) 1 and 2 are installed at downstream of BH2. On the other hand, Scattered Aerogel Čerenkov counter (SAC) 1 is located just behind the target.

In order to suppress the background caused by a decay process, that is, $K^- \to \pi^0\pi^-$, Scattered Pi 0 counter (SP0) is installed between SDC1 and SDC2. Iron blocks are placed between TOF and LC instead of LAC in order to veto the decay of $K^- \to \mu\nu$. The system consisting of iron blocks and LC is called Scattered Muon Filter (SMF). Furthermore, the hyperball-J is surrounding the target.

The most important difference between E10 an E13 is an arrangement of downstream detectors of the SKS system. The momentum of outgoing pion reaches 1.6 GeV/c using the (K^-, π^+) reaction at the beam momentum of 1.8 GeV/c. Since such high momentum particles cannot be detected with the present setup, the bending angle of the SKS system in E13 is shallower than that of E10; it is changed from 85 to 55 degree.

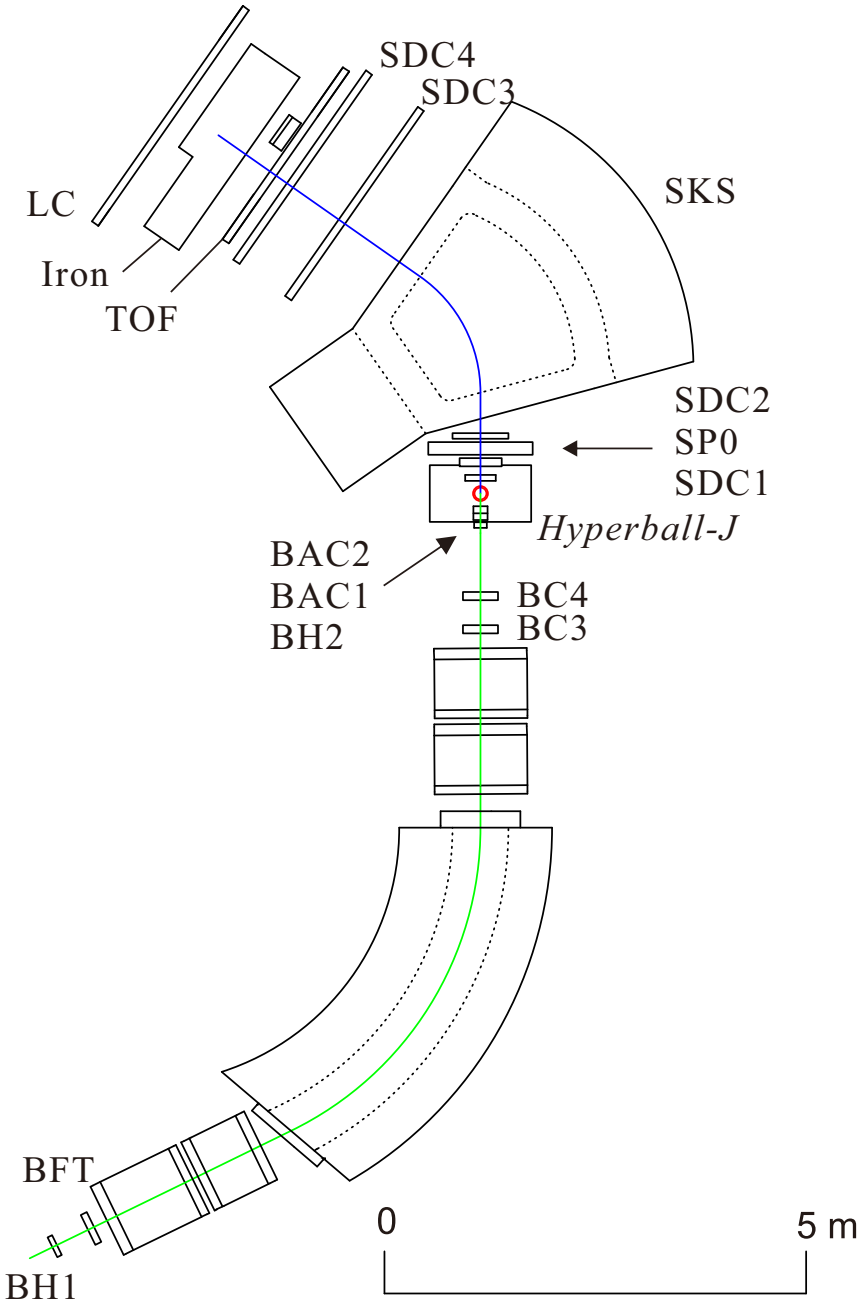

Figure B.1: *The setup of the E13 experiment.*

B.3 Beam through analysis

Table B.1: *Beam through data taken in E10 and E13.*

Data	Beam mom. (GeV/c)	Particle	target
E10			
Beam through	0.8, 0.9, 1.0, 1.2	π^+	none
E13			
Beam through	1.3, 1.5, 1.8	π^-	none

Beam through data taken in both experiments are summarized in Table B.1. The analysis procedures for E10 and E13 are the same. The energy loss in detectors are already corrected. At first, we plot $\Delta p = p_{SKS} - p_{K1.8}$ as a function of the beam momentum in Figure B.2. It is obvious that there is no way to correct them using linear functions. In the next, we plot Δp as a function of a bending angle of the SKS system. We can find a correlation between Δp and the bending angle; the correlation can explain both experimental data. Then, we conclude that the momentum linearity of the SKS system has a strong bending angle dependence in a small angle region.

It was historically believed that the linearity of the SKS system was good. However, this is true around its original bending angle of 100 degree. The use of the SKS system with the small bending angles of 85 or 55 degree is a first attempt. I claim that we have to use a higher-order polynomial as a correction function in such bending angle regions. In the present analysis, a third-order function is used as not a complete correction function but a better function than a linear function.

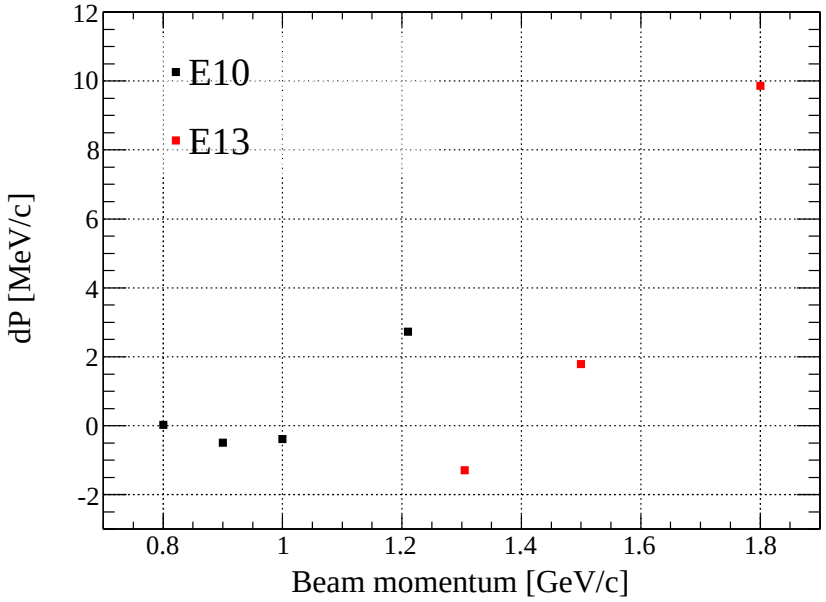

Figure B.2: *The Δp distribution as a function of the beam momentum.*

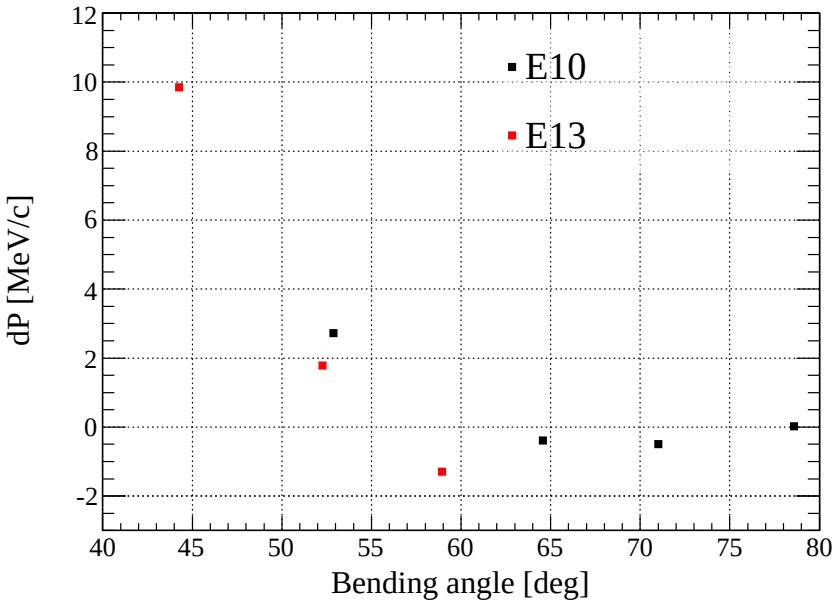

Figure B.3: *The Δp distribution as a function of a bending angle of SKS.*

Appendix C

DWIA calculation

In this appendix, we briefly introduce the present frame work of the DWIA calculation.

C.1 Impulse approximation

We consider the scattering between the incident beam particle and the nuclei. Although the incident particle in nuclei should be described according to the multi scattering theory, we can approximate such the complex multi scattering as a scattering between almost "free" two particles if the momentum of the incident particle is enough high to be the de Broglie wavelength of the incident particle shorter the distance between two nucleons in nuclei. A scattering is labeled by numbers as follows.

$$1 + 2 \to 3 + 4,$$

where 1 is the incident particle, 2 is nucleon in nuclei, 3 is outgoing particle such as outgoing kaon, 4 is a reaction product such as a Λ particle. Under this approximation, the double differential cross section from an initial state (i) to a final state (f) in the lab. system is described using t-matrix between free particles as

$$\left(\frac{d^2\sigma_{fi}}{d\Omega dE_3}\right) = \frac{p_3 E_3}{(2\pi)^2 v_1}|T_{fi}|^2\delta(\omega - E_1 + E_3), \tag{C.1}$$

$$T_{fi} = \langle\chi_3^{(-)}|\langle f|\sum_j t_j|i\rangle|\chi_1^{(+)}\rangle, \tag{C.2}$$

where $\sum$ represents a sum of the j-th nucleon, $v_1 = p_1/E_1$, ω is the energy transfer $(E_4 - E_2)$, and $\chi_3^{(-)}$ and $\chi_1^{(+)}$ are distorted wave functions of the outgoing and incident particle, respectively. This is impulse approximation.

The double differential cross section for the hypernuclear productions such as the (π^+, K^+) reaction is expressed by rewriting the above equation as

$$\left(\frac{d^2\sigma}{d\Omega dE_K}\right) = \beta\left(\frac{d\sigma}{d\Omega}\right)^{elem} S(\omega, \boldsymbol{q}). \tag{C.3}$$

Here, the momentum transfer is $\boldsymbol{q} = \boldsymbol{p}_\pi - \boldsymbol{p}_K$. $(d\sigma/d\Omega)^{elem}$ represents the elementary cross section for the hyperon productions. The strength factor $S(\omega, \boldsymbol{q})$ is written as

$$S(\omega, \boldsymbol{q}) = \sum_f |\langle f|\hat{O}|i\rangle|^2\delta(\omega - E_\pi + E_K), \tag{C.4}$$

$$\hat{O} = \sum_{j=1}^{A}\int d\boldsymbol{r}\chi_K^{(-)*}(\boldsymbol{r})\chi_\pi^{(+)}(\boldsymbol{r})\hat{U}_j\delta(\boldsymbol{r} - \boldsymbol{r}_j), \tag{C.5}$$

where $\hat{O}_j$ is an operator to convert a nucleon(2) to a hyperon(4). β in Eq. C.3 is a kinetic factor to transform from the two-body system to the many-body system ($\pi +^Z A$), and is defined as

$$\beta \equiv \left(1 + \frac{E_K^0}{E_Y^0}\frac{p_K^0 - p_\pi^0 cos\theta}{p_K^0}\right)\frac{p_K E_K}{p_K^0 E_K^0}, \tag{C.6}$$

where Y denotes hyperons, p_π^0 and p_K^0 (E_K^0 and E_Y^0) are momenta of π and K (energies of K and hyperon) in the two-body system. On the other hand, p_K (E_K) is a momentum (energy) of K in the many-body system.

The wave functions of mesons are distorted by the interaction between meson and nucleons in nuclei. The distorted wave functions are produced with the eikonal approximation using the distorted factor (D) as follows.

$$\chi_K^{(-)*}(\boldsymbol{r})\chi_\pi^{(+)}(\boldsymbol{r}) = \exp(i\boldsymbol{q}\cdot\boldsymbol{r})D(\boldsymbol{b}, z), \tag{C.7}$$

with

$$D(\boldsymbol{b}, z) \equiv \exp\left(-\frac{\sigma_\pi(1 - i\alpha_\pi)}{2}\int_\infty^z \rho(\boldsymbol{b}, z')dz' - \frac{\sigma_K(1 + i\alpha_K)}{2}\int_z^\infty \rho(\boldsymbol{b}, z')dz'\right) \tag{C.8}$$

where $\boldsymbol{r}$ is the distance between the meson and the nucleus, $\boldsymbol{b}$ is impact parameter, σ_π and σ_K denotes the total cross section of π (or K) + nucleon, and α_π and α_K represent the ratio of the real and imaginary parts amplitudes of the meson-nucleon scattering at the forward angle. The matter-density distribution with the Gaussian form is used in the present analysis.

In the theoretical study for the hypernuclear production, the eikonal approximation was historically used to described distorted-meson waves. The production cross section of ${}^{12}_{\Lambda}$C calculated with the DWIA framework using the eikonal approximation agree well with the experimental data [79]. Then, this seems to be a good approximation in the beam momentum range of $\sim$1 GeV/c.

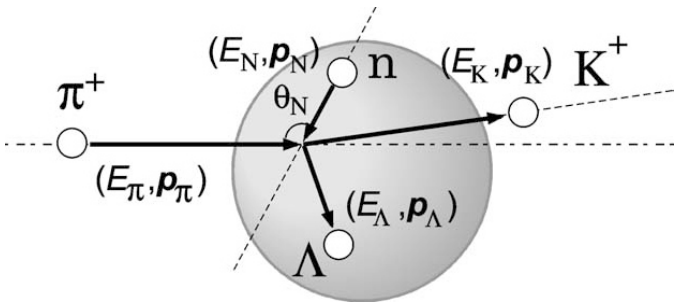

Figure C.1: *The schema of the hyperon production in the impulse approximation frame work. [28]*

C.2 Fermi-averaged t-matrix

In the impulse approximation frame work, the kinematics of the scattering does not satisfy the on-energy-shell condition due to the Fermi motion of nucleons. It is known that the DWIA calculation cannot reproduce the spectrum shape of quasi-free hyperon productions due to the difference of kinematics caused by the Fermi motion, if a complete elementary cross section of hyperon productions is used [28]. Here, the off-shell effect is taken into account by assuming that processes which meet the on-energy-shell condition can contribute the reaction events. Such a elementary $\pi N \to KY$ t-matrix are averaged over the Fermi-momentum distribution [28]. The "Fermi-averaged" t-matrix is given by a following equation.

$$t^{opt}(p_\pi;\omega,\boldsymbol{q}) = \left.\frac{\displaystyle\int_0^\pi sin\theta_N d\theta_N \int_0^\infty dp_N p_N^2 \rho(p_n) t(E_N;\boldsymbol{p}_\pi,\boldsymbol{p}_N)}{\displaystyle\int_0^\pi sin\theta_N d\theta_N \int_0^\infty dp_N p_N^2 \rho(p_N)}\right|_{\boldsymbol{p}_N=\boldsymbol{p}_N^*}, \tag{C.9}$$

where $\theta = \boldsymbol{p}_\pi \cdot \boldsymbol{p}_N$, and definition of terms in Eq. C.9 are shown in Figure C.1. $\boldsymbol{p_N^*}$ is a solution for the on-energy-shell equation as follows

$$\omega = \sqrt{(\boldsymbol{p}_N^* + \boldsymbol{q})^2 + m_\Lambda^2} - \sqrt{{\boldsymbol{p}_N^*}^2 + m_N^2}, \tag{C.10}$$

$$\simeq m_\Lambda - m_N + \frac{\boldsymbol{q}^2}{2m_\Lambda} + \frac{\boldsymbol{p}_N^* \cdot \boldsymbol{q}}{m^\Lambda} - \frac{m_\Lambda - m_N}{m^\Lambda}\frac{{\boldsymbol{p}_N^*}^2}{2m^N}. \tag{C.11}$$

The elementary t-matrix ($t(E_N;\boldsymbol{p}_\pi,\boldsymbol{p}_N)$) are integrated for various $\boldsymbol{p}_N^*$.

The elementary t-matrix for the $\pi^- p \to K^+\Sigma^-$ reaction is shown in Figure C.2 with experimental data used to construct this t-matrix. On the other hand, the Fermi-averaged production cross section for the $\pi^- p \to K^+\Sigma^-$ reaction as a function of the energy transfer is shown in Figure C.3. In the present DWIA calculation, the Fermi-averaged t-matrix for every 2 degree are prepared from data on the $\pi^- p \to K^+\Sigma^-$ at 1.37 GeV/c taken in the present experiment.

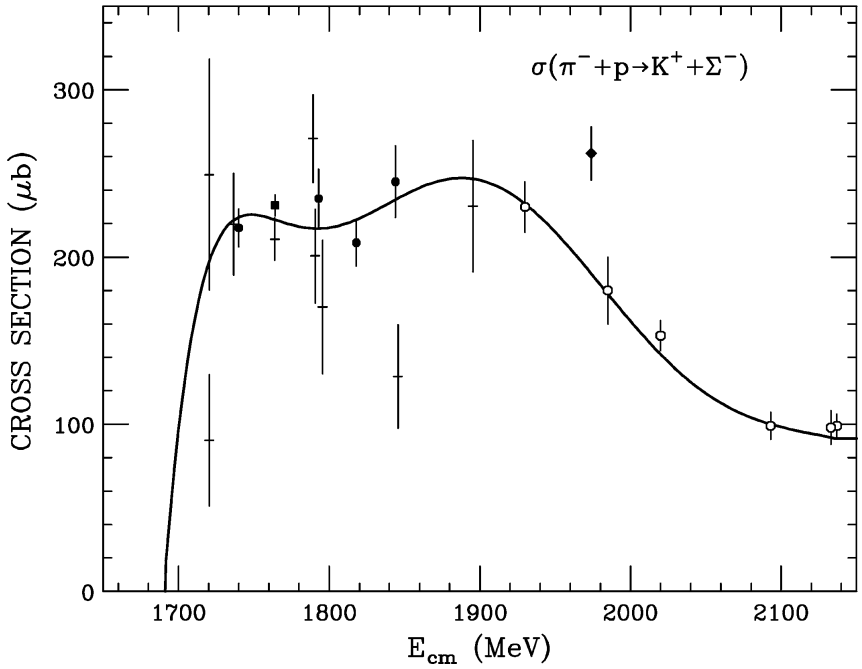

Figure C.2: *The elementary t-matrix for the $\pi^- p \to K^+\Sigma^-$ reaction and experimental data used to construct it. [77]*

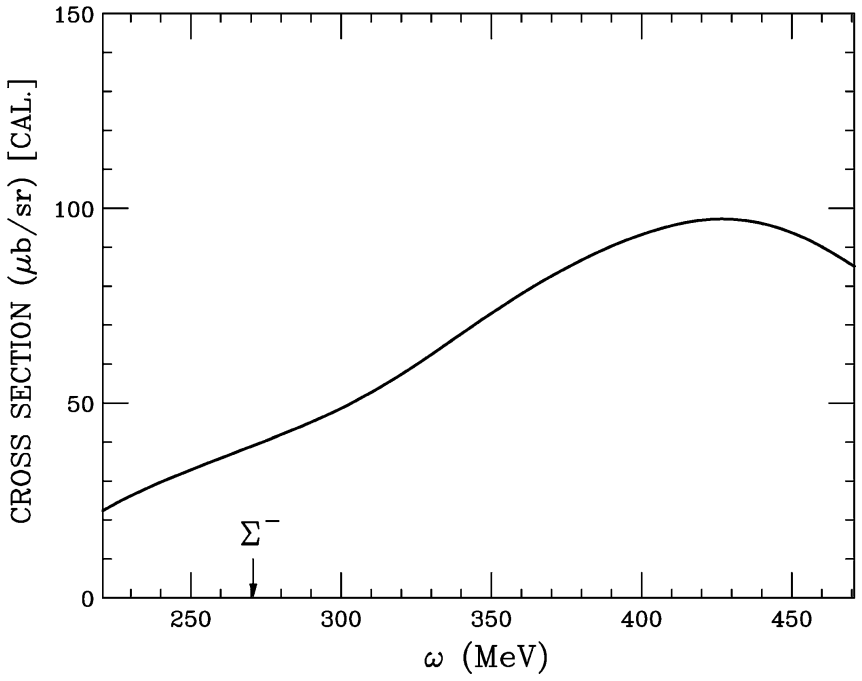

Figure C.3: *The Fermi-averaged t-matrix as a function of the energy transfer [77].*

C.3 Green's function method

The double differential cross section for the inclusive (π^-, K^+) reaction is described using the Fermi-averaged t-matrix and the Green's function (G).

$$\frac{d^2\sigma}{dE_K d\Omega_K} = \left(\frac{d\sigma}{d\Omega}\right)^{opt} S(\omega, \boldsymbol{q}). \tag{C.12}$$

In order to calculate including not only the bound states but also the quasi-free hyperon productions, Green's functions method [78] is usually used. The complete Green's function is given by

$$\hat{G} = \frac{1}{\omega - \hat{H} + i\epsilon}, \tag{C.13}$$

where the total Hamiltonian $\hat{H} = \hat{H}^0 + \hat{U}$ for the Y+nucleus system satisfies $\hat{H}|\Psi_N\rangle = E_f|\Psi_N\rangle$. $\hat{H}^0$ has intrinsic Hamiltonian of the core nucleus and the kinetic operator of a hyperon. On the other hand, $\hat{U}$ is a hyperon-nucleus potential. The complete Green's function can be calculated by solving the coupling channel equation as follows

$$\hat{G} = \hat{G}^0 + \hat{G}^0 \hat{U} \hat{G}, \tag{C.14}$$

and

$$\hat{G} = \begin{pmatrix} G_{\Lambda\Lambda} & G_{\Lambda\Sigma} \\ G_{\Sigma\Lambda} & G_{\Sigma\Sigma} \end{pmatrix}, \qquad \hat{U} = \begin{pmatrix} U_{\Lambda\Lambda} & U_{\Lambda\Sigma} \\ U_{\Sigma\Lambda} & U_{\Sigma\Sigma} \end{pmatrix}.$$

$\hat{G}^0$ is the free Green's function, of which the Hamiltonian is $\hat{H}^0$. Although the off-diagonal potential, which is related to the neutron-rich Λ hypernuclear state, should not be neglect in the present experiment, its strength is adjusted to be the amplitude of the hypernuclear state quite small. Therefore, the present calculation result completely comes from the diagonal potential. The diagonal potential which is the Σ-nucleus potential is assumed to be a WS form as follows

$$U_{\Sigma\Sigma} = (V_0^\Sigma + iW_0^\Sigma \cdot g(E_{ex}))[\exp((r-R)/a)]^{-1} \tag{C.15}$$

with $R = 1.1(A-1)^{1/3} = 1.9$ fm and $a = 0.67$ fm, $g(E_{ex})$ is a function of the excitation energy to describe the state width; it linearly increase from the Λ-binding threshold to the Σ-binding threshold. The width of the core nucleus states and the experimental resolution is included in ϵ.

According to the Green's function method [78], the sum of the final states can be written as

$$\sum_f |\Psi_f\rangle\langle\Psi_f|\delta(\omega - E_f) = -\frac{1}{\pi}\mathrm{Im}\hat{G}. \tag{C.16}$$

Then, the strength function is described as follows

$$S(\omega, \boldsymbol{q}) = (-)\frac{1}{\pi}\mathrm{Im}\sum_{\alpha\alpha'}\int d\boldsymbol{r}d\boldsymbol{r}' F_\alpha^\dagger(\boldsymbol{r}) G_{\alpha\alpha'}(E_f; \boldsymbol{r}, \boldsymbol{r}') F_{\alpha'}(\boldsymbol{r}'), \tag{C.17}$$

$$F_\alpha(\boldsymbol{r}) = \chi_K^{(-)*}\left(\frac{M_C}{M_A}\right)\chi_\pi^{(+)}\left(\frac{M_C}{M_A}\right)\langle\alpha, \boldsymbol{r}|\Psi_N\rangle, \tag{C.18}$$

where M_C and M_A are the masses of the target and core nucleus, respectively. $|\Psi_N\rangle$ denotes the wave function of the target nucleus while $|\alpha\rangle$ represents the eigenstates for the

core nucleus, in which a certain proton-hole state is populated. The wave function of the ^{6}Li target is based on a single-particle wave functions, which are obtained using the WS potential.

Furthermore, the strength function is decomposed to two terms according to the following relation,

$$\mathrm{Im}\hat{G} = (1 + \hat{G}^\dagger \hat{U}^\dagger)\mathrm{Im}\hat{G}^0(1 + \hat{U}\hat{G}) + \hat{G}^\dagger \mathrm{Im}\hat{U}\hat{G}. \tag{C.19}$$

The decomposed strength function is defined as

$$S(\omega, \boldsymbol{q}) = S^\uparrow_\Sigma(\omega, \boldsymbol{q}) + S^\downarrow_\Lambda(\omega, \boldsymbol{q}), \tag{C.20}$$

where

$$S^\uparrow_\Sigma = -\frac{1}{\pi} F^\dagger (1 + \hat{G}^\dagger \hat{U}^\dagger)\mathrm{Im}\hat{G}^0(1 + \hat{U}\hat{G})F, \tag{C.21}$$

and

$$S^\downarrow_\Lambda = -\frac{1}{\pi} F^\dagger \hat{G}^\dagger \mathrm{Im}\hat{U}\hat{G}F. \tag{C.22}$$

Here, $S^\uparrow$ and $S^\downarrow$ describe the Σ escape through the quasi-free production and the $\Sigma^- p \to \Lambda n$ conversion process.

Appendix D

Historical background

The understanding of the NN interaction is based on data on NN scattering. On the other hand, statistical quality of YN scattering data is poor due to experimental difficulties caused by the short lifetime of hyperons. Then, the ΛN interaction has been experimentally studied via Λ-hypernuclei. Properties of the ΛN interaction including spin-spin, spin-orbit and tensor parts are revealed from the reaction and γ-ray spectroscopies [10]. However, data on the ΣN interaction is further limited comparing with data on the ΛN interaction because Σ is not bound in nuclei except for ${}^{4}_{\Sigma}$He, probably due to the repulsive force in the $\Sigma N(s = 1, t = 3/2)$ channel. If a bound state exists, a Σ immediately converts to a Λ particle in nuclei via the $\Sigma N \to \Lambda N$ reaction. Therefore, precise reaction spectroscopy of Σ hypernuclei is difficult because a natural width is broadened.

In this section, we describe the historical background of experimental investigations for the ΣN interaction.

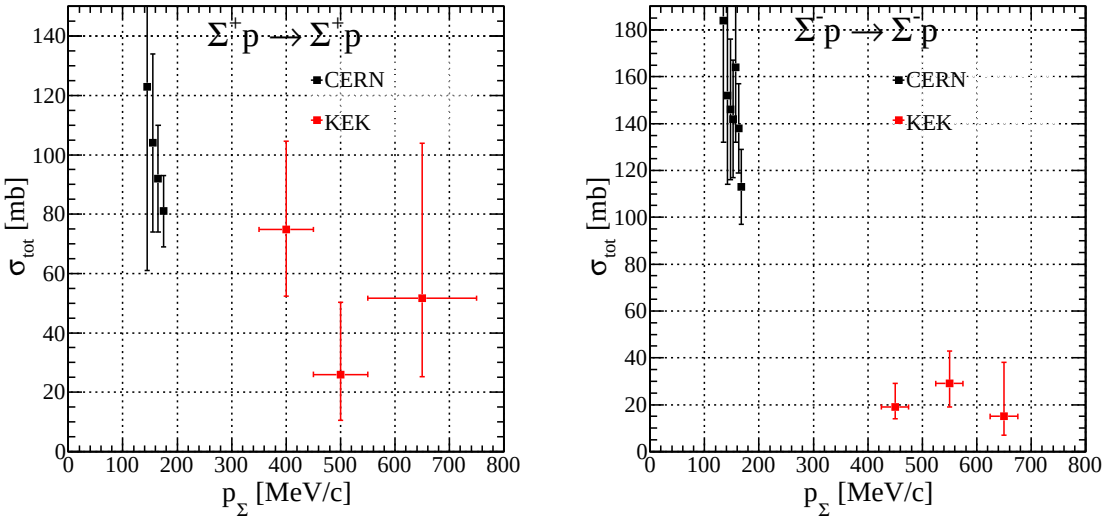

Figure D.1: *Total cross sections of $\Sigma^{\pm}p$ scattering obtained in CERN [11] and KEK experiments [18] [19].*

D.1 Study on a two-body (ΣN) system

As is the case for the NN interaction, a scattering experiment is one of the most direct ways to investigate the YN interaction. However, data on YN scatterings is still quite limited due to an experimental difficulty that scattered hyperons decay in a short time before reaching detectors. Then, the experimental method, recording images of scattering events and analyzing them by human eyes, was historically adopted.

In 1970s, a $\Sigma^{\pm}p$ elastic scattering experiment at a low energy region ($130 < p_\Sigma < 180$ MeV/c) [11] was carried out with a hydrogen bubble chamber using the CERN proton synchrotron (PS). In this experiment, the K^- capture reaction $K^-p \to \Sigma^{\pm}\pi^{\pm}$ was used to obtain a maximum $\Sigma^{\pm}$ production yield and about $7{\times}10^6$ kaons were stopped in the bubble chamber. The total number of scattering events observed was 283 for the Σ^+p elastic scattering and 1521 for the Σ^-p elastic scattering.

In 1990s, experiments on $\Sigma^{\pm}$ scatterings at a higher energy range ($300 < p_\Sigma < 750$ MeV/c), KEK-E251 and KEK-E289 [17][18][19], were performed with a scintillation fiber (SciFi) active target using KEK-PS. $\Sigma^{\pm}$ hyperons were produced via the in-flight reaction $\pi^{\pm}p \to K^+\Sigma^{\pm}$ on protons in the SciFi active target, and scattered off other protons again in the target. Σp scattering images were stored with the image intensifier tube (IIT) and outgoing kaons were analyzed by the kaon spectrometer. In this experiment, a quasi-free Σ production on carbon in SciFi became a serious background because a momentum of Σ could not be determined for such events. Then, many events were impossible to analyze, and consequently statistics was quite limited. These experimental results are summarized in Figure D.1.

D.2 Σ-atom

A hadron with a negative charge can be captured in an atomic orbit around nuclei. The overlap between the hadron and nuclei is more increase, the more the mass of hadrons is heavy. Then, such exotic atoms with heavy hadrons are a probe to the strong interaction between hadrons and nuclei. The energy of X-rays produced transitions between atomic orbits are shifted by the strong interaction from those calculated with the electromagnetic interaction. In addition, its state width are also broadened by an effect of an absorption. Since data on the ΣN scattering was poor, the study of the ΣN interaction through Σ^--hyperonic atoms were attempted in 1970s.

In order to make Σ^--atoms, a Σ^- particle has to be stopped and captured in material. However, it was difficult to study the Σ^- atom using a low-energy Σ^- beam because a Σ^- particle decays in flight due to its quite short lifetime. The Σ^- atom experiment was made possible by a fact that a low-energy Σ^- emission follows the K^- absorption in some cases [12]. The X-rays from Σ^--atoms were reported by the experiment in CERN for the first time [13]. In this experiment, the effect by the strong interaction did not be discussed because of the insufficient energy resolution of the X-ray detectors and the lack of statistics. Later, the Σ-nucleus interaction was reported by the experiment using targets of O, Mg, Al, Si and S in Rutherford laboratory [14]. Experimental data were fitted by the Σ-nucleus potential defined as

$$V(r) = -(4\pi\hbar^2/2\mu)(1 + m/M)a\rho(r), \tag{D.1}$$

where m, M,μ and $\rho(r)$ are the masses of Σ and nucleon, the reduced mass of the Σ-nucleus system and the nucleon density distribution, respectively. In addition, a is a complex scattering length of the Σ-nucleus system. Points circled in Figure D.2 are fitting results. As the result of the fitting, the scattering length was determined to be $a = (+0.35 \pm 0.04) + i(+0.19 \pm 0.03)$ fm. Thus, the Σ-nucleus potential is attractive and absorptive at the surface of nuclei. In 1990s, experimental data using heavier targets, W and Pb, were reported from the BNL-AGS experiment and also suggested that the Σ-nucleus potential is attractive [15].

Using these experimental data, several attractive/repulsive Σ-nucleus potentials were proposed by theorists. One example of the repulsive potentials is a Density Dependent (DD) potential proposed by C.J. Batty *et al.* [16]. Although the DD potential is weakly attractive at the surface of nuclei, it becomes repulsive in nuclei.

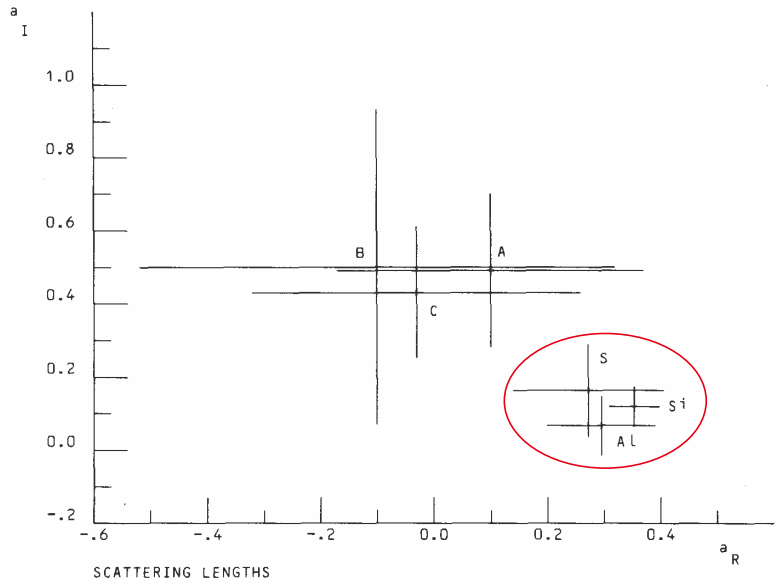

Figure D.2: *The Σ-nucleus complex scattering length obtained in the experiment [14]. Points circled are the results of the fitting.*

D.3 Problem of a narrow width of Σ-hypernuclei

In 1970s, an experiment to search for Σ-hypernuclei was carried out via the ^{9}Be(K^-, π^-)X reaction at a beam momentum of 720 MeV/c [20]. Outgoing pions were measured by the spectrometer SPES II which detected particles between reaction angles from 0° to 6°. In this experiment, a ^{9}Be target with thickness of 2 g/cm^2 was used and the total energy resolution was about 3 MeV (FWHM). The experimental result is shown in Figure D.3 as a function of the Λ-binding energy. On the left-hand side, we can find two prominent peaks correspond to ${}^{9}_{\Lambda}$Be hypernuclear states. On the other hand, structure similar to these Λ-hypernuclear peaks can be seen on the right-hand side in the figure. This structure was claimed as Σ-hypernucleus states. The peak width of this structure was surprisingly rather narrow, that is, about 8 MeV because the natural width about 20 MeV was suggested from the fact that the Σ-nucleus potential was absorptive from the Σ^--atom experiments. Hence, this narrow width of Σ-hypernuclei was unnatural. This experimental result triggered search for Σ-hypernuclei to settle this situation.

In 1990s, an experiment on the production of ${}^{9}_{\Sigma}$Be, BNL-AGS E887 [21], was carried out to reexamine the result at CERN PS with higher statistics using Alternating Gradient Synchrotron (AGS) in Brookhaven National Laboratory (BNL). The experiment was performed at the C6 beamline of the BNL-AGS. A ^{9}Be target was irradiated with K^- beams with the beam momentum of 600 MeV/c. Outgoing $\pi^{\pm}$'s produced via the in-flight $(K^-, \pi^{\pm})$ reaction were detected by the Moby Dick spectrometer, which was set at a reaction angle of 4°. Although the energy resolution of 4 MeV (FWHM) was slightly worse than that of the experiment at CERN-PS, it was sufficient to confirm the claimed result. The experimental result is shown in Figure D.4 surrounded by a red square, where the non-hatched spectrum corresponds to data on the (K^-, π^-) reaction. The $-B_\Sigma$ range between 0 to 30 MeV in Figure D.4 corresponds to the region, in which peaks exist in Figure D.3. No narrow peak structure observed in this experiment. Thus, the problem of the narrow width of Σ-hypernuclei reached to the end by this result.

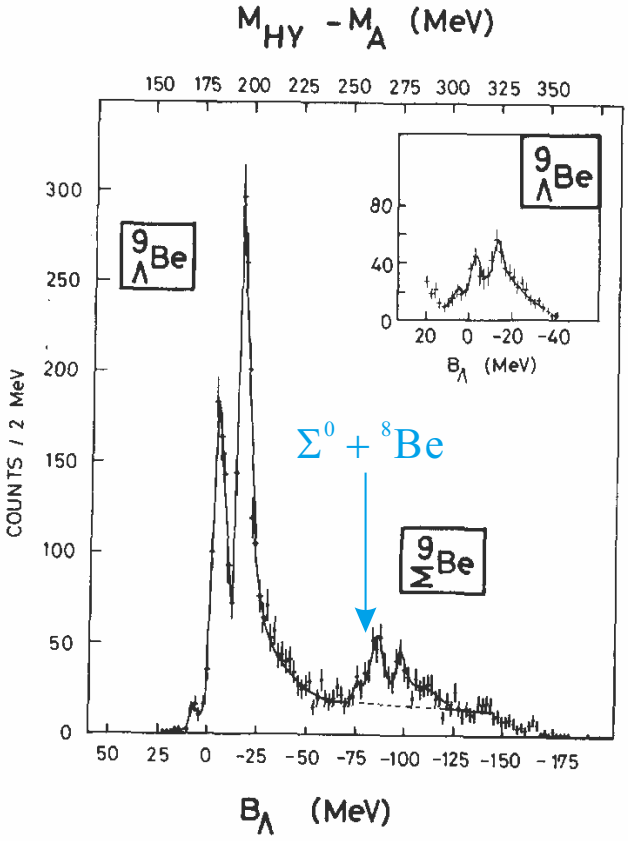

Figure D.3: *The spectrum obtained via the* ^{9}Be$(K^-,\pi^-)X$ *reaction at a beam momentum of 720 MeV/c. [20]*

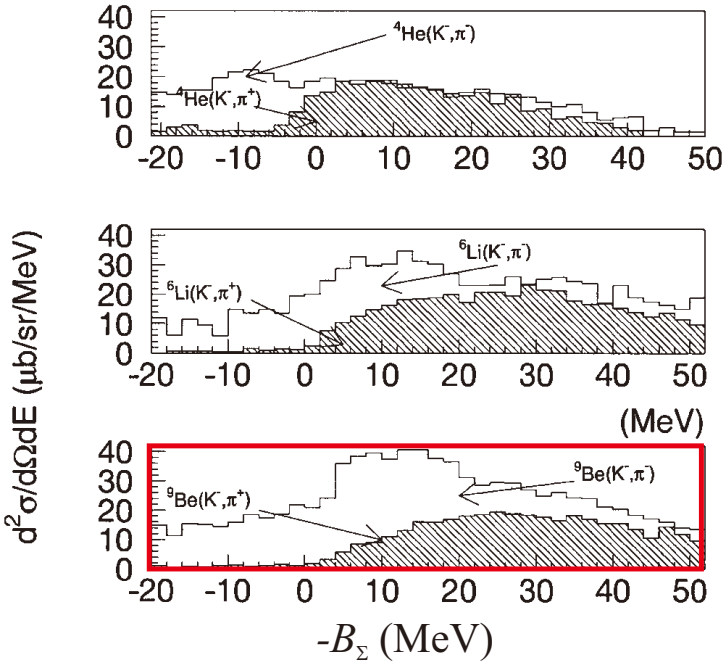

Figure D.4: *The spectrum obtained via the* ^{9}*Be*$(K^-,\pi^\pm)X$ *reaction is shown in the figure surrounded by a red square. [21]*

D.4 Bound state in the T=1/2 system

In 1980s, a bound state of Σ-hypernucleus, ${}^{4}_{\Sigma}$He, was theoretically predicted [22]. Soon after the prediction, a bump structure was observed in the spectrum obtained via the ^{4}He$(K^{-}_{stopped}, \pi^{-})$X reaction in the KEK-E167 experiment. It was interpreted as an evidence of the bound state of ${}^{4}_{\Sigma}$He hypernucleus [23]. The few-body calculation using a realistic ΣN potential [22], of which S-matrix is equivalent to the Nijmegen hard core model-D [3], reproduced this experimental result, suggesting the existence of ${}^{4}_{\Sigma}$He in the spin-isospin state of $(S = 0, T = 1/2)$ [22]. In 1996, the existence of the bound-state of ${}^{4}_{\Sigma}$He was eventually confirmed as shown in Figure 1.3 in the BNL-AGS E905 experiment [24]. The experiment was performed using a liquid ^{4}He target via the (K^{-}, π^{-}) reaction at a beam momentum of 600 MeV/c at the C6 beamline of the BNL-AGS. The Moby Dick spectrometer, which was set at a reaction angle of 4°, was used for the pion detection. The binding energy and the width of the state were $4.4 \pm 0.3 \pm 0.1$ MeV and $7 \pm 0.7^{+1.2}_{-0.0}$ MeV, respectively. Since the experimental energy resolution was 3.63 ± 0.12 MeV (FWHM), the obtained width reflected the natural width of the state. This width is much narrower than naively expected.

The result of BNL-AGS E905 was theoretically interpreted as follows [22][25]. The behavior of the Σ-nucleus potential is naturally based on the two-body ΣN interaction, which has the strong spin-isospin dependence. In Figure D.5, the realistic ΣN potential introduced above, Sigma-nucleon Absorptive Potential (SAP) [22], is shown. SAP was described with a simple two-range Gaussian

$$V_{ts} = v_C \exp(-(r/a_c)^2) + (v_A + i w_A)\exp(-(r/a_A)^2), \tag{D.2}$$

where ts represents isospin and spin for the ΣN system and the imaginary potential (w_A) describes the $\Sigma N \to \Lambda N$ conversion process. As shown in Figure D.5, $V_{\frac{3}{2}0}$ and $V_{\frac{1}{2}1}$ are attractive, while the attractive pockets in $V_{\frac{3}{2}1}$ and $V_{\frac{1}{2}0}$ are shallower than those in $V_{\frac{3}{2}0}$ and $V_{\frac{1}{2}1}$. The spin-isospin averaged potential with respect to the total isospin T and total spin S for the four-body ΣNNN system are listed in Table D.1. Therefore, it was found that the $(S = 0, T = 1/2)$ state is the most attractive. Here, we do not have to consider the $S = 1$ state because the spin-flip amplitude in this beam momentum region is quite small. By considering the case of $S = 0$ only and assuming that the core nucleus is rigid, complex potential for the $3N$-Y system can be represented as

$$\hat{U}_{C\Sigma}(\boldsymbol{R}) = \langle \phi_C \phi_\Sigma \boldsymbol{R}| \sum_{k=1}^{3} \hat{V}_{\Sigma N_k} |\Psi\rangle / \langle \phi_C \phi_\Sigma \boldsymbol{R}|\Psi\rangle \,, \tag{D.3}$$

$$= U^0(\boldsymbol{R}) + U^\tau(\boldsymbol{R})(\boldsymbol{T}_C \cdot \boldsymbol{t}_\Sigma), \tag{D.4}$$

where N_k represents k-th nucleon, ϕ_C,ϕ_Σ are internal wave function of the core nucleus and Σ, $\boldsymbol{R}$ is a relative distance between the core nucleus and Σ particle, Ψ is the four-body wave function, and $\boldsymbol{T}_C$ and $\boldsymbol{t}_\Sigma$ are the isospin operators of the core nucleus and Σ, respectively. The first term is the isospin independent potential and the second term is the isospin dependent are, namely, the Lane's term. The potentials U^0 and U^τ are also described by the two-range Gaussian form, which is used to express V_{ts}. Figure D.6 (a) and (b) show Σ-nucleus potentials for the state of $T = 1/2$ and $T = 3/2$ using parameters summarized in the paper [25], respectively. The narrow width of the state can be explained by the soft repulsive core existing in the real part of $T = 1/2$. Owing to this repulsive core, the Σ-density distribution is pushed out of the nucleus. Since an overlap between the Σ

Table D.1: *Spin-isospin averaged potential* $\overline{V}_{\Sigma N}$ *in the four-body* ΣNNN *system.*

T	S	$\overline{V}_{\Sigma N}$			
$\frac{3}{2}$	1	$\frac{1}{6}V_{\frac{3}{2}0}$	$+\frac{11}{18}V_{\frac{3}{2}1}$		$+\frac{2}{9}V_{\frac{1}{2}1}$
$\frac{3}{2}$	0	$\frac{5}{18}V_{\frac{3}{2}0}$	$+\frac{1}{2}V_{\frac{3}{2}1}$	$+\frac{2}{9}V_{\frac{1}{2}0}$	
$\frac{1}{2}$	1		$\frac{4}{9}V_{\frac{3}{2}1}$	$+\frac{1}{6}V_{\frac{1}{2}0}$	$+\frac{7}{18}V_{\frac{1}{2}1}$
$\frac{1}{2}$	0	$\frac{4}{9}V_{\frac{3}{2}0}$		$+\frac{1}{18}V_{\frac{1}{2}0}$	$+\frac{1}{2}V_{\frac{1}{2}1}$

and the nucleus is decreased, the $\Sigma N \to \Lambda N$ conversion is suppressed, and then the width becomes narrow.

Thus, the existence of the Σ bound state was confirmed in the four-body system with $T = 1/2$. ${}^{4}_{\Sigma}$He is still the only experimental sample of Σ hypernucleus bound state.

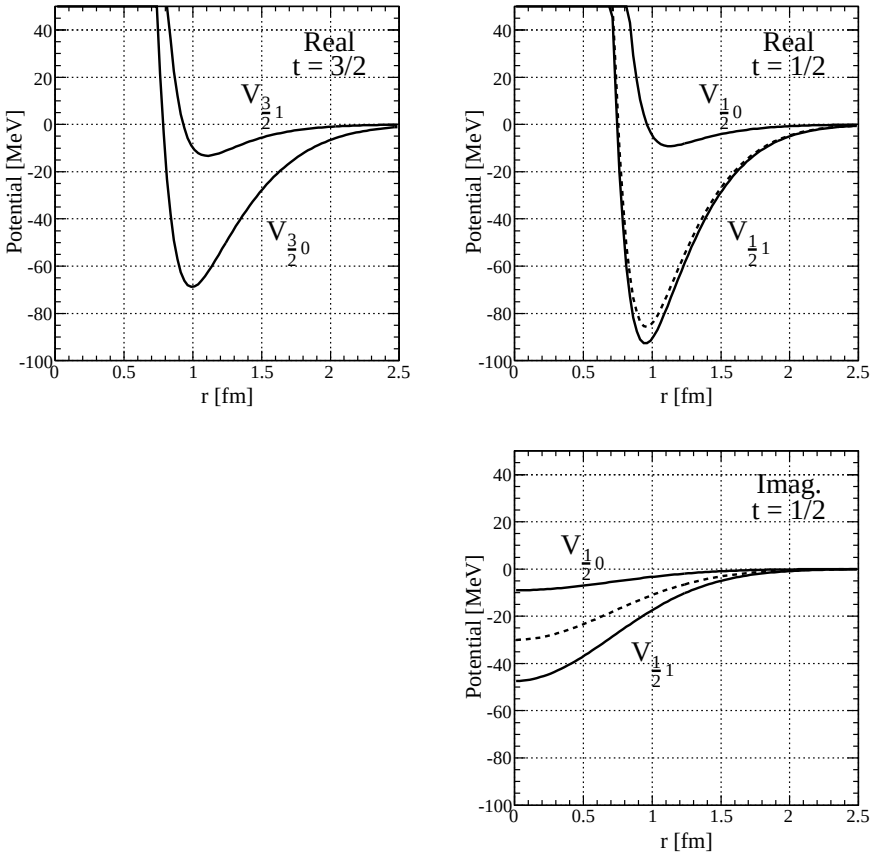

Figure D.5: *Sigma-nucleon Absorptive Potential (SAP), V_{ts}, with several different parameters for ΣN spin-isospin states [26].*

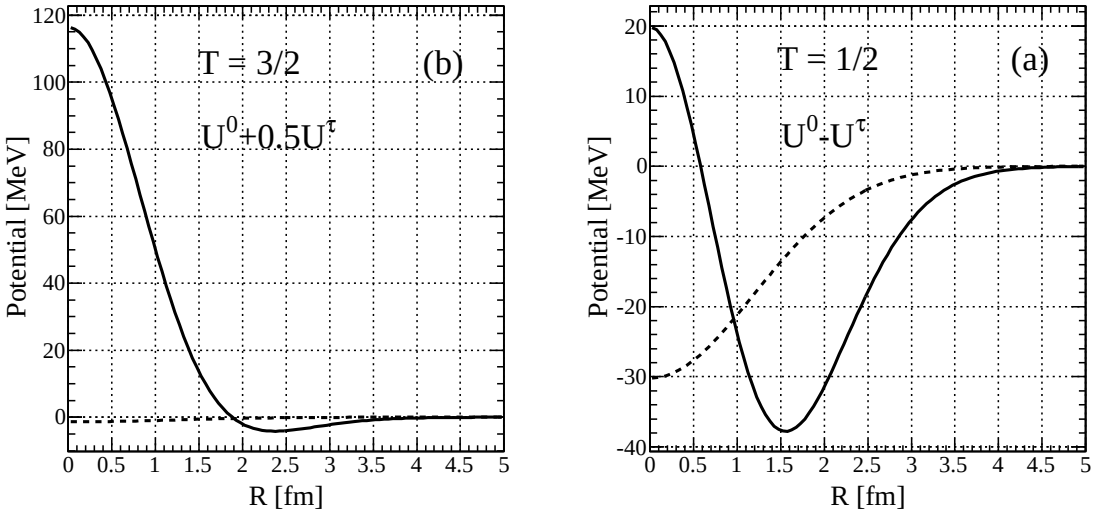

Figure D.6: *The Σ-nucleus potential for the $T = 1/2$ and $T = 3/2$ ΣNNN systems. The solid and dashed curve are the real and imaginary potential, respectively.*

D.5 Study in middle heavy nuclei

A systematic study of the Σ-nucleus potential in several nuclei, carbon, silicon, indium, and bismuth, was performed in the KEK-E438 experiment in KEK-PS [27]. The purpose of the experiment was to obtain information on the real and imaginary parts of the Σ-nucleus potential by analysing the shape of the continuum spectra obtained via the (π^-, K^+) reaction. The spectrum shape is affected by the potential as shown in Figure D.7. If the real part is repulsive, the spectrum is pushed to the higher mass region. In contrast, if the imaginary part is absorptive, a long tail is formed below the Σ binding threshold. By fitting data with the cross section calculated in the Distorted Wave Impulse Approximation (DWIA) framework, optimal potential strengths can be extracted. The Σ-nucleus potential is represented as $U_0^\Sigma + U_\tau^\Sigma(\mathbf{T}_C \cdot \mathbf{t}_\Sigma)/\mathrm{A_{core}}$, where U_0^Σ and U_τ^Σ are the isospin-independent term and the Lane's term, respectively. $\mathrm{A_{core}}$ is a mass number of the core nucleus. As the contribution from the Lane's term becomes small in heavy nuclei, they used only the isospin independent term, which is assumed to be a Woods-Saxon (WS) form as

$$U_\Sigma(r) = (V_0^\Sigma + iW_0^\Sigma)/[1 + \exp((r - R)/a)], \tag{D.5}$$

where V_0^Σ and W_0^Σ are the strengths of the real and imaginary parts of the potential.

The experiment was performed at the K6 beamline of KEK-PS with the Superconducting Kaon Spectrometer (SKS). These targets were irradiated with the π^- beam with the momentum of 1.2 GeV/c and outgoing kaons were detected by the SKS system. In Figure D.8, the spectrum for the Si target is shown with several DWIA calculation results. As the result of the χ^2 fitting, V_0^Σ and W_0^Σ were determined to be +90 MeV and −40 MeV with $R = 1.1(A-1)^{1/3} = 3.3$ fm and $a = 0.67$ fm, respectively. From this experiment, it was revealed that the isospin independent Σ-nucleus potential is strongly repulsive in the real part and has a sizable imaginary part.

Soon after the experimental report, a more precise theoretical analysis was performed using the same frame work [77]. In this analysis, more realistic t-matrix was constructed and used. By assuming the same WS form potential, the strengths of the real and imaginary parts were determined to be +30 and −40 MeV, respectively.

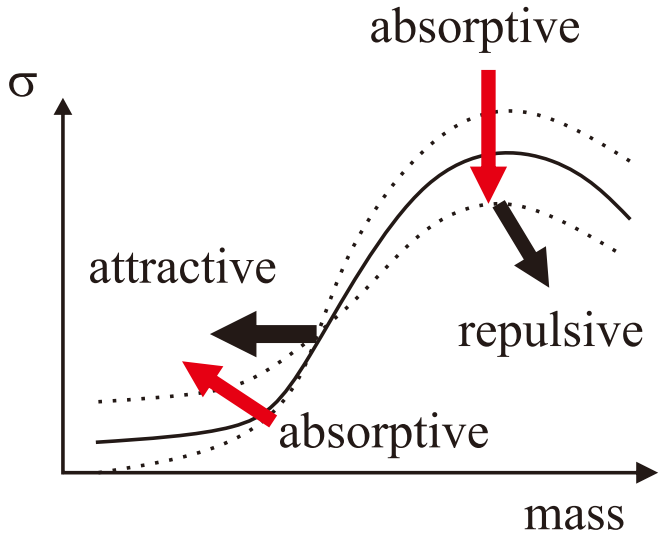

Figure D.7: *The spectrum behavior depending on the Σ-nucleus potential.*

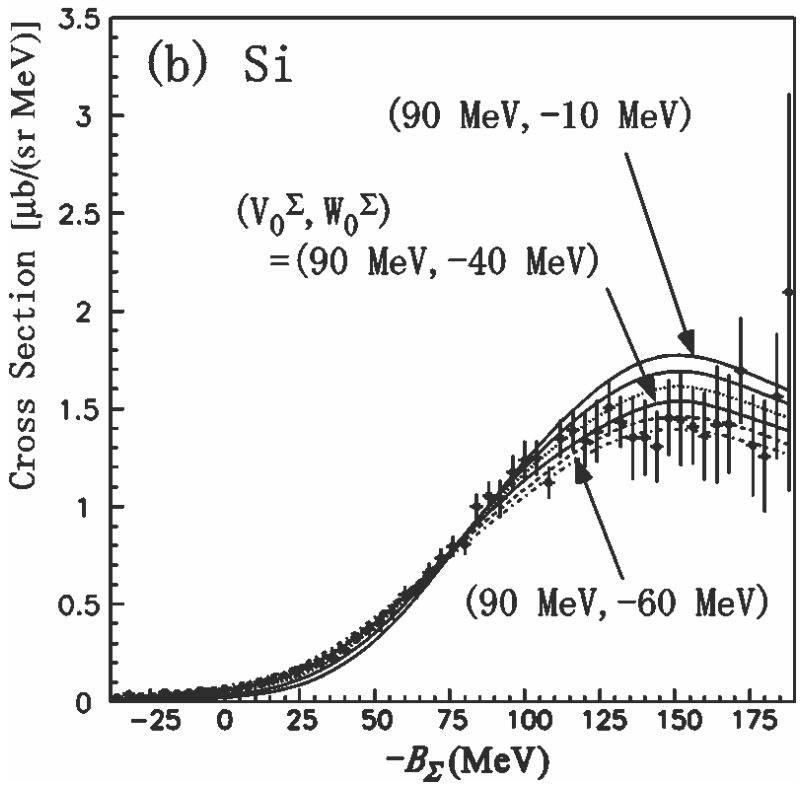

Figure D.8: *The spectrum for the $^{28}Si(\pi^-, K^+)X$ reaction with several DWIA calculation results [27].*

D.6 Production of neutron-rich Λ-hypernuclei

In 2002 and 2003, an experiment on the production of neutron-rich Λ-hypernuclei (KEK-PS E521 [29]) was performed. In this experiment, it was attempted to produce ${}^{10}_{\Lambda}$Li via the ^{10}B(π^-, K^+)X double charge-exchange reaction for the first time. To produce Λ-hypernuclei using the π^- beam, two protons must be converted to a Λ particle and a neutron. In this reaction, two different production mechanisms were considered, namely, the two-step process and the one-step process. The two-step process is based on the meson charge-exchange described below.

$$\pi^- p \to \pi^0 n,\ \pi^0 p \to K^+ \Lambda$$

or

$$\pi^- p \to K^0 \Lambda,\ K^0 p \to K^+ n$$

On the other hand, in the case of the one-step process, Λ is produced via virtual Σ^- doorways through the Σp-Λn mixing.

$$\begin{aligned} \pi^- p &\to K^+ \Sigma^- \\ \Sigma^- p &\leftrightarrow \Lambda n \end{aligned}$$

The difference between these processes is expected to appear in the beam momentum dependence of the production cross section. Since the cross section via the two-step process basically depends on the Λ production cross section via the single charge-exchange reaction, it is expected that the magnitude of the ${}^{10}_{\Lambda}$Li production becomes maximum at the beam momentum of 1.05 GeV/c [30], the optimal momentum to produce a Λ particle. The cross section is predicted to be 38-67 nb/sr at the beam momentum of 1.05 GeV/c (0°) [30].

The experiment was carried out at the K6 beamline in KEK-PS with the SKS system. A ^{10}B target with thickness of 3.5 g/cm^2 was irradiated with the π^- beam of 1.05 and 1.20 GeV/c. The total number of beam injected to the target was 0.44×10^{12} at $p_\pi = 1.05$ GeV/c and 1.08×10^{12} at $p_\pi = 1.20$ GeV/c, respectively. The energy resolution was checked by the ${}^{12}_{\Lambda}$C spectrum obtained via the (π^+, K^+) reaction using a graphite target, and consequently, it was 2.5 MeV (FWHM). Missing mass spectrum for each beam momentum is shown in Figure D.9. Although no clear peak is seen, a significant number of events exist below the Λ binding threshold. The production cross sections obtained by integrating the bound region for each momentum were 5.8 ± 2.2 nb/sr at 1.05 GeV/c and 11.3 ± 1.9 nb/sr at 1.20 GeV/c, respectively Since this result was inconsistent to the theoretical prediction for the two-step process, the one-step process might be favored rather than the two-step process.

To understand the mechanism of the (π^-, K^+) reaction, the spectrum was also theoretically analyzed using the DWIA calculation via the one-step process [31]. Since the bound state is populated via Σ^- doorways through the $\Sigma p \leftrightarrow \Lambda n$ coupling, the off-diagonal component in the hyperon-nucleus potential, which is related to the Σ^- admixture probability in the neutron-rich Λ-hypernucleus, must be considered. In this case, the hyperon-nucleus potential is described as

$$\boldsymbol{U} = \begin{pmatrix} U_{\Lambda\Lambda} & U_{\Lambda\Sigma} \\ U_{\Sigma\Lambda} & U_{\Sigma\Sigma} \end{pmatrix}. \tag{D.6}$$

The diagonal potentials given by the WS form are complex and defined as

$$U_{\Sigma\Sigma}(r) = (V_0^\Sigma + iW_0^\Sigma \cdot g(E_{ex}))f(r), \tag{D.7}$$

$$f(r) = [1 + \exp((r-R)/a)]^{-1}, \tag{D.8}$$

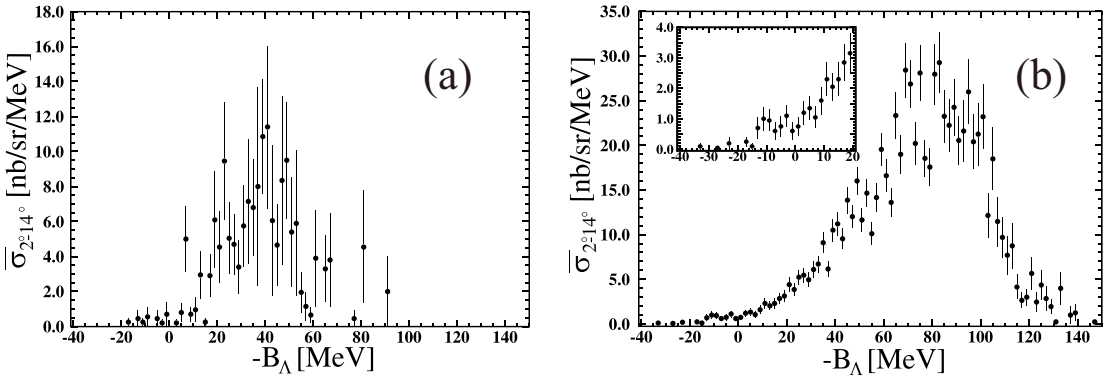

Figure D.9: *Missing mass spectra for the* $^{10}B(\pi^-, K^+)X$ *reaction taken in KEK-PS E521 experiment [29]. (a) The missing mass spectrum at* $p_\pi = 1.05$ *GeV/c. (b) The spectrum at* $p_\pi = 1.20$ *GeV/c.*

for $Y = \Lambda$ or Σ. On the other hand, off-diagonal potentials are assumed to be real, $U_{\Sigma\Lambda} = V_{\Sigma\Lambda} f(r)$. The calculated result reproduced the experimental data with $-W_\Sigma = 20$-30 MeV and $V_{\Sigma\Lambda} = 11$ MeV as shown in the Figure D.10 and Figure D.11. The $V_{\Sigma\Lambda}$ strength of 11 MeV corresponds to the Σ admixture probability of 0.57%, which is a few times lager than that of $^{7}_{\Lambda}$Li [32]. The feature of the one-step process is that the shape of the Λ continuum is convex downward. On the other hand, the shape of the Λ continuum via the two-step process is convex upward. This experimental data supports that the one-step process is dominant by considering the spectrum shape.

Although the neutron-rich Λ-hypernuclei was successful in KEK-E521, its structure and the reaction mechanism are not understood yet.

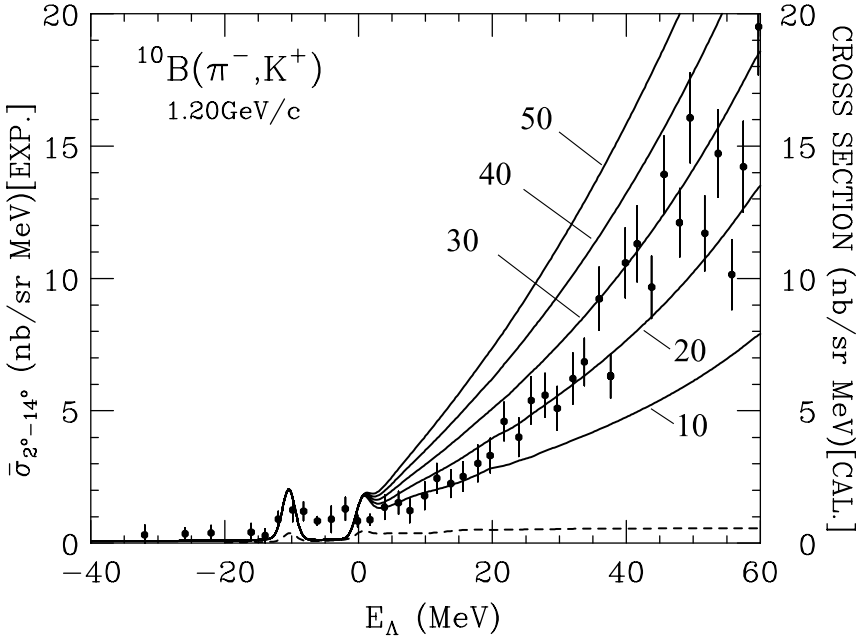

Figure D.10: *DWIA results calculated with several $-W_\Sigma$ when $V_{\Sigma\Lambda} = 11$ MeV [31], shown together with the measured spectrum for the $^{10}B(\pi^-, K^+)$ reaction at 1.20 GeV/c. Dashed line shows the calculation result through the two-step process.*

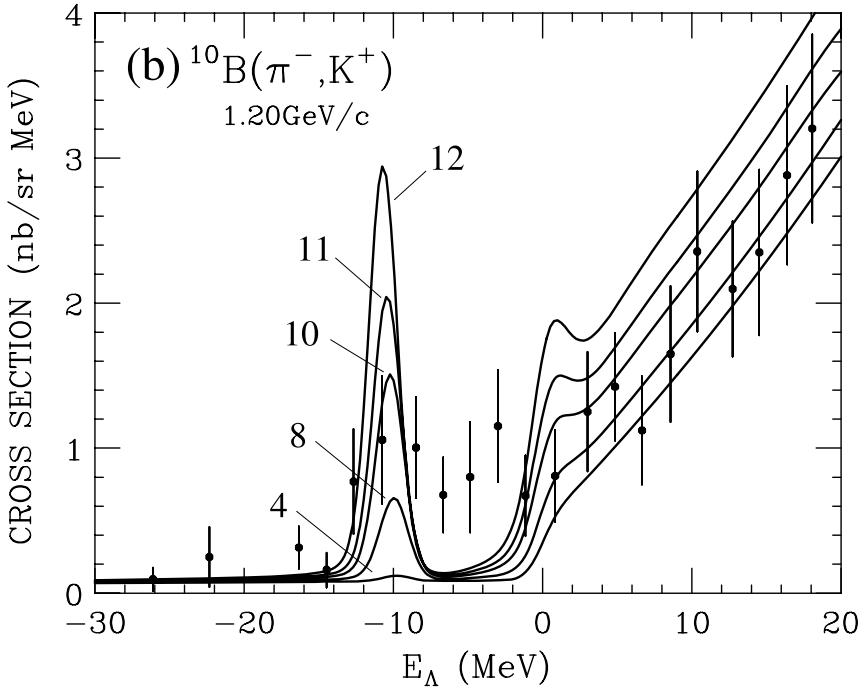

Figure D.11: *DWIA results calculated with several $V_{\Sigma\Lambda}$ when$-W_\Sigma = 20$ MeV [31], shown together with the measured spectrum for the $^{10}B(\pi^-, K^+)$ reaction at 1.20 GeV/c.*

Bibliography

[1] M. Oka, et al., Prog. Theor. Phys. Sup. **137** (2000) 1.

[2] Y. Akaishi, et al., Phys. Rev. Lett. **84** (2000) 3539.

[3] M. M. Nagels, T. A. Rijken and J. J. Swart, Phys. Rev. D **12** (1975) 744.

[4] M. M. Nagels, T. A. Rijken and J. J. Swart, Phys. Rev. D **15** (1977) 2547.

[5] M. M. Nagels, T. A. Rijken and J. J. Swart, Phys. Rev. D **20** (1979) 1633.

[6] T. A. Rijken, V. G. J. Stoks and Y. Yamamoto, Phys. Rev. C **59** (1999) 21.

[7] T. A. Rijken, M. M. Nagels and Y. Yamamoto, Nucl. Phys. A **835** (2010) 160.

[8] Y. Fujiwara et. al., Phys. Rev. C **70**, (2004) 024001.

[9] T. Inoue, et al., (HAL-QCD collaboration), Prog. Theor. Phys. **124** (2010) 591.

[10] O. Hashimoto, H. Tamura, Progress in Particle and Nuclear Physics **57**, (2006) 564.

[11] F. Eisele, H. Filthuth, W. Fohlisch, V. Hepp, G. Zech, Phys. Lett. **37B**, (1971) 204.

[12] European K^- Collaboration, Nuovo Cimento **14**, (1959) 315.

[13] G. Backenstoss, et. al., Z. Physik A **273**, (1975) 137-156.

[14] C.J. Batty, et. al., Phys. Lett. **74B**, (1978) 27.

[15] R.J. Powers, et. al., Phys. Rev. C **47**, (1993) 1263.

[16] C.J. Batty, E. Friedman, A. Gal, Physics Reports **287**, (1997) 385.

[17] J. K. Ahn, et al., Nucl. Phys. A **648**, (1999) 263.

[18] J. K. Ahn, et al., Nucl. Phys. A **761**, (2005) 41.

[19] Y. Kondo, et al., Nucl. Phys. A **676**, (2000) 371.

[20] R. Bertini, et al., Phys. Lett. **90B**, (1980) 375.

[21] S. Bart, et al., Phys. Rev. Lett. **83**, (1999) 5238.

[22] T. Harada, et al., Nucl. Phys. A **507**, (1990) 715.

[23] R. S. Hayano, et al., Phys. Lett. B **231**, (1989) 355.

[24] T. Nagae, et al., Phys. Rev. Lett. **80**, (1998) 1605.

[25] T. Harada, Nucl. Phys. A **672**, (2000) 181.

[26] T. Harada, Nucl. Phys. A **547**, (1992) 165c.

[27] P. K. Saha, et al., Phys. Rev. C **70** (2004) 044613.

[28] T. Harada, Y. Hirabayashi, Nucl. Phys. A **744**, (2004) 323.

[29] P. K. Saha, et al., Phys. Rev. Lett. **94** (2005) 052502.

[30] T. Y. Tretyakova, D. E. Lanskoy, Nucl. Phys. A **691** (2001) 51c.

[31] T. Harada, A. Umeya, Y. Hirabayashi, Phys. Rev. C **79** (2009) 014603-1.

[32] D. J. Millener, Lect. Notes. Phys. **724** (2007) 31; D. J. Millener, Nucl. Phys. A **804**, (2008) 84.

[33] M. Agnello, et al., Phys. Rev. Lett. **108**, (2012) 042501.

[34] R. H. Dalitz and R. Kevi-Setti, Nuovo Cimento 30, (1963) 489.

[35] L. Majling, et al., Nucl. Phys. A **585**, (1995) 211.

[36] Y. Akaishi, et al., Frascati Phyics Series, Vol. XVI, (1999) pp.59-74; private communication, 2001-2002.

[37] A. A. Korosheninnikov, et al., Phys. Rev. Lett. **87** (2001) 092501.

[38] S. I. Sidorchuk et al., Nucl. Phys. A **719** (2003) 13.

[39] M. S. Golovkov et al., Phys. Rev. C **72** (2005) 064612.

[40] G. M. Ter-Akopian et al., Eur. Phys. JA **25** (2005) 315.

[41] T. Hasegawa, et al., Phys. Rev. Lett. **74** (1995) 224.

[42] H. Hochi, et al., Phys. Rev. C**74** (2001) 0440302.

[43] K. H. Tanaka, et al., The technical report of the hadron experimental facility, KEK internal report 2007-1.

[44] K. Agari, et al., Prog. Theor. Exp. Phys. **2012**, 02B009

[45] T. Takahashi, et al., Nucl. Phys. A **835**, (2010) 88.

[46] Digital Teslameter 151 (DTM-151), http://www.group3technology.com

[47] S. Adachi, Master Thesis of Graduate school Kyoto Univ., (2009).

[48] M. Nakagawa, Master Thesis of Graduate school Osaka Univ., (2013).

[49] O. Sasaki and M. Yoshida, IEEE Trans. Nucl. Sci., vol. 46, (1999), 1871.

[50] Y. Unno, Nucl. Inst. and Meth. A **453**, (2000) 109.

[51] M. J. French, et al., Nucl. Inst. and Meth. A **453**, (2001) 359.

[52] R. Ota, Master Thesis of Graduate school Osaka Univ., (2012).

[53] Y. Igarashi, IEEE Trans. Nucl. Sci., vol. 52, (2005), 2866-2871.

[54] KEK Data Aquisition Development Working Group, KEK-PREPRINT-1985-10, Nov 1985.

[55] Y. Igarashi, IEEE Trans. Nucl. Sci., vol. 57 (2010), 618-624.

[56] EASIROC developed by Omega/IN2P3, http://omega.in2p3.fr/

[57] M. Shiozawa et al., IEEE Nucl. Sci. Symposium, vol. 2, (1994), 632-635.

[58] GE Fanuc, http://defense.ge-ip.com

[59] Electronics-2, http://www.hephy.at/project/electronics2/ELEC2/index.html

[60] Z-86 bag, http://kokorowo.shop-pro.jp/?pid=6204691

[61] Kuraray sintillation fiber, http:kuraraypsf.jp/index.html

[62] Hamamatsu Photonics K.K., http://www.hamamatsu.com/jp/ja/index.html

[63] R. Honda, et al., PoS PhotoDet2012 (2012) 031.

[64] T. Uchida, IEEE Trans. Nucl. Sci., vol. 55, (2008), 1631.

[65] BBT, http://www.bbtech.co.jp/index.html

[66] S. Morinobu, private communication

[67] J. Myrheim, L. Bugge, Nucl. Instr. Meth. **160**, (1979), 43-48.

[68] ANSYS, htpp://www.ansys.com

[69] Particle Data Group (PDG), htpp://www.pdg.lbl.gov

[70] D. H. Davis, Nucl. Phys. A **547**, Nucl. Instr. Meth. **160**, (1992), 369c.

[71] K. L. Brown, Ch. Iselin, D. C. Carey: Decay TURTLE, CERN 74-2 (1974), Urs Rohrer: Compendium of Decay Turtle Enhancements.

[72] K. Shirotori, et al., Phys. Rev. Lett. **109**, (2012) 132002.

[73] L. Myron, et al., Phys. Rev. **183**, (1969) 1142.

[74] ORIN I. Dahl, et al., Phys. Rev. **163**, (1967) 1430.

[75] T. Harada, Nucl. Phys. A **547**, (1992) 165c-174c.

[76] T. Harada, in the private communication (2014).

[77] T. Harada, Y. Hirabayashi, Nucl. Phys. A **759**, (2005) 143-169.

[78] M. Morimatsu, K. Yazaki, Prog. Part. Nucl. Phys. Vol. **33**, (1994) 679.

[79] T. Motoba et. al., Phys. Rev. C **49**, (1994) 1045.